From the holdings of the Department of Special Collections , Princeton University Library, Princeton, NJ

These documents are either in the public domain, or can only be used for educational and research purposes (Fair use) as per U.S. Copyright law (text below). By accessing this file, all users agree that their use falls in the public domain or within fair use as defined by the copyrightlaw. We do not charge any permission or usage fees for the publication of images of material inour collections, including those provided by Princeton University Library, via our website, catalog, or directly from staff.For more information regarding copyright, credit, and citation please review the information onthe Copyright, Credit and Citation Guidelines page of our website.
https://library.princeton.edu/special-collections/policies/copyright-credit-and-citation-guidelines. If you have any questions, including how to order higher-quality images from the collection, contact Special Collections Public Services via our Ask Us! Form. https://library.princeton.edu/special-collections/ask-us

---

Doctoral Dissertations, 2011-2026 Astrophysical Sciences

2022

The Dynamics of Stellar Wind-Driven Bubbles and Their Effect on Star Formation in Giant Molecular Clouds

Lancaster, Lachlan

Princeton, NJ : Princeton University

---

http://arks.princeton.edu/ark:/88435/dsp01nk322h567

U.S. Copyright law: The copyright law of the United States (Title 17, §108, United States Code) governs the making of photocopies or other reproductions of copyrighted material. Under certain conditions specified in the law, libraries and archives are authorized to furnish a photocopy or other reproduction. One of these specified conditions is that the photocopy or reproduction is not to be used for any purpose other than private study, scholarship, or research. If a user makes a request for, or later uses, a photocopy or reproduction for purposes in excess of fair use that user may be liable for copyright infringement. This institution reserves the right to refuse to accept a copying order if, in its judgment, fulfillment of the order would involve a violation of copyright law. https://www.copyright.gov/title17/title17.pdf

The Dynamics of Stellar Wind-Driven Bubbles and their Effect on Star Formation in Giant Molecular Clouds

Lachlan T. Lancaster

A Dissertation
Presented to the Faculty
of Princeton University
in Candidacy for the Degree
of Doctor of Philosophy

Recommended for Acceptance
by the Department of
Astrophysical Sciences
Adviser: Eve C. Ostriker

September 2022

© Copyright by Lachlan T. Lancaster, 2022.

All Rights Reserved

Abstract

Star formation in Giant Molecular Clouds (GMCs) is of fundamental importance to our understanding of star formation in our universe since it is in these massive, transient objects where almost all stars are formed. To understand the process of star formation in GMCs one must understand how star formation feedback from the massive stars that form within them acts to halt the star formation process. Massive stars ($M_* \gtrsim 8\,\mathrm{M}_\odot$) can inject significant amounts of energy in to the surrounding cloud, blowing apart the cloud and halting star formation. One way this can happen is when the radiative energy from these stars is injected directly in to their atmospheres, resulting in massive outflows moving at velocities of $> 1000\,\mathrm{km\,s^{-1}}$. These winds shock when they impact the ambient medium, creating highly over-pressurized, extremely hot $T \sim 10^8\,\mathrm{K}$ gas that expands rapidly in to the surrounding cloud. In this thesis, we seek to understand this process in the context of realistic star forming environments.

In this dissertation, we show how turbulent mixing between the wind-driven bubble and the surroundings can lead to efficient cooling at the $T \sim 10^4\,\mathrm{K}$ gas created through this mixing. We demonstrate that this cooling can be sufficient to cause the bubble's evolution to become momentum-driven, rather than energy driven, drastically decreasing the winds power to disperse its surroundings. In Chapter 2 we lay out the details of this theory, examine how the internal structure of the wind-driven bubble changes in this scenario, and show how such a theory would explain several outstanding observational mysteries. In Chapter 3, we validate this picture with a large suite of three-dimensional, hydrodynamic simulations. In Chapter 4 we test this theory in the context of self-gravitating, self-consistently star forming clouds and show that turbulent cooling is indeed the dominant mechanism for the removal of stellar wind energy. Finally, in Chapter 5 we present the final work of this thesis, where we investigate the effects of background magnetic fields and photo-ionized gas on this picture for stellar wind-driven bubble evolution before reviewing the prospects for future work in Chapter 6.

Acknowledgements

I would first like to thank my adviser, Eve Ostriker. I first set out to study physics out of a fascination with trying to understand our universe. As an undergraduate this drove me, at first, to studying high-energy physics. Realizing that this was an over-saturated field with diminishing experimental prospects for verifying the sea of potential theories, I came to astrophysics through cosmology, which I had thought would provide a link to the fundamental theories of the universe I had been so inspired by. Besides, there seemed to be excellent prospects for new and interesting data in astronomy. In my early career as a graduate student I tried several different projects on alternative cosmological theories as well as data-driven works. While these projects were interesting and fulfilling, the former often felt too separated from the physical world and the latter too separated from physics. I give this long-winded backstory here because, with the work of this dissertation, Eve showed me that there were problems to work on where I could have both of these things. I will be forever thankful to her for renewing my interest in physics. Besides this, Eve has been an exemplary mentor and advocate for my work, often, I have learned, doing this 'behind-the-scenes.' I also deeply appreciate Eve's patience with me at the beginning of my dissertation work, when I was learning a field of study that was almost entirely new to me.

The people who most deserve my thanks for their patience and their mentorship, along with Eve, are Jeong-Gyu Kim and Chang-Goo Kim. Without their consistently quick answering of my often simple questions, usually posed late at night, the work that I would have been able to complete in this thesis would have been much reduced or delayed. Their insights and expertise on numerical methods, as well as the nuances of C++ and python libraries are the reason that I have any myself.

I am also grateful to the several mentors I have had the distinct pleasure of working with throughout graduate school especially Jenny Greene, Yuan-Sen Ting, Philip Mocz, David Spergel, Vasily Belokurov, Sergey Koposov, and Wyn Evans. Without their help, I would have a significantly narrower view of astrophysics and of course would have missed out on the pleasure of working with them. The same can be said of my undergraduate mentors, Matthew Walker, Lloyd Knox, and Robert Swendsen, who introduced me to real scientific research for the first time.

Some of the best teachers throughout my academic career thus far have been my fellow students,

many of whom I have been fortunate to call close friends. Among many, I would especially like to thank Michael Matty, who inspired my more formal, mathematical approach to physics research, and Erin Kado-Fong for being my resource on talking through everything from interesting problems to simple mental roadblocks. I am additionally grateful for their close friendships along with those of Erin Flowers, Goni Halevi, Mackenzie Moody, and Amy Secunda. My many fellow graduate students at Princeton have also been excellent sources of knowledge and support especially, Christopher Bambic, Luke Bouma, Scott Carlsten, Rodrigo Córdova, Miles Cranmer, Roohi Dalal, Brianna Lacy, Zack Li, Alwin Mao, Eric Moseley, Kris Pardo, Oliver Philcox, Heather Prince, Vassilis Tsiolis, Samuel Yee, and Wenrui Xu; along with my fellow masters and undergraduate students, especially Joel Accorsi, Antón Baleato, Kate Borst, Connell Donaghy, Alexander Fritzsche, Alexander Gurvich, Paul Hamerski, Mithi de los Reyes, and Connor Richards.

Outside of my academic world I have been extremely lucky to be supported by a great group of excellent friends both in Princeton and around the world. First among these is my twin brother, Cameron, who's work you can actually find in this dissertation! Thanks for hanging out with your nerd brother. Thank you also to Al, Courtney, Greg, both Jakes, Max, Holly, Li and Travis, among many others who have helped me enjoy life, even when physics is really hard.

I am grateful for the endless pride and encouragement of my mom, Deborah, and my dad, Warren. My mom has been my fiercest and most tireless advocate throughout my life. It is thanks to her that I am now blessed[1] with a copy-editor's tolerance for bad grammar. Thankfully, this dissertation is too long to have all the commas checked by her. My dad was the first person who ever had to endure my endless questions about the world (the earliest one I can remember is 'Why does fire glow?'). Having a degree in physics himself, he did his best to answer these many questions, never trying to overly simplify things. If I have any talent for explaining things, it started with my dad. Now, I'm the one answering his questions!

Finally, I am thankful for the support and artistic direction of Megan Bednarczyk. Thank you for abiding my weekends of work, my needless explanations of random physics on walks, and my goofy sense of humor.

[1] read: cursed

Preface

This thesis consists of five chapters. The first chapter is a brief introduction to star formation in giant molecular clouds, the role that stellar winds play in that process, and a brief review of the current state of the field. The second through fourth chapters are all based on published articles, listed below. Chapter 5 consists of work that is not yet published but constitutes the final work in this thesis. Chapter 6 provides a brief review of possible future work.

Publications

1. Efficiently Cooled Stellar Wind Bubbles in Turbulent Clouds. I. Fractal Theory and Application to Star Forming Clouds
   Lachlan Lancaster, Eve C. Ostriker, Jeong-Gyu Kim, and Chang-Goo Kim
   (ApJ 914, 89)

2. Efficiently Cooled Stellar Wind Bubbles in Turbulent Clouds. II. Validation of Theory with Hydrodynamic Simulations
   Lachlan Lancaster, Eve C. Ostriker, Jeong-Gyu Kim, and Chang-Goo Kim
   (ApJ 914, 90)

3. Star Formation Regulation and Self-pollution by Stellar Wind Feedback
   Lachlan Lancaster, Eve C. Ostriker, Jeong-Gyu Kim, and Chang-Goo Kim
   (ApJL 922, L3)

I dedicate this dissertation to the many people who have helped and inspired me along the way, most of all my family, and to human wonder for the vastness of our universe and the beauty of the physical world, without which I certainly could not have written this.

Contents

Abstract . . . iii
Acknowledgements . . . iv
Preface . . . vi

1 Stellar Winds and Star Formation **18**

2 Fractal Theory for Efficiently Cooled Stellar Wind Bubbles **22**
2.1 Introduction . . . 22
2.2 Theory . . . 23
2.2.1 Classical Stellar Wind Bubble . . . 23
2.2.2 Pressure-Driven Bubble with Interface Cooling . . . 26
2.2.3 The Efficiently Cooled (EC) Solution . . . 29
2.2.4 The Turbulent Diffusivity . . . 33
2.2.5 Fractal Nature of the Turbulent Boundary Layer . . . 36
2.2.6 Conditions for Efficient Cooling . . . 39
2.3 Application to Star-Forming Clouds . . . 41
2.4 Discussion . . . 50
2.4.1 Observations . . . 50
2.4.2 Other models of momentum-driven bubbles . . . 53
2.4.3 Comparison to Radiative Feedback . . . 54
2.4.4 Other Physics . . . 56

2.5 Conclusion . . . 58
2.6 Appendix: The Wind Interior . . . 58

3 Validation of Theory with Simulations 62
3.1 Introduction . . . 62
3.2 Numerical Methods and Models . . . 64
3.2.1 Wind Injection . . . 64
3.2.2 Model Parameters and Set-Up . . . 67
3.3 Numerical Results . . . 70
3.3.1 Cloud and Bubble Structure and Thermal Distributions . . . 73
3.3.2 Gas Phase Definitions . . . 73
3.3.3 Bubble Evolution Comparisons . . . 75
3.3.4 Dimensionless Parameters . . . 83
3.3.5 Turbulent Structure Function . . . 88
3.3.6 Fractal Structure of Interface . . . 92
3.3.7 Cooling and Energetics . . . 101
3.4 Summary and Conclusion . . . 105
3.5 Appendix: Validation of Wind Implementation . . . 109
3.6 Appendix: Additional Tests . . . 109
3.6.1 Pure Thermal Feedback . . . 109
3.6.2 Reduced Mass Loss . . . 111
3.6.3 Changed Feedback Radius . . . 113
3.6.4 Different Turbulent Initial Conditions . . . 114
3.7 Appendix: Results for Different Mass Clouds . . . 118

4 Stellar Wind Regulated Star Formation 119
4.1 Introduction . . . 119
4.2 Methods . . . 122
4.2.1 Simulation Description . . . 125

4.3 Results . . . 126
4.3.1 Hot gas losses and cloud evolution . . . 126
4.3.2 Star Formation Efficiency . . . 131
4.3.3 Timescales . . . 140
4.3.4 Wind Pollution . . . 142
4.4 Summary and Discussion . . . 145
4.5 Appendix: Effects of Mass Limit on Feedback . . . 147
4.6 Appendix: Resolution Study . . . 152

5 The Effects of Magnetic Fields and H II Regions on the Dynamics of Wind-Driven Bubbles 155

5.1 Introduction . . . 155
5.2 Definitions . . . 156
5.3 Theory . . . 157
5.3.1 Stellar Wind Bubbles . . . 157
5.3.2 Spitzer Solution for an H II Region's Expansion . . . 163
5.3.3 Joint Evolution of Stellar Wind Bubbles and H II Regions . . . 166
5.4 Simulations . . . 168
5.5 Analysis and Results . . . 174
5.5.1 Momentum Evolution . . . 175
5.5.2 Bubble Radial Expansion . . . 181
5.5.3 Cooling . . . 185
5.5.4 Pressure . . . 189
5.5.5 Effective Mixing Velocity . . . 191
5.6 Discussion . . . 199
5.7 Appendix: Stages of Spherical Wind Expansion . . . 201
5.8 Appendix: Assumptions for Joint Evolution . . . 202
5.9 Appendix: Initial Conditions for Joint Evolution . . . 205

5.10 Appendix: Dimensionless Equation for Joint Evolution 207

6 Prospects for Future Work **210**

List of Figures

2.1 Schematic diagrams illustrating the structure of an expanding wind-driven bubble for (a) the classical pressure-driven bubble of Weaver et al. (1977), with a uniform background and cooling only at the leading shock; and (b) the case explored in the present work, where the background is a turbulent medium and there is efficient cooling at the interface between the wind and the shell. For both, the innermost region (i) is the same, consisting of a free-flowing (hypersonic) radial stellar wind. In both cases, there is strong shock in which much of the wind's kinetic energy is thermalized; outside of this is region (ii), consisting of hot, shocked stellar wind. Both phases of the stellar wind have low density and minimal cooling. In (b), dense clumps of gas create bow shocks which increase the overall obliquity of the shock front, so that the post-shock radial velocity remains higher. In (a), there is a contact discontinuity (and an evaporative flow, if conduction is included) at the interface between the shocked wind and the surrounding dense shell. In (b), the shocked wind flows into the dense shell, interacting strongly in a turbulent interface layer, which has a fractal structure. The intermediate-temperature mixture of hot shocked wind gas and dense shell gas cools rapidly and merges into the shell. In both (a) and (b), most of the mass in the shell consists of shocked ISM gas that has cooled down. The outermost region (iv) is ambient ISM gas, uniform in (a) but turbulent and inhomogeneous in (b). Image credit: Cameron Lancaster. 24

2.2 Temporal evolution of physical quantities for a wind-driven bubble in both the Weaver theory (dashed lines) and the theory presented here (solid lines). From top to bottom we show the bubble radius, the velocity and radial momentum of the swept-up gas surrounding the bubble, and the thermal pressure in shocked wind in the bubble interior. We consider a cloud with mass $M_{\rm cl} = 10^5 M_\odot$ and a radius of $R_{\rm cloud} = 20\,{\rm pc}$ (left panels) or $R_{\rm cloud} = 2.5\,{\rm pc}$ (right panels). The horizontal grey line in each of the top panels indicates the cloud radius. For every value we explore three different values of the mass of the star cluster driving the wind, $M_* = 10^3, 10^4, 10^5\,M_\odot$ in yellow, orange, and red respectively. 34

2.3 Evolution of several key wind quantities as calculated using the Starburst99 code (Leitherer et al., 1999). We show (a) the wind luminosity per unit mass of the star cluster, (b) mass-loss rate in the wind per unit stellar mass, (c) wind momentum injection rate per unit stellar mass, and (d) the ratio of wind momentum input rate to radiation momentum input rate. Solid lines show the result for a standard Kroupa IMF, dashed lines are for a "top-heavy" IMF in which $d\log N/d\log m$ is changed from -2.3 to -1.8 at $m > 0.5\,M_\odot$, and dotted lines show the results for a standard IMF but at low metallicity, $Z = Z_\odot/7$. 42

2.4 A comparison of several quantities as predicted by our theory (solid lines) and that of Weaver et al. (1977) (dashed lines). For the top two panels we show results as a function of cloud radius and star formation efficiency $\varepsilon_* = 1$, 10, 50%, while the bottom-left shows results for $M_* = 10^3, 10^4,\ 10^5 M_\odot$ (yellow, orange, and red respectively), using $M_{\rm sh} = 10^5 M_\odot$ for the dashed lines.. Panels show: *(a)* shell velocity $v_{\rm disp}$ when the bubble has reached the edge of the cloud; *(b)* time $t_{\rm disp}$ taken for this to occur; *(c)* the bubble interior pressure at this time. *(d)* the star formation efficiency needed to disperse the surrounding cloud. Here we show $\varepsilon_{*,{\rm disp}}$ as a function of $R_{\rm cl}$ for $M_{\rm cl} = 10^6$, $10^5\,M_\odot$ displayed as the thick and thin lines respectively. 43

3.1 Ratio of the wind parameters derived using the population synthesis code STARBURST99 (SB99) to the constant values for each parameter that we adopt in our simulations.The SB99 mass-loss rate and momentum input rate are respectively a factor ~ 5 and ~ 2 lower than the ones we adopt. We validate that using the SB99 values does not change our conclusions (see Appendix 3.6.2). 70

3.2 An example snapshot of the wind bubble structure and phase properties at time $t = 2.23\,\mathrm{Myr}$ after the initiation of the wind for the model with $M_{\rm cl} = 10^5\,M_\odot$, $R_{\rm cl} = 20\,\mathrm{pc}$, $\varepsilon_* = 1\%$, and $L_{\rm box}/\Delta x = 512$ simulation. The left and center columns show slices through the $z = 0$ plane, while the right column displays distributions. From left to right and top to bottom, panels show: gas number density, pressure, a cooling-weighted phase diagram of cooling time vs. pressure, radial momentum density, temperature, a volume-weighted temperature-density phase diagram, the wind mass fraction ($f_{\rm wind}$), the cooling rate per unit volume, and a cooling-weighted histogram of the gas temperature distribution (which depicts the total cooling occurring in each temperature bin). In the top-right panel, the highest concentration of cooling is in gas that has $t_{\rm cool} \propto P^{-1}$; this slope is indicated by a dashed red diagonal line for the coefficient in Equation 2.10 corresponding to $T_{\rm pk} = 9650\,\mathrm{K}$. The last panel uses vertical lines to delineate the phases described in Table 3.2, where the subscripts from the table are indicated. The label "wind" includes both the free (f) and post-shock (ps) wind phases. In this panel, $T_{\rm pk}$ is marked as a vertical dashed line within the "w" phase. 71

3.3 Same as Figure 3.2 but for the model with $M_{\rm cl} = 10^5\,M_\odot$, $R_{\rm cl} = 2.5\,\mathrm{pc}$, $\varepsilon_* = 100\%$, and $L_{\rm box}/\Delta x = 512$ simulation at $t = 0.125\,\mathrm{Myr}$. All quantities are as specified in Figure 3.2, though the range of many quantities are quite different. 72

3.4 Evolution of the total radial momentum of the bubble (interior plus shell) in each of our simulations for cases with cloud mass $M_{\rm cl} = 10^5 M_\odot$. Model cloud radii (from least dense, $R_{\rm cl} = 20\,{\rm pc}$, to most dense, $R_{\rm cl} = 2.5\,{\rm pc}$) are given within the individual panels (a) to (d); see Table 3.1 for parameters. For each case we show results for star cluster particles of mass $M_* = 10^3 M_\odot$, $10^4 M_\odot$, and $10^5 M_\odot$ (corresponding to star formation efficiencies of $\varepsilon_* = 1\%$, 10%, and 100%) in yellow, orange, and red respectively. At each value of $R_{\rm cl}$ and ε_* we show three separate lines (solid, dashed, dotted) corresponding to varying resolution, as shown in the key. For each simulation with 512^3 cells, we mark the time at which the first wind-polluted gas exits the simulation domain $t_{\rm esc}$ with a square, and only show results from each simulation up until $4t_{\rm esc}$ (though not all of the highest resolution simulations were run for this long). For each value of $R_{\rm cl}$ and ε_* we show $\dot{p}_w t$ (which should apply when cooling is maximally efficient, per Equation 2.14) in black. 76

3.5 Evolution of the effective radius $\mathcal{R}_b$ in each of our simulations for cases with cloud mass $M_{\rm cl} = 10^5 M_\odot$. Line styles are as in Figure 3.4. For each value of $R_{\rm cl}$ and ε_* we show (in black) the evolution prediction from the EC theory (Equation 2.19, with $\alpha_R = \alpha_p = 1$). The grey horizontal lines indicate $R_{\rm cl}$, while squares indicate the time when wind-contaminated gas first leaves the domain ($t_{\rm esc}$). As in Figure 3.4, we only show simulation results up until $4t_{\rm esc}$. 78

3.6 Evolution of the total energy in the interior of the bubble in each of our simulations for cases with cloud mass $M_{\rm cl} = 10^5 M_\odot$. Line styles are as in Figure 3.4. For each value of $R_{\rm cl}$ and ε_* we show in black the energy given by Equation 2.20 (taking $\mathcal{S} = \alpha_p = \alpha_R = 1$ and using Equation 2.19). 80

3.7 Evolution of the pressure in the shocked wind gas in cases with cloud mass $M_{\rm cl} = 10^5 M_\odot$. All panels show the evolution of the volume averaged mean pressure (solid colored lines) along with shading the $16^{\rm th}$ to $84^{\rm th}$ percentiles of the distribution of pressures in post-shock gas (colored shaded regions). We show the theoretical prediction (Equation 2.21, with $\alpha_p = 1$) in black. The time at which wind first escapes the domain is indicated by a colored square. 82

3.8 Evolution of the momentum (α_p) and energy ($\mathcal{S}$) enhancement factors shown as solid and dashed lines respectively. The evolution of α_p is only shown up to the point of breakout, which is indicated with colored squares on the curves for $\mathcal{S}$. We indicate the 'no enhancement' case with the horizontal black line. We show the highest resolution version of all simulations with $M_{\rm cl} = 10^5\, M_\odot$. 84

3.9 Evolution of the dimensionless parameter α_R. Line colors are associated with simulations of different ε_*. We use the highest resolution version of all simulations with $M_{\rm cl} = 10^5\, M_\odot$ and only show the evolution up to the point of breakout (square markers in Figure 3.4 and others). 85

3.10 Evolution of the ratio of turbulent kinetic energy to kinetic energy in radial motion, for shell gas. We show the highest resolution version of all simulations with $M_{\rm cl} = 10^5\, M_\odot$. The square symbols mark the point at which wind-polluted mass begins to leave the domain. 86

3.11 Magnitude of the tangential velocity in snapshots of the $R_{\rm cl} = 20\,{\rm pc}$ models at the time in each simulation when $\mathcal{R}_b = R_{\rm cl}/3$. The separate columns (left to right) are the $\varepsilon_* = 1\%$, 10%, and 100% cases. The hot gas (Shocked Stellar Wind and Ionized Gas) is shown with the purple-to-yellow color scale while the cold gas (Warm, Thermally Unstable, and Cold Gas) is shown with the green color scale. The top row of panels is a zoom-in of the bottom row, which itself zooms in on just the bubble region, to highlight the structure of turbulence in the bubble/shell interface. 89

3.12 Temporal evolution of the structure function of turbulent velocities in the hot gas (Shocked Stellar Wind and Ionized Gas) in the first 1 Myr of the simulation for the $R_{\rm cl} = 20\,{\rm pc}$, $M_{\rm cl} = 10^5 M_\odot$ simulations. The separate panels (left to right) are the $\varepsilon_* = 1\%, 10\%,$ and 100% cases. Temporal evolution is indicated by the color of the lines in each panel, moving from early times (dark blue) to the late times (bright green) in increments of 10^4 yrs. The characteristic velocity scale of the turbulence decreases in time and varies by at most a factor of 2 over the course of the simulation. The characteristic spatial scale of the structure function increases over time. Turbulent velocities are overall higher for higher wind power ($\mathcal{L}_w \propto \varepsilon_*$) models. 90

3.13 The structure function of turbulent velocities in the hot gas (Shocked Stellar Wind and Ionized Gas) when $\mathcal{R}_b = R_{\rm cl}/3$. These are measured in the highest resolution versions of all simulations with $M_{\rm cl} = 10^5 M_\odot$ and we show the simulations with $\varepsilon_* = 1\%, 10\%, 100\%$ in yellow, orange, and red respectively. For each panel we show scales from $4\Delta x$ to $R_{\rm cl}$ (solid lines) as well as the $25^{\rm th}$ to $75^{\rm th}$ percentiles of structure function measurements over the ensembles of 200 samples from the hot gas. In each panel we show in black the structure function of the background turbulent gas scaled up by a factor $20(R_{\rm cl}/20\,{\rm pc})^{1/2}$. The velocity scale of the turbulence is set by the strength of the wind (represented here by ε_*) while the characteristic length scale of the turbulence is likely set by the bubble size and turbulent density structure of the background. 91

3.14 The excess fractal dimension of the bubble surface as a function of scale using the two measurement techniques described in the text (see Section 3.3.6 and Section 3.3.6). *Left panel:* The excess fractal dimension of the bubble surface measured using a box-counting technique; boxes at different scales mark where cooling is taking place. *Right Panel*: The excess fractal dimension measured based on the logarithmic scaling of the area of an iso-temperature surface ($T = 10^5\,{\rm K}$ for all curves shown here) when measured on different scales. 93

3.15 The ratio of bubble surface area $A_b(T, \ell)$ to fractal area $4\pi\mathcal{R}_b^2(\mathcal{R}_b/\ell)^{1/2}$ as $\mathcal{R}_b(t)$ evolves in time. We only show the evolution up to the point of wind breakout. We set $\ell = 32\Delta x$ and measure the area for several iso-temperature surfaces as marked in key. Results for α_A from taking the area ratio (see Equation 3.20) are shown for $M_{\rm cl} = 10^5 M_\odot$, $R_{\rm cl} = 10\,{\rm pc}$ and $\varepsilon_* = 1\%$, 10%, and 100%. The near-constancy of α_A in time, especially at $\varepsilon_* = 10\%$ and 100%,is an excellent indication that a fractal with $d = 1/2$ describes the geometry of the bubble well. 97

3.16 The average value of the dot product of the outward normal vector to the bubble surface with the radial vector, which we term the "foldedness" of the bubble surface. The degree to which this is less than one quantifies the amount that the surface is "inward facing" or "crumpled." The same models are used as for Figure 3.15, along with the same calculations of the bubble iso-temperature surfaces. We also show $4\pi\mathcal{R}_b^2/A_b(10^6\,{\rm K}, 32\Delta x)$ in black. The degree to which the black curve matches the other curves reflects how close the effective area, $A_{\rm eff}$ is to the equivalent spherical surface $4\pi\mathcal{R}_b^2$. 98

3.17 The fraction $1 - \Theta$ of the input wind energy that is retained in the bubble and shell, including both kinetic and thermal terms, as a function of time. We show results for the $R_{\rm cl} = 20\,{\rm pc}$ in the top row and $R_{\rm cl} = 10\,{\rm pc}$ in the bottom row (both with $M_{\rm cl} = 10^5 M_\odot$), for $\varepsilon_* = 1\%$, 10%, and 100%. The time when the wind breaks out of the simulation box is denoted in each panel by a colored vertical line. The colored solid lines in each panel denote $1 - \Theta$ measured via the energy conservation method, while the dotted lines denote the same quantity measured using cooling in wind-polluted ($f_{\rm wind} > 10^{-4}$) gas. The shaded areas in each panel delimit the range expected from EC wind theory (see text). The black line in each panel shows the theoretical prediction from Equation 2.25 with values of $f_{\rm turb}$, $\mathcal{S}$, α_p, and α_R determined as described in Section 3.3.4. 100

3.18 Evolution of quan1tities related to the flow into and through the turbulent mixing/cooling boundary layer between the bubble and the background. The expected radial velocity (Equation 2.64) of shocked wind gas advected into the fractal interface is shown as dashed lines. The "equivalent velocity" of gas transiting the mixing/cooling layer (Equation 2.35 with $d = 1/2$) is shown as solid lines, including a factor of 0.25 chosen to match the dashed lines. These curves are shown for the model with $M_{\rm cl} = 10^5 M_\odot$, $R_{\rm cl} = 20$, and all ε_*. We use $\ell_{\rm min} = 8\Delta x$ for the measurement scale of the turbulent structure function. 104

3.19 Wind implementation tests for a uniform background, shown for a snapshot 10^4 yrs after the start of wind feedback. We show profiles (every cell is plotted) of pressure (top left), number density (top right), and velocity magnitude (bottom left) in radius for both the adiabatic run (in blue) and the run with cooling (red). The Weaver et al. (1977) solution for fully adiabatic evolution is shown in green for these same panels. In the bottom right panel we show a slice of number density through the $z = 0$ plane of the simulation for the run with cooling. One can clearly see the cooled, dense shell that has formed at the outer edge of the wind bubble. The Weaver et al. (1977) solution for the radius of the shell in the case that gas in the leading shock cools is indicated as a magenta circle. 110

3.20 Tests run with purely thermal energy injection, in comparison to the hybrid scheme explained in the main text. All panels are analogous to the top panels shown in Figure 3.21. Results using the hybrid injection scheme (thermal scheme) are shown with solid (dashed) lines. The evolution of the total radial momentum, p_r is very slightly delayed for the thermal scheme compared to the hybrid feedback mechanism, but reaches the same scaling by the time the bubble radius is $2 - 3$ pc. 112

3.21 Results of our test runs with smaller mass loss rates ($\dot{M}_w/M_*$). The top panels show comparisons to the EC theoretical predictions (black) for the bubble's effective radius (left), total radial momentum (middle), and total energy in the bubble interior (right) for simulations run with $\varepsilon_* = 1\%$ (yellow), 10% (orange), and 100% (red). The bottom panels show quantities related to the ratio of the simulated and theoretically predicted values (see Section 3.3.4). 113

3.22 Results of tests with standard ($r_{\rm fb} = 1\,{\rm pc}$, solid curve) and and smaller ($r_{\rm fb} = 0.5\,{\rm pc}$, dashed curve) feedback radius. All panels are analogous to those shown in Figure 3.20. There is excellent agreement amongst all quantities, indicating that the changed feedback radius (higher source resolution) does not impact our results. . . . 114

3.23 Results of our test runs comparing different initial realizations of the turbulent velocity field, which creates different cloud density structure. All panels are analogous to those shown in Figure 3.20 except here we use a linear scale for time. This choice is so as to not overemphasize differences in the early evolution which are due to differences in the density structure very near to the source particle. We show the original initialization as solid lines and the alternate initialization as dashed lines. There is clearly very good agreement at later times between the evolution, in spite of different density structures. 115

3.24 Comparisons of our theory (black curves) to our simulations (colored curves) for cases with cloud mass $M_{\rm cl} = 5\times10^4 M_\odot$ and (from top to bottom row) $R_{\rm cl} = 20\,{\rm pc}$, $10\,{\rm pc}$, $5\,{\rm pc}$, and $2.5\,{\rm pc}$. Columns from left to right show the bubble's effective radius, $\mathcal{R}_b$, the total radial momentum, p_r, and the total energy in the bubble interior E_b. All curves are calculated exactly analogously to those in Figure 3.5, Figure 3.4, and Figure 3.6. 116

3.25 Same as Figure 3.24 for cases with $M_{\rm cl} = 5\times10^5 M_\odot$. 117

4.1 Snapshots from simulations at the time when 75% of the final stellar mass has formed. Models **R20** to **R2.5** are shown from left to right, with all simulations shown here having the same initial turbulence realization (with differing amplitudes). *Top row*: the integrated gas surface density, together with projected locations of star particles colored by age with size scaled by mass. The "active" star particles producing winds are shown as stars while inactive star particles are shown as circles. *Bottom row*: slices of gas temperature (centered on the center of mass of the star particles). . . . 123

4.2 Evolution of the energy, momentum, and bubble radius from model **R20** (top row) and **R5** (bottom row) for the same simulations shown in Figure 4.1.The time axis is shifted to coincide with the formation of the first star particle in each model. The ticks at the top of each panel (vertical thin lines in the upper right panel) indicate certain key times: $t_{\rm pr}$, when enough momentum to disperse the cloud has been acquired (yellow, see Equation 4.2); $t_{\rm SF}$, when 95% of the stellar mass has formed (green); $t_{\rm br}$, when breakout occurs (blue); and $t_{\rm dest}$, when the cloud has been effectively destroyed (fuchsia). *Left Column*: The breakdown of input wind energy "spending" over time, normalized by the instantaneous wind luminosity. Losses due to cooling (dark purple), bulk advection off the grid (red), and the luminosity fraction retained on the grid (teal) are shown. *Middle Column*: The total radial momentum in wind-polluted ($f_{w,\rm grid} > 10^{-4}$) gas for the cold/warm component (blue), the hot component (red), and the equivalent momentum injected by winds for a single source (yellow). The reference radial momentum required to disperse the cloud ($p_{r,\rm esc}$) is indicated as a horizontal dotted line. *Right Column*: The effective bubble radius for the simulations, as defined in the text (red lines), with reference predictions for delta-function and linear SFHs (solid and dashed black lines respectively). 127

4.3 The final SFE realized in our simulations in comparison to analytic models. For each simulation parameter set (see Table 4.1) we show the median SFE as a point, with the range of the SFEs from all runs shown by the vertical error bars. Predictions for the SFE based on several different models are shown, as labeled. For lognormal-based models, solid lines denote $\sigma_{\ln \Sigma} = 1.5$ and dashed lines denote $\sigma_{\ln \Sigma} = 0.75$ (see text). 139

4.4 Timescales of key events, as measured in the simulations (see Section 4.3.3 for definitions); values are shown in units of the free-fall time. Lines of constant physical time are also shown as thin grey lines. The prediction of Thompson & Krumholz (2016) for $t_{\rm SF}$ is shown as beige lines for $\sigma_{\ln \Sigma} = 1.5$ (0.75) in solid (dashed) line styles. 141

4.5 Evolution of the global fraction of wind mass $f_{\rm wind}$ in the gas (solid lines), in the stars overall (dashed lines), and in individual star particles (points, where more opaque points indicate more massive star particles). We show results as a function of time in units of the initial free-fall time (top row), and as a function of the fraction of the final stellar mass that has formed (bottom row). For the individual star particles, we show the fraction of their *initial* mass in wind material as a function of the time when they first formed (or fraction of stellar mass formed when they first formed, in the bottom row). Each panel also includes $f_{\rm wind}$ in gas from other models as thin, transparent lines. We show $f_{\rm wind}$ for the gas (stars) as opaque curves up until $t_{\rm br}$ ($t_{\rm SF}$), after which more transparent lines are shown. We note that the dashed lines include *all* star particles, even those with negligible enrichment that do not appear on this plot. 143

4.6 A comparison of results from different methods of assigning wind luminosity to star particles. Line style denotes the assignment method (see text). For each model, we show mass of gas on the grid (black), mass of stars (yellow), and mass that has flowed out of the simulation domain (red). The shaded regions show the range of histories given by the higher resolution simulations described in the main body of the text, which differ from one another only in the random phases used to generate the initial turbulent velocity field. 150

4.7 A resolution study of key history parameters for model **R10**. The line style denotes results from simulations with low resolution (dotted), fiducial resolution (dashed), and high resolution (solid). *Upper left*: wind energy losses and retained fraction (see labels), as in left column of Figure 4.2. *Upper right*: radial momentum carried in cool/warm gas and hot gas, along with the net momentum injected by the wind, as in middle column of Figure 4.2. *Lower left*: effective radius of the wind driven bubble, as in the right column of Figure 4.2. *Lower right*: mass history, showing total gas mass on the grid, gas advected out of the domain, and stellar mass, as in Figure 4.6. Also shown is the mass of stars above $M_{\rm cut} = 10^3$ $M_\odot$, which produces winds. 151

5.1 Similar to Figure 3 of Kim et al. (2016), we present the force exerted by the bubble in our joint evolution model as a function of $\mathcal{R}_w/R_{\rm ch}$. In black we show the actual force exerted in the joint evolution model of Section 5.3.3, given by the right hand side (RHS) of Equation 5.25. We show approximations to this equation for $\mathcal{R}_w > R_{\rm ch}$ (Equation 5.32) and $\mathcal{R}_w < R_{\rm ch}$ (Equation 5.31). In blue we show the force exerted by an efficiently cooled wind, $\alpha_p \dot{p}_w$, in red we show the force in the Spitzer solution (RHS of Equation 5.20), we show the sum of these in purple. 165

5.2 We show slices through the $z = 0$ plane of our high resolution simulations, with $L_{\rm box}/\Delta x = 512$ at approximately the time when $\mathcal{R}_w = L_{\rm box}/6$. The rows give snapshots from each of four simulations, from top to bottom these are: `Hydro`, `MHD`, `Hydro Rad`, and `MHD Rad`. The columns show slices of different physical quantities, from left to right these are: (i) total pressure, including thermal and magnetic terms as appropriate, (ii) radial momentum of the gas, (iii) the total volumetric radiative cooling, and (iv) a schematic that separates the slice into different phases, indicated by color. 169

5.3 We show the radial momentum measured in each of our $L_{\rm box}/\Delta x = 256$ simulations. In each panel we show the evolution of the `Hydro` (blue), `Hydro Rad` (red), `MHD` (green), and `MHD Rad` (orange) runs. Squares on each simulation curve indicate the time when wind material first begins to leave the simulation domain, we should not expect our idealized simulations to apply after this point. We also show the expected theoretical radial momentum evolution in the Weaver model given by Equation 5.4 (black line) and the Efficiently Cooled model, given by Equation 5.5, with $\alpha_p = 3$ (black dashed line). *Left panel*: Total radial momentum evolution carried in wind-polluted material with $f_{\rm wind} > 10^{-4}$. *Right panel*: Total excess radial momentum in simulation, measurement described in text. 173

5.4 We show the evolution of the total radial momentum carried by the H II region for the `Hydro Rad Only` (purple) and `MHD Rad Only` (yellow) simulations. The simulations shown here have a resolution of $L_{\rm box}/\Delta x = 512$. Squares on each line indicate the time at which significant momentum begins to leave the simulation domain. We compare this evolution with the predicted radial momentum evolution for the Spitzer solution, as given by Equation 5.23 (red dotted line) and the adjusted Spitzer solution as given by Equation 5.24 (black dotted line). The adjusted solution is clearly a better match to the momentum evolution of the simulated H II regions. It is important to note that, unlike Figure 5.3, we use a linear scale here, which de-emphasizes the earliest time evolution. 177

5.5 We show a comparison of the momentum evolution of the `Hydro Rad` and `MHD Rad` simulation at $L_{\rm box}/\Delta x = 256$ resolution to various theoretical models. The evolution shown here is the same as that shown in the right panel of Figure 5.3 for these simulations. Squares on these curves indicate the time at which the wind bubble breaks out from the simulation domain. For theoretical comparisons we show (i) the adjusted Spitzer solution given in Figure 5.4 (black dotted line), (ii) the sum of this adjusted Spitzer solution and the momentum from a $\alpha_p = 3$ EC solution (black dot dashed line), and (iii) two different solutions to the ODE given by Equation 5.25 with different assumed initial conditions, discussed in Section 5.9 (blue and brown lines). The colors shown here for these ODE solutions correspond to the same colors and line-styles shown in Figure 5.15. 179

5.6 We show the evolution of the effective radii of the wind-driven bubbles in each of our simulations with stellar wind feedback. Color coding is identical to Figure 5.3 with squares indicating the time at which wind material begins to leave the simulation domain. For comparison we show the radial evolution of a wind-driven bubble according to the Weaver et al. (1977) solution, given by Equation 5.2 (black line) and the EC solution with $\alpha_p = 3$ (black dashed line). We also show the prediction for the wind bubble's evolution from the ODE solutions described in Section 5.10. Color coding here is identical to Figure 5.5. These curves are shifted forward in time so that they begin at t_E, the time at which the wind bubble is in equilibrium with the H II region, as described in Section 5.8. 181

5.7 We show the evolution of the effective radii of the full feedback bubbles (wind-driven bubble and H II region) in each of our simulations with both stellar winds and photo-ionizing radiation feedback. Color coding is identical to Figure 5.3 with squares indicating the time at which wind material begins to leave the simulation domain. For comparison we show the radial evolution of a D-type H II region given by the Spitzer solution, Equation 5.22. We also show the prediction for the feedback bubble's evolution from the ODE solutions described in Section 5.10. The model solution shown here are identical to those shown in Figure 5.6. 183

5.8 The evolution of the net integrated cooling displayed as a fraction of the net injected wind energy and split up by phase. The phases include (i) the 'Background' (dark blue) which is a sum of net cooling across the CNM/Molecular phase, the thermally unstable phase, and the WNM phase, (ii) the H II region (orange), (iii) the WHIM (yellow), and (iv) the wind-driven bubble's interior (dark red). Color coding for the WHIM and H II region phases correspond to the same coloring in the schematic phase plots of Figure 5.2. Panels represent the (clockwise from top left) `Hydro`, `Hydro Rad`, `MHD Rad`, and `MHD` simulations. Results show here are for the simulations run at $L_{\rm box}/\Delta x = 256$ resolution. In the panels on the right, we indicate t_E with a vertical grey line. Finally, we indicate the times at which wind material first begins to break out of the cloud as a vertical black line in each panel. 186

5.9 The fraction of the total injected wind energy that is retained within the simulation domain as a function of time for the same simulations displayed in Figure 5.8. As in other figures, the squares indicate the times at which the wind-driven bubble first breaks out to the simulation domain. As guides we also indicate the equilibrium time, t_E, and an evolution proportional to $t^{-1/2}$. 187

5.10 The pressure in the hot, shocked stellar wind in each simulation as a function of time (top panel) and the wind-driven bubble's effective radius (bottom panel). Squares indicate when the win-driven bubbles first breakout of the simulation domain. For comparison we show the pressure evolution of a EC wind-driven bubble, as given by Equation 5.8 (black dashed line) and the pressure evolution expected for an H II region according to the Spitzer Solution (black dotted line). We also indicate t_E (top panel) and $R_E = R_{\rm EC}(t_E)$ (bottom panel) with vertical grey lines. 190

5.11 The excess fractal dimension of the wind-driven bubbles in each of our simulations with stellar wind feedback at a spatial resolution of $L_{\rm box}/\Delta x = 512$. We measure d using the 'Area Method' of Fielding et al. (2020) and Lancaster et al. (2021a) with an iso-temperature surfaces at $T = 10^5\,{\rm K}$ and on scales $\ell = 8\Delta x \approx 0.6\,{\rm pc}$. 192

5.12 The scale of turbulent motions in the hot, shocked wind gas in each of our simulations with stellar wind feedback at a spatial resolution of $L_{\rm box}/\Delta x = 512$. Turbulent motions are measured on a spatial scale $\ell = 8\Delta x \approx 0.6\,{\rm pc}$, details given in text. . . 194

5.13 The effective mixing velocity, $v_{\rm eff}$, calculated using Equation 5.36 along with the measurements presented in Figure 5.11 and Figure 5.12 (solid lines) in each of our simulations with wind feedback. We compare this with the mean radial velocity of gas in the shocked wind gas as it reaches the mixing layer, calculated using Equation 5.37. We also include a scaled version of the $v_{\rm eff}$ measurements, equivalent to a choice of α_C in Equation 5.13, and chosen so that the scaled $v_{\rm eff}$ measurements best match the $v_{\rm ps}(\mathcal{R}_w)$ measurements (translucent solid lines). The values of α_C chosen are 0.4, 0.6, 0.75, and 0.6 for the `Hydro`, `Hydro Rad`, `MHD`, and `MHD Rad` simulations respectively. It is important to note that the results for the `Hydro` simulation are shown on a much larger scale than the other simulations. 196

5.14 The momentum enhancement factor of the wind-driven bubble as predicted using Equation 5.7. For reference we indicate $\alpha_p = 3$ with a horizontal grey line. 198

5.15 We examine solutions to our equation for an effective joint evolution of a wind-driven bubble and an H II region, Equation 5.49. *Left Panel*: For an assumed value of $\eta = 6.63$ (appropriate for the simulations presented in Section 5.5) we examine the effects of the various initial conditions proposed in Section 5.9, relative to the Spitzer solution, Equation 5.53. *Right Panel*: We compare our numerical solution for Equation 5.49 with the initial conditions corresponding to the solid, light blue line in the left panel, to the Spitzer solution for several values of η. 207

Chapter 1

Stellar Winds and Star Formation

Star formation is a notoriously inefficient process, with only a few percent of the gas mass in galaxies being converted to stellar mass over the relevant gravitational timescales (e.g. Kennicutt, 1998; Krumholz & Tan, 2007; Evans et al., 2009; Murray, 2011; Vutisalchavakul et al., 2016; Lee et al., 2016; Barnes et al., 2017; Utomo et al., 2018; Kruijssen et al., 2019). This inefficiency is thought to be caused and regulated by feedback from stars which inject mass, momentum, and energy to their surroundings. This injection happens from the scale of protostellar outflows in cores (e.g. Matzner & McKee, 2000; Bally, 2016; Offner & Chaban, 2017), to individual massive stars in their natal clouds (e.g. Rogers & Pittard, 2013; Geen et al., 2015b; Haid et al., 2018), to star clusters in galactic disks (e.g. Kim et al., 2013; Kim & Ostriker, 2017; Hennebelle & Iffrig, 2014; Gatto et al., 2017), with many different processes playing important roles.

On the scale of giant molecular clouds (GMCs), feedback is thought to be dominated by energy provided to the ISM by massive stars early in their lives (e.g. Krumholz et al., 2019; Girichidis et al., 2020; Chevance et al., 2020a). This energy can inject momentum in a number of forms. Primarily-outward photon momentum is imparted to gas and dust where stellar UV and optical radiation is primarily absorbed, known as 'direct radiation pressure' (e.g. Wolfire & Cassinelli, 1987; Krumholz & Matzner, 2009; Raskutti et al., 2016). That same momentum can be used again when dust grains re-radiate the absorbed energy in the infrared, 're-processed radiation pressure' (e.g.

Thompson et al., 2005; Murray et al., 2010; Skinner & Ostriker, 2015; Menon et al., 2022). Warm gas heated by photo-dissociating/ionizing radiation creates an over-pressured bubble that pushes on the surrounding medium, creating ionized and neutral outflows, 'photo-ionized gas pressure' (e.g. Whitworth, 1979; Franco et al., 1994; Matzner, 2002; Kim et al., 2018, 2021a). Finally, the radiation energy from hot stars can be injected directly in to their own atmospheres, resulting in high-velocity outflows which shock as they collide with the ambient gas: stellar winds (e.g. Avedisova, 1972; Castor et al., 1975; Weaver et al., 1977; Koo & McKee, 1992a,b; Vink et al., 2001).

The importance of these mechanisms has been debated in the recent observational literature, with several studies attempting to assess the relative contributions. This includes observations of evolved clusters in the Large Magellanic Cloud (LMC) by Pellegrini et al. (2011); Lopez et al. (2011, 2014); McLeod et al. (2019), in the Milky Way (Rosen et al., 2014), in nearby 'normal' galaxies (McLeod et al., 2020; Chevance et al., 2022), and in nearby galaxies with more extreme star-forming environments (Levy et al., 2020). The recent works of Olivier et al. (2020) and Barnes et al. (2020) have sought to make the same evaluation but at very early times (in deeply embedded clusters) in the Milky Way.

Prior to these recent empirical studies inter-comparing different feedback effects, earlier observations suggested that the X-ray luminosities of nebulae were too low to be explained by standard wind models (Dunne et al., 2003; Townsley et al., 2003, 2006, 2011). Other works sought to explain this deficit (Garcia-Segura et al., 1996a; Capriotti & Kozminski, 2001; Mackey et al., 2015; Toalá & Arthur, 2018; El-Badry et al., 2019), suggesting turbulent mixing and radiative cooling as sinks of energy, and Harper-Clark & Murray (2009) appealing to the leakage of hot wind gas out of the cloud interior due to turbulence-induced porosity.

The topic of star formation feedback in GMCs has also enjoyed much theoretical work over the past several years. While several recent efforts have used numerical radiation hydrodynamic simulations for in-depth studies of the effects of radiation feedback on star-forming clouds (Dale et al., 2012, 2013; Walch et al., 2012; Raskutti et al., 2016, 2017; Howard et al., 2017; Kim et al., 2018, 2019a, 2021a; Grudić et al., 2020; Geen et al., 2021; Fukushima et al., 2020), there have been

fewer detailed numerical studies of stellar wind feedback. These have included one-dimensional (1D) numerical models (Garcia-Segura et al., 1996a,b; Silich & Tenorio-Tagle, 2013; Krause et al., 2016; Fierlinger et al., 2016; Rahner et al., 2017) some of which have incorporated phenomenological accounts of three-dimensional processes such as energy leakage (Harper-Clark & Murray, 2009) and turbulent diffusivity that leads to cooling (El-Badry et al., 2019). These problems have also been explored in two-dimensional (2D) studies, which have sought to examine filamentation at reduced computational expense (Wünsch et al., 2008; Ntormousi et al., 2011; Dwarkadas & Rosenberg, 2013; Dwarkadas, 2022). Finally, numerical investigations of stellar wind feedback effects in 3D have ranged from targeted studies of winds (Rogers & Pittard, 2013; Wareing et al., 2017; Krause et al., 2013; Krause & Diehl, 2014; Dale & Bonnell, 2008; Dale et al., 2013), to comparisons of winds and photo-ionization heating over a range of parameter space (Dale et al., 2014; Geen et al., 2015b; Haid et al., 2018; Geen et al., 2021). These simulations have contributed to assessments of the relative contribution of winds in a number of scenarios and over a range of densities and cloud masses. Some have additionally tried to constrain the relative contribution of leakage and turbulent mixing.

The aim of this thesis is to expand upon this work by giving a focused numerical and theoretical analysis of the dynamics of stellar wind-driven bubbles. We aim to build a more fundamental understanding of these dynamics through a research program that builds in complexity: starting from the simplest realistic situation for bubble dynamics and using the knowledge gained at each step to inform the next. At each step we use numerical simulations that accurately treat the complex physics we are considering and use these simulations to inform and test the much simplified theoretical models that we develop in tandem. Star formation feedback is an inherently non-linear process, with many different interacting physical effects. It is our hope that through this incremental approach we can attempt to form a full theoretical picture of these dynamics.

The thesis thus proceeds by first developing, in Chapter 2, a theoretical model for how stellar-wind bubbles can lose significant fractions of their energy to radiative cooling at turbulent mixing layers when the wind-driven bubble is being blown in the highly inhomogeneous density structure of GMCs. We posit that such mixing leads to very efficient cooling, causing the stellar wind

driven bubbles to be momentum-driven. In Chapter 3 we test this model against a large suite of three-dimensional (3D) hydrodynamic simulations and show that the predictions of our model hold remarkably well. The next step in our approach, Chapter 4, consists of testing this efficient-cooling hypothesis in the context of self-gravitating and self-consistently star forming clouds, where star formation is regulated solely by stellar wind feedback. This also allows us to investigate how material injected by stellar winds can be mixed in to their surroundings and find their way in to subsequently formed stars. Finally, in Chapter 5, we return to our idealized, single wind-driven bubble picture in order to understand how the presence of magnetic fields and the addition of photo-ionizing radiative feedback change the dynamics of the bubble.

The drawback of our incremental approach is that, at each step, we have only developed a partial picture of reality. This means that observational comparison to the as-yet developed theory we always be accompanied by caveats. However, we believe with the work of Chapter 5 completed, we will have included sufficient physical realism in our models for meaningful comparison against existing observations of star-forming regions. This is the most important avenue for our next steps.

Chapter 2

Fractal Theory for Efficiently Cooled Stellar Wind Bubbles

2.1 Introduction

In this chapter, we present a model for the evolution of bubbles driven by stellar winds in the presence of strong interface cooling, induced by turbulent mixing. Turbulent motions in the hot gas are derived from the kinetic energy of the wind, with Kelvin-Helmholz and other instabilities growing at interfaces with the dense cloud material, itself highly structured due to background turbulence. Motivated by recent work on turbulent cooling-mixing layers in the context of multiphase galactic winds and the circumgalactic medium (Gronke & Oh, 2018; Fielding et al., 2020; Tan et al., 2021), we argue that this cooling can be very strong, removing up to 99% of the injected energy. The cooling is strong enough to make the dominant phase of the bubble evolution momentum-driven (i.e. $p \propto t$). Our model therefore differs significantly from the well-known Weaver et al. (1977) solution, which is energy-driven ($E \propto t$, with energy conserved interior to the bubble). Building on previous models for momentum-driven winds (Steigman et al., 1975), we derive predictions for the evolution of important quantities such as the bubble's size and expansion rate, the momentum

carried by the swept-up gas exterior to the bubble, and the energy and pressure interior to the bubble. Our goals are to characterize the dependence of bubble evolution on input wind power and ambient cloud properties, and to explain the physical mechanisms controlling the evolution.

In Chapter 3 we present numerical simulations to validate the theory we develop here, and to constrain its few free parameters. We have, by design, simplified the problem under consideration. Our model ignores the effects of magnetic fields and extended star formation (in both space and time, see Chapter 4). Real astronomical systems of course have multiple sources of energy and additional physical elements (such as magnetic fields and strong stellar radiation, see Chapter 5). By tackling a simpler problem, however, we are able to develop a theoretical framework and make quantitative predictions that can be applied to interpret observations of star-forming clouds. We regard this as a valuable first step towards comprehensive understanding of the role of winds within the array of feedback processes.

The structure of this chapter is as follows. In Section 2.2 we lay out the details of our theory for evolution of wind-driven bubbles in the turbulent ISM. In Section 2.3 we provide a guide to applying our theory in interpreting observations. Finally, we place our work in context in Section 2.4, and conclude with a summary of our findings in Section 2.5.

2.2 Theory

In this section we briefly review previous analytic theory of stellar wind bubble evolution and then provide an in-depth explanation of our new theory.

2.2.1 Classical Stellar Wind Bubble

The classical solution for the structure and evolution of the bubble produced by a constant luminosity wind expanding into a uniform background medium was described by Weaver et al. (1977) (see also e.g. Avedisova, 1972; Castor et al., 1975; McCray & Kafatos, 1987). We focus on the pressure driven (PD) stage of evolution. This stage was traditionally thought to characterize most of the evolution when a wind-blown bubble is produced in a star-forming cloud by a single massive star

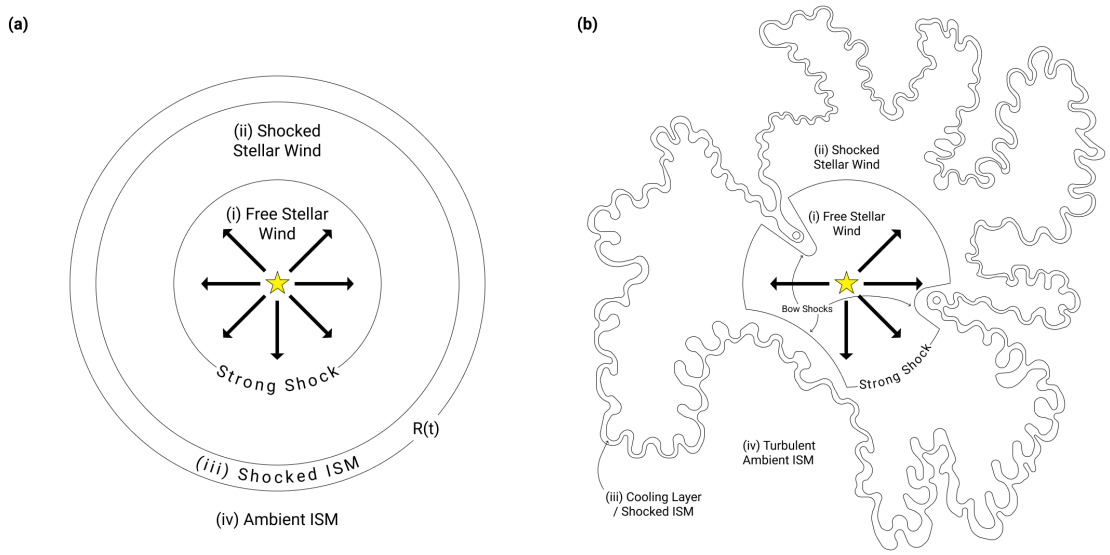

Figure 2.1 Schematic diagrams illustrating the structure of an expanding wind-driven bubble for (a) the classical pressure-driven bubble of Weaver et al. (1977), with a uniform background and cooling only at the leading shock; and (b) the case explored in the present work, where the background is a turbulent medium and there is efficient cooling at the interface between the wind and the shell. For both, the innermost region (i) is the same, consisting of a free-flowing (hypersonic) radial stellar wind. In both cases, there is strong shock in which much of the wind's kinetic energy is thermalized; outside of this is region (ii), consisting of hot, shocked stellar wind. Both phases of the stellar wind have low density and minimal cooling. In (b), dense clumps of gas create bow shocks which increase the overall obliquity of the shock front, so that the post-shock radial velocity remains higher. In (a), there is a contact discontinuity (and an evaporative flow, if conduction is included) at the interface between the shocked wind and the surrounding dense shell. In (b), the shocked wind flows into the dense shell, interacting strongly in a turbulent interface layer, which has a fractal structure. The intermediate-temperature mixture of hot shocked wind gas and dense shell gas cools rapidly and merges into the shell. In both (a) and (b), most of the mass in the shell consists of shocked ISM gas that has cooled down. The outermost region (iv) is ambient ISM gas, uniform in (a) but turbulent and inhomogeneous in (b). Image credit: Cameron Lancaster.

or cluster. In this evolutionary stage, energy injected by the wind builds up within the expanding bubble's interior, stored in hot gas that is highly over-pressured relative to the ambient surrounding cloud. As it expands into the ambient medium, the over-pressured bubble performs work on the background medium, accelerating ambient gas and collecting it in a dense shell surrounding the low-density bubble interior. Provided that the bubble expansion is supersonic with respect to ambient gas (always true for the cold gas in giant molecular clouds [GMCs]), the ambient gas is initially shocked to high temperature, then rapidly cools down to condense into the shell that surrounds the hot bubble interior.

Weaver et al. (1977) divide the structure of the solution into four distinct regions:

(i) Free Hyper-Sonic Wind

(ii) Shocked Stellar Wind

(iii) Shocked, Cooled Shell of Interstellar Gas

(iv) Ambient Interstellar Gas;

this structure is laid out schematically in panel (a) of Figure 2.1.

Under the assumption that all of the thermal energy created in the leading shock is radiated away while the bubble interior remains non-radiative, the similarity solution for the bubble radius is

$$R = R_{\rm W}(t) \equiv \left(\frac{125}{154\pi}\right)^{1/5} \left(\frac{\mathcal{L}_w t^3}{\bar{\rho}}\right)^{1/5}, \tag{2.1}$$

where $\mathcal{L}_w$ is the wind luminosity, $\bar{\rho}$ is the mass density of the background, and t the time. We use the "W" subscript to denote the Weaver solution. The dimensionless prefactor is approximately 0.76. During a short-lived earlier stage before the shocked ambient gas cools (analogous to the Sedov-Taylor stage of a supernova remnant), the self-similar solution for the outer radius has the same form, but with a dimensionless prefactor 0.88.

The pressure in the shocked stellar wind evolves as

$$P = P_{\rm W}(t) \equiv \frac{5}{22\pi} \left(\frac{125}{154\pi}\right)^{-3/5} \left(\frac{\mathcal{L}_w^2 \bar{\rho}^3}{t^4}\right)^{1/5}. \tag{2.2}$$

In the PD bubble solution, the radial momentum carried by the shell[1] is given by

$$p_r = p_{\rm W}(t) \equiv \frac{4\pi}{5}\left(\frac{125}{154\pi}\right)^{4/5}\left(\mathcal{L}_w^4\bar{\rho}t^7\right)^{1/5}\,. \tag{2.3}$$

Of the total wind energy $\mathcal{L}_w t$ emitted up to time t, nearly half (45%) is stored in thermal energy in the bubble interior:

$$E_{\rm th,W} = \frac{3}{2}P_{\rm W}V_W = \frac{5}{11}\mathcal{L}_w t\,, \tag{2.4}$$

where V_W is the volume of the bubble in this solution. Meanwhile a much smaller fraction (19%) has gone into the kinetic energy of the swept-up shell

$$E_{\rm kin,W} = \frac{1}{2}M_{\rm sh}\left(\frac{dR_{\rm W}}{dt}\right)^2 = \frac{15}{77}\mathcal{L}_w t \tag{2.5}$$

where $M_{\rm sh} = 4\pi\bar{\rho}R^3/3$ assuming all the swept-up gas is concentrated in the shell. The remaining $27/77 \approx 35\%$ of the wind energy is presumed to be radiated away from ISM gas that was shocked as it was swept into the advancing front of the bubble, and then cooled efficiently at high density. It is important to note that in the simplest version of the PD bubble solution, radiative cooling *only* occurs for post-shock, swept-up ISM gas. However, Weaver et al. (1977) do also discuss late-stage evolution when the interior of the bubble drops to low enough temperature that it becomes radiative.

2.2.2 Pressure-Driven Bubble with Interface Cooling

It is widely appreciated that it is difficult to maintain an idealized contact discontinuity, as exists in the classical PD bubble solution, between hot, diffuse gas in the bubble interior (shocked wind) and cool, dense gas of the shell surrounding it (swept-up ISM) (e.g. Garcia-Segura et al., 1996a; Capriotti & Kozminski, 2001). Turbulent motions at this interface, arising from ISM turbulence or from nonlinear development of instabilities (e.g. Vishniac, 1983, 1994; Vishniac & Ryu, 1989; Blondin et al., 1998; Bucciantini et al., 2004; Folini & Walder, 2006; Ntormousi et al., 2011; Michaut

[1]Throughout this work we will treat the total radial momentum of a given solution as synonymous with the radial momentum in the swept up shell, as the momentum in the bubble interior is negligible.

et al., 2012; Sano et al., 2012; Pittard, 2013; Badjin et al., 2016), will mix together the hot and cool gas. Given the efficiency of cooling at the resulting intermediate temperatures, most of energy carried into the interface by the hot gas would be radiatively cooled away.

El-Badry et al. (2019) used this fact to derive a simple modification to the PD bubble evolution for the case in which a fraction θ of the wind luminosity is lost to radiation due to turbulent mixing at the interface between the hot interior and the dense shell of the bubble:

$$\theta \equiv \frac{\mathcal{L}_{\rm int}}{\mathcal{L}_w}\,, \tag{2.6}$$

where $\mathcal{L}_{\rm int}$ denotes the total radiative loss from the interface. Allowing for these losses, and assuming that θ is constant in time, the overall bubble evolution follows the same form as in Equation 2.1 - Equation 2.5 with the substitution $\mathcal{L}_w \rightarrow (1-\theta)\mathcal{L}_w$. This solution has the same dependence that the Weaver solution has on all of the relevant parameters. For example, the shell radius and outward radial momentum would follow

$$R_{\rm EB}(t) \equiv \left(\frac{125}{154\pi}\right)^{1/5} \left(\frac{\mathcal{L}_w(1-\theta)t^3}{\bar{\rho}}\right)^{1/5} \tag{2.7a}$$

$$p_{\rm EB}(t) \equiv \frac{4\pi}{5}\left(\frac{125}{154\pi}\right)^{4/5} \left[(1-\theta)^4\mathcal{L}_w^4\bar{\rho}t^7\right]^{1/5}\,. \tag{2.7b}$$

We note that physically, the bubble expansion is still assumed to be primarily driven by the thermal pressure of the interior, just at a reduced rate.

The interface cooling, $\mathcal{L}_{\rm int}$, is quite distinct from the energy that is lost to radiation as shocked ISM gas cools down and joins the outside of the shell. In the El-Badry et al. (2019) solution, the radiative losses at the leading shock become $(27/77)(1-\theta)\mathcal{L}_w$, i.e. the same fraction of "available" energy is still lost to cooling in the swept-up, shocked ISM (region (iii) in Figure 2.1 panel *a*). To make this distinction more explicit we will define the total fraction of energy that is lost to radiative cooling as

$$\Theta \equiv \frac{\dot{E}_{\rm cool}}{\mathcal{L}_w}\,. \tag{2.8}$$

For the El-Badry et al. (2019) solution, $\Theta = 0.35 + 0.65\theta$ and thus[2] $1 - \Theta = 0.65\,(1 - \theta)$.

El-Badry et al. (2019) evaluated θ in the case where the mixing is governed by an effective turbulent diffusivity $\kappa_{\rm eff} = \lambda \delta v$, where the right-hand side represents the product of a spatial (λ) and velocity (δv) scale of turbulence in the mixing layer. Since the simulations were spherical, $\kappa_{\rm eff} = \lambda \delta v$ was treated as an arbitrary parameter, and a range of values were explored.

Based on a combination of predicted scaling relations and numerical measurements, El-Badry et al. (2019) showed that θ depends on the ambient medium density $\bar{\rho}$ and cooling rate $\Lambda(T_{\rm pk})$ at the temperature of maximal cooling, $T_{\rm pk}$, as

$$\frac{\theta}{1-\theta} \approx (\kappa_{\rm eff} \bar{\rho})^{1/2} \left[\frac{\Lambda(T_{\rm pk})}{(k_B T_{\rm pk})^2} \right]^{1/2} \tag{2.9}$$

where k_B is the Boltzmann constant.

The pressure is relatively constant in a mixing/cooling interface, but the temperature varies. It is useful to define the minimum cooling time as

$$t_{\rm cool} \equiv \frac{P}{n^2 \Lambda(T_{\rm pk})} = \frac{(k_B T_{\rm pk})^2}{P \Lambda(T_{\rm pk})}\,, \tag{2.10}$$

It is straightforward to show that Equation 2.9 is equivalent to $\theta/(1-\theta) \approx 1.1 (\kappa_{\rm eff}/t_{\rm cool})^{1/2} / \dot{R}_{\rm EB}$ for the modified PD bubble solution.

We further note that the El-Badry et al. (2019) simulations included classical microphysical ("Spitzer") thermal conduction in addition to turbulent diffusivity. As discussed in that paper (following Weaver et al., 1977), nonzero thermal conduction leads to evaporation of gas from the interface into the hot interior, which results in an increase of the hot gas mass and a decrease of its temperature (with pressure unchanged).[3] The thermal conduction does not lead to significant cooling because the conduction is only important at high temperatures when cooling is weak. The cooling that does occur is a result of turbulent mixing.

[2]Here, we use 0.65 (0.35) as approximate shorthand for 50/77 (27/77).

[3]Ablation (by conduction or Kelvin-Helmholz instabilities) of clouds that have been shocked and overtaken by the expanding high-velocity wind bubble can also add mass to the hot gas (e.g. Cowie & McKee, 1977; Klein et al., 1994; Scannapieco & Brüggen, 2015; Schneider & Robertson, 2017; Gronke & Oh, 2018).

2.2.3 The Efficiently Cooled (EC) Solution

We now suppose that the energy losses in the bubble/shell interface are so extreme that the PD regime is no longer relevant. A schematic of this scenario is given in Figure 2.1 panel *b*. In this limit, the mixing (and subsequent radiative cooling) of the shocked wind and dense shell gas is extremely efficient, so that little or no energy builds up in the interior of the bubble. When cooling is maximal, only momentum conservation need be considered. We adopt the term "efficiently cooled" (EC) to describe the solution in this limit.

Given a constant mechanical luminosity $\mathcal{L}_w$ and mass loss rate $\dot{M}_w$, the wind has asymptotic velocity $\mathcal{V}_w$ and momentum input rate $\dot{p}_w$ given by

$$\mathcal{V}_w \equiv \left(\frac{2\mathcal{L}_w}{\dot{M}_w}\right)^{1/2} \tag{2.11}$$

and

$$\dot{p}_w \equiv \mathcal{V}_w \dot{M}_w = 2\mathcal{L}_w/\mathcal{V}_w = \left(2\mathcal{L}_w \dot{M}_w\right)^{1/2} . \tag{2.12}$$

These parameters fully determine the fluid variables in the free wind (section (i) of Figure 2.1 panel b). For the shocked wind (section (ii) of Figure 2.1 panel b), in Section 2.6 we assume a steady subsonic radial flow to evaluate the fluid variables.

In the limit that no energy is able to build up within the wind bubble, the momentum evolution of the shell surrounding the bubble is entirely determined by the input momentum $\dot{p}_w$. In reality, the actual momentum can be somewhat larger than the input wind momentum, though we expect these deviations to be small. We parameterize any enhancement via a "momentum enhancement factor" α_p (the fundamental free parameter of our theory), and write the momentum equation as

$$\frac{d}{dt}\left(M_{\rm sh}\langle v_r\rangle\right) = \alpha_p \dot{p}_w \tag{2.13}$$

where $M_{\rm sh}$ is the mass swept into a shell by the expanding bubble from the ambient ISM and $\langle v_r\rangle$ is the mass-weighted average radial velocity of that swept-up gas. Assuming that α_p and $\dot{p}_w$ are

constant in time, the radial momentum of the shell is therefore

$$p_r = \alpha_p p_{\rm EC} \equiv \alpha_p \dot{p}_w t = 2\alpha_p \frac{\mathcal{L}_w}{\mathcal{V}_w} t \,, \tag{2.14}$$

where $p_{\rm EC}$ is the result for the case when $\alpha_p = 1$, when cooling is maximally efficient.

It is reasonable to assume, given the statistical homogeneity of the turbulent background mass density field, that the swept-up mass is approximately the product of the volume of the bubble and the mean background density

$$M_{\rm sh} \approx V_b \bar{\rho} \,. \tag{2.15}$$

Given the statistical isotropy of the background turbulence, it is also reasonable to assume that $\langle v_r \rangle$ is mainly dependent on the rate of change of the bubble volume and not on its specific geometry. To this end we define the bubble's "effective radius" as

$$\mathcal{R}_b \equiv \left(\frac{3V_b}{4\pi} \right)^{1/3} \tag{2.16}$$

and assume that

$$\langle v_r \rangle \approx \frac{d\mathcal{R}_b}{dt} \,. \tag{2.17}$$

The deviation from equality in Equation 2.15 and Equation 2.17 are essentially geometric and mostly driven by the inhomogeneity and anisotropy of the surrounding gas. For example, the bubble might preferentially expand in directions where the ambient gas has lower density, so that $M_{\rm sh} < V_b \bar{\rho}$.

We now rewrite Equation 2.13 as

$$\frac{d}{dt} \left(\frac{4\pi}{3} \bar{\rho} \mathcal{R}_b^3 \frac{d\mathcal{R}_b}{dt} \right) = \alpha_R \alpha_p \dot{p}_w \tag{2.18}$$

where α_R is an order-unity parameter that accounts for any departure from equality in Equation 2.15 and Equation 2.17. We note that, unlike the case for other parameters related to energy (see below), there is not a direct relationship between α_R and α_p. However, as we show in Chapter 3, α_R is very close to 1 for our simulated bubbles. Taking α_R to be approximately constant, Equation 2.18

can be integrated to obtain

$$\mathcal{R}_b(t) = \left(\frac{3\alpha_R\alpha_p}{2\pi}\frac{\dot{p}_w t^2}{\bar{\rho}}\right)^{1/4} \equiv (\alpha_R\alpha_p)^{1/4} R_{\rm EC}\,. \tag{2.19}$$

Here, $R_{\rm EC}$ denotes the solution for an exactly spherical bubble expanding in an uniform ambient medium when the shell momentum is taken to increase at a constant rate $\dot{p}_w$, as has been derived by many authors (e.g. Steigman et al., 1975; Koo & McKee, 1992a,b; Kim et al., 2017a); this would apply in the limit of no energy build-up within the bubble interior.

We now wish to determine the energetics of the bubble interior. In Section 2.6 we give a derivation of the expected values for the fluid variables in the bubble interior under the assumption of spherical geometry with a perpendicular shock dividing the free wind from the post-shock subsonic, steady, radial downstream flow.

Under these assumptions the energy of the bubble interior can be expressed as

$$E_b = \frac{1}{2}\dot{p}_w \mathcal{S}\mathcal{R}_b = (\alpha_R\alpha_p)^{1/4}\mathcal{S}E_{b,\rm EC}\,. \tag{2.20}$$

Here, $E_{b,\rm EC} = \dot{p}_w R_{\rm EC}/2$ is the bubble energy in the case where the bubble is occupied solely by the free wind, with $\mathcal{S} = \alpha_p = 1$. More generally, $\mathcal{S}$ encodes the extra energy contained within the bubble ($\mathcal{S} > 1$ when $\alpha_p > 1$), with Equation 2.70 and Equation 2.67 relating $\mathcal{S}$ to α_p. $\mathcal{S}$ is approximately linear in α_p, with $\mathcal{S} \approx \alpha_p$ within 6%.

The pressure in the shocked wind is nearly constant, equal to its immediate post-shock value, $3\dot{p}_w/(16\pi\mathcal{R}_f^2)$, where $\mathcal{R}_f$ is the outer radius of the free wind region, defined analogously to Equation 2.16. Written in terms of $\mathcal{R}_b$ and α_p, this is

$$P_b = \frac{3\dot{p}_w}{16\pi\mathcal{R}_b^2}\left[\frac{2}{3}\alpha_p + \left(\left(\frac{2}{3}\alpha_p\right)^2 - \frac{1}{3}\right)^{1/2}\right], \tag{2.21}$$

where the term in square brackets is $\approx (3\alpha_p - 1)/2$ within 4% for the range $1 \leq \alpha_p \leq 4$ we find in Chapter 3.

We now consider the kinetic energy of the shell driven by the bubble. If we assume that the vast majority of the input momentum at any time is stored in the shell, we may write its radial kinetic energy as:

$$E_{\rm r,sh} = \frac{p_r^2}{2M_{\rm sh}} = \frac{3\left(\alpha_p \dot{p}_w t\right)^2}{8\pi\bar{\rho}\mathcal{R}_b^3} = \frac{\alpha_p}{4\alpha_R}\dot{p}_w\mathcal{R}_b. \tag{2.22}$$

The ratio of the bubble interior's energy to the radial kinetic energy of the shell is only weakly dependent on time as

$$\frac{E_b}{E_{\rm r,sh}} = 2\frac{\alpha_R}{\alpha_p}\mathcal{S}\,, \tag{2.23}$$

which should be approximately 2 since $\mathcal{S} \approx \alpha_p$ and $\alpha_R \sim 1$. This can be compared to the ratio between Equation 2.4 and Equation 2.5, which is equal to $7/3 = 2.3$. Thus, even though the EC solution has two (or more) orders of magnitude lower energy than the Weaver solution because most energy is radiated away, the ratio of interior to shell energy is comparable.

In addition to expanding radially, the shell may also acquire turbulent motion, such that $E_{\rm sh} = E_{\rm r,sh} + E_{\rm turb,sh}$ is its total kinetic energy. This shell turbulence is a side-effect of the interface instabilities that induce mixing and cooling. There is no *a priori* prediction for the turbulent energy, but we can describe the level of turbulent energy relative to the radial kinetic energy as

$$f_{\rm turb} \equiv \frac{E_{\rm turb,sh}}{E_{\rm r,sh}}\,. \tag{2.24}$$

With this definition, the total energy of the shell plus bubble interior (neglecting the small thermal energy of the shell) will be $E_{\rm sh} + E_b = (1 + f_{\rm turb} + 2\alpha_R\mathcal{S}/\alpha_p)E_{\rm r,sh}$.

We can use the above to formulate an expression for the fraction of the energy input rate lost to cooling, Θ. From conservation of energy, the energy that is *not* lost to cooling is $\mathcal{L}_w\int(1-\Theta)dt$, and this must be equal to $E_{\rm sh} + E_b$. Using Equation 2.12 and Equation 2.22 and taking a derivative in time, we obtain

$$1 - \Theta = \left(\frac{1}{2}(1 + f_{\rm turb})\frac{\alpha_p}{\alpha_R} + \mathcal{S}\right)\frac{\dot{\mathcal{R}}_b}{\mathcal{V}_w}\,. \tag{2.25}$$

Evidently, because $\dot{\mathcal{R}}_b \propto t^{-1/2}$, the fraction of energy available after cooling is expected to be initially large, but decreasing in time. Correspondingly, the fraction Θ of energy lost to cooling

is expected to be initially small, but increasing with time. In the EC solution, the bubble energy increases as $E \propto \mathcal{R}_b \propto t^{1/2}$; this may be contrasted with $E \propto t$ in classical wind-driven bubble solutions.

Since the dimensionless prefactor in Equation 2.25 is order-unity, the fraction of energy retained $(1 - \Theta)$ is comparable to the ratio of the shell expansion velocity to the original wind velocity $(\dot{\mathcal{R}}_b/\mathcal{V}_w)$, which we show (in Chapter 3) drops to $\sim 1\%$ or lower over time for bubbles expanding in the dense environments of star-forming clouds.

Having explained the evolution of the main physical quantities in the EC theory, we illustrate the significant differences between our theory and that of Weaver et al. (1977) (reviewed in Section 2.2.1) in Figure 2.2. Specifically, we show the evolution of the bubble's radius (or $\mathcal{R}_b$ in our theory), the velocity, and radial momentum carried by the swept-up gas, and the pressure in shocked wind in the bubble's interior. We show results for three different wind strengths (set by $M_* = 10^3,\ 10^4,\ 10^5 M_\odot$), considering a cloud with mass $M_{\rm cl} = 10^5 M_\odot$ and radius $R_{\rm cl} = 20\,{\rm pc}$ or $R_{\rm cl} = 2.5\,{\rm pc}$. The mean ambient density for the larger (smaller) cloud is $n_H = 86\,{\rm cm^{-3}}$ ($n_H = 4.4 \times 10^4\,{\rm cm^{-3}}$). For all cases the central source has specific luminosity $\mathcal{L}_w/M_* = 10^{34}\,{\rm erg\ s^{-1}\ M_\odot^{-1}}$ and specific mass loss rate of $\dot{M}_w/M_* = 10^{-2.5}\,{\rm Myr^{-1}}$, based on Starburst99 (Leitherer et al., 1999). As shown below in Figure 2.3, these values are appropriate for the first $\sim 2.5\,{\rm Myrs}$ of star cluster evolution at solar metallicity. We have assumed $\alpha_R = \alpha_p = \mathcal{S} = 1$ for this comparison, so $\mathcal{R}_b$ is equivalent to $R_{\rm EC}$. The difference between our theory and that of Weaver et al. (1977) is striking. In particular, for the radial momentum and interior pressure, the predictions differ by factors of 10-100.

2.2.4 The Turbulent Diffusivity

We now consider expectations for the properties of the mixing layer and magnitude of the effective diffusivity $\kappa_{\rm eff}$. In general, a mixing/cooling interface layer of thickness $L_{\rm mc}$ must have a balance between diffusion of energy at volumetric rate $\sim \kappa_{\rm eff} P/L_{\rm mc}^2$ and radiative losses at volumetric rate $\sim n^2\Lambda = P/t_{\rm cool}$ in the mixed gas. For resolved interface layers with a range of $\kappa_{\rm eff}$, El-Badry et al. (2019) numerically evaluated profiles and found $L_{\rm mc} \approx 2(\kappa_{\rm eff} t_{\rm cool})^{1/2}$, consistent with this expectation; this $t_{\rm cool}$ is is based on the maximal cooling rate at a given pressure, defined in

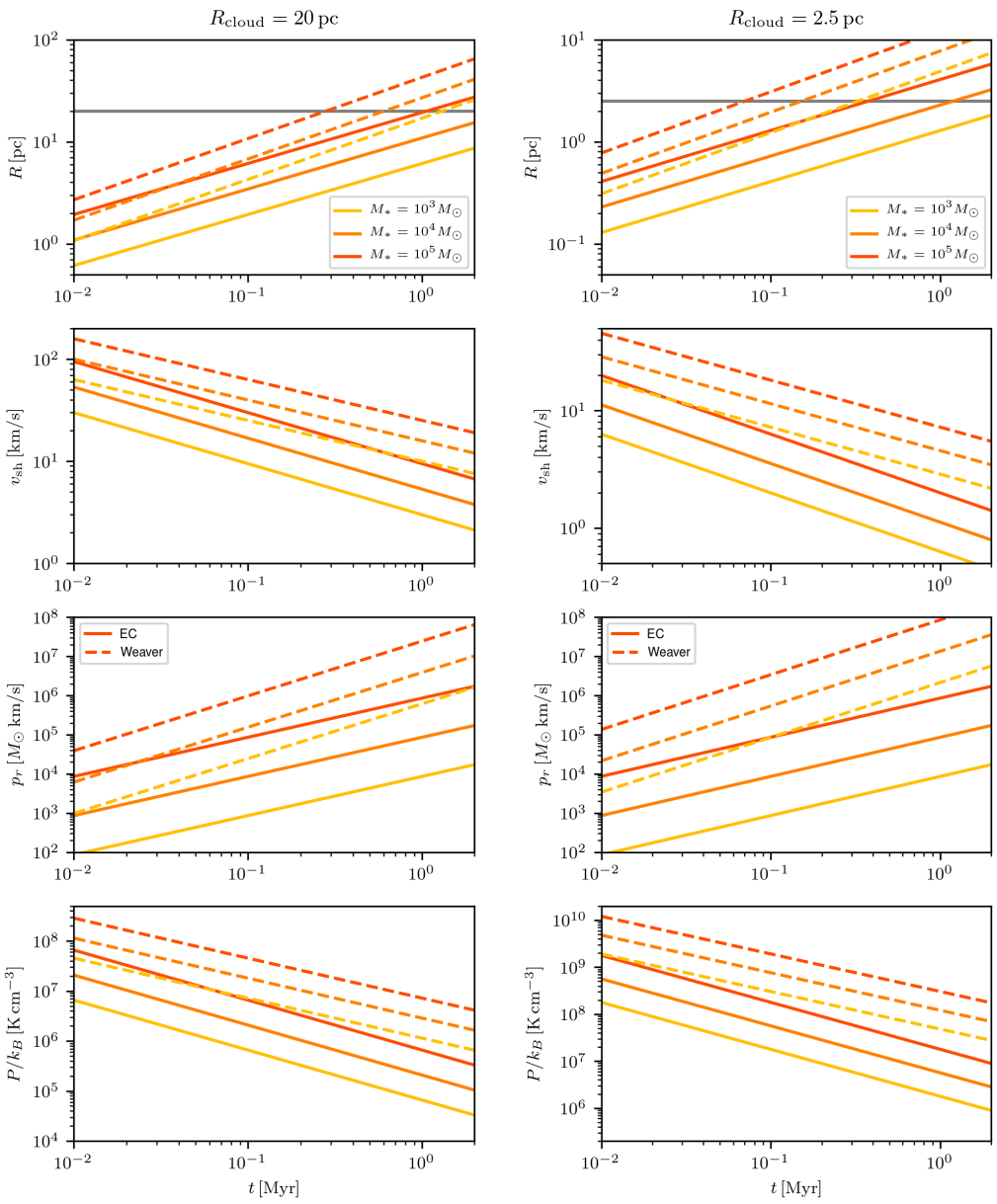

Figure 2.2 Temporal evolution of physical quantities for a wind-driven bubble in both the Weaver theory (dashed lines) and the theory presented here (solid lines). From top to bottom we show the bubble radius, the velocity and radial momentum of the swept-up gas surrounding the bubble, and the thermal pressure in shocked wind in the bubble interior. We consider a cloud with mass $M_{\rm cl} = 10^5 M_\odot$ and a radius of $R_{\rm cloud} = 20\,{\rm pc}$ (left panels) or $R_{\rm cloud} = 2.5\,{\rm pc}$ (right panels). The horizontal grey line in each of the top panels indicates the cloud radius. For every value we explore three different values of the mass of the star cluster driving the wind, $M_* = 10^3, 10^4, 10^5\,M_\odot$ in yellow, orange, and red respectively.

Equation 2.10.

If we consider a flow entering a mixing/cooling interface at velocity $v_{\rm rel}$, it carries an enthalpy flux $(5/2)v_{\rm rel}P$. This flux must be balanced by the cooling per unit area, $n^2\Lambda L_{\rm mc} = PL_{\rm mc}/t_{\rm cool}$. Equating these rates, we obtain $v_{\rm rel} = (2/5)L_{\rm mc}/t_{\rm cool} \approx 0.8(\kappa_{\rm eff}/t_{\rm cool})^{1/2}$.

What sets $\kappa_{\rm eff}$? A turbulent boundary layer would in general have a range of physical scales ℓ, with corresponding velocities $v_t(\ell)$.[4] The spectrum of velocity fluctuations is usually assumed to follow a power law,

$$v_t(\ell) = v_t(L)\left(\frac{\ell}{L}\right)^p \tag{2.26}$$

where p is the power-law index of this scaling, L is the largest scale on which this turbulent structure function applies, and $v_t(L)$ is the velocity at that scale.

At scale ℓ, the eddy-turnover (or flow-crossing) time is

$$t_e(\ell) \equiv \frac{\ell}{v_t(\ell)} = \left(\frac{\ell}{L}\right)^{1-p}\frac{L}{v_t(L)} = \left(\frac{\ell}{L}\right)^{1-p} t_e(L). \tag{2.27}$$

Since $p < 1$ in general, $t_e(\ell)$ increases with ℓ. Thus, if the cooling time is short enough that $t_{\rm cool} < t_e(L) = L/v_t(L)$, there always exists some scale $\ell_{\rm cool}$ such that $t_{\rm cool} = t_e(\ell_{\rm cool}) = \ell_{\rm cool}/v_t(\ell_{\rm cool})$ is satisfied. In the language of Tan et al. (2021), this condition is the same as saying that the Damköhler Number is greater than 1, which is generally true in our simulations (see Chapter 3). As noted by Fielding et al. (2020), it is this critical scale, which has $\ell_{\rm cool} = v_t(\ell_{\rm cool})t_{\rm cool}$, that is most relevant for mixing-mediated cooling. Turbulent eddies at $\ell > \ell_{\rm cool}$ will be too slow to directly mix gas in a way that enables rapid cooling, while eddies at $\ell < \ell_{\rm cool}$ will simply further enhance mixing. Thus, the most relevant value for the effective turbulent diffusivity is

$$\kappa_{\rm eff} = \ell_{\rm cool}v_t(\ell_{\rm cool}) = t_{\rm cool}[v_t(\ell_{\rm cool})]^2\,. \tag{2.28}$$

Using this diffusivity, the thickness of the mixing/cooling layer would be $L_{\rm mc} \approx 2\ell_{\rm cool}$ and the

[4]Here, $v_t(\ell)$ refers to turbulence in the hot gas; Fielding et al. (2020) discusses the relation between turbulent amplitudes in the hot and cool (mixed) gas.

inflow velocity of hot gas to the interface would be

$$v_{\rm rel} = 0.8 v_t(\ell_{\rm cool}) \approx \frac{\ell_{\rm cool}}{t_{\rm cool}} \,. \tag{2.29}$$

The scale at which mixing/cooling occurs, and the characteristic velocity at that scale, can be written in terms of the turbulent properties at the energy-containing scale as

$$\ell_{\rm cool} = L \left[\frac{v_t(L) t_{\rm cool}}{L} \right]^{\frac{1}{1-p}} \tag{2.30}$$

and

$$v_t(\ell_{\rm cool}) = v_t(L) \left[\frac{v_t(L) t_{\rm cool}}{L} \right]^{\frac{p}{1-p}} \,. \tag{2.31}$$

The above describe expectations for the turbulent diffusion and the velocity of flow into the interface. In addition to the inflow velocity, the rate of energy loss also depends on the area of the interface. If the main energy-containing scale for the turbulence is L, the interface will be irregular at scales $\lesssim L$. While turbulent mixing and cooling would still lead to inflow to the interface at $v_{\rm rel} \sim v_t(\ell_{\rm cool})$, the net cooling is enhanced by having a surface that is highly corrugated at small scales. We turn to this in the next section.

2.2.5 Fractal Nature of the Turbulent Boundary Layer

In a recent investigation of turbulent, cooling boundary layers driven by Kelvin-Helmholtz instabilities between hot diffuse gas and cool dense gas, Fielding et al. (2020) pointed out that the surface of the interface obeys a fractal scaling law (see also Tan et al. 2021, who connect this to results in the combustion literature). Fielding et al. (2020) used this fractal nature to derive a prediction for the rate of mixing and cooling that occurs at shearing interfaces between cool, dense gas and hot, diffuse gas.

In particular, Fielding et al. (2020) argue that the rate of thermal energy loss to cooling will be equal to the rate at which energy can be simultaneously mixed and cooled into the turbulent

interface,

$$\dot{E} \approx \frac{5}{2} P v_t(\ell_{\rm cool}) A(\ell_{\rm cool}) \,,$$

where $A(\ell_{\rm cool})$ is the area of the (fractal) interface at scale[5] $\ell_{\rm cool}$. The above corresponds to the same characteristic inflow velocity of hot gas $v_{\rm rel} \approx v_t(\ell_{\rm cool}) = \ell_{\rm cool}/t_{\rm cool}$ as given in Equation 2.29, while the total cooling rate takes into account the fractal area $A(\ell_{\rm cool})$ of the interface at the scale $\ell_{\rm cool}$. The above relation is valid up to an order unity constant, which is quantified in Fielding et al. (2020) for the case where the interface is planar on large scales. The coefficient may depend somewhat on the details of the problem (including how turbulence is driven and large-scale geometry), so for present purposes we concentrate on scalings.

For the wind-blown bubble problem, we define an "equivalent" thermal energy flux $\Phi_{\rm cool}$ that can be lost to cooling via interface mixing as the rate of energy loss divided by the surface area of an equivalent sphere,

$$\Phi_{\rm cool} \approx \frac{5}{2} P v_t(\ell_{\rm cool}) \frac{A_b(r; \ell_{\rm cool})}{4\pi r^2} \,. \tag{2.32}$$

Here $A_b(r; \ell_{\rm cool})$ is now the full fractal surface area of the wind-blown bubble when the bubble has some linear scale (for example, its radius) r.

We will make the assumption that the thin interface between the shocked wind and the cool shell (i.e. between regions (ii) and (iii) in panel b of Figure 2.1) can be described by a fractal of dimension $D > 2$ (as it is an interface). We will refer to its "excess dimensionality" as $d \equiv D - 2$.

Physically, this means that if the bubble has an overall linear scale r, the area of the bubble surface measured on scale ℓ will be

$$A_b(r; \ell) \approx 4\pi r^2 \left(\frac{r}{\ell}\right)^d \,. \tag{2.33}$$

As in Section 2.2.4, we assume that the energy-containing scale of turbulence in hot gas near the interface is L and that the turbulence can be described by a structure function of the form of Equation 2.26 for $\ell \leq L$. The power law index is expected to take on a value $p \sim 1/3$ because the

[5]Fielding et al. (2020) adopt the notation w for the critical scale that here we denote $\ell_{\rm cool}$.

turbulence in the hot gas is generally subsonic. The amplitude $v_t(L)$ likely depends primarily on instabilities at the interface since the wind is the main source of free energy, but the background cloud turbulence may be important in seeding them.

Using Equation 2.30 and Equation 2.31, the equivalent energy flux is expected to follow

$$\Phi_{\rm cool} \approx \frac{5}{2} P v_t(\ell_{\rm cool}) \left(\frac{r}{\ell_{\rm cool}}\right)^d \tag{2.34a}$$

$$\approx \frac{5}{2} P v_t(L) \left(\frac{\ell_{\rm cool}}{L}\right)^{p-d} \left(\frac{r}{L}\right)^d \tag{2.34b}$$

$$\approx \frac{5}{2} P v_t(L) \left[\frac{v_t(L) t_{\rm cool}}{L}\right]^{\frac{p-d}{1-p}} \left(\frac{r}{L}\right)^d . \tag{2.34c}$$

This gives us an effective mixing velocity $v_{\rm eff} = 2\Phi_{\rm cool}/5P$ of

$$v_{\rm eff}(\ell) = v_t(L) \left[\frac{v_t(L) t_{\rm cool}}{L}\right]^{\frac{p-d}{1-p}} \left(\frac{r}{L}\right)^d \tag{2.35}$$

We emphasize that the fractal nature of the interface plays a major role in enhancing energy losses, given by the factor $(r/\ell_{\rm cool})^d$ in Equation 2.34a. It is important to note that strong inhomogeneity in a cloud (due to preexisting high Mach number turbulence) can make the fractal structure global, with $r \gg L$; from Equation 2.34c this strongly enhances cooling.

Fielding et al. (2020) measured $d \approx 1/2$ for the excess dimensionality of the fractal interface in the mixing/cooling layer of their simulations. Combining this with $p = 1/3$ for subsonic turbulence yields

$$\Phi_{\rm cool} \approx \frac{5}{2} P v_t(L) \left[\frac{v_t(L) t_{\rm cool}}{L}\right]^{-1/4} \left(\frac{r}{L}\right)^{1/2} . \tag{2.36}$$

Since the Fielding et al. (2020) simulations were for a local rectangular box with a shear layer, rather than a global expanding bubble, in the situation they studied $r/L \to 1$. The predicted scaling $\Phi_{\rm cool} \propto v_t(L)^{3/4} t_{\rm cool}^{-1/4}$ with the measured large-scale turbulent velocity $v_t(L)$ and imposed cooling time $t_{\rm cool}$ were found to be in excellent agreement with numerical results.

For present purposes, in order to keep the relation to the spherical case more explicit and use the variables that we have already developed to represent the linear scale of the bubble, we will

write the fractal area relation

$$A_b(\mathcal{R}_b;\ell) \equiv 4\pi\alpha_A \mathcal{R}_b^2 \left(\frac{\mathcal{R}_b}{\ell}\right)^d \tag{2.37}$$

where α_A is an order unity constant, which we quantify in Chapter 3.

Finally, we note that even if a properly-calibrated $\kappa_{\rm eff} = v_t(\ell_{\rm cool})\ell_{\rm cool}$ were used and the cooling length were resolved in one-dimensional simulations, it would not be possible to capture the fractal nature of the interface and hence the total cooling would not be correctly captured. To achieve the proper energy loss rate, an "area-corrected" effective diffusivity $\kappa_{\rm corr,1D} = v_t(\ell_{\rm cool})\ell_{\rm cool}(r/\ell_{\rm cool})^{2d}$ would have to be adopted instead, where r here now denotes the radius of the interface between the hot bubble and ambient medium in the 1D simulation. From Equation 2.30, this can be written in terms of the energy-containing scale of the turbulence as

$$\kappa_{\rm corr,1D} = v_t(L)L\left[\frac{v_t(L)t_{\rm cool}}{L}\right]^{\frac{1+p-2d}{1-p}} \left(\frac{r}{L}\right)^{2d}. \tag{2.38}$$

2.2.6 Conditions for Efficient Cooling

Here we analyze the conditions under which a wind can become "efficiently cooled." One such condition could be stated as the point at which the momentum incurred by pressure work, given for the PD bubble with cooling by Equation 2.7b, is less than the direct momentum input from the wind, $\dot{p}_w t = p_{\rm EC}$ (Equation 2.14, which is the total momentum in the EC case). This condition can be expressed formally as

$$1-\Theta < 4\left(\frac{5}{6}\right)^{1/4} \frac{\dot{R}_{\rm EC}}{\mathcal{V}_w}. \tag{2.39}$$

Since $R_{\rm EC} \propto t^{1/2}$, the term on the right above varies as $t^{-1/2}$. If cooling losses are sufficiently weak, the efficient cooling condition may be satisfied only at the earliest times. If, however, cooling losses are strong, $1-\Theta \ll 1$, essentially the whole bubble evolution may be in the efficient-cooling regime.

The above gives us a necessary condition on Θ for the wind to be "efficiently cooled." If an estimate of the cooling losses were known, then this test would decide whether the cooling-modified

PD (Section 2.2.2) or EC (Section 2.2.3) bubble solution is valid. Since, however, we have no *a priori* knowledge of Θ (except through Equation 2.9 and Equation 2.38), it is more useful to obtain a physically motivated condition for the EC solution to apply.

To this end, we compare the estimated thermal energy flux that can be lost to cooling at a turbulent interface, $\Phi_{\rm cool}$ (Equation 2.34c), to the thermal energy flux that an unimpeded shocked wind would carry. Immediately after the shock, at radius $\mathcal{R}_f$, this flux is $\Phi_{\rm w} \approx (5/2) P_{\rm ps} v_{\rm ps}$ with $P_{\rm ps} = 3\dot{p}_w/(16\pi\mathcal{R}_f^2)$ $v_{\rm ps} = \mathcal{V}_w/4$ for a spherical shock. Since the pressure is approximately constant in the subsonic post-shock region while energy is conserved (see Section 2.6), the energy flux carried into the boundary layer is $\Phi_{\rm w} \approx (5/2) P_{\rm ps} v_{\rm ps} (\mathcal{R}_f/\mathcal{R}_b)^2$.

The condition for efficient cooling is that the capacity for mixing/cooling matches or exceeds the rate at which thermal energy is advected to the interface ($\Phi_{\rm w} \lesssim \Phi_{\rm cool}$), which may be expressed as

$$\frac{2}{3\alpha_p - 1} v_{\rm ps} \lesssim v_t(L) \left[\frac{v_t(L) t_{\rm cool}}{L}\right]^{\frac{p-d}{1-p}} \left(\frac{\mathcal{R}_b}{L}\right)^d . \tag{2.40}$$

For the numerical coefficient on the left-hand side we have used the small-α_p approximation given in Equation 2.68; when $\alpha_p \gg 1$ the prefactor would instead become $3/(4\alpha_p)$, from Equation 2.67. The exponent $(p-d)/(1-p)$ depends on the exact fractal dimension as well as the power of the turbulent structure function. If $d \approx 1/2$ and $p \approx 1/3$, as previously suggested by Fielding et al. (2020), this exponent is $-1/4$, but in any case it is likely to be small and negative. Still, $t_{\rm cool}$ can be as small as $\sim 10 - 100\,{\rm yr}$ in dense clouds (see Chapter 3 for numerical results). With typical $v_t(L) \sim 0.1\mathcal{V}_w \gtrsim 100\,{\rm km\,s^{-1}}$ and $L \sim 0.1\mathcal{R}_b \lesssim 1$ pc, the efficient-cooling condition is satisfied for a strong shock with $v_{\rm ps} = \mathcal{V}_w/4$. Even if oblique shocks yield a larger hot-gas velocity $v_{\rm ps} \lesssim \mathcal{V}_w$, the efficient-cooling condition is likely to be at least marginally satisfied.

If we think of Equation 2.40 as representing an outer boundary condition on the flow within the bubble, it shows that lower turbulence levels will allow for larger α_p, i.e. more buildup of shocked gas within the bubble. Very high turbulence levels and large fractal dimension, in contrast, would lead to extremely efficient mixing, with $\alpha_p \sim 1$.

Finally, we remark that in numerical simulations, limited numerical resolution may impose a

minimum resolved scale $\ell_{\rm min} \sim \Delta x$, where $\ell_{\rm cool} < \ell_{\rm min} < L$. Following the arguments leading to Equation 2.34a-Equation 2.34b and then Equation 2.40, mixing at $\ell_{\rm min}$ would provide sufficient cooling for the EC solution to be satisfied provided

$$\frac{2}{3\alpha_p - 1} v_{\rm ps} \lesssim v_t(\ell_{\rm min}) \left(\frac{\mathcal{R}_b}{\ell_{\rm min}} \right)^d \tag{2.41a}$$

$$\sim v_t(L) \left(\frac{\ell_{\rm min}}{L} \right)^{p-d} \left(\frac{\mathcal{R}_b}{L} \right)^d . \tag{2.41b}$$

With $p - d \sim -1/6$, the cooling rate would tend to *increase* as resolution and $\ell_{\rm min}$ get smaller. Thus, if Equation 2.41a is already satisfied for resolved turbulence at scale $\ell_{\rm min}$ of a few Δx, further improvement in the resolution would not alter the behavior given by Equation 2.19.

In Chapter 3 we use Equation 2.41a as an additional check whether we are in the efficiently cooled regime. However, due to resolution effects, the structure function of the turbulence is often steeper than it should be, meaning that cooling does not necessarily increase with decreasing scale *all the way* to the resolution limit. If the true mixing rate is higher than the rate achieved in our simulations due to resolution limitations, the EC conditions in reality would be even better satisfied, with α_p even closer to unity.

2.3 Application to Star-Forming Clouds

Here we write down several formulae that will equip the reader to make practical use of our theory. To inform this discussion, we show in Figure 2.3 the evolution in time of several quantities related to stellar winds as calculated using the Starburst99 code (Leitherer et al., 1999). We show the evolution of the specific wind luminosity, the specific mass loss rate, the specific momentum input rate, and the so-called "wind efficiency parameter," which is the ratio of momentum input rate in the wind and in radiation, $\dot{p}_w/(L_{\rm bol}/c)$.

For all quantities we show the evolution for both a standard solar metallicity ($Z = 0.014$), Kroupa initial mass function (IMF) (Kroupa, 2001) (solid lines); for a "top-heavy" IMF with a shallower slope at $m > 0.5 M_\odot$ and solar metallicity (dashed lines); and for a standard IMF

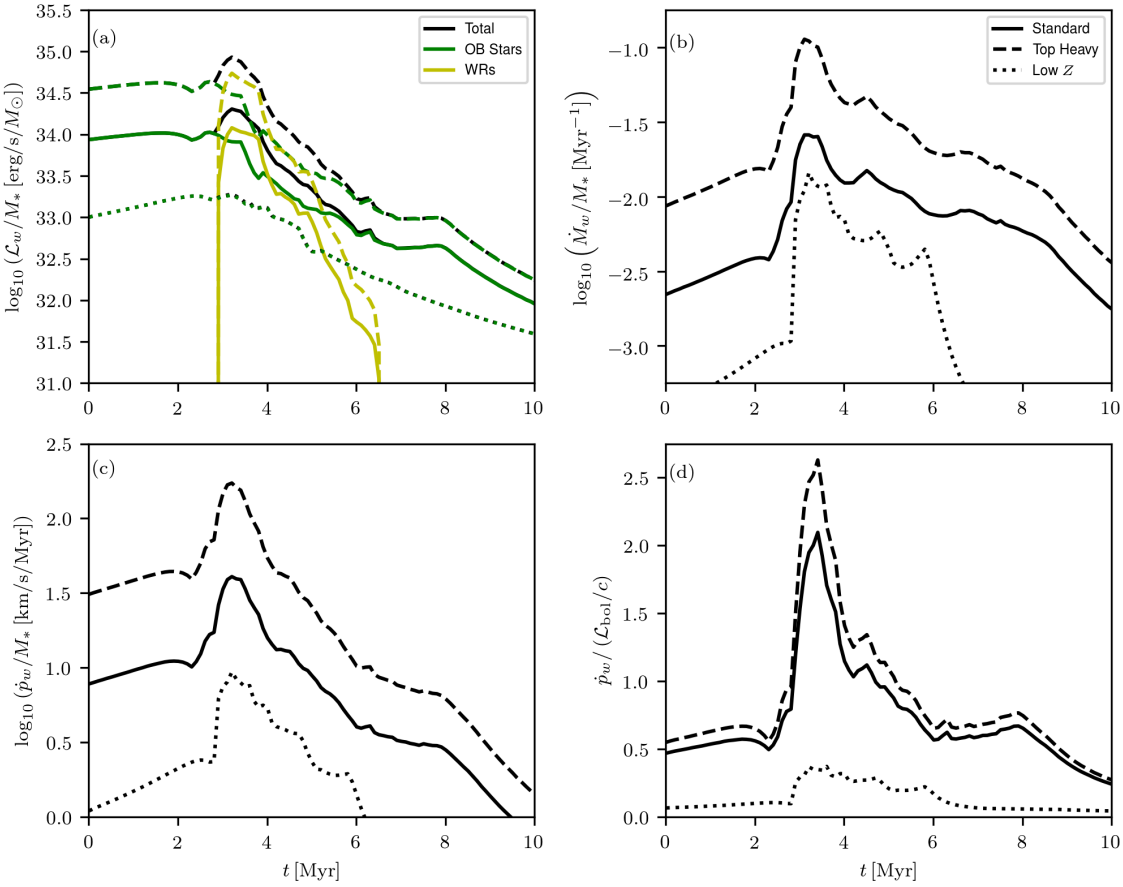

Figure 2.3 Evolution of several key wind quantities as calculated using the Starburst99 code (Leitherer et al., 1999). We show (a) the wind luminosity per unit mass of the star cluster, (b) mass-loss rate in the wind per unit stellar mass, (c) wind momentum injection rate per unit stellar mass, and (d) the ratio of wind momentum input rate to radiation momentum input rate. Solid lines show the result for a standard Kroupa IMF, dashed lines are for a "top-heavy" IMF in which $d\log N/d\log m$ is changed from -2.3 to -1.8 at $m > 0.5\,M_\odot$, and dotted lines show the results for a standard IMF but at low metallicity, $Z = Z_\odot/7$.

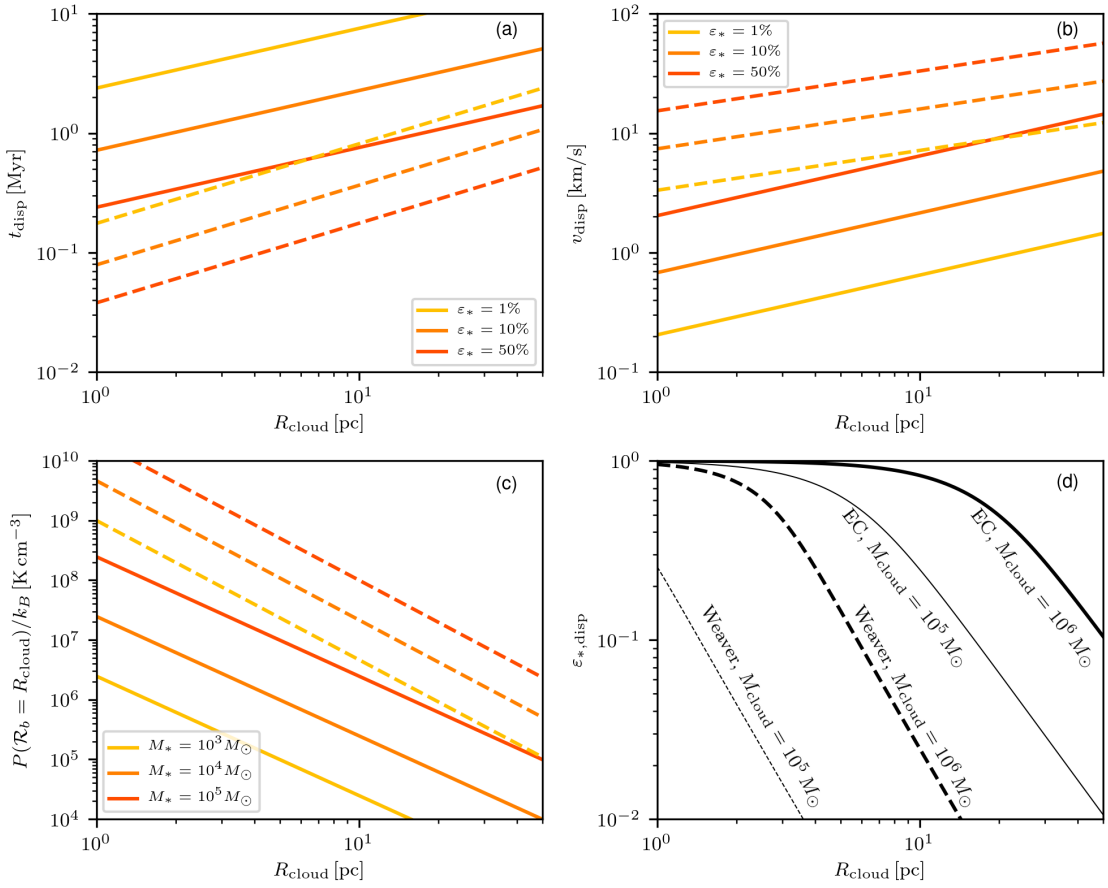

Figure 2.4 A comparison of several quantities as predicted by our theory (solid lines) and that of Weaver et al. (1977) (dashed lines). For the top two panels we show results as a function of cloud radius and star formation efficiency $\varepsilon_* = 1$, 10, 50%, while the bottom-left shows results for $M_* = 10^3, 10^4,\ 10^5 M_\odot$ (yellow, orange, and red respectively), using $M_{\rm sh} = 10^5 M_\odot$ for the dashed lines.. Panels show: *(a)* shell velocity $v_{\rm disp}$ when the bubble has reached the edge of the cloud; *(b)* time $t_{\rm disp}$ taken for this to occur; *(c)* the bubble interior pressure at this time. *(d)* the star formation efficiency needed to disperse the surrounding cloud. Here we show $\varepsilon_{*,\rm disp}$ as a function of $R_{\rm cl}$ for $M_{\rm cl} = 10^6$, $10^5\,M_\odot$ displayed as the thick and thin lines respectively.

with $Z = 0.002 \approx 10^{-0.85} Z_\odot$ (dotted lines, same as 'low-Z' models in Leitherer et al. (2014)). Additionally, in panel a we separately show the contributions from OB stars (green lines), Wolf-Rayet (WR) stars (yellow lines), and the total (black lines). There are also very minor contributions to the total $\mathcal{L}_w/M_*$ from luminous blue variable stars and red super-giant stars. We do not show these separately but they are included in the displayed total. The choice of the slope for the alternative IMF, $d\log N/d\log m = -1.8$ (instead of -2.3 for the standard IMF) is motivated by observations indicating that super star clusters, including those in the Galactic Center, may be top-heavy (McCrady et al., 2005; Lu et al., 2013; Hosek et al., 2019).

Our theory, as well as the simulations of Chapter 3, assumes that all the wind properties are constant in time. Figure 2.3 shows that this assumption is reasonable during the first $\sim 2\,\mathrm{Myr}$ of wind evolution, before the onset of significant energy input from WR stars. For all of the numerical estimates below, we adopt the standard Kroupa IMF. With a top-heavy IMF, $\dot{p}_w$ would be a factor of 4 higher, whereas $\dot{p}_w$ would be an order of magnitude lower with a low-metallicity IMF.

For the purposes of enabling quick calculations, the formulae we present below are written as simply as possible, setting $f_{\rm turb} = 0$, $\alpha_R = 1$. Where appropriate, we comment on the range of adjustments that would be expected based on the numerical results presented in Chapter 3. Additionally, in Figure 2.4 we provide a comparison of the predictions of our theory and that of Weaver et al. (1977) for several key quantities of interest. As we shall show, the shell velocities, cloud dispersal timescales, and hot-gas pressures in the EC solution can be orders of magnitude below the corresponding values for the Weaver et al. (1977) solution. This also implies much higher star formation efficiency would be required to disperse the cloud when interface cooling is taken into account.

The primary application of our results is to bubbles collectively driven by the winds from young massive stars in clusters within star-forming clouds. We shall take the total stellar mass of the cluster (including both low- and high-mass stars) as M_*, and assume a centrally concentrated wind source. Using the result from SB99 with a standard Kroupa IMF, the direct wind momentum input rate is

$$\dot{p}_w = 8.6\,\mathrm{km\,s^{-1}\,Myr^{-1}} M_*; \tag{2.42}$$

here the coefficient is based on an average over the first Myr, while the value would be slightly lower (≈ 7.85) for an average over 0.1 Myr. Averaging over the same time period, $\mathcal{V}_w = 3512\,\mathrm{km\,s^{-1}}$. Our solution allows for the momentum input rate to be enhanced by a factor α_p relative to the ideal "momentum-conserving" limit (see Equation 2.14).

We shall assume that after a time t the gas surrounding the central cluster has been swept up in a shell of mass $M_{\rm sh}$ by the wind. The shell's velocity will then be

$$v_{\rm sh} = 8.6\,\mathrm{km\,s^{-1}}\alpha_p \frac{M_*}{M_{\rm sh}} \frac{t}{\mathrm{Myr}}. \tag{2.43}$$

When the input wind power is very low (e.g $M_* \lesssim 10^3 M_\odot$) we show in Chapter 3 that $\alpha_p \sim 1.5-4$. This range could apply in moderate density GMCs, where the efficiencies of star cluster formation are only $M_*/M_{\rm cloud} \equiv \varepsilon_* \sim 1-10\%$ (Lada et al., 2010; Vutisalchavakul et al., 2016). However, winds are likely to be most important relative to other feedback processes in very dense clouds, such as those forming super star clusters (SSCs), where $\varepsilon_* \gtrsim 10\%$ (Leroy et al., 2017; Emig et al., 2020; Levy et al., 2020). For this range, the momentum enhancement above the direct wind input is modest, $\alpha_p \sim 1.2-2$ (see Chapter 3).

The evolutionary time is difficult to ascertain in observations, but from Equation 2.19 the shell velocity can also be expressed in terms of its mass $M_{\rm sh}$, radius $R_{\rm sh} = \mathcal{R}_b$, and $\dot{p}_w$ as

$$v_{\rm sh} = \left(\frac{\alpha_p \dot{p}_w}{2} \frac{R_{\rm sh}}{M_{\rm sh}}\right)^{1/2} \tag{2.44a}$$

$$= 2.0\,\mathrm{km\,s^{-1}} \left(\alpha_p \frac{M_*}{M_{\rm sh}} \frac{R_{\rm sh}}{1\ \mathrm{pc}}\right)^{1/2} \tag{2.44b}$$

where we have assumed $M_{\rm sh} = 4\pi R_{\rm sh}^3 \bar{\rho}/3$. Given that $\alpha_p^{1/2} \sim 1-2$, Equation 2.44b makes clear that a wind-driven shell can only reach velocity $> 10\,\mathrm{km\,s^{-1}}$ if $M_* \gg M_{\rm sh}$, assuming $R_{\rm sh}$ is in the range $\sim 1-25\,\mathrm{pc}$ of observed star-forming clouds. We note, however, that a top-heavy IMF would increase the shell momentum and velocity somewhat.

We can also use Equation 2.19, setting $\mathcal{R}_b = R_{\rm cloud}$, to obtain an estimate for the time required for a wind-driven bubble from an embedded cluster to disperse the entire surrounding parent cloud.

For this simple estimate, we set $M_* = \varepsilon_* M_{\rm cl}$ and $M_{\rm sh} = (1-\varepsilon_*) M_{\rm cl}$. The cloud dispersal time can then written as

$$t_{\rm disp} = \left(\frac{M_*}{2\alpha_p \dot{p}_w} \frac{1-\varepsilon_*}{\varepsilon_*} R_{\rm cl} \right)^{1/2} \tag{2.45a}$$

$$= 0.24\,{\rm Myr} \left(\frac{1}{\alpha_p} \frac{1-\varepsilon_*}{\varepsilon_*} \frac{R_{\rm cl}}{1\ {\rm pc}} \right)^{1/2}. \tag{2.45b}$$

The shell velocity $v_{\rm disp}$ at this time is obtained by replacing $M_*/M_{\rm sh} \rightarrow \varepsilon_*/(1-\varepsilon_*)$ and $R_{\rm sh} \rightarrow R_{\rm cl}$ in Equation 2.44b. It is interesting that these expressions are not (explicitly) dependent on the total cloud mass. As before, the enhancement of the momentum input rate relative to the ideal ($\alpha_p = 1$) EC solution would imply at most a $\sim 30\%$ reduction in $t_{\rm disp}$ for cases with $\varepsilon_* \gtrsim 10\%$. A key point is that compact clouds with high ε_* would be dispersed by wind feedback very rapidly, well before supernovae commence.

It is important to note that the expansion rate, and therefore other derived values such as the cloud dispersal time, are very different in the EC solution from what they would be if the classical Weaver et al. (1977) solution applied. For example, using the Weaver et al. (1977) solution, equivalent calculations to the above would instead yield

$$t_{\rm disp,W} = 0.038\,{\rm Myr} \left(\frac{1-\varepsilon_*}{\varepsilon_*} \right)^{1/3} \left(\frac{R_{\rm cl}}{1\,{\rm pc}} \right)^{2/3} \tag{2.46}$$

and

$$v_{\rm disp,W} = 15.4\ {\rm km\,s^{-1}} \left(\frac{\varepsilon_*}{1-\varepsilon_*} \right)^{1/3} \left(\frac{R_{\rm cl}}{1\,{\rm pc}} \right)^{1/3} \tag{2.47}$$

for the cloud dispersal time and the shell velocity at that time.

In the top two panels of Figure 2.4, we compare the EC and Weaver solutions for the breakout time and corresponding velocity. For the EC solution, the breakout velocity (breakout time) is a factor $\sim 5-10$ lower (higher). Since Equation 2.46 underestimates the dispersal timescale by up to an order of magnitude, we caution against its use. We also caution that the estimates in Weaver et al. (1977) and Mac Low & McCray (1988) of the cooling time for wind-blown bubbles cannot be

used to modify the solution of Equation 2.1, as they are obtained under the assumption that the hot bubble interior is itself cooling, rather than cooling losses occurring due to turbulent mixing at the interface between hot and cool gas.

Our above estimates, and the analysis and simulations of this paper and Chapter 3 more generally, neglect the effects of gravity. In reality, the rate at which the expanding shell gains momentum will be instantaneously reduced by the gravitational force of the cluster on the shell, $GM_* M_{\rm sh}/R_{\rm sh}^2$, and the gravitational force of the shell on itself, $GM_{\rm sh}^2/(2R_{\rm sh}^2)$. Allowing for gravity, the wind can drive expansion only provided

$$M_{\rm sh} + \frac{M_{\rm sh}^2}{2M_*} < \alpha_p \frac{\dot{p}_w}{M_*} \frac{R_{\rm sh}^2}{G} \, .$$

For a self-gravitating cloud to be fully dispersed by an expanding wind bubble, we again set $R_{\rm sh} = R_{\rm cl}$, $M_* = \varepsilon_* M_{\rm cl}$, and $M_{\rm sh} = (1-\varepsilon_*) M_{\rm cl}$, and solve the inequality to obtain a condition on the SFE, ε_*. We express this condition in terms of the original surface density of gas in the cloud, $\Sigma_{\rm cloud} \equiv M_{\rm cl}/(\pi R_{\rm cl}^2)$:

$$\frac{1-\varepsilon_*^2}{\varepsilon_*} < \frac{2\alpha_p}{\pi} \frac{\dot{p}_w}{M_*} \frac{1}{G\Sigma_{\rm cloud}} \tag{2.48a}$$

$$= 1.2\alpha_p \left(\frac{\Sigma_{\rm cloud}}{10^3 \, {\rm M_\odot \, pc^{-2}}} \right)^{-1} . \tag{2.48b}$$

The point at which ε_* is large enough that this inequality is satisfied is a simple estimate for the star formation efficiency needed to disperse the cloud, $\varepsilon_{*,\rm disp}$. For "normal" GMCs with $\Sigma_{\rm cloud} \sim 10^2 \, {\rm M_\odot \, pc^{-2}}$, Equation 2.48b reduces to

$$\varepsilon_{*,\rm disp} \approx \frac{0.08}{\alpha_p} \frac{\Sigma_{\rm cloud}}{10^2 \, {\rm M_\odot \, pc^{-2}}} \, . \tag{2.49}$$

For high surface density clouds $\Sigma_{\rm cloud} \sim 10^4 - 10^5 \, {\rm M_\odot \, pc^{-2}}$ such as those forming SSCs, this reduces to

$$1 - \varepsilon_{*,\rm disp} \approx 0.06\alpha_p \left(\frac{\Sigma_{\rm cloud}}{10^4 \, {\rm M_\odot \, pc^{-2}}} \right)^{-1} . \tag{2.50}$$

Clearly, extremely high surface densities would translate to an expected SFE very close to unity if

winds were the only form of feedback acting. In the bottom right panel of Figure 2.4, we compare the estimate for $\varepsilon_{*,\rm disp}$ based on the EC solution with an equivalent calculation based on the Weaver et al. (1977) theory. Evidently, the loss of energy to cooling renders winds far less effective at limiting star formation in molecular clouds.

It is worth noting that Equation 2.48a also applies in estimating the SFE for momentum sources other than winds, by substituting an alternative specific momentum input rate for $\alpha_p \dot{p}_w/M_*$. For example, for the same fully-sampled Kroupa IMF (Kroupa, 2001), SB99 gives a specific momentum injection rate from radiation of $L_*/(cM_*) \approx 20\,{\rm km\,s^{-1}\ Myr^{-1}}$, a factor of 2.3 larger than that stellar wind momentum input rate in Equation 2.42 (see Figure 2.3). With $\alpha_p \sim 1-4$ as obtained from our simulations (Chapter 3), the direct momentum input rates from radiation and winds would be comparable. Allowing for the combined momentum injection rate would respectively reduce the RHS of Equation 2.49, or increase the RHS of Equation 2.50, by a factor of ~ 2.

The above simple estimates of SFEs are interesting, but important caveats should be kept in mind. First, there is an implicit assumption that all wind momentum is retained in a cloud, but in fact it is likely that a significant portion is lost once the bubble size becomes comparable to that of the parent cloud, because the fractal bubble can break out through fingers and vent the shocked wind gas. For radiation feedback, estimates of the SFE based on the simple spherical assumption significantly underestimate the SFE obtained from simulations with realistic turbulent clouds due to cancellation from multiple sources and escape through low-density channels (e.g., Dale, 2017; Raskutti et al., 2016, 2017; Kim et al., 2018, 2019b), and this is likely to be true for winds as well. Thus, Equation 2.49 and Equation 2.50 should not be taken too seriously as direct predictions but more properly as bracketing the potential impact of winds on ε_*.

Second, the effects of mass loss due to photoevaporation and ionized gas pressure acting on neutrals are not considered above. In fact, at low and moderate surface densities photoionization (and to a lesser extent direct radiation pressure) is quite effective in limiting star formation and dispersing clouds (e.g. Dale et al., 2012; Krumholz & Matzner, 2009; Raskutti et al., 2016; Geen et al., 2017; Kim et al., 2018; Grudić et al., 2018; He et al., 2019; Kim et al., 2021a). Our expectation is that stellar winds would aid in quenching star formation, but are likely to rival the importance

of photoevaporation only in clouds of quite high surface density (see Section 2.4).

Our results also provide an estimate for the thermal pressure of hot gas in the interior of the bubble, which is a key observable. Equation 2.21 gives the pressure as a function of bubble radius $\mathcal{R}_b$; writing this in dimensional form, the result is

$$\frac{P_b}{k_B} \approx 2.46 \times 10^6 \,\mathrm{K\,cm^{-3}} \frac{M_*}{10^3\,\mathrm{M_\odot}} \left(\frac{\mathcal{R}_b}{1\ \mathrm{pc}}\right)^{-2} \frac{3\alpha_p - 1}{2}. \tag{2.51}$$

In the bottom left panel of Figure 2.4, we compare the bubble pressure when $\mathcal{R}_b = R_{\rm cl}$ to the bubble pressure predicted by the Weaver et al. (1977) theory for several different cluster masses. It is striking that the pressures differ by two or three orders of magnitude over much of the parameter space.

Even with cooling losses, the pressure given by Equation 2.51 would be quite high for small bubbles powered by luminous, massive clusters. Larger bubbles around lower-mass clusters would have much more moderate pressure. For the wind bubbles around single O stars rather than stellar clusters, the predicted pressure in hot gas is

$$\begin{aligned}\frac{P_b}{k_B} \approx & 2.86 \times 10^5 \,\mathrm{K\,cm^{-3}} \\ & \times \frac{\dot{p}_{w,1}}{10^3\,\mathrm{M_\odot\,km\,s^{-1}\,Myr^{-1}}} \left(\frac{\mathcal{R}_b}{1\ \mathrm{pc}}\right)^{-2} \frac{3\alpha_p - 1}{2},\end{aligned} \tag{2.52}$$

where $\dot{p}_{w,1} = (2\dot{E}_{w,1}\dot{M}_{w,1})^{1/2}$ is the single-star wind momentum input rate.

For our simulations, as presented in Chapter 3 (see Figs. 1 and 2 there), the hot gas pressure is far lower than that predicted in the original Weaver solution, because most of the energy deposited by the wind is lost to cooling. Chapter 3 shows that the measured energy reduction factor $1 - \Theta \sim 0.1 - 0.01$ is in good agreement with Equation 2.25. Taking $\mathcal{S} \approx \alpha_p$, the instantaneous fraction of the injected wind energy that is not radiated away is predicted to be

$$1 - \Theta \approx 4 \times 10^{-3} \alpha_p \frac{v_{\rm sh}}{10\,\mathrm{km\,s^{-1}}} \tag{2.53}$$

in terms of the shell's expansion velocity $v_{\rm sh} = \dot{\mathcal{R}}_b$. Even if this velocity is not measured directly, it may be estimated from other observables through Equation 2.44b.

The comparisons of this section between results obtained using the EC solution and the classical Weaver et al. (1977) solution show that neglect of energy losses due to interface mixing can lead to erroneous conclusions regarding the importance of stellar winds compared to other feedback mechanisms. For star clusters prior to breakout from molecular clouds, the EC conditions of this paper will generally apply, and we recommend use of formulae in this section. For a cluster after breakout or for runaway stars, the ambient density would be lower, leading to a longer cooling time $t_{\rm cool}$. Lower power sources than the clusters of $M_* \gtrsim 10^3\,{\rm M}_\odot$ considered here would produce lower turbulent velocities v_t. In the longer-$t_{\rm cool}$, smaller-v_t situations where interface energy losses are more moderate, we instead recommend use of the formulae in El-Badry et al. (2019) with an appropriate diffusion parameter (such as Equation 2.38).

2.4 Discussion

2.4.1 Observations

This work was inspired in part by observations of evolved HII regions, which suggest that the classical model of Castor et al. (1975) and Weaver et al. (1977) – in which nearly half of the wind energy remains in a hot bubble that can emit X-rays and drive rapid shell expansion ($\sim 10-50\,{\rm km\,s^{-1}}$ from Figure 2.4) – is not in agreement with observations (Townsley et al., 2003, 2006; Harper-Clark & Murray, 2009; Lopez et al., 2011, 2014; Rosen et al., 2014). Instead, observations suggests that wind energy must be lost either through leakage (Harper-Clark & Murray, 2009) or through radiative cooling at intermediate temperatures. The former is encouraged by the highly inhomogeneous structure of clouds, while the latter is facilitated by turbulent mixing. We have explored the consequences of turbulent mixing and cooling as a major energy sink for shocked wind gas. In Chapter 3, we show that such extreme cooling is not only possible but quite typical. These effects are expected to be especially important for early evolution before wind bubbles break out of their natal cloud. We have proposed (and show in Chapter 3) that the interfaces between hot

and cool gas in wind bubbles are fractals; this is crucial in enhancing mixing, and also important to breakout as bubble "fingers" can vent gas earlier than would otherwise occur.

The EC model may be able to explain several observations. Rosen et al. (2014) showed that, for the four dense star clusters they studied, only 3-30% of the energy deposited by stellar winds could be accounted for by radiative cooling internal to the bubble (negligible for the most part) combined with mechanical work on the surroundings (Bottom left panels of Figures 6-9 in that work), suggesting up to 97% of the wind energy is lost. While Rosen et al. (2014) were able to explain the missing energy in some of the clusters by appealing to thermal conduction (under the assumption that energy is lost, rather than leading to evaporation) and dust-reprocessed radiation, these calculations are more uncertain and sometimes over-account for the lost energy. Rosen et al. (2014) also raised the possibility of significant energy losses by "turbulent conduction" (turbulent mixing+cooling in our terminology), but they did not attempt to estimate this. Since we find (see Chapter 3, Figure 17) that as little as 1% of the input energy remains in our simulation, we conclude that radiative cooling in turbulent mixing layers would easily account for the missing wind energy in observed star-forming regions.

Olivier et al. (2020) recently observed deeply embedded HII regions, where our theory should be most applicable, but were only able to put upper limits on effects of stellar winds due to a lack of long-exposure X-ray observations. Further work on this front should allow a quantitative test of our theory.

The nearby Orion Molecular Cloud has some of the best observations of on-going star formation feedback in action. Using X-ray observations with the XMM-Newton satellite, Güdel et al. (2008) showed that the bubble being driven by the Trapezium cluster is pervaded by $1.7 - 2.1 \times 10^6\,\mathrm{K}$ gas, and estimated an electron density $n_e = 0.2 - 0.5\,\mathrm{cm}^{-3}$, implying thermal pressure of $P_b/k_B = 2n_eT = 0.68 - 2.1 \times 10^6 \mathrm{K\,cm}^{-3}$. Using the wind parameters quoted for θ^1 Ori C (the most massive star in the Trapezium) by Güdel et al. (2008), $\dot{M}_w = 0.8\,M_\odot/\mathrm{Myr}$ and $\mathcal{V}_w = 1650\ \mathrm{km\,s}^{-1}$, we get $\dot{p}_w = 1.32 \times 10^3\,M_\odot\,\mathrm{km/s/Myr}$. Using Equation 2.52 and an effective radius 2 pc (Güdel et al. 2008 suggest a range 1 - 4 pc, uncertain due to geometry) we find we would require $\alpha_p \approx 5$ to obtain pressure agreement at the lower end of the estimated range. This value of α_p is similar to the

results we find in our simulations for our lowest momentum input rate, $\dot{p}_w = 1.8 \times 10^4\, M_\odot$ km/s/Myr (Chapter 3), considering the considerable uncertainties in the observational parameters; for example, substituting estimated wind momentum input rate of Gagné et al. (2005) would increase the pressure by a factor of two.

Our work helps to explain why observational (listed above) and numerical (Dale et al., 2014; Geen et al., 2015a, 2020) works have found winds to be inefficient at cloud dispersal compared to effects from ionizing radiation. However, taking these results to mean that winds are unimportant is an over-simplification. Winds remain important not only because they pollute the gas surrounding nascent star clusters, perhaps changing the chemical composition of subsequent stellar populations (e.g. Bastian & Lardo, 2018; Gratton et al., 2019), but also because they may be the primary mechanism for cloud dispersal *in some environments*.

Very recently, new empirical evidence of feedback in extreme environments was obtained by Levy et al. (2020), who observed the environment of nascent super star clusters in NGC 253 with 0.5 pc resolution ALMA observations in multiple molecular lines. From analysis of P-Cygni profiles, indicative of cluster-scale outflows, Levy et al. (2020) obtained estimates of the mass and momentum carried by outflows around three of the SSCs in NGC 253 and applied our theory of stellar wind feedback to test whether this could explain the observations. They found that given modest momentum enhancement factors, $\alpha_p \sim 1 - 4$, winds could plausibly be the dominant feedback mechanism. However, our numerical findings (see Chapter 3 Figure 8) suggest that $\alpha_p \sim 1 - 1.5$ in the dense environments of SSCs (assuming high SFE). Given the uncertainty in the measurements, winds could still be the main drivers of feedback in these systems. The inferred $\alpha_p \gtrsim 2$ could, however, also be a sign of the contribution of other feedback mechanisms, such as radiation. A top-heavy IMF (see Figure 2.3) or a super-solar metallicity (not shown) stellar population could also boost the input momentum/stellar mass (Leitherer et al., 1992; Vink et al., 2001; Leitherer et al., 2014).

2.4.2 Other models of momentum-driven bubbles

In Section 2.3, we explicitly compared our results to what would be predicted based on the classic "Weaver-type" solution described in Section 2.2.1. This type of solution can be classified as "energy-driven" evolution because the energy of the bubble increases linearly in time, with the bubble radius expanding as $\mathcal{R}_b \propto t^{3/5}$. In contrast, in our EC solution it is the *momentum* that increases linearly in time, while energy only increases as the square-root of time. Evolution in the EC solution may therefore be classified as "momentum-driven."

Momentum-driven solutions for wind bubble expansion are characterized by $\mathcal{R}_b \propto t^{1/2}$, and have been considered by several previous authors. Steigman et al. (1975) simply assumed momentum-driven evolution, disregarding the importance of shocks and internal bubble structure. Avedisova (1972), Castor et al. (1975), and Weaver et al. (1977) clarified the role of internal wind shocks and argued for the importance of energy build-up within the bubble. Subsequent authors discussed the possibility of momentum-driven evolution due to enhanced cooling within the bubble interior, due to a variety of mechanisms described below. Two key differences of our theory from these earlier proposals are that (1) in our model energy is lost through strong radiative cooling at intermediate temperature in a turbulent mixing layer at the surface of the bubble, and (2) fractal structure of the interface is essential to efficient cooling.

The wind models of Koo & McKee (1992a,b) specify a so-called "slow wind" which leads to momentum-driven bubble evolution. However, in this model the momentum-driven evolution is caused by the interior of the bubble being radiative when the wind is sufficiently dense and slow, where "slow" here is hundreds of $\mathrm{km\,s^{-1}}$, much slower than the $\mathcal{V}_w > 10^3\ \mathrm{km\,s^{-1}}$ winds under consideration in this paper.

Similarly, Section 7B of Ostriker & McKee (1988) considers that interior radiative losses could be enhanced due to the evaporation of clouds overtaken by the wind (c.f. Cowie & McKee, 1977). In this scenario, the majority of the cooling would still occur in the shocked bubble interior.

In Silich & Tenorio-Tagle (2013) as well as Mac Low & McCray (1988) (following Weaver et al. 1977) it is emphasized that conduction acting at the boundary between the shocked wind and

swept-up material creates a temperature gradient and includes a regime where cooling would be efficient, which would eventually lead to the evolution becoming momentum-driven. This is the scenario most similar to our model. However, as discussed in Silich & Tenorio-Tagle (2013), for typical parameters this transition is only expected to occur after $\sim 10\,\mathrm{Myr}$, long past the timescales of evolution considered here or over which the wind can be treated as constant-luminosity (as evidenced by Figure 2.3). In our model, radiative cooling in a turbulent mixing layer is far more efficient than the conduction-induced cooling, due in part to the fractal nature of the interface, and the bubble becomes momentum-driven at much earlier times.

2.4.3 Comparison to Radiative Feedback

Several studies have argued analytically or demonstrated numerically that radiation feedback becomes much less efficient at dispersing clouds and limiting star formation in very high density environments (e.g. Fall et al., 2010; Dale et al., 2012; Kim et al., 2016; Raskutti et al., 2016; Kim et al., 2018; Grudić et al., 2018; Rahner et al., 2019; Fukushima et al., 2020), even allowing for reprocessed radiation (Skinner & Ostriker, 2015; Tsang & Milosavljević, 2018). In such dense clouds, the evolutionary timescales are also too short for supernovae to be important in dispersing cloud material.

Quantitatively, Kim et al. (2018) (Figures 8 and 12) show that when the surface density of a cloud exceeds $\sim 10^3\,\mathrm{M_\odot\,pc^{-2}}$, the total momentum injection rate per stellar mass due to EUV and FUV radiation pressure[6] drops below that in Equation 2.42 for winds. This suggests that winds could potentially be the dominant feedback process in higher density environments. In particular, our theory may be able to explain several aspects of the extremely compact molecular clouds seen to be forming super star clusters in nearby galaxies (Johnson et al., 2015; Oey et al., 2017; Turner et al., 2017; Leroy et al., 2018; Emig et al., 2020). As super star clusters/young massive clusters (e.g. Whitmore, 2003; Portegies Zwart et al., 2010) are the densest redshift-zero loci of star formation, understanding their formation is not only interesting in itself, but provides a window on globular

[6]From Fig. 7 of Kim et al. (2018), direct radiation pressure dominates over effects of photoevaporation and ionized gas pressure in this regime.

cluster formation.

It may be noted that the linear dependence of ε_* on surface density given by Equation 2.49 is similar to the case of radiation-pressure driven cloud dispersal under the idealization of a spherical system (Fall et al. 2010; Kim et al. 2016; see also Grudić et al. 2018; Li et al. 2019a). This differs from the $\varepsilon_* \propto \Sigma_{\rm cloud}^{1/2}$ dependence reported by Fukushima et al. (2020). A relation $\varepsilon_* \propto \Sigma_{\rm cloud}^{1/2}$ is close to what would be predicted if the cloud lifetime scales linearly with the propagation time of a self-similarly expanding ionization front, while the star formation rate scales inversely with the cloud free-fall time. However, the generality of the Fukushima et al. (2020) result may be questioned, since their simulations adopted very strongly self-gravitating clouds with a limited range of initial gas surface density. In contrast, the radiation-hydrodynamic simulations of Kim et al. (2018) found a non-power-law scaling of ε_* with $\Sigma_{\rm cloud}$ (see their Eq. 26) over a wider parameter range for clouds that were initially marginally bound. The difference between simple scaling predictions and full numerical results for the case of radiation-driven cloud destruction serves as a caution against taking Equation 2.48a as more than a general indicator of the trend in SFE. Full numerical simulations will be needed to assess the effectiveness of winds in limiting star formation in clouds of varying conditions.

Regardless of the environment, winds may be more important than ionizing radiation at early stages of evolution when the radius of the H Roman2 region is small. Similar to the approach in Krumholz & Matzner (2009), one can make a simple comparison of the wind momentum input rate $\alpha_p \dot{p}_w$ to the nominal force imposed by thermal pressure of photoionized gas. For an effective bubble radius $\mathcal{R}_b$, the latter is $2 n_e k_{\rm B} T_{\rm II} (4\pi \mathcal{R}_b^2) \propto (Q_{\rm i} \mathcal{R}_b)^{1/2}$, where we have used $n_e = [3 f_{\rm ion} Q_{\rm i} / (\alpha_{\rm B} 4\pi \mathcal{R}_b^3)]^{1/2}$ for ionization equilibrium with a source of ionizing photon rate Q_i and a fraction $f_{\rm ion}$ of photons available for ionization, and $T_{\rm II}$ denotes the temperature of the photoionized gas. The force from the wind would exceed that from radiation when the radius is smaller than a characteristic radius

$$\mathcal{R}_{b,\rm ch} = \frac{\alpha_{\rm B}}{12\pi (2 k_{\rm B} T_{\rm II})^2} \frac{\alpha_p^2 \dot{p}_w^2}{f_{\rm ion} Q_{\rm i}} \,. \tag{2.54}$$

Adopting $T_{\rm II} = 8000\,{\rm K}$, $\alpha_{\rm B} = 3.03 \times 10^{-13}\,{\rm cm^3\,s^{-1}}$, and $f_{\rm ion} = 0.5$, the characteristic radius

for a bubble driven by a single massive star with $\dot{p}_w = 10^4\,\mathrm{M}_\odot\,\mathrm{km\,s^{-1}\,Myr^{-1}}$ and $Q_\mathrm{i} = 4 \times 10^{49}\,\mathrm{s^{-1}}$ is $\mathcal{R}_{b,\mathrm{ch}} = 0.11\alpha_p^2$ pc. For a star cluster with $Q_\mathrm{i} \approx 4 \times 10^{46}\,\mathrm{s^{-1}}(M_*/\,\mathrm{M}_\odot)$ and $\dot{p}_w = 8.6\,\mathrm{km\,s^{-1}\,Myr^{-1}}M_*$, we obtain $\mathcal{R}_{b,\mathrm{ch}} \approx 0.79\alpha_p^2(M_*/10^4\,\mathrm{M}_\odot)\,\mathrm{pc}$; the wind is expected to play a greater role than photoionization for bubbles created by massive cluster stars and in early stage of evolution.

Therefore, similar to the situation analyzed by Kim et al. (2016) where the role of wind momentum input is played by radiation pressure, for sufficiently small radii it would be expected that the wind dominates the dynamics. The ionized gas layer would be compressed by the wind into a narrow layer near the ionization front. The wind would indirectly drive the shell expansion by enhancing density and thermal pressure of the H Roman2 region. The relative volumes of the hot-gas and photoionized-gas regions can be obtained by requiring that the pressures match. In the regime where winds dominate, radiation pressure is expected to contribute to the expansion by further increasing the density at the ionization front (Kim et al., 2016; Rahner et al., 2017). Later in evolution when the radius of the H Roman2 region is large, the photoionized gas would instead compress the hot interior of the bubble. Expansion would be driven primarily by photoionized gas that fills most of the bubble volume.

We note that the quantitative predictions above are based on the assumption that there is no significant leakage of hot gas and radiation. At late stage of bubble evolution ($\mathcal{R}_b \sim R_\mathrm{cloud}$), both (hot and photoionized) gas and radiation are expected to break out through low-density holes created by turbulence.

2.4.4 Other Physics

The theory presented here, as well as the simulations described in Chapter 3, are highly idealized, not considering many aspects of physical processes and the astronomical parameter space that could be important to the problem at hand. We briefly discuss some of these issues here.

First, the relevance of our results may be metallicity dependent. We note that wind mass loss is almost linear with metallicity, $d\log\dot{M}_w/d\log Z \sim 0.7$, while the wind velocity has a weak dependence on metallicity ($V_w \propto Z^{0.13}$), so that the wind momentum input rate is almost linear in

metallicity (Vink et al., 2001). Lower metallicity in the cloud could in principle also make cooling less effective. However, we show in Chapter 3 that most cooling in the turbulently-mixed interface gas occurs near $T \sim 10^4\,\mathrm{K}$ where cooling is mostly due to Hydrogen (Lyman α), implying a change in metallicity should not have a strong effect. Therefore, the effect of winds is expected to decrease at lower metallicity.

Second, we ignore thermal conduction. As noted above and in El-Badry et al. (2019), thermal conduction can act to increase the density and decrease the temperature of the bubble interior at fixed pressure. While it is not known whether the effect of thermal conduction in the presence of genuine turbulent mixing acts the same as for a parameterized diffusivity, if this is the case we might still expect the thermal pressure to follow Equations 2.51 and 2.52.

Finally, while we do not include magnetic fields in our models, in general we would expect them to have at least two effects. Firstly, they would add to the external pressure and tension that the bubble must "fight against" to expand. However, our power-law solutions already neglect external turbulent and thermal stresses; when accounted for, these and the magnetic stresses would slow expansion when $\dot{p}_w/(4\pi\mathcal{R}_b^2)$ becomes comparable to the total external stress (and depending on the field geometry the bubble may also expand preferentially along the field lines). Secondly, a magnetic field could act to inhibit development of the turbulent mixing that leads to cooling. For example, the Kelvin-Helmholtz instability is suppressed if the Alfvén speed in the shell gas exceeds $v_{\mathrm{shear}}/\chi^{1/2}$, where v_{shear} is the shear velocity and χ is the ratio between the density of shell gas and shocked wind gas. Even if primary instabilities take place, magnetic tension may limit turbulent cascades to small scales. Also, inclusion of radiation, as discussed above, would imply that the hot gas may principally interact with a layer of photoevaporated gas rather than directly with the shell gas. Numerical study will be needed to assess the parameter regime where the mixing/cooling process and bubble evolution are strongly affected.

2.5 Conclusion

We have presented a theory for stellar wind bubble evolution with extremely efficient energy losses to radiative cooling, such that bubble expansion is determined by the original wind momentum injection rate. In this theoretical model, the extreme energy losses are the result of turbulent mixing and subsequent radiative cooling at the interface between hot and cool gas at the bubble surface, strongly enhanced by the large interface area that arises from the fractal geometry of the bubble.

In a Chapter 3 we validate our theory using three-dimensional hydrodynamic simulations of wind-driven bubble evolution, demonstrating excellent agreement. In Chapter 3 we quantify the few free parameters of our theory and provide a full analysis of thermal and dynamical structure and evolution.

The treatment of stellar winds in this paper and its companion has been largely simplified (constant luminosity with central point-like star clusters put in by hand). This treatment allowed us to gain a deeper theoretical understanding of the stellar wind bubble physics that controls evolution. Still, a fully self-consistent treatment of star formation with wind feedback for a range of cloud parameters – both normal GMCs and clouds capable of forming SSCs – remains an important goal. The fractal theory developed here will serve as a valuable tool aiding interpretation in this kind of numerical effort, as well as observational studies of star-forming cloud structure and evolution. In addition, the theory developed here may potentially be applied to understanding the history of chemical enrichment of natal clouds by embedded clusters, which would illuminate many longstanding problems involving multiple stellar populations within globular clusters (e.g. Wünsch et al., 2017; Lochhaas & Thompson, 2017; Bastian & Lardo, 2018; Gratton et al., 2019).

2.6 Appendix: The Wind Interior

Here we provide a derivation for some of the properties of the free and shocked wind phases. This analysis allows us to write the energy enhancement factor $\mathcal{S}$, post-shock pressure, and the relative volume of free and shocked wind in terms of a "momentum enhancement factor" α_p.

We assume spherical geometry for the bubble with $r < \mathcal{R}_f$ occupied by the free wind phase, where $\mathcal{R}_f = (3V_{\rm f}/4\pi)^{1/3}$ for $V_{\rm f}$ the volume occupied by the free wind, and $\mathcal{R}_f < r < \mathcal{R}_b$ occupied by shocked wind gas.

In the free wind the flow expands with hypersonic wind velocity $\mathcal{V}_w$ and the thermal energy is negligible, so that

$$\rho(r) = \frac{\dot{M}_w}{4\pi r^2 \mathcal{V}_w} \quad , \quad v_r = \mathcal{V}_w \, . \tag{2.55}$$

At $\mathcal{R}_f$ the wind then goes through a strong shock (assumed perpendicular), with immediate post-shock conditions

$$\rho_{\rm ps} = 4\rho(\mathcal{R}_f) = \frac{\dot{M}_w}{\pi \mathcal{R}_f^2 \mathcal{V}_w} \, , \tag{2.56}$$

$$v_{\rm ps} = \frac{\mathcal{V}_w}{4} \, , \tag{2.57}$$

and

$$P_{\rm ps} = 3\rho_{\rm ps} v_{\rm ps}^2 = \frac{3\dot{p}_w}{16\pi \mathcal{R}_f^2} \, . \tag{2.58}$$

The shocked wind region is assumed to have a steady flow,

$$\frac{\rho}{\rho_{\rm ps}} = \frac{\mathcal{R}_f^2}{r^2} \frac{v_{\rm ps}}{v} \, , \tag{2.59}$$

with an adiabatic equation of state

$$\frac{P}{\rho} = \frac{P_{\rm ps}}{\rho_{\rm ps}} \left(\frac{\rho}{\rho_{\rm ps}} \right)^{2/3} \, , \tag{2.60}$$

and Bernoulli parameter

$$\frac{1}{2} v^2 + \frac{5}{2} \frac{P}{\rho} = \frac{1}{2} v_{\rm ps}^2 + \frac{5}{2} \frac{P_{\rm ps}}{\rho_{\rm ps}} \, . \tag{2.61}$$

By substituting in for P and ρ in the Bernoulli equation we obtain

$$\left(\frac{v}{v_{\rm ps}} \right)^2 + 15 \left(\frac{v_{\rm ps}}{v} \left(\frac{\mathcal{R}_f}{r} \right)^2 \right)^{2/3} = 16, \tag{2.62}$$

which can be rearranged to arrive at

$$\frac{v}{v_{\rm ps}} = \left(\frac{\mathcal{R}_f}{r}\right)^2 \left(\frac{15}{16 - (v/v_{\rm ps})^2}\right)^{3/2} . \tag{2.63}$$

While this equation does have an analytic solution, it is quite complicated; an approximation that is good to within 10% is

$$\frac{v}{v_{\rm ps}} \approx \left(\frac{\mathcal{R}_f}{r}\right)^2 . \tag{2.64}$$

With Equation 2.64, both the density and pressure are approximately constant throughout the post-shock region, equal to their immediate post-shock values given in Equation 2.56 and Equation 2.58, $\rho = \rho_{\rm ps}$ and $P = P_{\rm ps}$

The total rate of momentum transport across a surface of radius r is

$$\dot{p}(r) = 4\pi r^2 \left(P + \rho v^2\right) ,$$

which in the free wind region is $\dot{p}(r) = \dot{p}_w$. Using our solution in the shocked-wind region, this becomes

$$\dot{p}(r) = \frac{\dot{p}_w}{4}\left[3\left(\frac{r}{\mathcal{R}_f}\right)^2 + \left(\frac{r}{\mathcal{R}_f}\right)^{-2}\right] . \tag{2.65}$$

This function is strictly increasing for $r/\mathcal{R}_f > 1$.

The total momentum input to the shell is obtained by taking $r \to \mathcal{R}_b$, which from the definition in Equation 2.13 implies

$$\alpha_p = \frac{1}{4}\left[3\left(\frac{\mathcal{R}_b}{\mathcal{R}_f}\right)^2 + \left(\frac{\mathcal{R}_b}{\mathcal{R}_f}\right)^{-2}\right] , \tag{2.66}$$

We can invert to obtain $\mathcal{R}_b/\mathcal{R}_f$ in terms of α_p as

$$\left(\frac{\mathcal{R}_b}{\mathcal{R}_f}\right)^2 = \frac{2}{3}\alpha_p + \left[\left(\frac{2}{3}\alpha_p\right)^2 - \frac{1}{3}\right]^{1/2} . \tag{2.67}$$

A useful and simple approximation for the above, which is good to within 4% for $1 \leq \alpha_p \leq 4$ is

given by

$$\left(\frac{\mathcal{R}_b}{\mathcal{R}_f}\right)^2 \approx \frac{1}{2}\left(3\alpha_p - 1\right) ; \tag{2.68}$$

alternatively, at large α_p, $(\mathcal{R}_b/\mathcal{R}_f)^2 \approx 4\alpha_p/3$. The free wind's volume is a fraction $(\mathcal{R}_b/\mathcal{R}_f)^{-3}$ of the whole wind bubble.

Finally, under the assumption of spherical symmetry, the total energy in the bubble interior is

$$E_b = 4\pi \int_0^{\mathcal{R}_b} \left(\frac{3}{2}P + \frac{1}{2}\rho v^2\right) r^2 dr \, .$$

Given that only the kinetic energy term contributes in the free wind, we can use Equation 2.55 to derive the total energy in the free wind as $\dot{p}_w \mathcal{R}_f/2$. For the shocked wind we can derive the energy as

$$E_{\rm ps} = \frac{\dot{p}_w \mathcal{R}_f}{8}\left[3\left(\frac{\mathcal{R}_b}{\mathcal{R}_f}\right)^3 - 2 - \frac{\mathcal{R}_f}{\mathcal{R}_b}\right] .$$

Putting these together, the total energy in the bubble interior is

$$E_b = \frac{\dot{p}_w \mathcal{R}_b \mathcal{S}}{2} \, , \tag{2.69}$$

where

$$\mathcal{S} = \frac{3}{4}\left(\frac{\mathcal{R}_b}{\mathcal{R}_f}\right)^2 - \frac{1}{4}\left(\frac{\mathcal{R}_b}{\mathcal{R}_f}\right)^{-2} + \frac{1}{2}\left(\frac{\mathcal{R}_b}{\mathcal{R}_f}\right)^{-1} \tag{2.70}$$

is the enhancement in energy above the case where the whole wind bubble is made up of free wind ($\mathcal{R}_b = \mathcal{R}_f$ and $\mathcal{S} = 1$). Using Equation 2.66, one can show that $\mathcal{S} \approx \alpha_p$ to within 6%.

We note that to account for the shock between the free and post-shock wind being oblique[7], Equation 2.57 can be multiplied by a factor $4 - 3\mu^2$ to obtain the post-shock radial velocity, while for the post-shock pressure Equation 2.58 is multiplied by μ^2. Here, μ is the average value of the dot product of the unit radial vector ($\hat{\mathbf{r}}$) with the unit normal to the shock ($\hat{\mathbf{n}}_{\rm shock}$).

[7]This is always the case, see Chapter 3.

Chapter 3

Validation of Theory with Simulations

3.1 Introduction

In Chapter 2 we have theoretically investigated the dynamics of expanding stellar wind bubbles in the case that most of the wind's energy is radiated away. There, we argue that the interface between hot bubbles and the surrounding gas is subject to strong turbulent mixing, which subsequently leads to efficient radiative cooling in intermediate-temperature gas. We also argue that the surface of the hot bubble is a fractal, and the large associated area enhances cooling. We hypothesize that efficient cooling leads to the dominant phase of bubble evolution being momentum-driven rather than energy-driven. In this work, we support the theoretical model of Chapter 2 with a suite of three-dimensional (3D) hydrodynamic simulations, which we analyze to provide quantitative corroboration of the arguments made there. Each simulation follows the expansion of a hot bubble driven into the surrounding dense, turbulent ISM by a constant luminosity point source.

In this paper, we explore a set of questions related to the detailed structure and evolution of bubbles driven by stellar winds in turbulent clouds. Our goals are to characterize the dependence

of bubble evolution on input wind power and ambient cloud properties, and to explain the physical mechanisms controlling the evolution. Using numerical simulations, we quantify (1) the temporal evolution of wind bubble sizes and the energy and momentum that bubbles/shells contain; (2) the properties of the turbulence that drives mixing at the interface between a bubble's hot/diffuse interior and cool/dense shell; (3) the fractal structure and foldedness of the cooling interface; and (4) the total energy losses to cooling due to turbulent mixing. Confirming the theory laid out in Chapter 2, we shall show that for the conditions typical of star-forming clouds, the vast majority of wind energy is expected to be lost due to turbulent mixing followed by radiative cooling, and that the large area associated with the fractal geometry of the bubble/cloud interface is crucial to enhancing losses. Our physical picture of turbulent, cooling mixing layers is much informed by insights from recent numerical and analytic investigations of the Kelvin-Helmholtz instability in the context of multiphase galactic winds and the circumgalactic medium (Gronke & Oh, 2018; Fielding et al., 2020; Tan et al., 2021).

The numerical model we adopt is intentionally idealized. It is designed to provide a testing ground for the theory presented in Chapter 2 that represents key real-world features (to the extent that is computationally practical), while still having that theory be applicable. To that end, we (i) have ignored the effects of star formation that is extended in both space and time (see Chapter 4), (ii) approximated the winds as having constant mechanical luminosity, (iii) ignored the effects of magnetic fields and stellar radiation (see Chapter 5), and (iv) adopted the assumption of collisional and ionization equilibrium for computing cooling losses in ionized gas, and a simple analytic fit for cooling in warm/cold neutral gas. Thus, our simulations are designed to test our theoretical predictions, rather than faithfully represent the real world. By tackling an idealized numerical problem, however, we are able to validate our theoretical framework and quantitative predictions that can be extrapolated beyond the necessarily limited scope of any single simulation suite.

The structure of this chapter is as follows. In Section 3.2 we describe our numerical methods for implementing winds in the *Athena* code, as well as our simulation set-up and the parameters of our model suite. We present the analysis of our results in Section 3.3 and conclude with a summary of our findings in Section 3.4.

3.2 Numerical Methods and Models

To test the theory presented in Chapter 2, we use the *Athena* code (Stone et al., 2008) in running a series of three-dimensional (3D) hydrodynamic simulations of constant luminosity stellar winds injected into turbulent clouds. We do not include any magnetic fields in the present simulations, but we do include cooling in the gas that is implemented as part of the *Athena*-TIGRESS code base for the star-forming multiphase ISM (Kim & Ostriker, 2017, 2018). This implements cooling in an operator-split manner following Koyama & Inutsuka (2002) at $T < 10^{4.2}$K and Sutherland & Dopita (1993) at $T > 10^{4.2}$K.

There is also uniform background heating of $2 \times 10^{-26}\,\mathrm{erg\,s^{-1}\,H^{-1}}$ which decreases in hot, ionized gas; more details can be found in Section 2.3.1 of Kim & Ostriker (2017). All of our simulations are run using the linearized Roe Riemann solver (Roe, 1981), second-order spatial reconstruction, and the unsplit van Leer integrator (Stone & Gardiner, 2009).

3.2.1 Wind Injection

Here we describe our treatment of stellar winds, which we implement in *Athena* in an operator-split fashion. We provide a quantitative test of this implementation in Section 3.5. Each simulation contains a single wind source, which we refer to as a "star particle," although in practice it represents a stellar cluster. This source particle is put in "by hand" and does not exert any gravitational force on the surrounding gas. Our approach employs a hybrid thermal/kinetic energy injection scheme which interpolates between pure thermal injection close to a source and pure kinetic injection towards the edge of the feedback region. There are multiple benefits to this hybrid energy injection approach. From a physical perspective, it more directly represents the reality of a bubble driven by a cluster of massive stars, wherein the majority of the energy close to the center of the bubble is thermal (due to shock thermalization through colliding winds of individual stars) while it is mostly kinetic towards the edges (where this thermal energy has managed to drive expansion). From a numerical perspective, for a purely kinetic feedback implementation the vector momentum field cannot be properly resolved immediately adjacent to the source. By transitioning to thermal

energy injection near the source, it is only necessary to resolve a scalar field. An advantage of the hybrid approach over purely thermal energy injection is that the latter can require a larger spatial scale for pressure gradients to accelerate the flow modeling the primary wind.

Given a star particle at position $\mathbf{x}_{\rm star}$ within the domain of the simulation, we deposit energy in the grid cells surrounding the star particle using a subcell method based on the implementation of Ressler et al. (2020). We specify $r_{\rm fb}$, the radius of the spherical feedback region, and $N_{\rm sc}$ is the number of subcells per grid cell along a grid-aligned direction. When initializing the simulation we loop through a cube of $N_{\rm sc,tot}^3$ subcells where

$$N_{\rm sc,tot} = 2N_{\rm sc} \lceil r_{\rm fb}/\Delta x \rceil \tag{3.1}$$

is the total number of subcells that could possibly lie within the feedback sphere along a grid-aligned direction and $\lceil \cdot \rceil$ denotes the ceiling function. The subcells within this cube are equally spaced along each grid-aligned direction between $-\Delta x \lceil r_{\rm fb}/\Delta x \rceil$ and $+\Delta x \lceil r_{\rm fb}/\Delta x \rceil$.

For each subcell in this cube with position $\mathbf{x}_{{\rm sc},i}$ relative to the source, we determine if $|\mathbf{x}_{{\rm sc},i}| < r_{\rm fb} + \Delta x/2N_{\rm sc}$ (i.e. if the subcell is within half a subcell spacing of the feedback radius or fully within the feedback radius). If it is, we then record the position of the subcell $\mathbf{x}_{{\rm sc},i}$ for use within the full simulation. In order to account for the subcell volume only partially overlapping the actual feedback region, we additionally assign each subcell a weight $w_{{\rm sc},i}$ according to

$$w_{{\rm sc},i} = \begin{cases} 1 & |\mathbf{x}_{{\rm sc},i}| \leq r_{\rm fb} - \frac{\Delta x}{2N_{\rm sc}} \\ \frac{1}{2}\left(\frac{2N_{\rm sc}(r_{\rm fb} - |\mathbf{x}_{{\rm sc},i}|)}{\Delta x} + 1\right) & |\mathbf{x}_{{\rm sc},i}| > r_{\rm fb} - \frac{\Delta x}{2N_{\rm sc}} \end{cases} . \tag{3.2}$$

This formula is simply a linear interpolation between 1 and 0 over the radial range of $\pm$ half a subcell spacing from the feedback radius, which approximates the true volume fraction (Jones & Williams, 2017). We additionally store the total effective volume that wind energy is injected into, defined as

$$V_{\rm inj} = \left(\frac{\Delta x}{N_{\rm sc}}\right)^3 \sum_i w_{{\rm sc},i} \, . \tag{3.3}$$

Once the positions and weights of the subcell template are initialized, they are used for the hybrid thermal/kinetic energy injection.

Given a mechanical luminosity $\mathcal{L}_w$ and mass loss rate $\dot{M}_w$ for the wind, the mean mass density ρ_w and energy density ϵ_w to be injected in a time Δt are

$$\rho_w = \frac{\dot{M}_w \Delta t}{V_{\rm inj}} \ , \ \epsilon_w = \frac{\mathcal{L}_w \Delta t}{V_{\rm inj}} \, . \tag{3.4}$$

For a given subcell in our template, indexed by i, we determine the grid cell in which it resides at location $\mathbf{x}_{\rm star} + \mathbf{x}_{{\rm sc},i}$, and increment the mass density by $\delta\rho_i = w_{{\rm sc},i}\rho_w/N_{\rm sc}^3$. For the purposes of the current paper, $\mathbf{x}_{\rm star}$ is always at the origin.

The total energy density in the target cell is similarly incremented by $\delta\epsilon_i = w_{{\rm sc},i}\epsilon_w/N_{\rm sc}^3$. To compute the injected momentum, we specify the variable $f_{\rm kin}$ at a given subcell position $\mathbf{x}_{{\rm sc},i}$ according to

$$f_{\rm kin}(|\mathbf{x}_{{\rm sc},i}|) = \max\left(1, |\mathbf{x}_{{\rm sc},i}|/r_{\rm fb}\right) \, , \tag{3.5}$$

Once $f_{\rm kin}$ is determined we define the injected momentum density as

$$\delta\mathbf{q}_i = \left(2 f_{\rm kin}(|\mathbf{x}_{{\rm sc},i}|)\delta\epsilon_i\delta\rho_i\right)^{1/2} \frac{\mathbf{x}_{{\rm sc},i}}{|\mathbf{x}_{{\rm sc},i}|} \, . \tag{3.6}$$

As was noted in Wall et al. (2020), the presence of momentum and mass within the grid cell to which we are adding these quantities means that the kinetic energy added by the above change in momentum density *is not* $f_{\rm kin}\delta\epsilon_i$, but actually somewhat less depending on what the initial density and momentum of the cell are. The discrepancy between the actual injected kinetic energy density and $f_{\rm kin}\delta\epsilon_i$ is especially important at the early times of wind onset, when the surrounding density is high, but becomes negligible once the wind has evacuated the feedback region. In the case where there is negligible pre-existing energy and momentum, our prescription deposits 75% of the total energy as kinetic energy.

In order to make sure that our results are not affected by the details of our feedback mechanism, we run tests with $f_{\rm kin} = 0$ (purely thermal feedback) in Appendix 3.6.1. This scenario might be

Table 3.1. Parameters of simulation suite.

Cloud Mass $[M_\odot]$	Cloud Radius [pc]	$\overline{n}_{\rm H}$ $[{\rm cm}^{-3}]$	v_t $[{\rm km\,s}^{-1}]$	$\Delta x^{\rm a}$ [pc]	Resolution[a]
5×10^4	20	43.1	3.59	0.15	256^3
5×10^4	10	345.	5.08	0.08	256^3
5×10^4	5	2760	7.18	0.04	256^3
5×10^4	2.5	22800	10.2	0.02	256^3
10^5	20	86.3	5.08	0.08	512^3
10^5	10	690.	7.18	0.04	512^3
10^5	5	5520	10.2	0.02	512^3
10^5	2.5	44200	14.4	0.01	512^3
5×10^5	20	431	11.4	0.15	256^3
5×10^5	10	3450	16.1	0.08	256^3
5×10^5	5	27600	22.7	0.04	256^3
5×10^5	2.5	228000	32.1	0.02	256^3

Note. — Each model is run with three different values for the mass of the wind source particle, $M_*/M_{\rm cl} \equiv \varepsilon_* = 0.01, 0.1$, and 1.

closer to the truth of a cluster of stars whose colliding winds shock and turn initially kinetic energy into bulk thermal energy. We found that this pure thermal feedback scenario simply leads to a minor delay in the wind's evolution, but broadly the results remain unchanged.

When we inject the wind mass into the feedback region we add an equal amount of "mass" to a passive scalar variable, which is simply passively advected with the gas. We use this scalar to track the mixing of the wind material with the surrounding gas as well as a means of separating mass that has been swept up by the wind from the ambient medium, as we will explain in Section 3.3.

3.2.2 Model Parameters and Set-Up

Our goal is to span a large range of the potential parameter space for stellar winds originating from young star clusters within massive molecular clouds, which is where most star formation takes place. To that end, we consider three cloud masses $M_{\rm cl}$ of $5\times10^4 M_\odot$, $10^5 M_\odot$, and $5\times10^5 M_\odot$ and four different cloud radii $R_{\rm cl}$ of 20 pc, 10 pc, 5 pc, and 2.5 pc. The largest radii represent "normal"

star-forming GMCs, cases with intermediate radii may represent infrared dark clouds (IRDCs), and cases with the smallest radii may represent extremely dense cluster-forming clumps within larger GMCs or the natal clouds in which super star clusters are born in starbursting galactic centers.

Each choice of $M_{\rm cl}$ and $R_{\rm cl}$ corresponds to a choice of mean mass density $\bar{\rho}$ as

$$\bar{\rho} = \frac{3M_{\rm cl}}{4\pi R_{\rm cl}^3} = \mu m_p \overline{n}_{\rm H} \ , \tag{3.7}$$

where $\mu_{\rm H} = 1.4271$ is the mean molecular weight of the gas, m_p is the mass of a proton, and $\overline{n}_{\rm H}$ is the mean number density of the Hydrogen nuclei. Rather than creating spherical clouds within our cubic domain, we apply uniform density $\bar{\rho}$ everywhere within a domain of side length $L_{\rm box} = 2R_{\rm cl}$. The "global cloud" parameters are just used for reference in setting the ambient conditions with which the wind interacts.

The grid has uniform spatial resolution in each dimension with $L_{\rm box}/\Delta x = 128$, 256, 512 for the simulations with $M_{\rm cl} = 10^5\,M_\odot$ and only $L_{\rm box}/\Delta x = 128$, 256 for the simulations at higher and lower cloud mass. The parameters describing the simulation initial density conditions and numerical resolution are outlined in Table 3.1. Only the highest resolution is listed for each model.

We initialize all the simulations at a uniform pressure of $P/k_B = 3 \times 10^4\,{\rm cm^{-3}\,K}$. Since we evolve the simulations long enough for thermal relaxation to occur before initiating the wind, this particular choice of initial pressure is not important to our results. We also ran test simulations at a initial pressure of $P/k_B = 3 \times 10^3\,{\rm cm^{-3}\,K}$ and found no differences.

Each simulation is initialized with a turbulent velocity field which is a Gaussian random field with power spectrum $|v_k|^2 \propto k^{-4}$ for $2 \leq kL_{\rm box}/(2\pi) \leq 64$. For higher resolution runs, the realization of the power spectrum uses an identical set of modes to the lower-resolution case. The amplitude of the turbulence is chosen so that the initial kinetic energy per unit mass is equivalent to twice that of the gravitational potential for a sphere of radius $R_{\rm cl}$ and mass $M_{\rm cl}$, i.e.

$$\tilde{E}_{\rm kin,i} = 2|\tilde{W}_{\rm sphere}| = \frac{6GM_{\rm cl}}{5R_{\rm cl}} \ , \tag{3.8}$$

where the tildes are used to indicate energy per unit mass. We note, however, that self-gravity is not included in the simulations.

For each simulation, we allow the turbulent velocity field to evolve and decay, without any additional driving, until the average kinetic energy per unit mass has decayed to $\tilde{W}_{\rm sphere}$ (i.e. it has been reduced by half). At the end of this initial evolution each simulation has a turbulent velocity scale $v_t = (\tilde{E}_{\rm kin,i})^{1/2}$. For each model, v_t is listed in Table 3.1.

At the same time as turbulence is decaying, the Reynolds stresses create inhomogeneous density structure throughout the simulation domain. The turbulent decay period is generally one tenth of the initial flow crossing time ($L_{\rm box}/v_{t,i}$) of the simulation domain, amounting to 0.03-0.7 Myr. Over this period, the thermal energy also relaxes, with temperature approaching thermal equilibrium; in the cold gas this is $\sim 30 - 200\,{\rm K}$.

After the initial period of turbulent decay, we create a star particle at the center of the simulation domain of mass $M_* = \varepsilon_* M_{\rm cl}$. The parameter ε_* can be thought of as akin to a total star formation efficiency. For each set of initial conditions laid out in Table 3.1 we run simulations at $\varepsilon_* = 0.01, 0.1,$ and 1. The star particles inject energy and mass proportional to their own mass in accordance with the method described in Section 3.2.1, with a feedback radius $r_{\rm fb} = L_{\rm box}/40$ at all resolutions, meaning that the feedback radius is resolved by a minimum of 3.2 resolution elements at the lowest resolution. We test this choice of feedback radius in Appendix 3.6.3 and find it does not affect our results.

We adopt a constant wind luminosity per unit mass of $\mathcal{L}_w/M_* = 10^{34}\,{\rm erg\,s^{-1}}\,M_\odot^{-1}$ and mass loss rate per unit mass $\dot{M}_w/M_* = 10^{-2}\,{\rm Myr^{-1}}$. This mass loss rate is about a factor of five larger than that expected for a standard solar metallicity population, with a Kroupa IMF (Kroupa, 2001) as calculated by STARBURST99 (SB99) (Leitherer et al., 1999). A comparison between the constant values that we adopt and those determined from SB99 is given in Figure 3.1. We use the larger mass loss rate because this reduces the temperature of the shocked wind, yielding a less stringent time step.

Our adopted wind parameters correspond to a wind velocity of $\mathcal{V}_w = (2\mathcal{L}_w/\dot{M}_w)^{1/2} = 1780\,{\rm km\,s^{-1}}$ and a momentum injection rate per unit mass of $\dot{p}_w/M_* = \mathcal{V}_w\dot{M}_w/M_* = 17.8\,{\rm km\,s^{-1}\,Myr^{-1}}$.

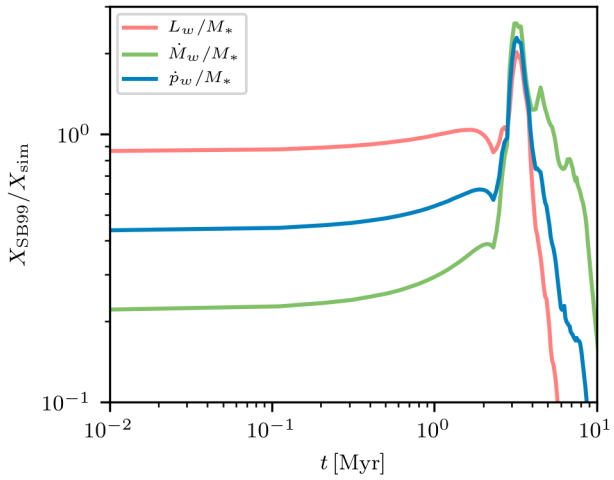

Figure 3.1 Ratio of the wind parameters derived using the population synthesis code STARBURST99 (SB99) to the constant values for each parameter that we adopt in our simulations.The SB99 mass-loss rate and momentum input rate are respectively a factor ~ 5 and ~ 2 lower than the ones we adopt. We validate that using the SB99 values does not change our conclusions (see Appendix 3.6.2).

At the lower mass loss rates consistent with the SB99 calculations, the wind velocity (momentum injection rate) is larger (smaller) by a factor $\sim \sqrt{5} \approx 2.2$, i.e. $\mathcal{V}_w \sim 3750\,{\rm km\,s^{-1}}$ and $\dot{p}_w/M_* \sim 8.6\,{\rm km\,s^{-1}\,Myr^{-1}}$. This only corresponds to a difference in radial evolution (according to our theory) of a factor of $5^{1/8} \approx 1.2$, so this should not effect the interpretation of our results. We have additionally run simulations with a standard mass loss rate and have obtained consistent results, as described in Appendix 3.6.2.

3.3 Numerical Results

Here we lay out the results of the simulations described in Section 3.2.2. In our presentation, we shall focus on cases with $M_{\rm cl} = 10^5\,M_\odot$ and use the remaining simulations for validation of the generality of our results, as summarized in Appendix 3.7.

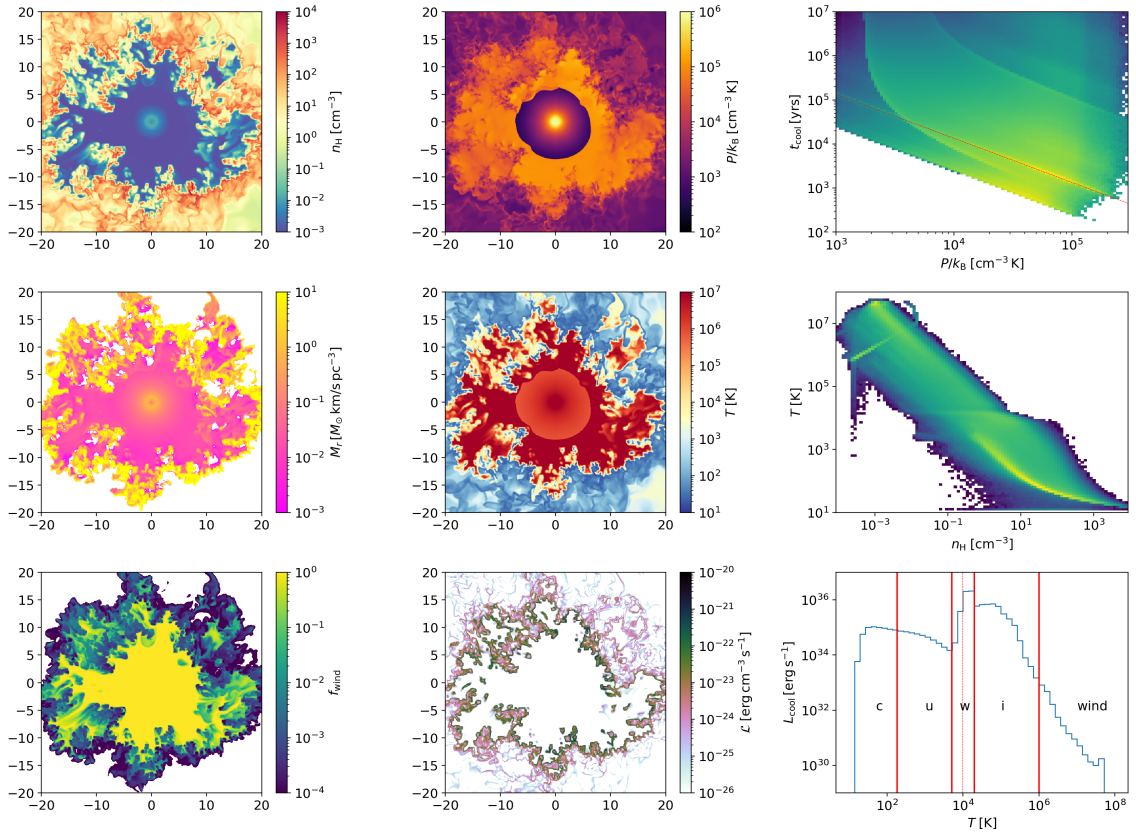

Figure 3.2 An example snapshot of the wind bubble structure and phase properties at time $t = 2.23\,\mathrm{Myr}$ after the initiation of the wind for the model with $M_{\rm cl} = 10^5\,M_\odot$, $R_{\rm cl} = 20\,\mathrm{pc}$, $\varepsilon_* = 1\%$, and $L_{\rm box}/\Delta x = 512$ simulation. The left and center columns show slices through the $z = 0$ plane, while the right column displays distributions. From left to right and top to bottom, panels show: gas number density, pressure, a cooling-weighted phase diagram of cooling time vs. pressure, radial momentum density, temperature, a volume-weighted temperature-density phase diagram, the wind mass fraction ($f_{\rm wind}$), the cooling rate per unit volume, and a cooling-weighted histogram of the gas temperature distribution (which depicts the total cooling occurring in each temperature bin). In the top-right panel, the highest concentration of cooling is in gas that has $t_{\rm cool} \propto P^{-1}$; this slope is indicated by a dashed red diagonal line for the coefficient in Equation 2.10 corresponding to $T_{\rm pk} = 9650\,\mathrm{K}$. The last panel uses vertical lines to delineate the phases described in Table 3.2, where the subscripts from the table are indicated. The label "wind" includes both the free (f) and post-shock (ps) wind phases. In this panel, $T_{\rm pk}$ is marked as a vertical dashed line within the "w" phase.

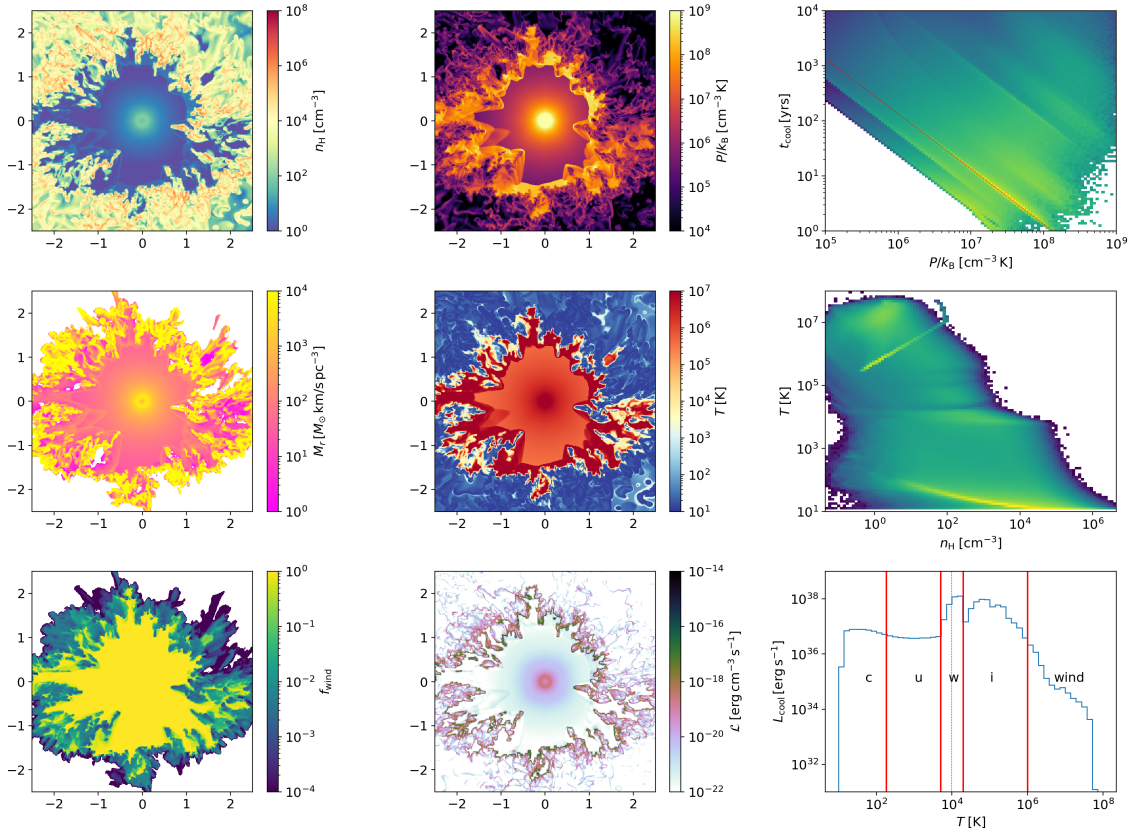

Figure 3.3 Same as Figure 3.2 but for the model with $M_{\rm cl} = 10^5\,M_\odot$, $R_{\rm cl} = 2.5\,{\rm pc}$, $\varepsilon_* = 100\%$, and $L_{\rm box}/\Delta x = 512$ simulation at $t = 0.125\,{\rm Myr}$. All quantities are as specified in Figure 3.2, though the range of many quantities are quite different.

3.3.1 Cloud and Bubble Structure and Thermal Distributions

Example snapshots from our simulations are provided in Figure 3.2 ($R = 20\,\mathrm{pc}$ and $\varepsilon_* = 1\%$ model) and Figure 3.3 ($R = 2.5\,\mathrm{pc}$ and $\varepsilon_* = 100\%$ model) in order to provide a more concrete reference. These two models are deliberately chosen to span the range of cloud size and star formation efficiency parameters.

In both figures, the "wind-blown bubble" is the low-density, high-temperature region filling the central region of the simulation domain, with fingers extending outward. Outside of the bubble, the inhomogeneous density structure generated by the background turbulence in the cold cloud is evident; higher density portions of the ambient gas are also left behind in the bubble interior, although they are ablated over time by KH instabilities as the high-velocity wind flows past them.

As expected, the cooling rate (bottom center panel) is greatest at the (fractal) interface between the hot bubble and cool shell, where mixing is driven by turbulence. The outward momentum originally carried by the wind is deposited at the bubble boundary by interface mixing, where it builds up in the expanding cool shell (middle left panel). The degree of mixing is also evident in the fraction of wind gas in each cell (bottom left panel).

Figure 3.2 and Figure 3.3 also include (right column) information on the statistical distribution functions of gas in density, temperature, pressure, and cooling time. The top right panel shows that the highest concentration of cooling is in gas with $t_{\mathrm{cool}} \propto P^{-1}$, as predicted in Chapter 2 (see definition in Equation 2.10) . Quantitatively, we find that

$$t_{\mathrm{cool}} = 135\,\mathrm{yr}\left(\frac{P/k_B}{10^6\,\mathrm{Kcm^{-3}}}\right)^{-1} \tag{3.9}$$

follows well the prominent linear feature at short cooling time for both cases, as well as our other models. The corresponding T_{pk} would be $9650\,\mathrm{K}$.

3.3.2 Gas Phase Definitions

We define several different gas phases as an aid in quantifying the structure and evolution of the wind-driven bubbles. These definitions can be thought of as an expansion on the phases laid out

Table 3.2. Definitions of gas phases.

Phase	Temperature Condition	Velocity Condition	Subscript	Schematic Region
Free Hyper-Sonic Wind	$T > 10^5\,\mathrm{K}$	$v_r > \mathcal{V}_w/2$	f	(i)
Shocked Stellar Wind	$T > 10^6\,\mathrm{K}$	$v_r < \mathcal{V}_w/2$	ps	(ii)
Ionized Gas	$2 \times 10^4\,\mathrm{K} < T < 10^6\,\mathrm{K}$	$v_r < \mathcal{V}_w/2$	i	(iii)
Warm Neutral Gas	$5050\,\mathrm{K} < T < 2 \times 10^4\,\mathrm{K}$		w	(iii)/(iv)
Thermally Unstable Gas	$184\,\mathrm{K} < T < 5050\,\mathrm{K}$		u	(iii)/(iv)
Cold Neutral Gas	$T < 184\,\mathrm{K}$		c	(iv)

Note. — Names assigned to gas phases based on temperature and velocity conditions, with (second-from-right column) subscript used to denote each phase. The final column indicates the rough correspondence between gas phases and locations in the schematic Figure 1b of Chapter 2.

for the classical stellar wind bubble in Chapter 2, in order to better account for the cooling of the gas. These definitions (see Table 3.2) are based on the temperature T and radial velocity v_r of the gas. The table also lists subscripts used to denote quantities associated with each phase (such as volume, momentum, energy, etc.). These subscripts label the thermal phases of the wind in the bottom right panels of Figure 3.2 and Figure 3.3.

The first two phases listed in Table 3.2 are analogous to the two wind phases described in Weaver et al. (1977). The Ionized Gas is contained within the cooling layer, and cooling in this phase is dominated by collisional excitation of transitions of H, He, C, N, and O (primarily). This phase is produced via mixing and subsequent cooling of shocked wind and shell gas, and would not exist as part of the undisturbed/ambient ISM in either the uniform or turbulent cases.

The Warm Neutral Gas has cooling dominated by collisionally-excited Lyα emission and recombination on dust grains. The Thermally Unstable Gas is in the range between the stable equilibrium warm and cold phases in the static case, for our adopted cooling function. This phase is continually populated because of the turbulence in the system. Finally, at the lowest temperature there is the Cold Neutral Gas, which in reality would include both atomic and molecular phases, but here we do not follow the detailed chemistry.

The final three phases would all usually exist to varying degrees as part of the background

in a turbulent, dense cloud. We wish to separate the portions that are ISM gas that has been shocked and then cooled after being swept into the expanding bubble shell from the portions that are undisturbed ambient gas. We do this using cuts based on the fraction of the mass in a given cell that originates in the wind, $f_{\rm wind}$. The wind mass is tracked using a scalar that is injected with the wind (see Section 3.2.1) and then passively advected.

For each of the Ionized, Warm, Thermally Unstable, and Cold phases of the gas we track all quantities of interest in gas with $f_{\rm wind} > 10^{-3}, 10^{-4}$, and 10^{-5} (each subsequent selection being a superset of the previous selection). Unless otherwise stated, we use $f_{\rm wind} > 10^{-4}$ to separate the swept-up and ambient parts of these phases, as this gives the best agreement between different methods of measuring the total cooling, as described in Section 3.3.7. The tracking of gas properties at different $f_{\rm wind}$ values also allows us to quantify the mixing of the wind with the turbulent gas.

As is evident in the bottom right panels of Figure 3.2 and Figure 3.3, the majority of the cooling is occurring in the Warm and Ionized phases. These are the phases that primarily occupy the boundary region between the bubble and surrounding cloud, as is clear from the temperature and cooling slices in these figures.

3.3.3 Bubble Evolution Comparisons

Here we present results from our simulations of the temporal evolution of the radial momentum of the gas (p_r), the wind bubble's effective radius ($\mathcal{R}_b$), and the interior bubble energy (E_b). We compare these results with the theory developed in Chapter 2. When measuring quantities in the shell of the wind bubble, we include the measurement of this quantity in all gas with a wind mass fraction greater than 10^{-4}. We found this was the best way of differentiating between the swept-up shell and the background gas.

In this section we show results for the $M_{\rm cl} = 10^5\,M_\odot$ cases, while results for other cloud masses are presented in Appendix 3.7 (Figure 3.24 and Figure 3.25).

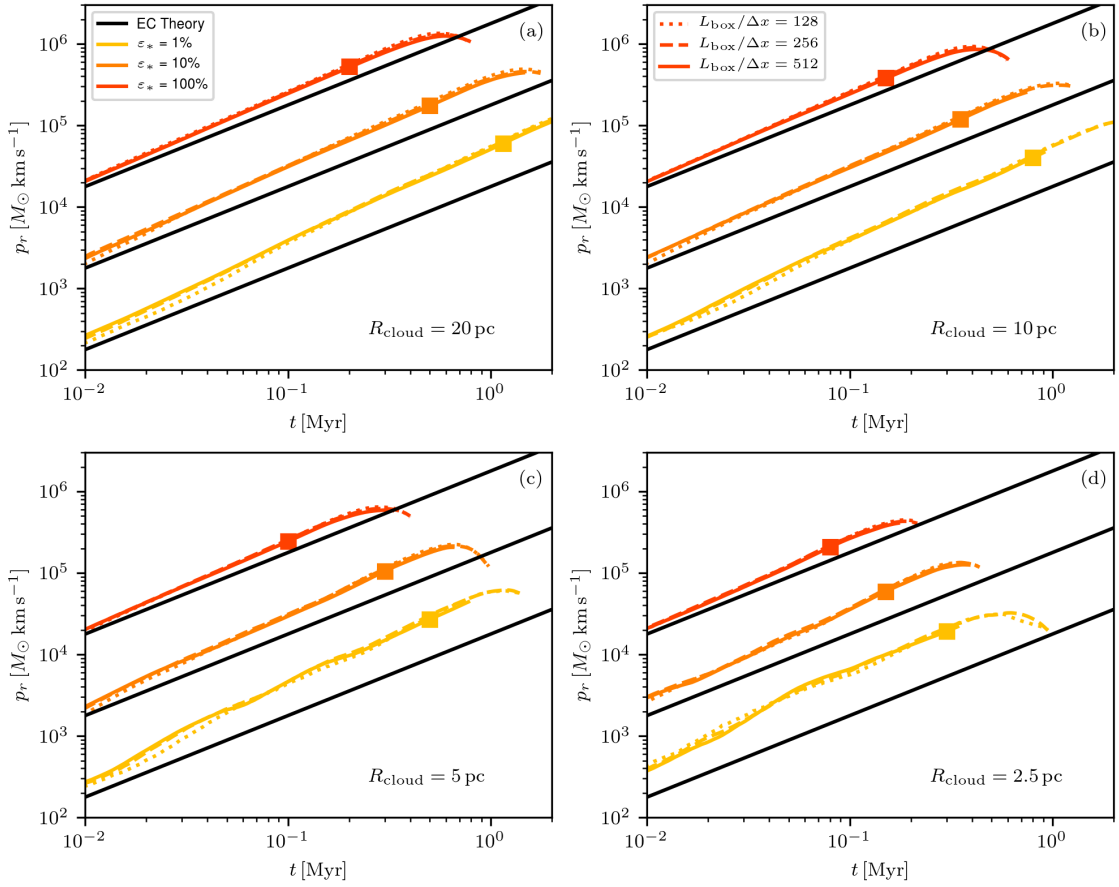

Figure 3.4 Evolution of the total radial momentum of the bubble (interior plus shell) in each of our simulations for cases with cloud mass $M_{\rm cl} = 10^5 M_\odot$. Model cloud radii (from least dense, $R_{\rm cl} = 20\,{\rm pc}$, to most dense, $R_{\rm cl} = 2.5\,{\rm pc}$) are given within the individual panels (a) to (d); see Table 3.1 for parameters. For each case we show results for star cluster particles of mass $M_* = 10^3 M_\odot$, $10^4 M_\odot$, and $10^5 M_\odot$ (corresponding to star formation efficiencies of $\varepsilon_* = 1\%$, 10%, and 100%) in yellow, orange, and red respectively. At each value of $R_{\rm cl}$ and ε_* we show three separate lines (solid, dashed, dotted) corresponding to varying resolution, as shown in the key. For each simulation with 512^3 cells, we mark the time at which the first wind-polluted gas exits the simulation domain $t_{\rm esc}$ with a square, and only show results from each simulation up until $4t_{\rm esc}$ (though not all of the highest resolution simulations were run for this long). For each value of $R_{\rm cl}$ and ε_* we show $\dot{p}_w t$ (which should apply when cooling is maximally efficient, per Equation 2.14) in black.

Shell Momentum

As is evident in Figure 3.2 and Figure 3.3, most of the radial momentum is carried by the dense shell of swept-up gas, thus we define the momentum as:

$$p_r \equiv p_{r,\mathrm{i}} + p_{r,\mathrm{w}} + p_{r,\mathrm{u}} + p_{r,\mathrm{c}}. \tag{3.10}$$

As mentioned above, only cells with a wind mass fraction greater than 10^{-4} are included in this definition. We found no significant changes in our measurement when considering $f_{\mathrm{wind}} > 10^{-5}$ gas or even $f_{\mathrm{wind}} > 0$ gas, which we took to indicate that there was no significant momentum carried in "completely unpolluted" gas. In Figure 3.4 (for the $M_{\mathrm{cl}} = 10^5\,M_\odot$ models), we compare this measurement of the momentum in the simulations with $p_r = \dot{p}_w t$, as predicted by the EC theory with $\alpha_p = 1$ (Equation 2.14).

The results at different resolutions show that the radial momentum carried by the bubble is extremely well converged in our simulations. Overall, results are within a factor of 1.2-4 of the EC prediction. The results are quantitatively closest to $\dot{p}_w t$ for more luminous winds (corresponding to higher star formation efficiency).

The momentum in excess of $\dot{p}_w t$ can be attributed to nonzero buildup of thermal energy in the shocked wind that aids in driving expansion (see Appendix of Chapter 2). This is parameterized in our theory by α_p in Equation 2.14.

We note that once the bubble has reached the edge of the simulation domain (identified by nonzero outflow of wind-contaminated gas), we cannot expect the numerical solution to continue to follow the EC theoretical prediction. We mark this first "blowout" time in Figure 3.5 with large squares (for the highest-resolution models). Some time after blowout, the rate of momentum increase falls below $\dot{p}_w$ because a fraction of the wind exits the domain without interacting with cloud gas.

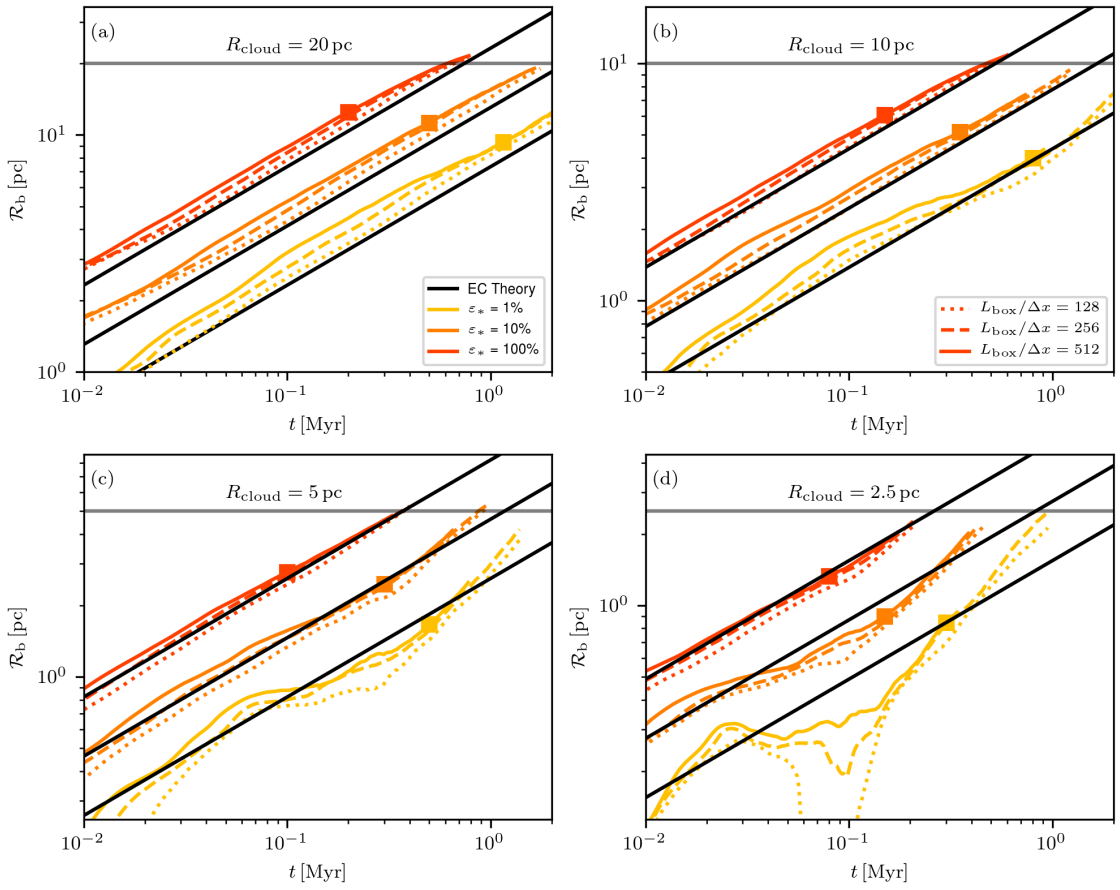

Figure 3.5 Evolution of the effective radius $\mathcal{R}_b$ in each of our simulations for cases with cloud mass $M_{\rm cl} = 10^5 M_\odot$. Line styles are as in Figure 3.4. For each value of $R_{\rm cl}$ and ε_* we show (in black) the evolution prediction from the EC theory (Equation 2.19, with $\alpha_R = \alpha_p = 1$). The grey horizontal lines indicate $R_{\rm cl}$, while squares indicate the time when wind-contaminated gas first leaves the domain ($t_{\rm esc}$). As in Figure 3.4, we only show simulation results up until $4t_{\rm esc}$.

Effective Radius

The effective bubble radius $\mathcal{R}_b$ is defined from Equation 2.16 based on the bubble volume, V_b. For this volume, we include just the hot phases of the gas, the Free Wind (volume $V_{\rm f}$) and the Shocked Wind (volume $V_{\rm ps}$):

$$V_b \equiv V_{\rm f} + V_{\rm ps}\,. \tag{3.11}$$

Comparisons between our simulations with $M_{\rm cl} = 10^5\,M_\odot$ and the prediction given by Equation 2.19 (with $\alpha_R = \alpha_p = 1$) are given in Figure 3.5. It is clear that the EC theory very well explains the salient features of the radial expansion. The only exceptions are the smallest two clouds for $\epsilon_* = 0.01$, which is the least realistic parameter regime since high density regions are observed to have very high SFE (e.g. Leroy et al., 2018). These deviations are mainly caused by the Reynolds stress in the surrounding turbulent gas being non-negligible compared to the wind pressure, given the low ε_*.

We note in particular that the scaling $\mathcal{R}_b \propto t^{1/2}$ represents the numerical results better than the steeper scaling $R \propto t^{3/5}$ of Weaver et al. (1977) or El-Badry et al. (2019) for pressure-driven expansion. For the majority of cases that follow the $\mathcal{R}_b \propto t^{1/2}$ scaling well, the numerical result is within 20% of Equation 2.19. Quantitatively, the EC theory works especially well at higher densities (where cooling is most efficient) and at higher $\mathcal{L}_w$ (i.e. higher ε_*, where $\dot{p}_w$ and $\dot{\mathcal{R}}_{\rm b}$ are larger, and therefore the constraint on Θ as given by Equation 2.39 is not as stringent).

At the time of first blowout, the mean bubble expansion rates range from $\sim 10 - 100\,{\rm km\,s^{-1}}$ in the least dense cloud to $\sim 3 - 10\,{\rm km\,s^{-1}}$ in the most dense cloud, with larger velocities applying in the cases with higher wind power $\mathcal{L}_w \propto \varepsilon_*$. Note that the first blowout (shown with colored squares) occurs much earlier than the time when $\mathcal{R}_b(t) = R_{\rm cl}$ (shown with a horizontal grey line) due to the fractal nature of the bubble interface, where parts of the bubble surface are at much larger radii than others.

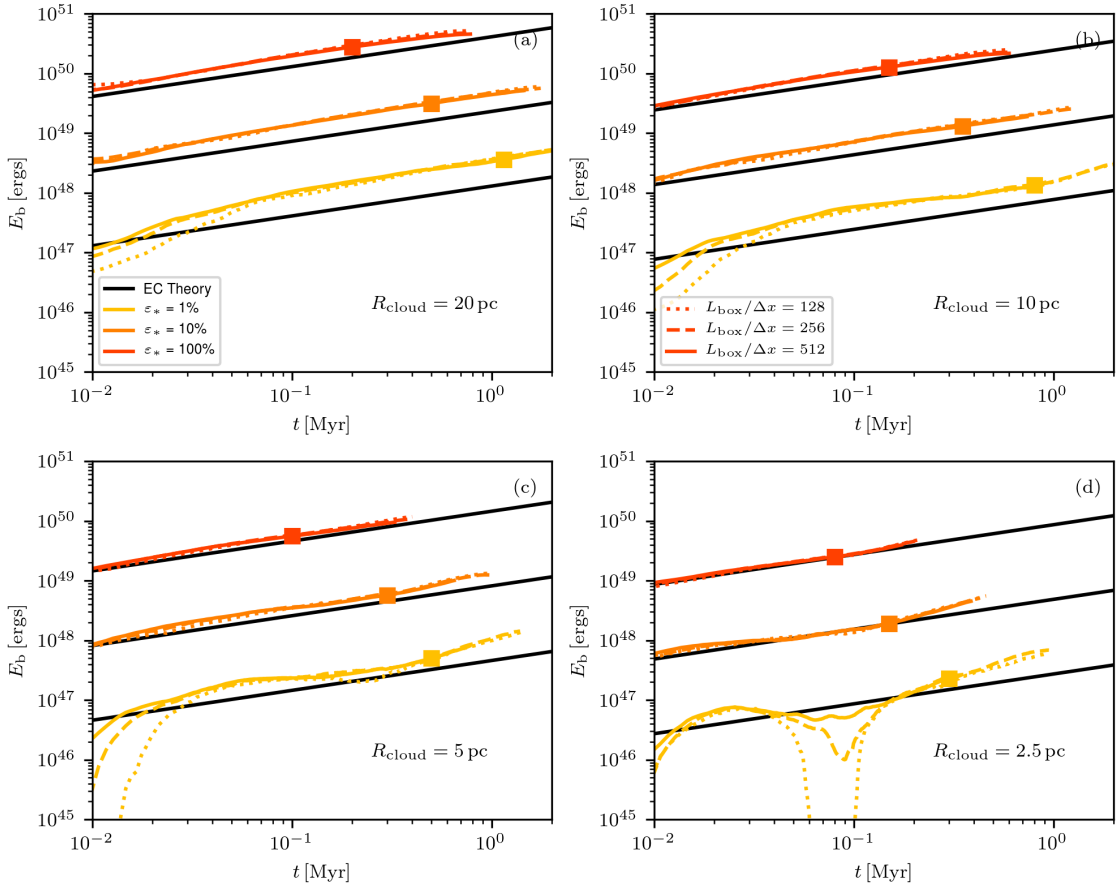

Figure 3.6 Evolution of the total energy in the interior of the bubble in each of our simulations for cases with cloud mass $M_{cl} = 10^5 M_\odot$. Line styles are as in Figure 3.4. For each value of R_{cl} and ε_* we show in black the energy given by Equation 2.20 (taking $\mathcal{S} = \alpha_p = \alpha_R = 1$ and using Equation 2.19).

Bubble Interior Energy

In keeping with the definition of the bubble interior given by Equation 3.11, we measure the bubble's interior's energy using

$$E_b \equiv E_{\rm f,kin} + E_{\rm f,thm} + E_{\rm ps,kin} + E_{\rm ps,thm} \tag{3.12}$$

where the "kin" and "thm" subscripts refer to kinetic and thermal energy respectively. We note that the thermal energy within the free wind ($E_{\rm f,thm}$) is negligible compared to its kinetic energy, but we include it here for completeness.

Figure 3.6 compares the energy measurement from the simulations with the prediction given by Equation 2.20, employing Equation 2.19 and taking $\mathcal{S} = \alpha_p = \alpha_R = 1$. When comparing the theory and simulations, we see similar trends as those observed in the evolution of bubble radii and momenta: the EC theory is most accurate at higher ε_* and higher density $\bar{\rho}$.

We also note that given the agreement with theoretical predictions for the shell momentum (as evidenced by Figure 3.4) and the bubble internal energy (as evidenced by Figure 3.6), we expect the shell's radial kinetic energy to be half that of the bubble's interior energy, as predicted in Chapter 2 (see Equation 23 there). This is indeed the case.

Hot Gas Pressure

Finally, we compare the prediction for the pressure in the shocked wind gas given by Equation 2.21 and that measured in our simulations. We measure the pressure by selecting the shocked wind gas (conditions specified in Table 3.2) in simulation snapshots and calculating the volume-averaged mean thermal pressure. We use the $L_{\rm box}/\Delta x = 256$ simulations for these comparisons as the pressure is computed directly from snapshots, which are taken at higher cadence in the lower resolution simulations. We also compute the $16^{\rm th}$, $50^{\rm th}$, and $84^{\rm th}$ percentiles of the distribution of pressures in this gas.

In Figure 3.7 we compare the evolution of the pressure with the prediction of Equation 2.21. For this comparison, we use $\alpha_p = \alpha_R = 1$, and we see that the theoretical prediction closely matches the evolution in the simulations. As we discuss below, the simulations actually have $\alpha_p > 1$. From

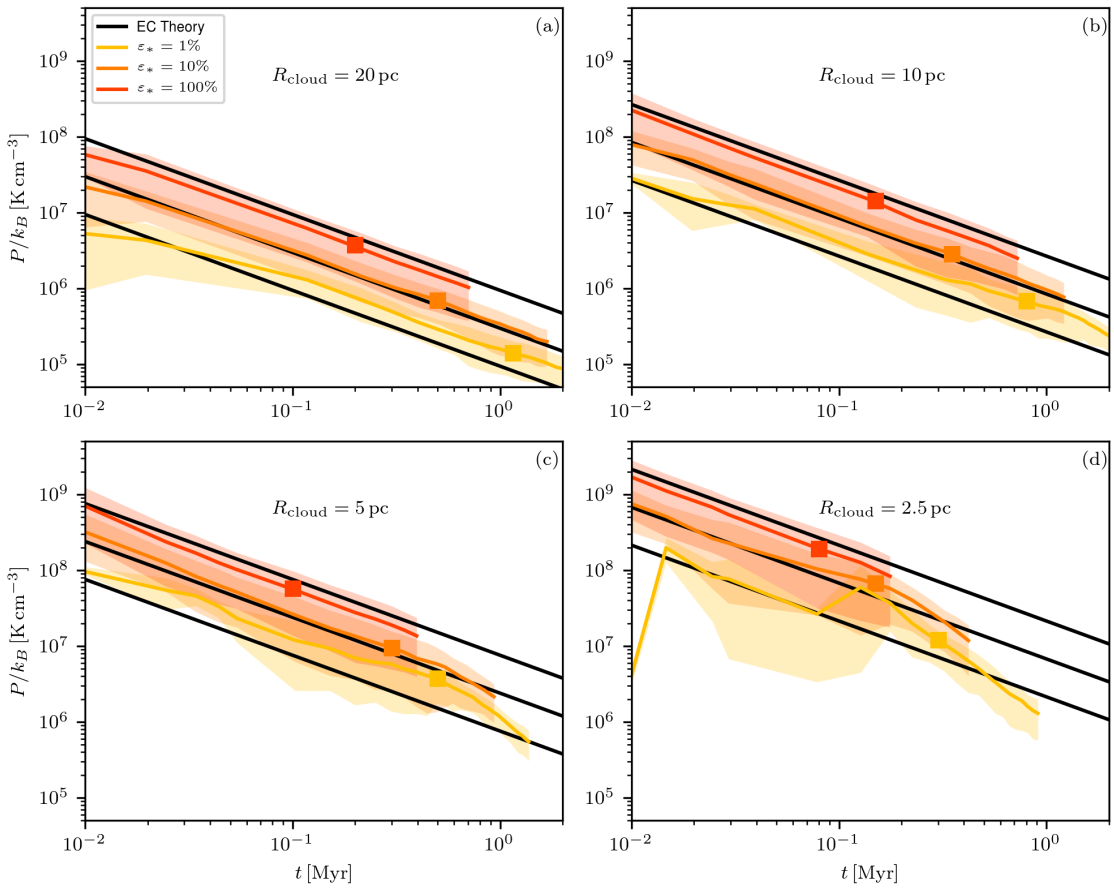

Figure 3.7 Evolution of the pressure in the shocked wind gas in cases with cloud mass $M_{\rm cl} = 10^5 M_\odot$. All panels show the evolution of the volume averaged mean pressure (solid colored lines) along with shading the $16^{\rm th}$ to $84^{\rm th}$ percentiles of the distribution of pressures in post-shock gas (colored shaded regions). We show the theoretical prediction (Equation 2.21, with $\alpha_p = 1$) in black. The time at which wind first escapes the domain is indicated by a colored square.

Equation 2.21 this would tend to increase the theoretical prediction (black curves in Figure 3.7), bringing the prediction closer to the 'observed' simulation value for the low ε_* cases (which have the largest α_p), but further away from agreement for high ε_* cases. The missing component here is the obliquity of the shock surface: the more oblique the shock the less thermalised the shocked wind becomes, hence lowering the pressure (discussed at the end of Appendix A in Chapter 2). As is clear from Figure 3.2 and Figure 3.3, the high ε_* winds have more oblique shocks, explaining this discrepancy.

3.3.4 Dimensionless Parameters

In the above comparisons we explicitly set the dimensionless, order-unity parameters of our theory equal to unity. However, the values and time evolution of these parameters provides interesting insight into the validity of the assumptions in the EC theory for different regimes (see Section 3.3.3). As is explained in Appendix A of Chapter 2, some of these parameters are interdependent.

The first dimensionless parameter is α_p, which is defined as the rate of momentum input to the surrounding medium divided by the rate of momentum injection by the wind. Specifically, we measure

$$\alpha_p = \frac{p_{\mathrm{r,b}}}{\dot{p}_w t} \tag{3.13}$$

where p_r is as measured in Equation 3.10. This measurement of α_p is shown as solid lines in Figure 3.8.

Another quantity in the EC theory is the energy enhancement factor $\mathcal{S}$, defined in Equation 2.20. As explored in depth in Appendix A of Chapter 2, $\mathcal{S}$ and α_p are expected to track each other (with $\mathcal{S} \approx \alpha_p$) because both are associated with buildup of energy in the bubble interior. For the same reason, we expect $\mathcal{S}$ to be higher when the shocked wind makes up a larger portion of the bubble volume, i.e. larger $\mathcal{R}_b/\mathcal{R}_f$. We also expect larger $\mathcal{S}$ when shock surfaces are less oblique. In order to directly compare $\mathcal{S}$ with α_p, we show in Figure 3.8 a measured value of $\mathcal{S}$ as dashed lines.

The measured value of $\mathcal{S}$ is taken as the ratio of the bubble energy in the simulations, measured according to Equation 3.12, to $\dot{p}_w \mathcal{R}_b/2$, where $\dot{p}_w$ is taken as the fixed wind momentum input rate

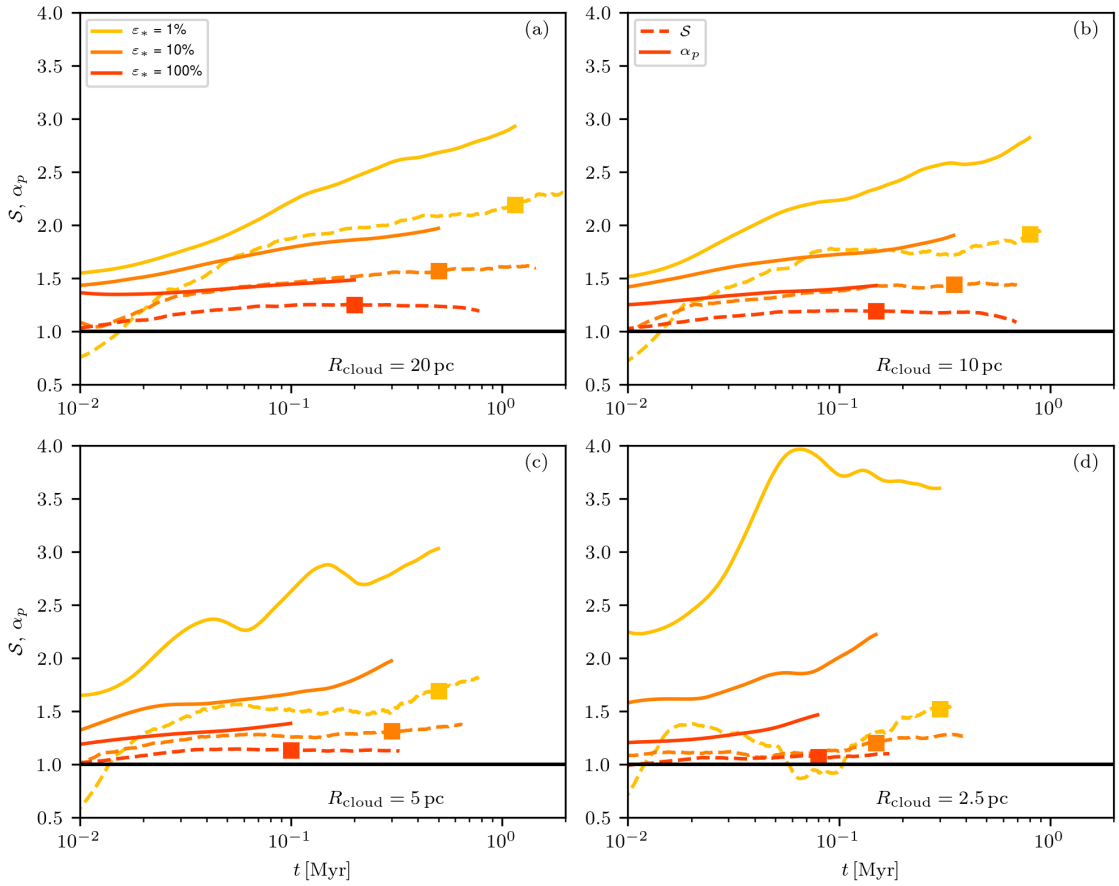

Figure 3.8 Evolution of the momentum (α_p) and energy ($\mathcal{S}$) enhancement factors shown as solid and dashed lines respectively. The evolution of α_p is only shown up to the point of breakout, which is indicated with colored squares on the curves for $\mathcal{S}$. We indicate the 'no enhancement' case with the horizontal black line. We show the highest resolution version of all simulations with $M_{\rm cl} = 10^5\,M_\odot$.

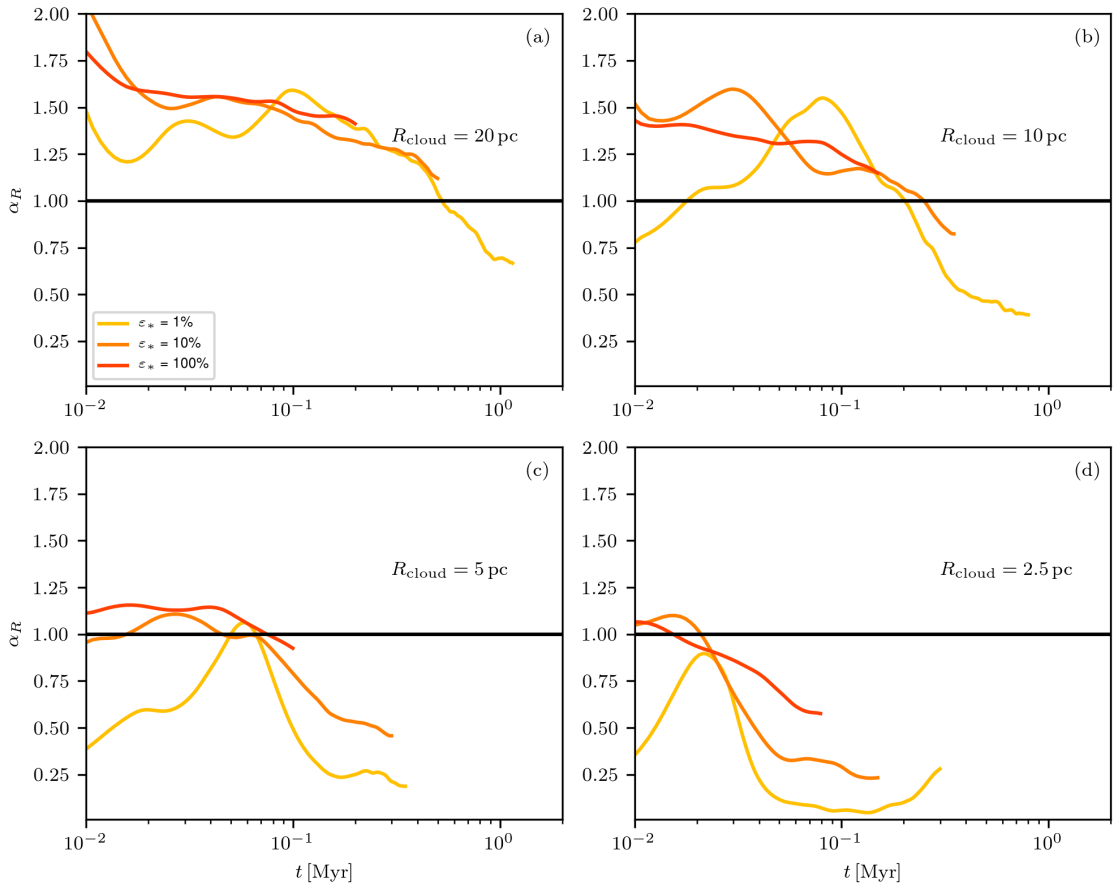

Figure 3.9 Evolution of the dimensionless parameter α_R. Line colors are associated with simulations of different ε_*. We use the highest resolution version of all simulations with $M_{\rm cl} = 10^5\,M_\odot$ and only show the evolution up to the point of breakout (square markers in Figure 3.4 and others).

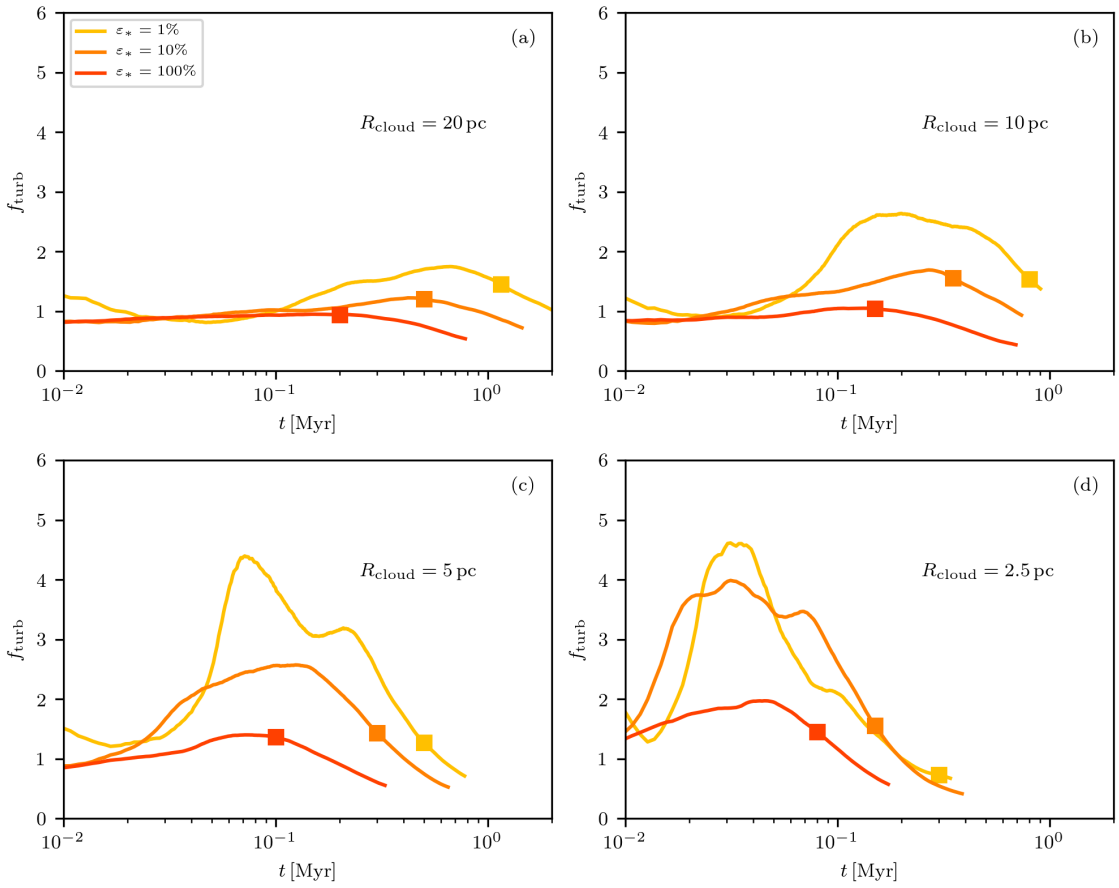

Figure 3.10 Evolution of the ratio of turbulent kinetic energy to kinetic energy in radial motion, for shell gas. We show the highest resolution version of all simulations with $M_{\rm cl} = 10^5\,M_\odot$. The square symbols mark the point at which wind-polluted mass begins to leave the domain.

and $\mathcal{R}_b$ is computed from the simulations as detailed in Section 3.3.3.

The next dimensionless parameter we introduce is α_R, which encodes geometric factors. Using Equation 2.19,

$$\alpha_R = \frac{\mathcal{R}_b^4}{\alpha_p} \left(\frac{3}{2\pi} \frac{\dot{p}_w t^2}{\bar{\rho}} \right)^{-1} . \tag{3.14}$$

We evaluate this using the measured $\mathcal{R}_b$ (see Section 3.3.3) and α_p (Equation 3.13). We note that we have no explicit theoretical prediction for α_R other than expecting it to be near unity. Figure 3.9 shows the measured values of α_R over time. We see that α_R remains quite close to unity, remaining in the range $0.5 - 1.5$ for the majority of the evolution. There is also some indication that α_R takes on lower values in the higher density clouds.

The *radial* kinetic energy of the shell in the EC theory is determined by momentum input from the wind, but there is no prediction for the kinetic energy in non-radial, turbulent motion. Given that the theory relies on efficient cooling facilitated through a turbulent interface, we expect a significant fraction of the kinetic energy in the shell (and around the shell-bubble interface) to be in turbulent motion. The simplest way to quantify this is in terms of the $f_{\rm turb}$ parameter defined in Equation 2.24.

To measure this parameter we write the total radial kinetic energy in the shell as

$$E_{r,\rm sh} \equiv \sum_{j \in \rm i,w,u,c} \frac{p_{r,j}^2}{2M_j} \tag{3.15}$$

where the sum is performed over the indicated phases, and as in Equation 3.10 we sum over zones where $f_{\rm wind} > 10^{-4}$. The total kinetic energy is measured in an analogous way.

The ratio $f_{\rm turb} = E_{\rm tot,sh}/E_{\rm r,sh} - 1$ is displayed in Figure 3.10. Surprisingly, for much of the bubble evolution and most of the parameter space, the energy in turbulent motion is at least as large as the energy in radial motion, with $f_{\rm turb} \approx 1$ (equipartition between radial and turbulent motion) over much of the parameter space. This fact emphasizes how important the turbulence is for the evolution of the bubble, especially the turbulence driven by the wind. We observe that the more powerful winds instill a larger fraction of their kinetic energy in radial motion.

In all simulations the fraction of turbulent kinetic energy in the shell increases in time until

seemingly reaching a set value before decreasing again. As we will see upon further inspection of the turbulent motion below, this reflects a saturation of turbulence as more and more radial energy is provided to the wind.

3.3.5 Turbulent Structure Function

Both the amplitude and spectral shape of turbulence are important to the mixing and cooling that dictate the bubble evolution. These are quantified via the turbulent structure function.

Following the theory outlined in Chapter 2, we particularly wish to measure the turbulence in the hot gas near the interface. To this end, we select gas with $T > 2 \times 10^4\,\mathrm{K}$ and $v_r < \mathcal{V}_w/2$ (the Ionized Gas and the Shocked Stellar Wind). In order to isolate the turbulent motion from the bulk radial outflow in this gas, we apply our structure function analysis only to the non-radial components of the velocity field. We will refer to this proxy for the turbulent velocity field (which is really the tangential velocity field) as $\mathbf{u}_t$ defined as

$$\mathbf{u}_t \equiv \mathbf{v} - (\mathbf{v} \cdot \hat{\mathbf{r}})\,\hat{\mathbf{r}}\,. \tag{3.16}$$

where $\mathbf{v}$ is the full velocity field. Of course, there are also turbulent contributions to the radial motion, but directly quantifying this is problematic due to contamination by the strong background radial flow. Figure 3.11 shows example snapshots of the magnitude of $\mathbf{u}_t$ from the $R_{\mathrm{cl}} = 20\,\mathrm{pc}$ model (in the purple to yellow color scheme).

To measure the turbulent structure function, we randomly select a cell i from the region under consideration. We then compute two histograms. The first histogram is the number of cells at position j with a spatial separation $\ell = |\mathbf{x}_j - \mathbf{x}_i|$ from cell i, binned by width Δx. The second histogram is as above, except now the histogram is weighted by the square of the difference in the tangential velocity field between positions i and j:

$$|\delta \mathbf{u}_t|^2 \equiv |\mathbf{u}_t(\mathbf{x}_i) - \mathbf{u}_t(\mathbf{x}_j)|^2\,. \tag{3.17}$$

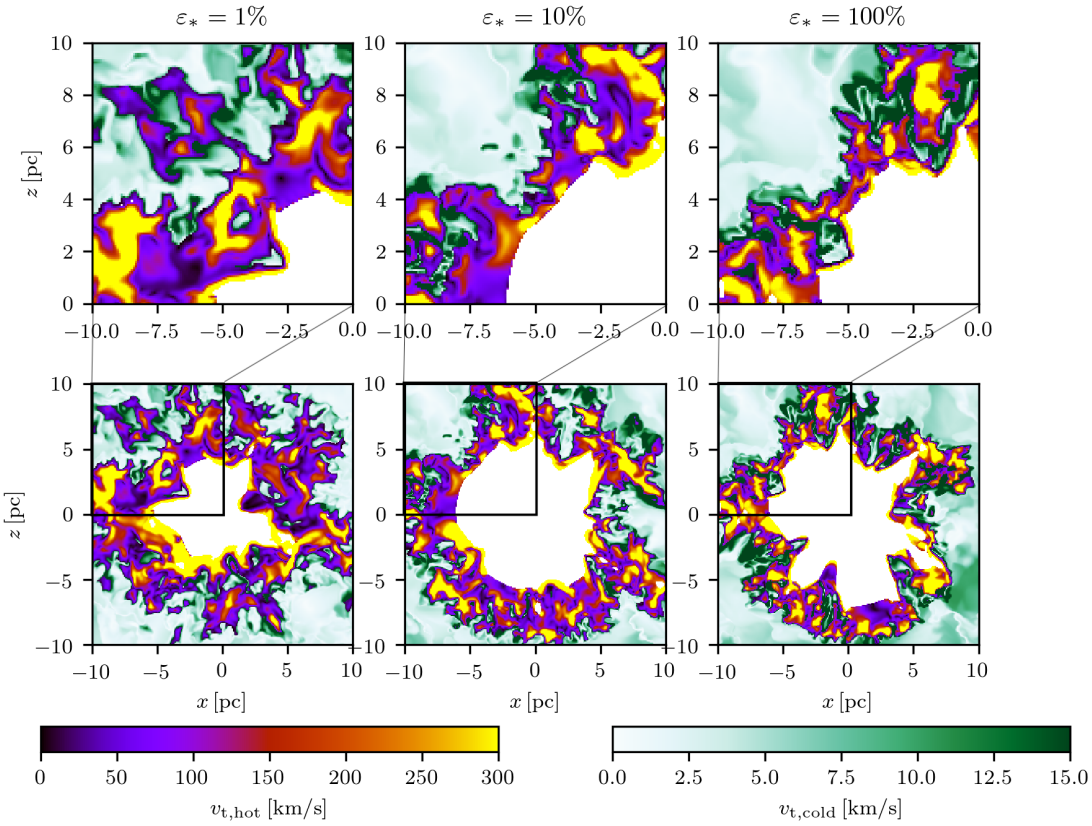

Figure 3.11 Magnitude of the tangential velocity in snapshots of the $R_{\rm cl} = 20\,{\rm pc}$ models at the time in each simulation when $\mathcal{R}_b = R_{\rm cl}/3$. The separate columns (left to right) are the $\varepsilon_* = 1\%$, 10%, and 100% cases. The hot gas (Shocked Stellar Wind and Ionized Gas) is shown with the purple-to-yellow color scale while the cold gas (Warm, Thermally Unstable, and Cold Gas) is shown with the green color scale. The top row of panels is a zoom-in of the bottom row, which itself zooms in on just the bubble region, to highlight the structure of turbulence in the bubble/shell interface.

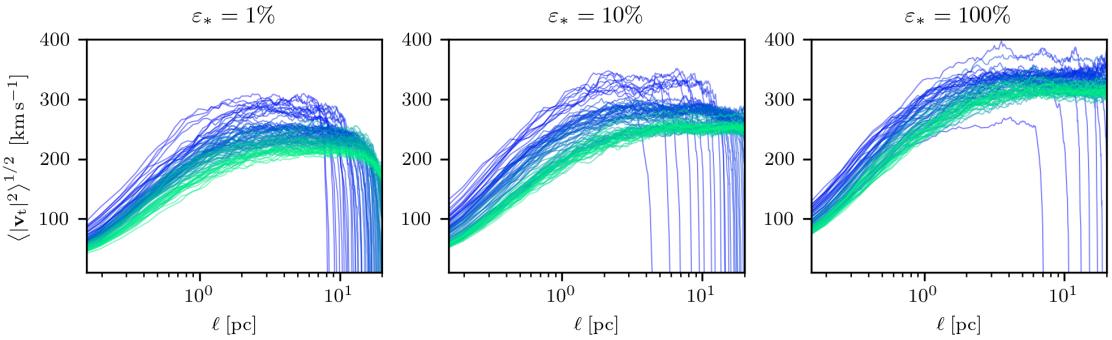

Figure 3.12 Temporal evolution of the structure function of turbulent velocities in the hot gas (Shocked Stellar Wind and Ionized Gas) in the first 1 Myr of the simulation for the $R_{\rm cl} = 20\,{\rm pc}$, $M_{\rm cl} = 10^5 M_\odot$ simulations. The separate panels (left to right) are the $\varepsilon_* = 1\%$, 10%, and 100% cases. Temporal evolution is indicated by the color of the lines in each panel, moving from early times (dark blue) to the late times (bright green) in increments of 10^4 yrs. The characteristic velocity scale of the turbulence decreases in time and varies by at most a factor of 2 over the course of the simulation. The characteristic spatial scale of the structure function increases over time. Turbulent velocities are overall higher for higher wind power ($\mathcal{L}_w \propto \varepsilon_*$) models.

Dividing the second histogram by the first and taking a square root gives us a single sampling of the root-mean-square velocity offset as a function of separation scale ℓ. In order to account for the (unmeasured) radial component of the true turbulent velocity field, we additionally multiply by $\sqrt{3/2}$ (assuming that the turbulence is isotropic). We repeat the above process for 200 cells randomly selected from the Ionized Gas and Shocked Stellar wind.

With this factor of $\sqrt{3/2}$ we refer to the measured structure function as $\left\langle \delta \mathbf{v}_t^2(\ell) \right\rangle^{1/2}$. With these 200 samples of $\left\langle \delta \mathbf{v}_t^2(\ell) \right\rangle^{1/2}$ we take the median value in each radial bin (over the ensemble of samples) to represent the structure function. We also calculate the $25^{\rm th}$ to $75^{\rm th}$ percentiles over these 200 samples to quantify the width of the distribution of velocity deviations at each scale.

As the calculation described above is quite computationally expensive, we only calculate the full time evolution of the structure function for a subset of our simulations ($R_{\rm cl} = 20\,{\rm pc}$, $M_{\rm cl} = 10^5\,M_\odot$, and $L_{\rm box}/\Delta x = 512$). The results of these calculations are illustrated in Figure 3.12, where the turbulent structure function is shown in time increments of 10^4 yrs varying from early times (shown in dark blue) to late times (shown in bright green). The beginning time is 0.01 Myr and the ending

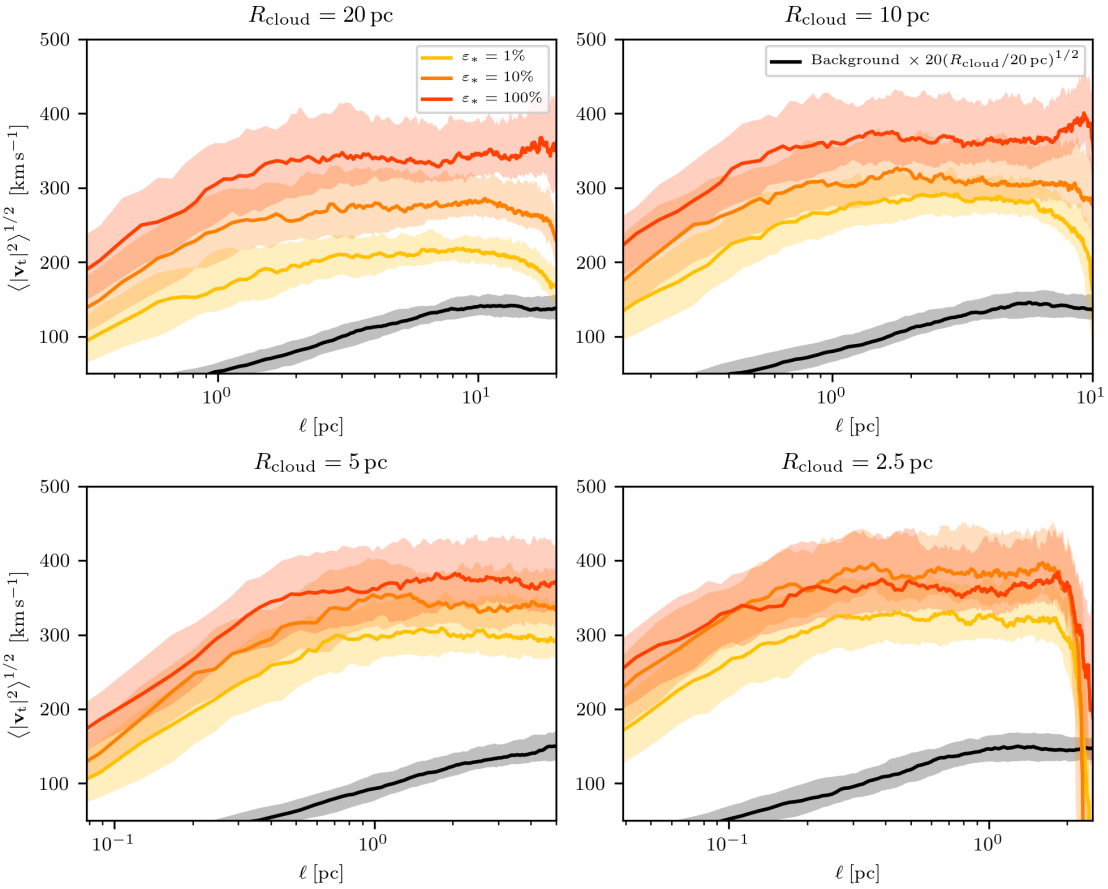

Figure 3.13 The structure function of turbulent velocities in the hot gas (Shocked Stellar Wind and Ionized Gas) when $\mathcal{R}_b = R_{\rm cl}/3$. These are measured in the highest resolution versions of all simulations with $M_{\rm cl} = 10^5 M_\odot$ and we show the simulations with $\varepsilon_* = 1\%, 10\%, 100\%$ in yellow, orange, and red respectively. For each panel we show scales from $4\Delta x$ to $R_{\rm cl}$ (solid lines) as well as the $25^{\rm th}$ to $75^{\rm th}$ percentiles of structure function measurements over the ensembles of 200 samples from the hot gas. In each panel we show in black the structure function of the background turbulent gas scaled up by a factor $20(R_{\rm cl}/20\,{\rm pc})^{1/2}$. The velocity scale of the turbulence is set by the strength of the wind (represented here by ε_*) while the characteristic length scale of the turbulence is likely set by the bubble size and turbulent density structure of the background.

times are 2.23, 1.21, and 0.88 Myr for the $\varepsilon_* = 1\%$, 10%, and 100% cases respectively. At all star formation efficiencies the characteristic velocity scale of the turbulence decreases in time but only by at most a factor of two. In comparison, the shell velocity decreases by a factor of 10 over the same time interval.

For the rest of our simulations with $M_{\rm cl} = 10^5\,M_\odot$ and $L_{\rm box}/\Delta x = 512$, we measure the structure function of the turbulence at the individual time when $\mathcal{R}_b = R_{\rm cl}/3$. We show these structure functions, along with the $25^{\rm th}$ to $75^{\rm th}$ percentiles of velocity deviations, in Figure 3.13. To provide a reference for the background turbulence, we calculate in the same way the structure function of the turbulent background in the full simulation volume just before the initiating of the wind. This background turbulence has a much lower velocity than the turbulence in the hot gas, so we scale the background measurements by a factor $20(R_{\rm cl}/20\,{\rm pc})^{1/2}$; this scale choice is purely for plotting purposes. This scaling also adjusts for the differences in initial turbulent velocity scales $v_t \propto R_{\rm cl}^{-1/2}$ amongst the different size clouds (as laid out in Table 3.1) so that all background structure functions appear essentially identical.

It is clear from Figure 3.13 that the velocity scale of the turbulence is determined primarily by the strength of the wind, which is represented here by ε_*. However, the characteristic spatial scale of the turbulence, which is where the structure function flattens out, is consistently $\sim R_{\rm cl}/10$, suggesting that this scale may be set by the size of the bubble and/or the spatial scale of the background turbulence. This variation in turbulent velocity magnitude with ε_* could be explained by the more oblique shocks in the higher ε_* cases: when a shock is more oblique the post-shock flow will have a larger speed.

Along those lines, we note that for the $\varepsilon_* = 100\%$ case in the $R_{\rm cl} = 2.5$ pc cloud, the amplitude of the turbulent velocity is lower than expected. This is because the $v_r < \mathcal{V}_w/2$ restriction cuts out much of the shocked wind due to the strongly-oblique shocks in this case (see Figure 3.3).

3.3.6 Fractal Structure of Interface

In this section we explore the fractal nature of the shell-bubble interface. These results also

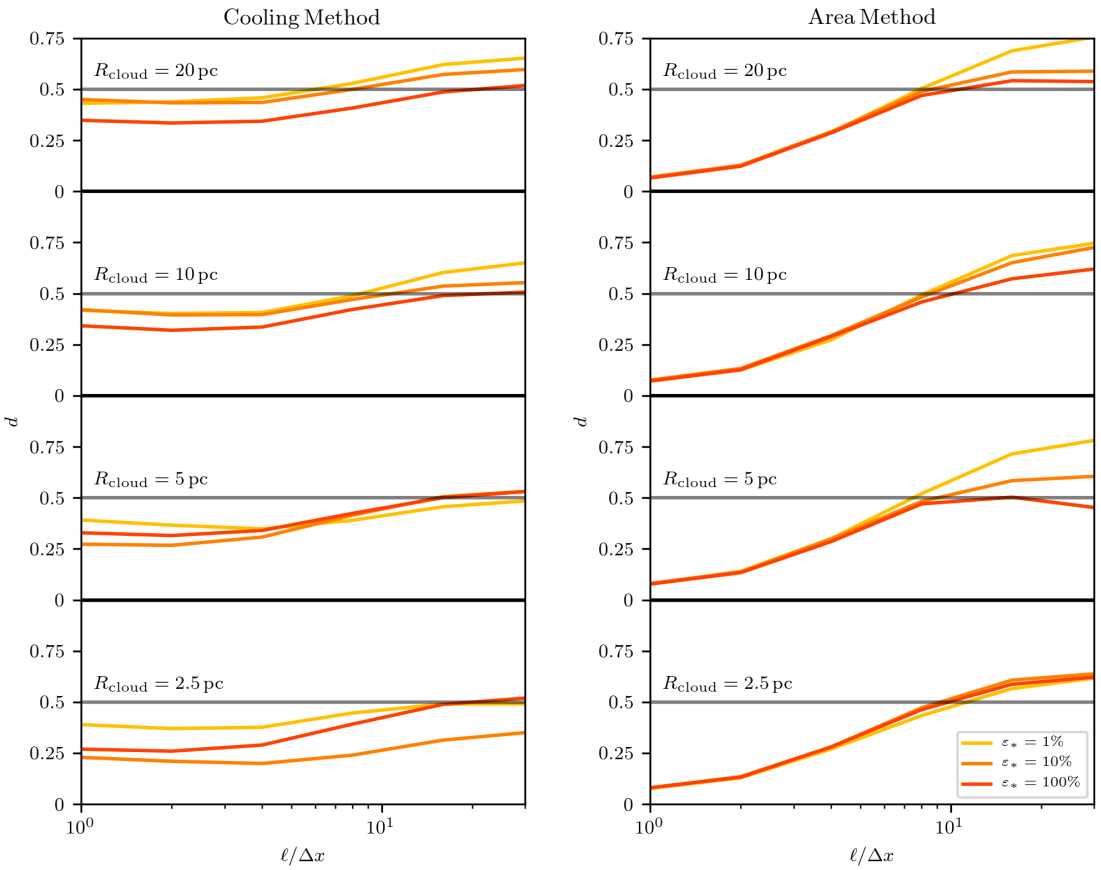

Figure 3.14 The excess fractal dimension of the bubble surface as a function of scale using the two measurement techniques described in the text (see Section 3.3.6 and Section 3.3.6). *Left panel:* The excess fractal dimension of the bubble surface measured using a box-counting technique; boxes at different scales mark where cooling is taking place. *Right Panel*: The excess fractal dimension measured based on the logarithmic scaling of the area of an iso-temperature surface ($T = 10^5\,{\rm K}$ for all curves shown here) when measured on different scales.

inform the discussion of turbulence-induced mixing and cooling in Chapter 2.

Fractal Dimension from Cooling

We measure the fractal dimension of the bubble surface in two different ways. Since the details of the fractal structure of the bubble/shell interface affect the cooling, it makes sense to measure the fractal dimension using the cooling itself. To that end we determine the fractal dimension using a box-counting or Minkowski-Bouligand algorithm (Schroeder, 1991) where membership in or out of the fractal is determined based on cooling.[1] To maximize dynamic range we use simulations with $L_{\rm box}/\Delta x = 512$. To be consistent with the turbulent structure function measurements of Section 3.3.5, we analyze the fractal structure at the time when $\mathcal{R}_b = R_{\rm cl}/3$.

We first choose a fraction $f_{\rm cool} \in (0, 1)$. For a given time snapshot we measure the total amount of cooling, $\dot{E}_{\rm cool}$. We denote $\dot{e}_{{\rm cool},i}$ as the cooling rate in the $i^{\rm th}$ hydrodynamical cell, for a sorted list starting with the maximal cooling rate. We then compute the cumulative sum up to I such that $\sum_{i=0}^{I} \dot{e}_{{\rm cool},i} \approx f_{\rm cool}\dot{E}_{\rm cool}$. The count I of cells contributing to the specified cooling fraction at the minimum scale $\ell = \Delta x$ (the resolution of the simulation) is hereafter denoted by $I(\Delta x)$.

We next reduce the size of the simulation grid by a factor of two in each direction, so that merged cells have length $\ell = 2\Delta x$, and the cooling of adjacent cells is combined. We repeat the above sort-and-accumulate process to measure the number of cells $I(2\Delta x)$ needed for $\sum_{i=0}^{I(2\Delta x)} \dot{e}_{{\rm cool},i} \approx f_{\rm cool}\dot{E}_{\rm cool}$. We iteratively repeat this process for $\ell/\Delta x = 1,\, 2,\, 4,\, 8,\, 16,$ and 32 and use these measurements to calculate the fractal dimension as

$$D = d + 2 = -\frac{d \log I(\ell)}{d \log \ell}\,. \tag{3.18}$$

This quantity will vary with scale, ℓ. However, we expect d to take on a roughly constant value on large scales, dropping below this at sufficiently small scale due either to limited numerical resolution or to some physical dissipation scale such as the cooling length, $\ell_{\rm cool}$. In practice the former is more relevant as the cooling length is usually below our resolution limit.

[1] The measurement technique we adopt was suggested to the authors by Drummond Fielding.

At sufficiently large $f_{\rm cool}$, d is close to zero on large scales and becomes very large (based on our fitting method) on small scales. This is because $I(f_{\rm cool}, \ell)$ becomes a very steep function of $f_{\rm cool}$ when transitioning beyond the concentrated cooling in the interface boundary layer. Above a certain $f_{\rm cool}$, essentially the whole domain is included, implying that the true $d \to 1$ at small ℓ.

We believe that the most physical d to associate with the fractal structure of the cooling interface is the value at large scales for the largest value of $f_{\rm cool}$ that does not exhibit the discontinuous behaviour explained above. On the left hand side of Figure 3.14, we therefore show the dependence of d on scale for the largest choice of $f_{\rm cool}$ that does not result in this discontinuous behavior. This choice of $f_{\rm cool}$ varies between simulations.

The scale dependent nature of the "excess" fractal dimension d is evident in Figure 3.14, where d decreases at small scales. We see that d tends to be larger at smaller values of ε_* (this is clearest in the larger/lower density clouds). In part, this may be because turbulence at the bubble-shell interface, which is responsible for creating the fractal structure, makes up a much larger fraction of the kinetic energy at low ε_*, as was shown in Figure 3.10.

Overall, this measurement method suggests a fractal dimension $d \approx 1/2$ in most simulations, with larger values (up to $\sim 0.6 - 0.7$) in models with very low ε_* and large $R_{\rm cl}$.

Fractal Dimension from Iso-Temperature Surfaces

Our second method of measuring the fractal dimension, paralleling Fielding et al. (2020), uses the area of iso-temperature surfaces for temperatures that should be characteristic of the interface between the wind bubble and the shell. Specifically, we measure the area of iso-temperature surfaces for $T = 10^4$, $10^{4.5}$, 10^5, $10^{5.5}$, and 10^6 K. We use the `marching_cubes` algorithm from the `scikit-image` package to measure these surface areas, using step sizes $\ell/\Delta x = 1$, 2, 4, 8, 16, and 32.

The excess dimension d is then given by the logarithmic derivative of the area with respect to the scale on which the area is measured

$$d = -\frac{d \log A_b(\ell)}{d \log \ell} \,. \tag{3.19}$$

As with the previous method, this value should be a constant over a large range of scales, decreasing at some small scale due to numerical or physical dissipation (usually the former). Our measurements are made at the time when $\mathcal{R}_b = R_{\rm cl}/3$. The scale-dependent results are shown at the right side of Figure 3.14. For the sake of brevity we only show the results for the iso-temperature surfaces measured at $T = 10^5\,{\rm K}$ for each simulation.

Figure 3.14 clearly shows that this measurement technique consistently finds $d \to 0$ at small scale, as expected. We also found (not shown) that the value of d on large scales depends on temperature: the higher temperature surfaces have more fractal (higher d) structures than the lower temperature surfaces, with the effect most extreme in the smallest-ε_*, largest-$R_{\rm cl}$ models. On large scales, the range of d from this technique falls roughly within $d \sim 1/2 - 3/4$.

It is also interesting to note that at all cloud sizes, the bubble surface tends to become less fractal at higher wind luminosity (or ε_*), as seen in the previous measurement technique, but now to a higher degree. Physically, the more-fractal structure in the lower-ε_* models at large scales may potentially be explained by their greater buildup of hot gas (higher $\mathcal{S}$), which can more effectively create "fingers" of high-temperature gas within the lower-density parts of the turbulent cloud at large scales.

Area Measurements

Using the results of Section 3.3.6, we can now assess the relationship between the bubble's surface area and its effective radius, $\mathcal{R}_b$, as defined by Equation 2.37. In particular, this allows us to test whether a single fractal dimension can describe the surface, and to evaluate the free parameter α_A in that equation. For this analysis we consider the models with $R_{\rm cl} = 10\,{\rm pc}$ and $M_{\rm cl} = 10^5\,M_\odot$ at all values of ε_*.

We set

$$\alpha_A(\mathcal{R}_b, \ell) = \frac{A_b(T, \ell)}{4\pi \mathcal{R}_b^2 (\mathcal{R}_b/\ell)^{1/2}} \tag{3.20}$$

where $A_b(T, \ell)$ denotes the scale dependent area measurement of the iso-temperature surface (at a range of T), and ℓ is the measurement scale. We shall use $\ell = 32\Delta x$, the scale on which the fractal

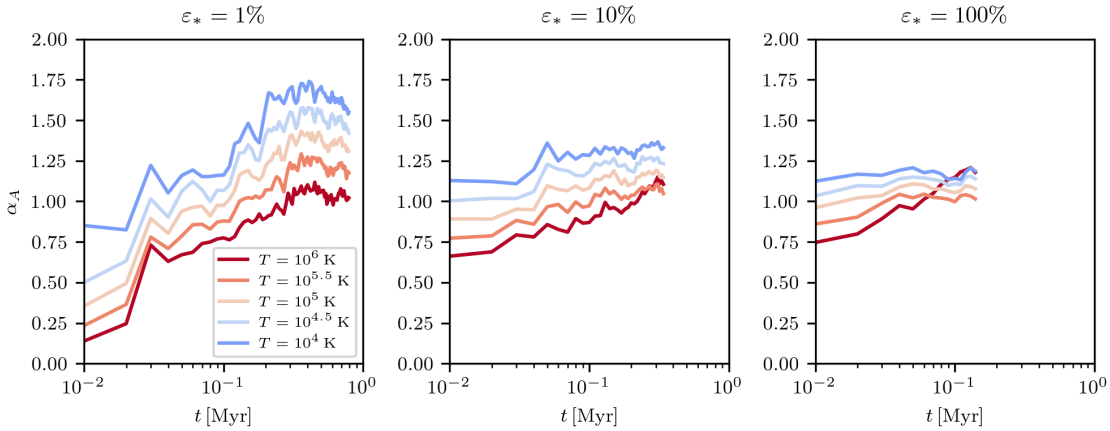

Figure 3.15 The ratio of bubble surface area $A_b(T, \ell)$ to fractal area $4\pi\mathcal{R}_b^2(\mathcal{R}_b/\ell)^{1/2}$ as $\mathcal{R}_b(t)$ evolves in time. We only show the evolution up to the point of wind breakout. We set $\ell = 32\Delta x$ and measure the area for several iso-temperature surfaces as marked in key. Results for α_A from taking the area ratio (see Equation 3.20) are shown for $M_{\rm cl} = 10^5 M_\odot$, $R_{\rm cl} = 10\,{\rm pc}$ and $\varepsilon_* = 1\%$, 10%, and 100%. The near-constancy of α_A in time, especially at $\varepsilon_* = 10\%$ and 100%,is an excellent indication that a fractal with $d = 1/2$ describes the geometry of the bubble well.

structure begins to saturate (as is evident in Figure 3.14). Equation 3.20 compares the actual area with the prediction for a fractal with excess dimension $d = 1/2$ as this value is broadly consistent across the range of parameters investigated and measurement techniques used.

We present the time evolution of Equation 3.20 in Figure 3.15. Especially for the larger-ε_* cases, we conclude that the simple $d = 1/2$ fractal agrees extremely well with bubble's true surface area.

Bubble Geometry

Finally, we consider an additional characteristic of the bubble geometry, which we term its "foldedness." We define this as the value of the dot product of the unit normal to the bubble surface ($\hat{\mathbf{n}}$) and the unit radial vector ($\hat{\mathbf{r}}$). There are physical reasons that this quantity matters. In the spherically symmetric, pressure-driven bubble of Weaver et al. (1977), El-Badry et al. (2019), and others, the bubble expands due to a pressure gradient force normal to the bubble surface. Since the bubble is spherical, the normal vector to the surface is always directed exactly radially outwards, so that the pressure force and expansion velocity are exactly aligned. In the case of a bubble in

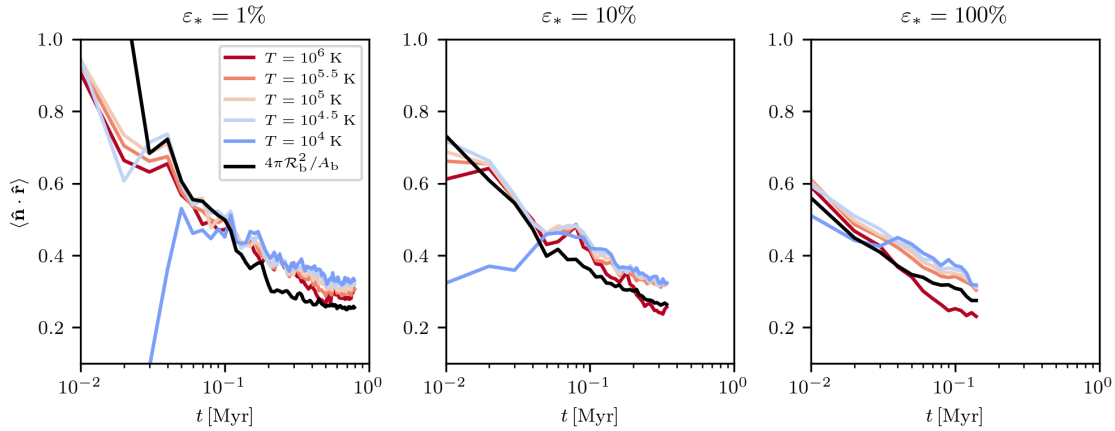

Figure 3.16 The average value of the dot product of the outward normal vector to the bubble surface with the radial vector, which we term the "foldedness" of the bubble surface. The degree to which this is less than one quantifies the amount that the surface is "inward facing" or "crumpled." The same models are used as for Figure 3.15, along with the same calculations of the bubble iso-temperature surfaces. We also show $4\pi\mathcal{R}_b^2/A_b(10^6\,\mathrm{K}, 32\Delta x)$ in black. The degree to which the black curve matches the other curves reflects how close the effective area, $A_{\rm eff}$ is to the equivalent spherical surface $4\pi\mathcal{R}_b^2$.

a turbulent medium, the surface will have a complicated geometry, as Figure 3.2 and Figure 3.3 illustrate. For any pressure force acting normal to the bubble surface, only a fraction of the force will act radially outward. The radial contribution from a normal force can be then be quantified by this foldedness quantity $\langle \hat{\mathbf{n}} \cdot \hat{\mathbf{r}} \rangle$.

The quantity $\langle \hat{\mathbf{n}} \cdot \hat{\mathbf{r}} \rangle$ is our measure of the foldedness of the surface in the case of our wind-driven bubbles, and this is important in setting the radial force that drives the overall expansion. Specifically, if there is a uniform internal pressure P, the effective outward radial force on the bubble surface can be written as

$$F_r \approx P A_{\rm eff}(T, \ell)\,, \tag{3.21}$$

for an appropriate effective area, $A_{\rm eff}(T, \ell)$. We define $A_{\rm eff}(T, \ell)$ using the area of iso-temperature surfaces $A_b(T, \ell)$ from Section 3.3.6 and the foldedness $\langle \hat{\mathbf{n}} \cdot \hat{\mathbf{r}} \rangle$ as

$$A_{\rm eff}(T, \ell) = A_b(T, \ell)\, \langle \hat{\mathbf{n}} \cdot \hat{\mathbf{r}} \rangle\ . \tag{3.22}$$

Again, using the `marching-cubes` algorithm, we evaluate $\langle \hat{\mathbf{n}} \cdot \hat{\mathbf{r}} \rangle$ by taking the dot product of the unit normal to each triangular face output by the algorithm with the unit radial vector pointing to the center of that triangular face. We then average these values over the set of faces. The results are displayed in Figure 3.16 for the $M_{\rm cl} = 10^5 M_\odot$, $R_{\rm cl} = 10\,{\rm pc}$ model at all values of ε_*. In Figure 3.16, we also show that the scaling of $\langle \hat{\mathbf{n}} \cdot \hat{\mathbf{r}} \rangle$ in time is very similar to the temporal behaviour of $4\pi \mathcal{R}_b^2 / A_b$. Both of these quantities decrease in time $\propto t^{-1/4} \propto \mathcal{R}_b^{-1/2}$. But more important than the specific time dependence is the fact that the scaling of the excess fractal dimension is compensated by the foldedness of the surface, such that $A_{\rm eff}(T, \ell) \propto \mathcal{R}_b^2$.

Our findings on scalings imply that the effective area for radial pressure forces is the same as for a spherical surface. We posit that this property is generally true. That is, for any bubble, the quantity $A_{\rm eff}$ defined in Equation 3.22 scales as the square of its associated linear scale defined through the cube root of volume. Though the divergence theorem can be used to show that $A_{\rm eff} \equiv \int \hat{r} \cdot \hat{n} dA = 4\pi \langle R_{\rm max}^2 \rangle_{\theta,\phi}$ for $R_{\rm max}$ the bubble radius at a given spherical polar angle, we have not found a proof to connect this to Equation 2.16; nevertheless, it seems intuitively reasonable.

The above proposition that $A_{\rm eff} \propto \mathcal{R}_b^2$ points to the self-consistency of the assumption in the EC solution that the angle-averaged radial force in the momentum equation does not explicitly depend on detailed geometry, even for a fractal bubble.

It is the combination $\rho v_r^2 + P$ that drives outward expansion of the bubble. The Reynolds stress term is radially directed and therefore always contributes to the shell momentum in the $\hat{r}$ direction, but the pressure term would produce a normal force where it acts on the shell, and therefore would contribute to the radial momentum as in Equation 3.21. Our conclusion that $A_{\rm eff} \propto \mathcal{R}_b^2$ is then what allows us to treat the total momentum input rate via an equivalent spherical calculation, with the breakdown of the two contributing terms provided in the Appendix of Chapter 2 (see Equation A11 there).

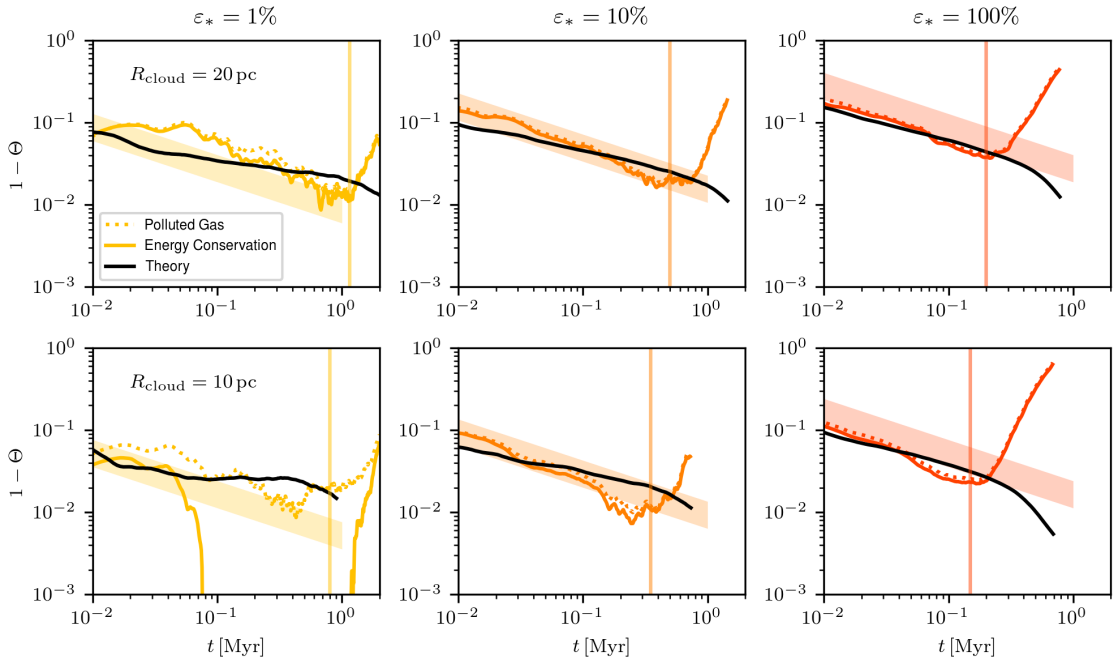

Figure 3.17 The fraction $1 - \Theta$ of the input wind energy that is retained in the bubble and shell, including both kinetic and thermal terms, as a function of time. We show results for the $R_{\rm cl} = 20\,{\rm pc}$ in the top row and $R_{\rm cl} = 10\,{\rm pc}$ in the bottom row (both with $M_{\rm cl} = 10^5 M_\odot$), for $\varepsilon_* = 1\%$, 10%, and 100%. The time when the wind breaks out of the simulation box is denoted in each panel by a colored vertical line. The colored solid lines in each panel denote $1 - \Theta$ measured via the energy conservation method, while the dotted lines denote the same quantity measured using cooling in wind-polluted ($f_{\rm wind} > 10^{-4}$) gas. The shaded areas in each panel delimit the range expected from EC wind theory (see text). The black line in each panel shows the theoretical prediction from Equation 2.25 with values of $f_{\rm turb}$, $\mathcal{S}$, α_p, and α_R determined as described in Section 3.3.4.

3.3.7 Cooling and Energetics

Measured Cooling and Retained Energy

Energy inputs from the wind are split between the (thermal and kinetic) energy in the interior of the bubble, E_b, the radial kinetic energy of the shell, $E_{\rm r,sh}$, the turbulent kinetic energy in the shell, $E_{\rm turb}$, and energy that is lost to cooling, $\dot{E}_{\rm cool}$. The EC theory presented in Chapter 2 provides predictions for E_b and $E_{\rm r,sh}$ and thus (through the total input energy $\mathcal{L}_w t$) for the sum of the energy lost to cooling and the energy in turbulent motion. The exact split between turbulent energy dissipation and cooling is not predicted by our theory, but we can account for it in simulations using the quantity $f_{\rm turb}$, shown in Figure 3.10. In this section we will endeavor to measure the cooling that is occurring in our simulations directly and check that this is consistent with the prediction given by Equation 2.25.

First, we must measure the cooling directly from the simulations. Since, however, there is cooling present in the background gas, mixing between the background gas and the wind, and cooling occurring in the background gas that is shock-accelerated by the wind, this is not a trivial task. The measurement is further complicated by the fact that the cooling will be a large fraction of $\mathcal{L}_w$, so that an inclusion of only a small amount of background cooling in our measurement can make our inference of $\Theta \equiv \dot{E}_{\rm cool}/\mathcal{L}_w$ greater than 1. To address these issues we proceed by measuring the cooling in two separate ways so that we may check for consistency between our methods.

The first way follows our method for measuring momentum, as laid out in Section 3.3.3. Specifically, we sum the cooling in all gas with $f_{\rm wind} > 10^{-4}$ in our simulations. The justification of this otherwise arbitrary cut in $f_{\rm wind}$ is based on the excellent agreement among measurements of the radial momentum at different resolutions when using this criterion, as evidenced in Figure 3.4 and also its agreement with our second measurement method, detailed below.

We measure the cooling in another way by using conservation of energy. The time derivative of the total energy in the simulation domain can be written as

$$\dot{E} = \mathcal{L}_w - \dot{E}_{\rm cool} - \dot{E}_{\rm out} - \dot{E}_{\rm bkgnd}\,, \tag{3.23}$$

where $\dot{E}_{\rm cool}$ is the sum of cooling that occurs in the swept up ambient gas and the bubble/shell interface, $\dot{E}_{\rm out}$ is the rate at which energy moves out of the simulation domain through the boundaries, and $\dot{E}_{\rm bkgnd}$ is the net cooling (= cooling - heating) in the ambient gas that is not due to the wind. While it is straightforward to measure the total energy in the simulation domain, and hence its time derivative $\dot{E}$, as well as the rate at which energy leaves the box, it is not so easy to define what the cooling due to the background ambient gas is.

We address this by running the simulations that we initialized before turning on a wind (as described in Section 3.2.2) forward in time without a wind and measuring the net cooling that occurs throughout the volume. We will denote the cooling that occurs in these simple turbulent evolution simulations as $\dot{E}_{\rm tev}$. To account for the fact that part of the simulation volume that would normally be cooling as background gas will have been displaced by the wind bubble in our simulations, we measure $\dot{E}_{\rm bkgnd}$ as

$$\dot{E}_{\rm bkgnd} = \left(1 - \frac{V_b}{L_{\rm box}^3}\right) \dot{E}_{\rm tev} \,. \tag{3.24}$$

With this measurement of the background cooling we can use Equation 3.23 to determine $\dot{E}_{\rm cool}$.

The results of the two methods for calculating $\Theta = \dot{E}_{\rm cool}/\mathcal{L}_w$ are displayed in Figure 3.17 as solid and dotted lines for the $M_{\rm cl} = 10^5 M_\odot$, $R_{\rm cl} = 20$ and 10 pc cases, for all ε_* values. We only show these lower density cases as, in the higher density simulations, the background cooling becomes too strong and difficult to separate from the cooling associated with the wind, especially at low values of ε_*. In fact, this effect is already evident in the $R_{\rm cl} = 10\,$pc, $\varepsilon_* = 1\%$ case shown in the bottom left panel of Figure 3.17.

There is excellent agreement between our two measurement methods, with only moderate deviations at low ε_* values. The dramatic increase in $1 - \Theta$ (decrease in cooling) towards the end of each simulation can be attributed to breakout and venting of the wind outside of the simulation domain, the onset of which is indicated by the colored vertical line.

In Figure 3.17 we also show, as indicated by the shaded region in each panel, where we expect the solutions for $1 - \Theta$ to lie. This is bounded above by the locus at which the EC condition

applies as given by Equation 2.39, and bounded below the locus of maximum cooling as given by Equation 2.25 with $f_{\rm turb} = 0$ and $\mathcal{S} = \alpha_R = \alpha_p = 1$, so that the right-hand side becomes $(3/2)\dot{R}_{\rm EC}/\mathcal{V}_w$. Both of these limits have retained energy fraction $1 - \Theta \propto \dot{R}_{\rm EC}/\mathcal{V}_w$ with different coefficients (3.8 and 1.5, respectively), decreasing in time as $1 - \Theta \propto t^{-1/2}$. Finally, as black lines, we show the prediction of Equation 2.25 in its entirety, with time-varying values for $f_{\rm turb}$, $\mathcal{S}$, α_p, and α_R measured as described in Section 3.3.4.

Overall, Figure 3.17 shows that the different numerical measurements of $1 - \Theta$ are in good agreement with each other and with theoretical estimates. At early times ($\sim 10^4\,{\rm yr}$), the energy retained in the bubble amounts to $\sim 10\%$ of the input, slightly increasing for lower density clouds and for more powerful winds (larger ε_*). This decreases $\propto t^{-1/2}$ until the time breakout occurs, $t \sim 10^5 - 10^6\,{\rm yr}$ (decreasing at higher wind power and for denser clouds).

Total Possible Cooling

Finally, we connect our results to the expected requirements for the EC solution based on the theory of cooling and mixing at turbulent, fractal interfaces, as discussed in Chapter 2. To this end, we measure two quantities. The first is the expected radial velocity of shocked wind gas being advected to the boundary mixing layer ($v_{\rm hot}(\mathcal{R}_b)$, given by Equation 2.64) The second is the "equivalent velocity" of gas flowing through the mixing/cooling layer, as given by Equation 2.35; this takes into account the fractal structure of the bubble surface, but is only really defined up to a multiplicative factor from our theoretical analysis.

For this exercise, we use the time dependent measurements for the evolution of the bubble's effective radius (Figure 3.5), the shock radius ($\mathcal{R}_f$), and the turbulent structure function (Figure 3.12) in models with $M_{\rm cl} = 10^5 M_\odot$, $R_{\rm cl} = 20$, and all ε_*. We choose $\ell_{\rm min} = 8\Delta x$, and calculate $v_{\rm eff} = v_t(\ell_{\rm min})(\mathcal{R}_b/\ell_{\rm min})^{1/2}$. Note that we have implicitly adopted a fractal dimension of $d = 1/2$, which is broadly consistent with our results in Section 3.3.6 and Section 3.3.6. As noted above, the "equivalent velocity" in Equation 2.35 is only predicted up to an order-unity coefficient. We therefore multiply $v_{\rm eff}$ by a factor 0.25, and show the results of this calculation in Figure 3.18.

Figure 3.18 shows that there is excellent agreement between the expected velocity at which

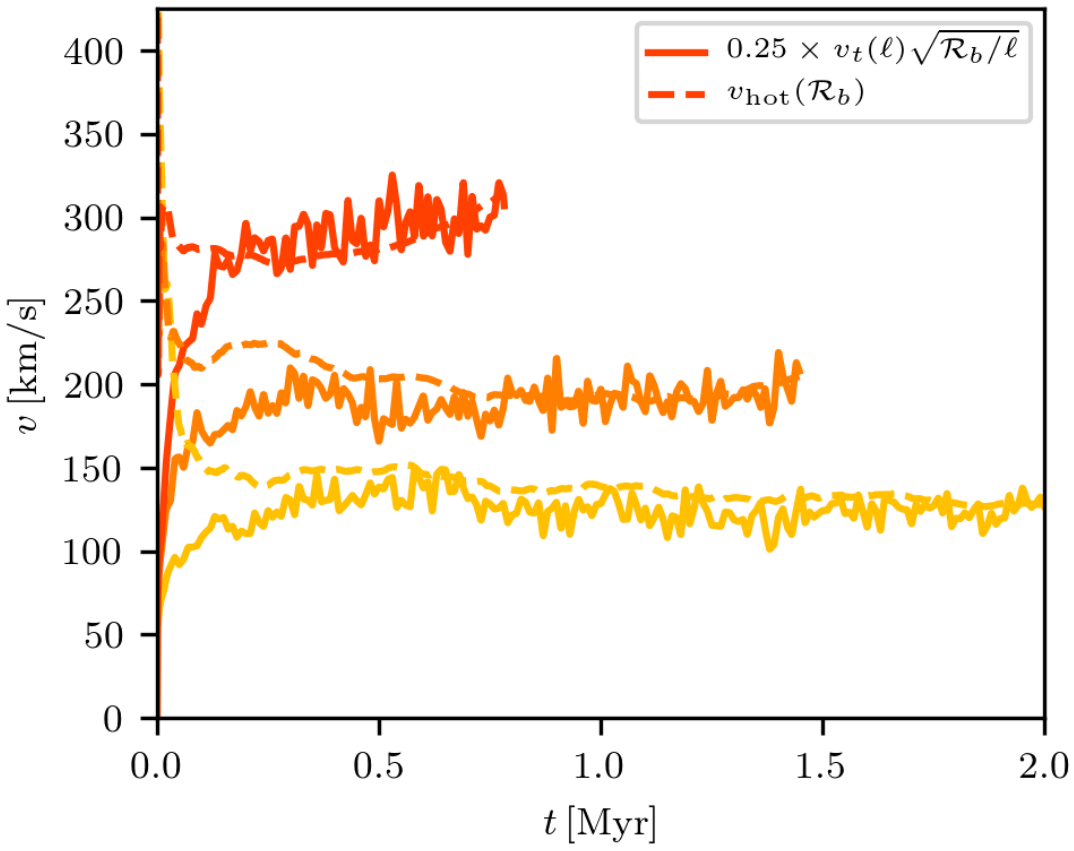

Figure 3.18 Evolution of quan1tities related to the flow into and through the turbulent mixing/cooling boundary layer between the bubble and the background. The expected radial velocity (Equation 2.64) of shocked wind gas advected into the fractal interface is shown as dashed lines. The "equivalent velocity" of gas transiting the mixing/cooling layer (Equation 2.35 with $d = 1/2$) is shown as solid lines, including a factor of 0.25 chosen to match the dashed lines. These curves are shown for the model with $M_{\rm cl} = 10^5 M_\odot$, $R_{\rm cl} = 20$, and all ε_*. We use $\ell_{\rm min} = 8\Delta x$ for the measurement scale of the turbulent structure function.

energy and mass arrives at the surface of the bubble (an advection speed), and the effective flow velocity through the mixing/cooling boundary layer (a diffusion speed). This directly demonstrates a key feature of our model: all thermal energy that is delivered to the turbulent interface is efficiently mixed in and radiated away as rapidly as it arrives.

3.4 Summary and Conclusion

In Chapter 2 we described a theory for the expansion of a stellar wind-driven bubble into the dense, turbulent ISM, characterized by strong cooling losses due to turbulent mixing of the hot gas with denser gas at the bubble surface. We posited that this cooling was large enough to cause the dominant phase of the bubble's evolution to be momentum driven.

A solution in which momentum input (rather than energy input) controls bubble evolution has been discussed in the past by several authors in various contexts (Steigman et al., 1975; Ostriker & McKee, 1988; Koo & McKee, 1992a,b; Kim et al., 2017a; Silich & Tenorio-Tagle, 2013), and others have suggested that such solutions could be associated with efficient mixing and cooling at boundary layers (Garcia-Segura et al., 1996a; Dale & Bonnell, 2008; Mackey et al., 2015; Fierlinger et al., 2016), but none have previously demonstrated that this regime generally applies within star-forming molecular clouds. We do this by conducting a large suite of 3D hydrodynamic simulations with winds injected into dense, turbulent ISM material. Analysis of our simulations shows that the predictions of our theory very accurately describe the evolution of the wind bubble's volume, the momentum that it carries, and its energetics. Our simulations demonstrate that the limit of maximally efficient cooling in our theory is most appropriate for the strongest stellar winds (parameterized in our model by high values of the star formation efficiency ε_*).

Our theory and simulations explore in detail where energy is stored and explain physically how most of it is radiated away, via processes analogous to those that have been investigated in recent simulations of Kelvin-Helmholtz unstable mixing layers with fractal geometries (e.g. Fielding et al., 2020; Tan et al., 2021). The fractal theory of the bubble interface also accurately predicts essential quantities of the bubble such as the area of its interface with the ambient ISM and properties of the

geometry of this interface. We additionally demonstrate that it is the fractal nature of the bubble that allows for such efficient cooling by showing that the cooling capacity under our fractal theory is greater than the energy being provided by the stellar wind.

The main conclusions from our simulations can be summarized as follows:

1. The effective or mean bubble radius expands in a momentum-driven manner as $\mathcal{R}_b \propto t^{1/2}$ (Equation 2.19). This is shallower than the original Weaver et al. (1977) solution or the modified El-Badry et al. (2019) solution ($\mathcal{R}_b \propto t^{3/5}$).

2. The total momentum carried by the bubble increases approximately linearly in time (Equation 2.14) and is typically only slightly larger (at most a factor 4) than the total momentum injected by the wind, with the smallest enhancement for the most luminous winds (largest ε_*), as shown in Figure 3.4. The momentum enhancement factor α_p reflects buildup of hot shocked gas within the bubble; higher turbulence levels in models with more powerful winds drive stronger interface mixing and limit this buildup, keeping α_p very close to unity.

3. From analysis of the shells in our simulations, we find (see Figure 3.10) that the energy carried in tangential motion is typically greater than that carried in radial motion (turbulence dominated). These results show that shells typically become more turbulence-dominated in time up to the point of bubble 'breakout' from the simulation domain. We also find that cases with less luminous winds and denser environments are more turbulence dominated.

4. We measure the turbulence in the hot gas directly, and find typical velocities of $150-350\,\mathrm{km/s}$ (amplitude increasing with input momentum rate; see Figure 3.13), which are about $10-15\%$ of the wind velocity $\mathcal{V}_w$. This turbulence has characteristic energy-containing or outer scale that is larger in larger clouds (Figure 3.13), suggesting that the background inhomogeneity induced by turbulence helps to define it. The outer scale is typically $\sim 10\%$ of the bubble size, growing with the bubble (Figure 3.12).

5. We quantify the excess fractal dimension d of the shell-bubble interface in two different ways (see Figure 3.14), and find that this generally falls in the range of $d = 0.4 - 0.7$. Lower

luminosity winds generally have higher fractal dimensions, which is consistent with the shells driven by these winds being more turbulence dominated, as it is the turbulence that induces the fractal structure. We also find that the fractal characterization of the shell interface is in excellent agreement with the measured area (Figure 3.15) and geometry (Figure 3.16).

6. We use $1-\Theta$ to denote the fraction of the energy input rate from the wind that remains in the bubble as either thermal or kinetic energy at any given time. We find that $1-\Theta \sim 0.1-0.01$, decreasing in time $\propto t^{-1/2}$ (Equation 2.25) for all models (Figure 3.17). The very small value of $1-\Theta$ is consistent with observational constraints (see Chapter 2 discussion).

We have demonstrated that our simulations are well converged in all of the quantities that we investigate here. Higher resolution should only increase cooling, so we believe our results for the efficient-cooling bubble evolution solution are robust. However, our present simulations do not resolve the scale $\ell_{\rm cool}$ at the wind bubble interface where mixing and cooling timescales would be comparable in the real ISM. Full validation of the small scale processes discussed here will therefore require higher resolution simulations, an important direction for future work.

Finally, we reiterate that the simulations presented here include only a limited set of the relevant physical processes. In particular, we have not included radiation or magnetic fields. EUV radiation would photoevaporate gas from the shell surfaces that "face" the cluster, while FUV radiation absorbed by dust (where it is not destroyed) directly deposits photon momentum; both effects drive expansion of the bubble surrounding the cluster. The free wind and shocked wind regions would then in general interact with photoionized gas that has been evaporated from the shell, rather than directly with the denser shell gas (e.g. Dwarkadas & Rosenberg, 2013; Geen et al., 2021). With a lower density contrast, Kelvin-Helmholz instabilities at hot/warm interfaces would have higher growth rates than for hot/cold interfaces at the same pressure. The turbulent mixing process would likely occupy a larger volume of photoionized gas compared to the situation here, since the turbulence levels in the interaction region depend on the density contrast (Fielding et al., 2020). Magnetic fields presumably also affect the mixing/cooling process. Given the extremely high velocities of the shocked wind, field strengths in the cloud would have to be very (unrealistically)

high to prevent primary instabilities at the interface, but magnetic tension could still limit the turbulent cascade at small scales (and render it anisotropic). Numerical magnetohydrodynamic studies including both winds and radiation will be needed to assess how the turbulent mixing/cooling process and overall dynamical evolution are quantitatively affected.

3.5 Appendix: Validation of Wind Implementation

We test our implementation of stellar winds by comparing to analytic solutions given by Weaver et al. (1977) for a spherical wind expanding into a uniform, static background medium. In our test the background medium has a number density of $n_{\rm H} = 2\,{\rm cm}^{-3}$. The wind has a mechanical luminosity of $\mathcal{L}_w = 10^{37}\,{\rm ergs\,s}^{-1}$ and a mass loss rate of $\dot{M}_w = 10^{-5} M_\odot\,{\rm yr}^{-1}$. This corresponds to a wind velocity of $\mathcal{V}_w = 1.78 \times 10^3\,{\rm km\,s}^{-1}$. The simulation was run in a $L = 5\,{\rm pc}$ box with 128^3 cells. The feedback radius was set as $r_{\rm fb} = 0.25\,{\rm pc}$ ($r_{\rm fb}/\Delta x = 6.4$), and we used $N_{\rm sc} = 4$ subcells. We run simulations both with and without cooling (the latter is fully adiabatic). The results of these tests are displayed in Figure 3.19.

Comparison of the profile for the Weaver et al. (1977) fully adiabatic solution (described in Section 2 of that paper, shown in green) and our adiabatic simulation (shown in blue) makes clear that the code accurately captures the expected behaviour. In the realistic non-adiabatic case the shell of swept up ambient gas is expected to cool and collapse once the cooling time in the shell is much shorter than the lifetime of the wind. The profile of the simulation with cooling (in red) shows that this has occurred, and that the dense shell is at smaller radius than in the adiabatic case. From the density slice of the non-adiabatic simulation shown in the bottom right panel of Figure 3.19, it is clear that this solution matches the expected evolution of the non-adiabatic phase of wind evolution (where the expected radius of the shell in this case, given by Equation 1 of Chapter 2, is shown as a magenta circle) and retains a high degree of spherical symmetry.

3.6 Appendix: Additional Tests

In this appendix we display various tests and extensions of our theory.

3.6.1 Pure Thermal Feedback

As described in Section 3.2, we use a hybrid thermal/kinetic energy injection scheme which provides for larger time-steps while at the same time avoiding issues of discontinuity in the injected energy

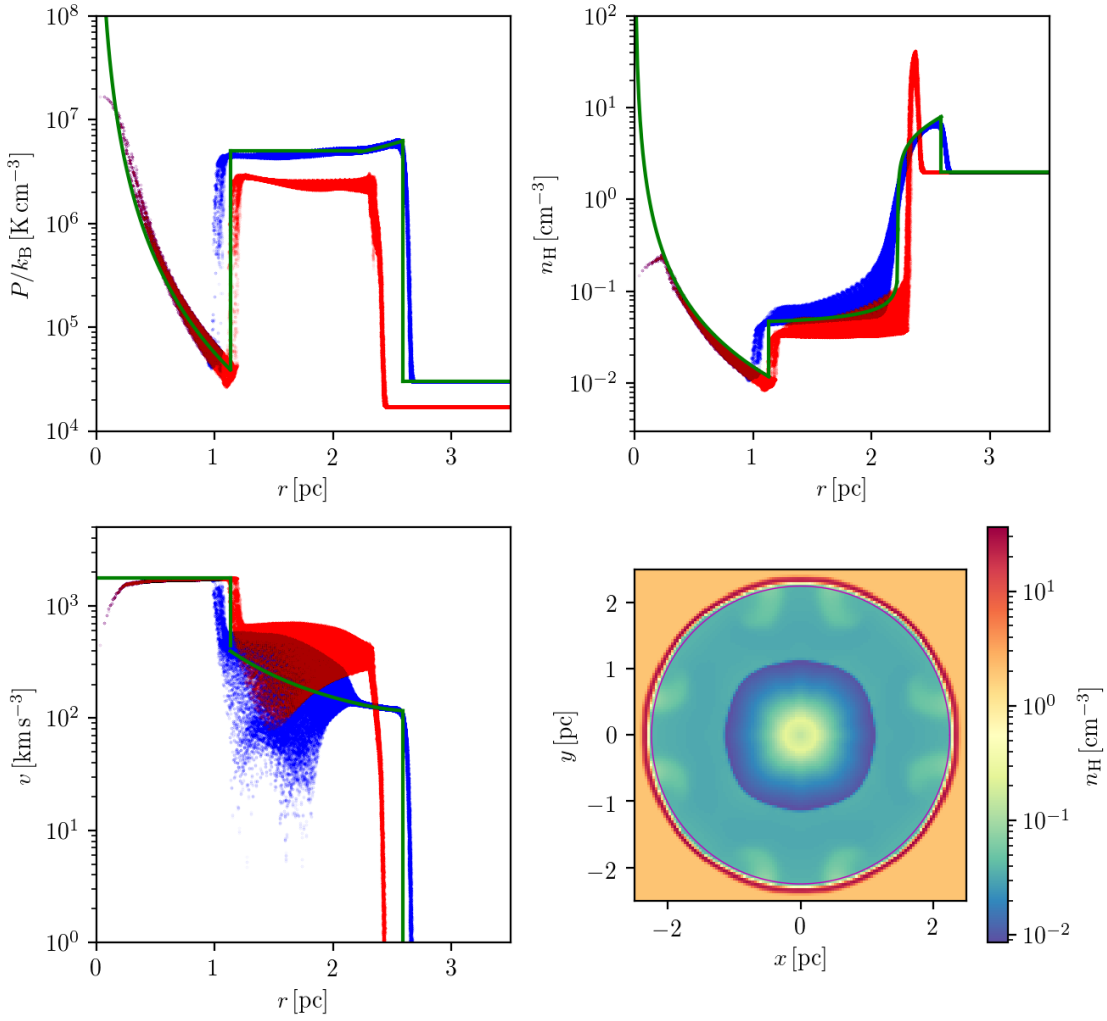

Figure 3.19 Wind implementation tests for a uniform background, shown for a snapshot 10^4 yrs after the start of wind feedback. We show profiles (every cell is plotted) of pressure (top left), number density (top right), and velocity magnitude (bottom left) in radius for both the adiabatic run (in blue) and the run with cooling (red). The Weaver et al. (1977) solution for fully adiabatic evolution is shown in green for these same panels. In the bottom right panel we show a slice of number density through the $z = 0$ plane of the simulation for the run with cooling. One can clearly see the cooled, dense shell that has formed at the outer edge of the wind bubble. The Weaver et al. (1977) solution for the radius of the shell in the case that gas in the leading shock cools is indicated as a magenta circle.

field near the source particle. However, in a real star cluster, winds initially emanate from a few massive stars in the form of bulk kinetic energy through line driving (Lucy & Solomon, 1970; Abbott, 1982; Sundqvist et al., 2014). The winds from these separate stars then collide and shock-heat, converting the initial kinetic energy into thermal energy within the cluster region (Krause et al., 2013; Cantó et al., 2000). The concentrated thermal energy is then yet again converted into bulk kinetic energy as pressure gradients produce acceleration on slightly larger scale, as in (Chevalier & Clegg, 1985). Since the energy injection zones in our simulations are comparable to the size of a star cluster, perhaps a more realistic scheme would be simply to inject purely thermal energy into the feedback region. This is also interesting to test given that thermal energy is lost very efficiently in our model (but only at the outer edge of the bubble).

To this end we perform the same simulations described in Appendix 3.6.2 except adopting the value of $\dot{M}_w/M_*$ used in the main text, and now injecting purely thermal energy rather than using the hybrid injection scheme described in Section 3.2. The results of these tests are shown in Figure 3.20 for the main parameters of interest ($\mathcal{R}_b$, p_r, and E_b), in comparison with results for the hybrid injection scheme. The simulations with thermal energy injection lag those with the hybrid energy injection, but only very slightly. This is most noticeable for radial momentum, p_r, while $\mathcal{R}_b$ and E_b are both relatively insensitive to this change. These results indicate that the bubble evolution is not strongly dependent on the energy injection method.

3.6.2 Reduced Mass Loss

For practical reasons, our simulations use a value for the wind mass loss rate per unit stellar mass, $\dot{M}_w/M_*$, that is about a factor of 5 larger than that predicted by the SB99 code for a Kroupa IMF. From Figure 3.1, this results in a wind momentum injection rate a factor of $\sqrt{5} \approx 2.2$ larger than from SB99. To confirm that our theory still applies when using a lower value for $\dot{M}_w/M_*$, we ran tests with $\dot{M}_w/M_* = 2 \times 10^{-3}\,\mathrm{Myr}^{-1}$, similar to the SB99 level. This correspondingly reduces the momentum injection rate to $\dot{p}_w/M_* = 7.96\,\mathrm{km\,s}^{-1}\,\mathrm{Myr}^{-1}$. With a lower momentum injection rate, the right-hand side of Equation 2.39 is reduced, and more cooling (larger Θ) would be required to satisfy the condition for efficient cooling. If this EC condition is not satisfied, energy

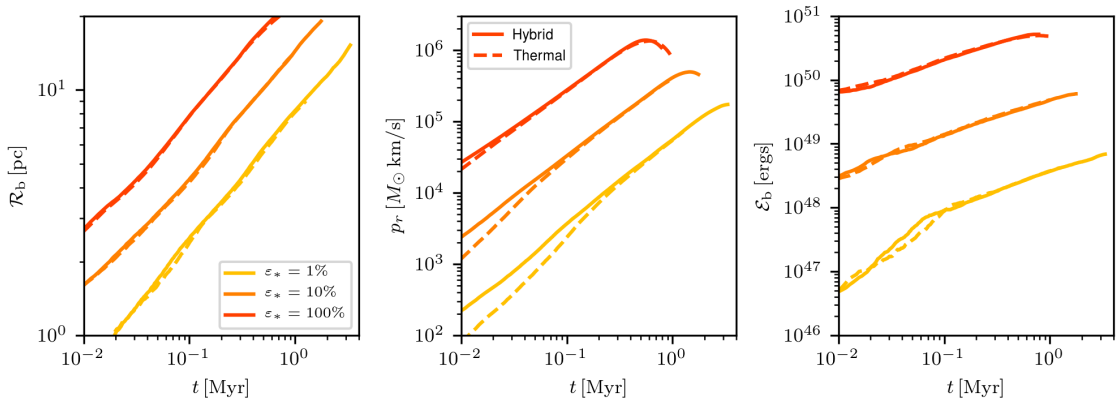

Figure 3.20 Tests run with purely thermal energy injection, in comparison to the hybrid scheme explained in the main text. All panels are analogous to the top panels shown in Figure 3.21. Results using the hybrid injection scheme (thermal scheme) are shown with solid (dashed) lines. The evolution of the total radial momentum, p_r is very slightly delayed for the thermal scheme compared to the hybrid feedback mechanism, but reaches the same scaling by the time the bubble radius is $2 - 3\,\mathrm{pc}$.

will build within the bubble, so that the EC predictions for radius, momentum, and energy would underestimate the true values.

For the reduced mass-loss rate, we run three simulations ($\varepsilon_* = 1$, 10, 100%) with $R_{\rm cl} = 20\,\mathrm{pc}$, $M_{\rm cl} = 10^5 M_\odot$, and $L_{\rm box}/\Delta x = 128$. We note that the choice $R_{\rm cl} = 20\,\mathrm{pc}$ (the low density regime) is the *worst case scenario* for application of the EC theory since cooling is least efficient at low densities, already making it harder for Equation 2.39 to be satisfied.

The evolution of the bubble's effective radius ($\mathcal{R}_b$), the total momentum carried by the bubble (p_r), and the total bubble internal energy (E_b) are shown in the top panels of Figure 3.21. Similar to the figures shown in Section 3.3, we display the quantities derived from simulations using yellow, orange, and red lines compared to the theoretical predictions of the EC model in black. As expected, the EC theory underestimates $\mathcal{R}_b$, p_r, and E_b. However, these differences are small, especially in the case of the radial evolution.

Moreover, the temporal dependence of each quantity is still very well described by the EC theory. This is exemplified by the bottom panels of Figure 3.21, which display quantities related

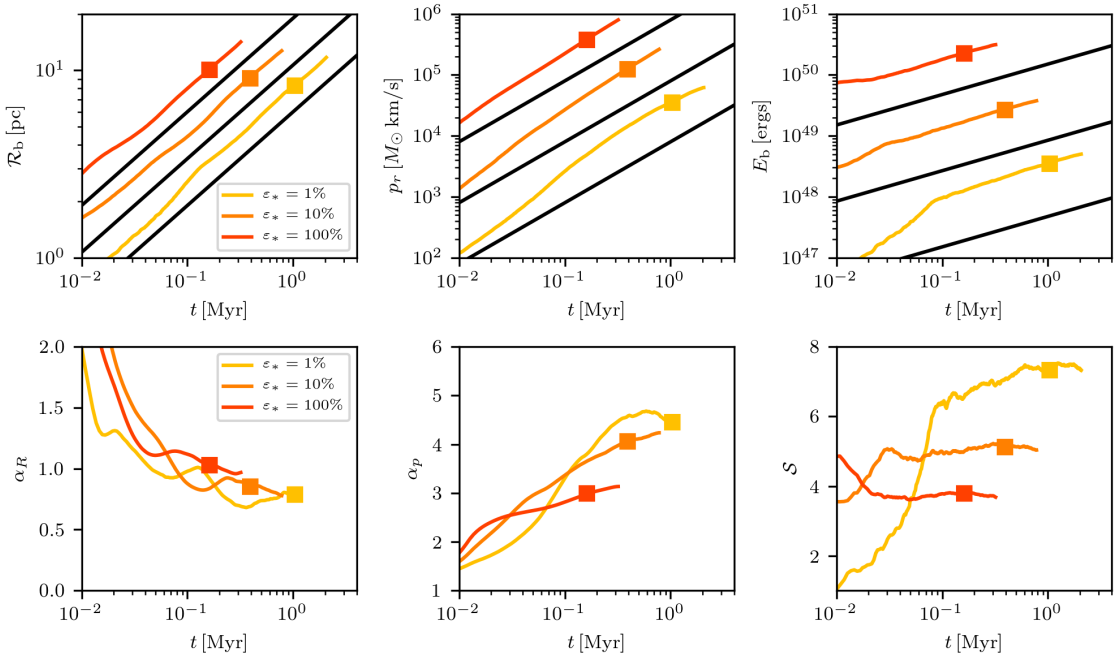

Figure 3.21 Results of our test runs with smaller mass loss rates ($\dot{M}_w/M_*$). The top panels show comparisons to the EC theoretical predictions (black) for the bubble's effective radius (left), total radial momentum (middle), and total energy in the bubble interior (right) for simulations run with $\varepsilon_* = 1\%$ (yellow), 10% (orange), and 100% (red). The bottom panels show quantities related to the ratio of the simulated and theoretically predicted values (see Section 3.3.4).

to the ratio of the simulated values to the values predicted by our EC theory. The fact that these quantities are roughly constant and order-unity over the course of the simulation, especially for higher-luminosity clusters, reflects that the EC theory still describes evolution reasonably well.

3.6.3 Changed Feedback Radius

For all the simulations in the main text, we keep the feedback radius, which determines the region where wind energy is injected, constant. As a further test of numerical robustness and convergence, we perform a set of simulations with a feedback radius that is half that given in the main text, $r_{\rm fb} = 0.5\,{\rm pc}$. The set of models is as described in Appendix 3.6.2 but with the normal $\dot{M}_w/M_*$ values described in the text and now with $L_{\rm box}/\Delta x = 256$, so that $r_{\rm fb}/\Delta x \gtrsim 2$ (i.e. the feedback region is

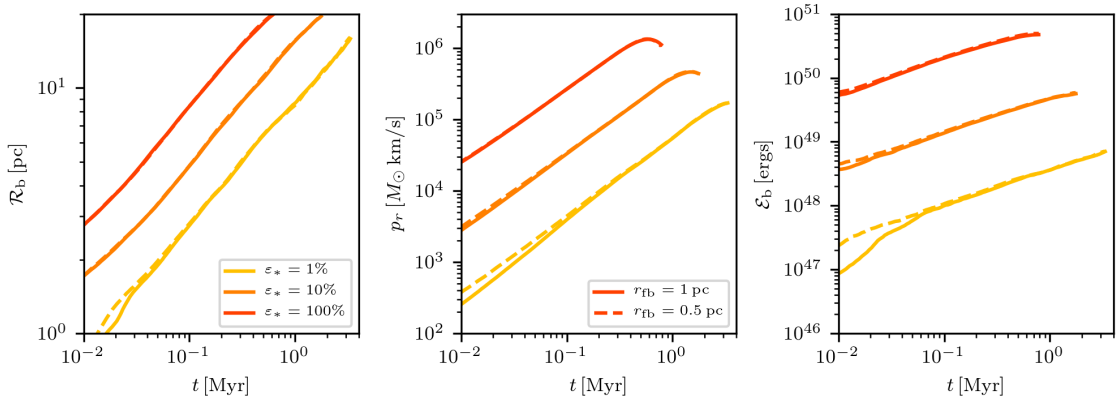

Figure 3.22 Results of tests with standard ($r_{\rm fb} = 1\,$pc, solid curve) and and smaller ($r_{\rm fb} = 0.5\,$pc, dashed curve) feedback radius. All panels are analogous to those shown in Figure 3.20. There is excellent agreement amongst all quantities, indicating that the changed feedback radius (higher source resolution) does not impact our results.

still well resolved). We compare to the standard simulations with $r_{\rm fb} = 1\,$pc and $L_{\rm box}/\Delta x = 256$.

The results of the comparison between $r_{\rm fb} = 1\,$pc and $r_{\rm fb} = 0.5\,$pc cases is shown in Figure 3.22 for the standard quantities of relevance to our theory. As expected, the results for the smaller feedback radius simulations appear to enter the scaling regime earlier than those simulations with larger $r_{\rm fb}$.

3.6.4 Different Turbulent Initial Conditions

When initializing the velocity fields in our simulations, we generally use the same set of amplitudes and phases (based on the same sequence of random seeds) to create the turbulent velocity field. With a different initial velocity field (even for the same initial kinetic energy), the background density structure into which the bubble expands would be different. To check whether the results are sensitive to the specific realization of the turbulent velocity field, we perform the same simulations as in Appendix 3.6.2, using the standard $\dot{M}_w/M_*$, except we initialize the velocity field with a different random seed.

While the cloud will still have the same statistical density structure, the gas in the immediate

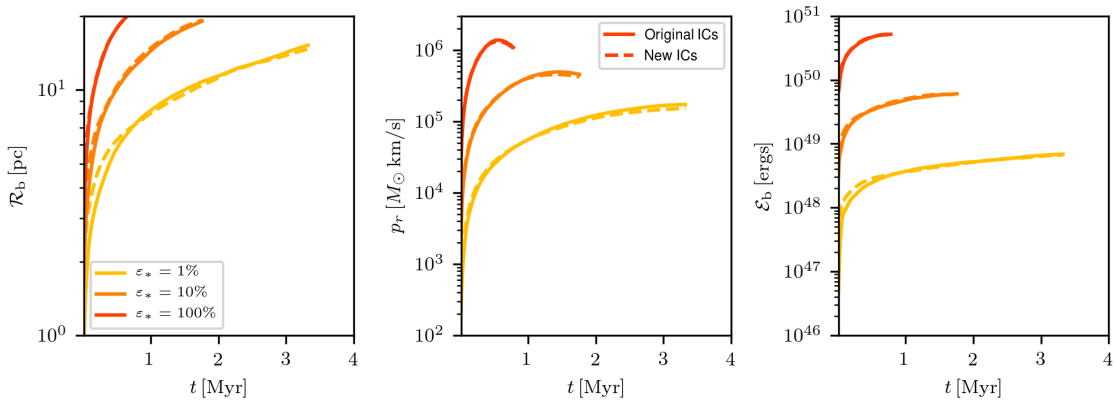

Figure 3.23 Results of our test runs comparing different initial realizations of the turbulent velocity field, which creates different cloud density structure. All panels are analogous to those shown in Figure 3.20 except here we use a linear scale for time. This choice is so as to not overemphasize differences in the early evolution which are due to differences in the density structure very near to the source particle. We show the original initialization as solid lines and the alternate initialization as dashed lines. There is clearly very good agreement at later times between the evolution, in spite of different density structures.

vicinity of the star particle will likely be different. We expect this to result in a slightly different early-time evolution of the wind bubble, while the same overall evolution would be followed once the bubble has probed a significant fraction of the cloud size. In reality, the massive stars that create these high-powered winds will preferentially form at density maxima, but such a self-consistent treatment is left for later work.

The results of these tests are shown in Figure 3.23. So as not to over-emphasize the differences at early times, we display these results on a linear (rather than logarithmic) time scale. Comparing to the standard simulation with a different set of turbulent phases, we see that indeed the overall evolution of the wind-driven bubbles is insensitive to the specific density structure within the turbulent cloud.

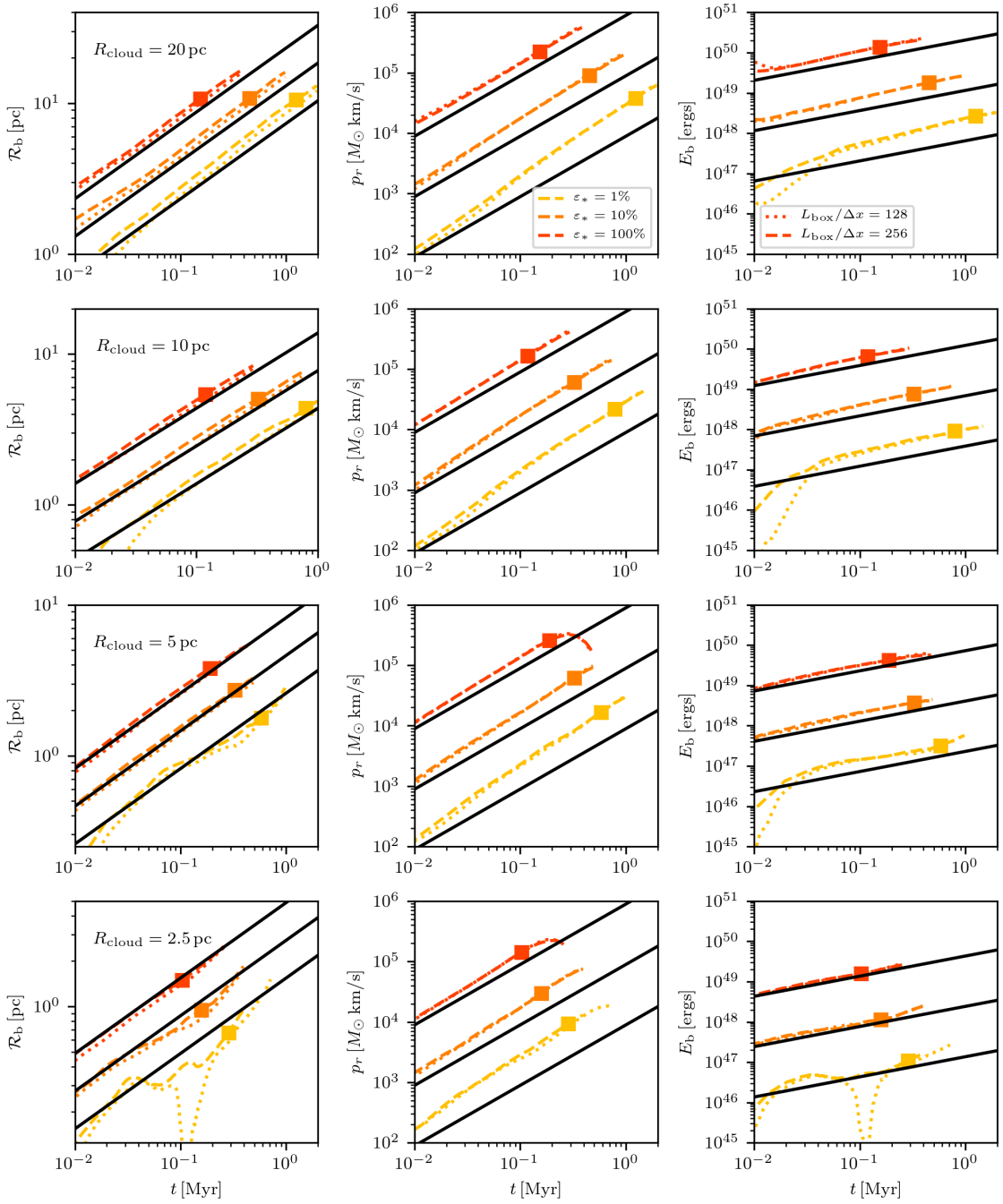

Figure 3.24 Comparisons of our theory (black curves) to our simulations (colored curves) for cases with cloud mass $M_{\rm cl} = 5\times10^4 M_\odot$ and (from top to bottom row) $R_{\rm cl} = 20\,{\rm pc}$, $10\,{\rm pc}$, $5\,{\rm pc}$, and $2.5\,{\rm pc}$. Columns from left to right show the bubble's effective radius, $\mathcal{R}_b$, the total radial momentum, p_r, and the total energy in the bubble interior E_b. All curves are calculated exactly analogously to those in Figure 3.5, Figure 3.4, and Figure 3.6.

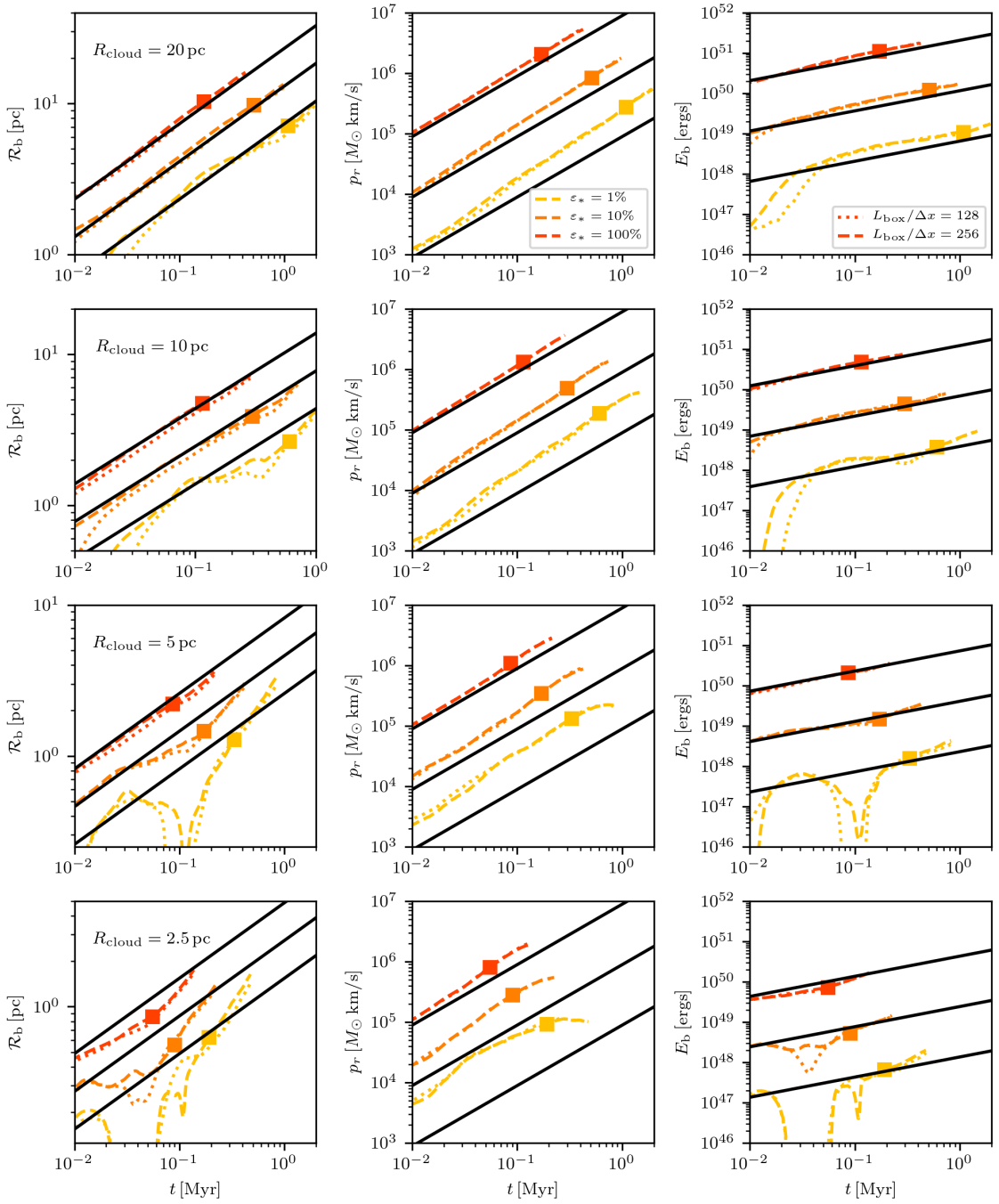

Figure 3.25 Same as Figure 3.24 for cases with $M_{\rm cl} = 5 \times 10^5 M_\odot$.

3.7 Appendix: Results for Different Mass Clouds

In Table 3.1 we lay out the full range of simulations that we ran. In the main body of the text we only displayed and discussed results for the cases with $M_{\rm cl} = 10^5\,M_\odot$. In this appendix we display results from the runs with cloud masses of $M_{\rm cl} = 5 \times 10^4 M_\odot$ and $5 \times 10^5 M_\odot$, given in Figure 3.24 and Figure 3.25, respectively. Results for both 128^3 and 256^3 resolution are shown.

Chapter 4

Stellar Wind Regulated Star Formation

4.1 Introduction

Self-gravitating molecular clouds are observed to be star-forming in a wide range of environments, from dwarf galaxies (Lopez et al., 2011; Cheng et al., 2021), to the Solar neighborhood (Schneider et al., 2020; Fujita et al., 2021), to galactic center starbursts (Johnson et al., 2015; Leroy et al., 2018; Levy et al., 2020; Emig et al., 2020). On the scale of molecular clouds, the lifetime star formation efficiency (SFE) depends on the processes that truncate star formation (SF) by destroying the cloud, some of which are external and some of which are internal (e.g. Chevance et al., 2020a). For giant molecular clouds (GMCs) that create massive stars, internal processes associated with SF feedback dominate the regulation of this process.

Previous numerical work has extensively investigated the effects of radiation feedback from star clusters on the surrounding GMC – i.e. ionized gas pressure, direct radiation pressure, and reprocessed radiation pressure, for a range of cloud conditions (e.g. Dale et al., 2012, 2013; Skinner & Ostriker, 2015; Raskutti et al., 2016, 2017; Howard et al., 2017; Kim et al., 2018, 2019a, 2021b).

In these models, photoionization usually dominates cloud destruction for "normal" GMCs ($\Sigma_{\rm cl} \sim 10^2$ $M_\odot$ pc^{-2}), while radiation pressure becomes relatively more important for clouds with very high surface density, following general trends predicted with analytic models (e.g. Krumholz & Matzner, 2009; Kim et al., 2016). The direct injection of kinetic energy and mass (so-called "mechanical" feedback) may also be important – sources are stellar winds at early stages followed by supernovae (SNe) (Agertz et al., 2013; Rogers & Pittard, 2013; Walch & Naab, 2015; Iffrig & Hennebelle, 2015; Geen et al., 2016). For clouds that are relatively diffuse and have long evolutionary timescales, SNe are effective, and indeed SFRs in large-scale simulations with SN feedback are consistent with observations for these conditions even when dynamical effects of radiation are omitted (e.g. Kim & Ostriker, 2017). For very high surface density clouds, where super star clusters (SSCs) form, the SF timescales are too short for SNe to affect evolution significantly, but winds can potentially play a key role.

In Chapter 2 we proposed a new theoretical model for the expansion of stellar wind bubbles under conditions present in the turbulent molecular clouds where stars are born. In Chapter 3, we presented a large suite of three-dimensional (3D) hydrodynamical simulations to validate this theory. However, our previous work did not take into account the effects of gravity, either for dynamical evolution of the large-scale cloud, or for establishing a self-consistent star formation history (SFH) by inducing small-scale collapse.

Investigating the interplay between gravity, turbulence, and stellar wind feedback is the main goal of this chapter. A key motivation is to confirm that energy losses are still large, consistent with the solution proposed in Chapter 2. If not, it would be difficult to understand the observed high SFEs of SSC-forming clouds (Johnson et al., 2015; Leroy et al., 2018; Emig et al., 2020; Levy et al., 2020). If evolution were to follow the wind-driven bubble solution from Weaver et al. (1977), the large momentum injection from an inefficiently-cooling bubble would easily destroy GMCs even with very low SFE and very high surface density, as we discussed in Chapter 3. We have previously argued that with much-reduced momentum injection driven by cooling, winds would be compatible with observed high SFEs in SSC-forming clouds; here we directly test this prediction with simulations.

In real clouds, multiple feedback processes operate simultaneously, and several numerical simulations have included treatment of both wind and radiation feedback in some form (Dale et al., 2014; Geen et al., 2021; Wall et al., 2020; Grudić et al., 2021). Here, our goal is instead to isolate the effects of winds independent of other feedback processes, and to systematically explore cloud dynamical evolution and SFH for varying parent cloud properties. This allows us to develop and test simple theoretical models, while providing a baseline for more comprehensive studies.

Our self-gravitating models allow us to investigate another important question. In the literature, two modes of energy loss have been proposed in order to explain weak observed signatures of winds: enhanced radiative cooling (Rosen et al., 2014; Lancaster et al., 2021b) *or* bulk advection of wind energy out of the cloud – so called "leakage" (Harper-Clark & Murray, 2009). In Chapter 3, we showed that interface mixing leading to strong cooling can be very effective, and explains the low pressure of X-ray emitting gas observed in pre-SN systems (see discussion in Chapter 2). Here we are able to investigate the roles of mixing/cooling vs. leakage in removing energy from winds that develop in a cloud with self-consistent star formation. As we shall show, both are important but at different times.

Beyond their potential importance in helping to control star formation, winds are also interesting for the way in which they act to chemically pollute the gas in a molecular cloud, leading to so-called "self-enrichment" of subsequent populations of stars that form within the molecular clouds. The details of this process are important to fields ranging from galactic archaeology, where the process of self-enrichment may undermine the strategy of so-called "chemical tagging" (Freeman & Bland-Hawthorn, 2002), to multiple stellar populations with different abundances within globular clusters (GCs), where nearly all proposed models for explaining these populations involve "self-enrichment" (Wünsch et al., 2017; Lochhaas & Thompson, 2017; Bailin, 2018; Tenorio-Tagle et al., 2019; Bastian & Lardo, 2018). To be clear, the winds from massive OB stars explored here do not have drastically different chemical abundances from progenitor gas, especially before the Wolf-Rayet phase, and therefore would not, themselves, cause strong self-enrichment. In tracking the re-integration of wind material in subsequent stars we provide a first look at how this process may work for stellar winds more generally. For this reason we refer to the process explored here as

"self-pollution."

The layout of this chapter is as follows. In Section 4.2 we briefly review our numerical methods. Results of our simulations, and connection to other theoretical work, is presented in Section 4.3. Finally, we summarize our conclusions and connect to observations in Section 4.4.

4.2 Methods

We simulate the collapse and subsequent dispersal by stellar wind feedback of self-gravitating, turbulent gaseous clouds. The simulation framework we employ is built on the 3D magneto-hydrodynamics (MHD) code *Athena* (Stone et al., 2008), though we do not include magnetic fields in this study. We run all of our simulations on a fixed, Cartesian grid using the Roe approximate Riemann solver (Roe, 1981), second order spatial reconstruction, and the unsplit van Leer integrator (Stone & Gardiner, 2009).

We include cooling in the gas as implemented in the *Athena*-TIGRESS code base (Kim & Ostriker, 2017). This cooling module assumes a simple cooling coefficient $\Lambda(T)$ using the fitting formula of Koyama & Inutsuka (2002, see Kim et al. (2008) for corrections) for $T < 10^{4.2}$ K gas and the tabulated results from Sutherland & Dopita (1993) for $T > 10^{4.2}$ K gas (assuming collisional ionization equilibrium). We adopt a uniform background heating rate of $2 \times 10^{-26}\,\mathrm{erg\,s^{-1}\,H^{-1}}$ which decreases smoothly to zero in higher temperature gas.

We employ sink/star particles as implemented in Gong & Ostriker (2013), with modifications described in Kim et al. (2020a). Sink particles, representing stellar (sub-) clusters, are created when a density threshold (based on the collapse solution of Larson, 1969; Penston, 1969) is reached, the cell forming the particle is at a minimum of the gravitational potential, and the flow is converging along all grid directions.

We include star formation feedback in the form of energy and momentum representing the collective stellar wind inputs from a coeval population of O and B stars (Vink et al., 2001; Vink & Sander, 2021; Leitherer et al., 1992). We use prescriptions for the energy and momentum from Starburst99 (Leitherer et al., 1999, 2014) for two different initial stellar mass functions (IMFs, described

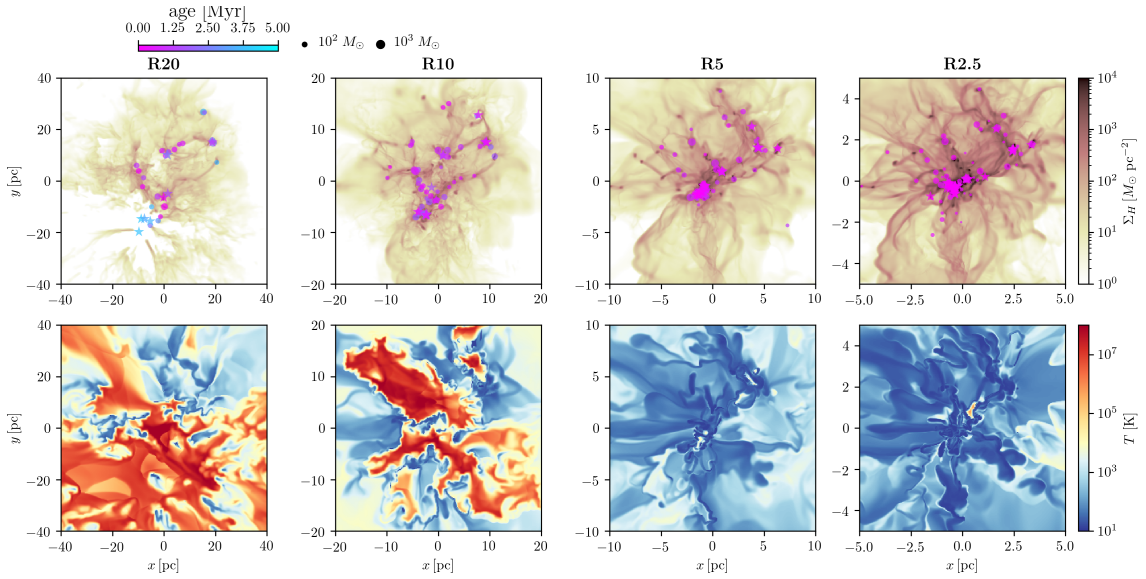

Figure 4.1 Snapshots from simulations at the time when 75% of the final stellar mass has formed. Models **R20** to **R2.5** are shown from left to right, with all simulations shown here having the same initial turbulence realization (with differing amplitudes). *Top row*: the integrated gas surface density, together with projected locations of star particles colored by age with size scaled by mass. The "active" star particles producing winds are shown as stars while inactive star particles are shown as circles. *Bottom row*: slices of gas temperature (centered on the center of mass of the star particles).

further below), both employing the Geneva, non-rotating stellar evolutionary tracks (Ekström et al., 2012). These calculations use the wind prescriptions of Vink et al. (2001), which are thought to over-estimate the mass-loss rates, $\dot{M}_w$, by a factor of 2-3 (Smith, 2014); $\dot{p}_w = \sqrt{2\mathcal{L}_w \dot{M}_w}$ would also be affected by this. This energy and momentum is injected within a radius $r_{\rm fb}/\Delta x = 3.2$ of the star particle using the hybrid kinetic/thermal injection scheme described in Lancaster et al. (2021a), which employs a subcell method for dividing the energy and (vector) momentum more accurately over the injection region (see also Ressler et al., 2020). When mass from a wind is injected to the grid, we also inject an equal mass in a passive scalar which is advected with the grid gas, allowing us to track subsequent mixing of the wind material.

In our simulations, we impose a minimum mass $M_{\rm cut} = 10^3\,{\rm M}_\odot$ for the initialization of a stellar wind from a sink particle. That is, for all sink particles with mass $M_{*,\rm sink} < M_{\rm cut}$ accretion is

permitted, but for higher mass particles accretion is turned off and wind injection proportional to $M_{*,\rm sink}$ is initiated. We do this both to reduce the computational cost of injecting wind material and to represent the correlation of winds with high mass stars, which are relatively rare. In addition, since the most massive stars contribute a disproportionate fraction of the power, the number of "important" wind sources is limited. The mean specific wind luminosity and mass loss rates increase while the variances decrease for more fully-sampled mass functions. For example, clusters of mass 500, 1000, and 5000 $\rm M_\odot$ sampled from a Kroupa IMF have respective expectation values of the wind luminosity per stellar mass $\mathcal{L}_w/M_* = 4\times10^{32}$, 10^{33}, and $4\times10^{33}\,\rm erg/s/M_\odot$ with interquartile ranges spanning 1.8, 1.5, and 0.5 dex, respectively. All of our simulations have total sink particle mass $> 10^4\,\rm M_\odot$, well into the fully-sampled regime, so it is appropriate to assign wind power based on a fully sampled IMF.

If we make $M_{\rm cut}$ too low, the simulations become expensive due to having many sources, and they are also unphysical in having the wind power nearly equally divided among an unrealistically large number of sources. If we make $M_{\rm cut}$ too high, we artificially suppress feedback. We therefore choose $M_{\rm cut} = 10^3\,\rm M_\odot$ as a compromise. For a cluster of mass $3-9\times10^4$ $\rm M_\odot$ (the range for our simulations) divided among particles of mass $10^3\,\rm M_\odot$, there would be 30-90 active sources. This can be compared to the expectation value 29-85 for the number of stars that would provide 95% of the wind luminosity in a cluster of this mass range that fully samples the Kroupa IMF[1].

We explore the implications of our prescription and parameter choice, and compare with alternative ways of assigning feedback to star particles, in Section 4.5. In Section 4.6, we show that with our simple prescription the mass in wind source star particles is converged with respect to resolution, although in the situation where star particles stop accreting before reaching $M_{\rm cut}$ the total stellar mass is not converged. It is also important to note that our simulations are not suited to studying the mass spectrum of either stars or clusters; the initial mass spectrum of sink particles depends on grid resolution, and their growth via accretion is truncated when winds turn on after $M = M_{\rm cut}$.

[1]Calculations in the last two paragraphs were performed using the Leitherer et al. (1992) wind prescriptions along with the Choi et al. (2016) isochrones at solar metallicity, without rotation, resulting in small differences between the results of Leitherer et al. (1992).

Table 4.1. Parameters and results of simulation suite.

$\overline{n}_{\rm H,cl}$ [cm^{-3}]	v_t [km s^{-1}]	$t_{\rm ff,0}$ [Myr]	Δx [pc]	$\varepsilon_{*,\rm f}$ %	$\varepsilon_{*,\rm nfb}$ %	$t_{\rm br}$ [Myr]	$t_{\rm dest}$ [Myr]	$t_{\rm SF}$ [Myr]	$t_{\rm pr}$ [Myr]
86.3	5.08	4.68	0.31	28^{+2}_{-7}	75^{+5}_{-4}	8.1 ± 1.4	$14.8^{+5.4}_{-0.6}$	$8.2^{+2.8}_{-1.2}$	$6.1^{+0.4}_{-0.2}$
690	7.18	1.66	0.16	51^{+4}_{-10}	82^{+3}_{-1}	$5.0^{+0.6}_{-1.0}$	$6.1^{+0.7}_{-0.5}$	$3.6^{+0.8}_{-0.5}$	$4.3^{+0.2}_{-0.7}$
5520	10.2	0.586	0.08	71^{+3}_{-4}	87 ± 1	3.1 ± 0.5	$3.5^{+0.3}_{-0.4}$	$2.1^{+0.1}_{-0.3}$	$2.9^{+0.2}_{-0.4}$
44200	14.4	0.207	0.04	85^{+1}_{-3}	88 ± 1	$1.7^{+0.2}_{-0.1}$	$1.8^{+0.04}_{-0.2}$	$1.0^{+0.2}_{-0.03}$	1.8 ± 0.1

Note. — Parameters of each model cloud **R20**, **R10**, **R5**, and **R2.5** from the top to bottom row with cloud radii $R_{\rm cl} = 20$, 10, 5 and 2.5 pc, respectively. Each model is run with five different Gaussian random-phase turbulent velocity field realizations. The quantities given in the rightmost six columns quote the median and full range over these realizations. $\varepsilon_{*,\rm nfb}$ indicates the final SFE reached in simulations run with the same initial conditionas over the same time without any stellar winds.

4.2.1 Simulation Description

We run a set of simulations of initially uniform density spherical clouds of radius $R_{\rm cl}$ and mass $M_{\rm cl}$ placed at the center of a cubic domain with side length $L_{\rm box} = 4R_{\rm cl}$. Our standard simulations are run on a uniform grid with $L_{\rm box}/\Delta x = 256$, though we explore the effects of resolution in Section 4.6. In each simulation the cloud is initially surrounded by gas that is 1000 times less dense and in pressure equilibrium with the cloud, contributing about 1% of the cloud mass to the total simulation domain. We initialize a Gaussian random field for the turbulent velocity, with power spectrum $|v_k|^2 \propto k^{-4}$ for wave modes $2 \leq kL_{\rm box}/2\pi \leq 64$. The normalization of the velocity field is chosen so that the initial kinetic energy of the cloud is equal to its gravitational binding energy (i.e. a virial parameter of $\alpha_{\rm vir} = 2$).

We set $M_{\rm cl} = 10^5\,{\rm M}_\odot$ for all of our simulations, and consider models with four different cloud radii, $R_{\rm cl} = 20$, 10, 5, and 2.5 pc, denoted **R20**, **R10**, **R5**, and **R2.5**. For each cloud radius we run five simulations with different random-phase turbulent initial conditions. Our parameter space spans nearly 3 orders of magnitude in initial density, enabling us to investigate the regulation of star formation by stellar winds for conditions ranging from typical Milky Way GMCs (Heyer &

Dame, 2015; Evans et al., 2021) to the birth clouds of SSCs (Johnson et al., 2015; Oey et al., 2017; Turner et al., 2017; Leroy et al., 2018; Emig et al., 2020). Each simulation is run (at least) until only 5% of the cold gas mass remains on the grid, corresponding to a median duration over the turbulent realizations of 14.8, 6.14, 3.49, and 1.75 Myrs for model **R20**-**R2.5**, respectively.

For the purpose of setting stellar wind feedback through the SB99 code, we adopt an IMF consisting of stepped power laws $dN/dM \propto M^{-\alpha}$. Our main simulation follow a standard Kroupa IMF with the lowest mass range omitted, that is $\alpha = 1.3$ for $0.1 < M/\,\mathrm{M}_\odot < 0.5$ and $\alpha = 2.3$ for $0.5 < M/\,\mathrm{M}_\odot < 100$ (Kroupa, 2001). We have also experimented with a second, top-heavy IMF which has $\alpha = 1.8$ for the higher mass range, but is otherwise identical. Except as noted, all models shown adopt a standard IMF.

4.3 Results

In Figure 4.1 we show snapshots of the simulations in gas surface density and gas temperature at the time when 75% of the total stellar mass has formed, corresponding to $t - t_{\mathrm{SF},0} = 5.5$, 3.0, 1.5, and 0.6 Myrs for the **R20**, **R10**, **R5** and **R2.5** models, respectively. Notably, cooling is so efficient in the high surface density clouds that even though a very large stellar mass has accumulated and produced winds, there is still no significant volume of hot gas on the grid.

4.3.1 Hot gas losses and cloud evolution

In the high-density regions where star clusters form, the pressure from shocked winds would lead to a momentum input rate exceeding that from radiation feedback unless some of the wind energy is lost (Krumholz et al., 2019; Lancaster et al., 2021b). Two mechanisms for wind energy loss are bulk advection of hot gas out of the dense cloud ("leakage," as advocated by Harper-Clark & Murray (2009)), or turbulent interface mixing followed by cooling (explored in depth in Lancaster et al., 2021b,a). Here we show that both effects are important, but at different times.

In this section we shall consider evolution of energy, momentum, and bubble size, focusing on the **R20** and **R5** models, which are representative of the trends that we see in the other models.

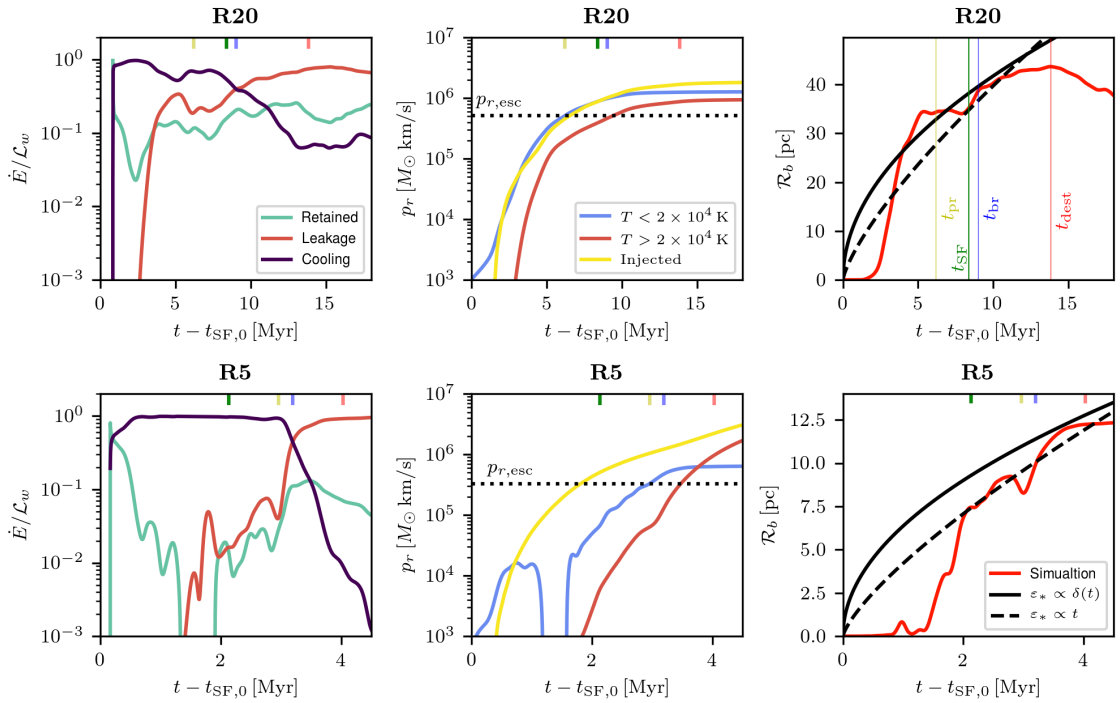

Figure 4.2 Evolution of the energy, momentum, and bubble radius from model **R20** (top row) and **R5** (bottom row) for the same simulations shown in Figure 4.1.The time axis is shifted to coincide with the formation of the first star particle in each model. The ticks at the top of each panel (vertical thin lines in the upper right panel) indicate certain key times: t_{pr}, when enough momentum to disperse the cloud has been acquired (yellow, see Equation 4.2); t_{SF}, when 95% of the stellar mass has formed (green); t_{br}, when breakout occurs (blue); and t_{dest}, when the cloud has been effectively destroyed (fuchsia). *Left Column*: The breakdown of input wind energy "spending" over time, normalized by the instantaneous wind luminosity. Losses due to cooling (dark purple), bulk advection off the grid (red), and the luminosity fraction retained on the grid (teal) are shown. *Middle Column*: The total radial momentum in wind-polluted ($f_{w,\mathrm{grid}} > 10^{-4}$) gas for the cold/warm component (blue), the hot component (red), and the equivalent momentum injected by winds for a single source (yellow). The reference radial momentum required to disperse the cloud ($p_{r,\mathrm{esc}}$) is indicated as a horizontal dotted line. *Right Column*: The effective bubble radius for the simulations, as defined in the text (red lines), with reference predictions for delta-function and linear SFHs (solid and dashed black lines respectively).

Energy Evolution

From our simulations, we can measure the total instantaneous mechanical luminosity in winds, $\mathcal{L}_w$, the net radiative cooling rate in wind-polluted gas[2], $\dot{E}_{\rm cool}$, and the rate at which energy is advected out of the simulation domain in wind-polluted gas, $\dot{E}_{\rm leak}$ (including contributions from thermal and kinetic energy).

Because we are now considering global clouds, we extend the definition of the fractional energy loss rate from Lancaster et al. (2021b) to include both cooling, $\dot{E}_{\rm cool}$, and bulk advection out of the domain, $\dot{E}_{\rm leak}$:

$$\Theta \equiv \frac{\dot{E}_{\rm cool} + \dot{E}_{\rm leak}}{\mathcal{L}_w} \,. \tag{4.1}$$

We refer to $1 - \Theta$ as the fraction of wind energy that is retained within the cloud.

In the left column of Figure 4.2 we show the evolution of $\dot{E}_{\rm cool}/\mathcal{L}_w$, $\dot{E}_{\rm leak}/\mathcal{L}_w$, and the retained energy fraction $(1-\Theta)$ over time in models **R20** (top row) and **R5** (bottom row). Losses transition from being dominated by cooling (at early times) to leakage (at late times). The transition between these two regimes is rapid in the denser models. We define the time at which leakage losses dominate cooling losses as the "breakout time" $t_{\rm br}$.

The low fraction of retained energy indicated by the left column of Figure 4.2 is consistent with the picture, as previously demonstrated in Lancaster et al. (2021a), in which turbulently-mediated energy losses are sufficient to explain the low observed hot-gas pressures in wind-driven bubbles (Rosen et al., 2014; Lopez et al., 2011). The measured hot gas pressures in our simulations are broadly consistent with the predictions of Lancaster et al. (2021b). The deviations (at most $\sim 0.5\,$dex) between the simulations and theory are consistent with moderate momentum enhancement (expected in the theory) or decrement (caused by multiple wind sources, discussed below) along with variations in $\dot{p}_w/M_*$.

The fraction of energy that remains after cooling and leakage, $1 - \Theta$, is only $\sim 1 - 10\%$, which, during the cooling-dominated period, is consistent with the results of Lancaster et al. (2021b,a). For the denser models, other than the earliest times, $1 - \Theta$ is largest after $t_{\rm br}$. As we shall show,

[2]Similarly to Lancaster et al. (2021a) we define wind polluted gas as gas where the fraction of mass in wind material in a given grid cell, $f_{w,\rm grid}$, is greater than 10^{-4}.

this is due to an expansion in the volume filled by hot gas.

Momentum Evolution

The middle column of Figure 4.2 shows the evolution of the gas radial momentum, measured with respect to the center of the simulation domain. We separate into a cold/warm component ($T < 2 \times 10^4$ K), which is mostly cloud gas, and a hot component ($T > 2 \times 10^4$ K), which mostly consists of the expanding wind bubble. For both components, measured momentum includes contributions from gas on the grid as well as wind-polluted ($f_{w,\rm grid} > 10^{-4}$) gas that has been advected out of the domain. We also show the total outward momentum that has been injected by winds in the simulations for an equivalent single central source ($\int \dot{p}_w(t)dt$). This total equivalent injected momentum can significantly exceed the actual momentum in the gas, as we discuss further below.

For reference we mark the radial momentum needed to disperse the gas remaining after star formation, $p_{r,\rm esc}$, which we define as

$$p_{r,\rm esc} \equiv M_{\rm cl}(1 - \varepsilon_{*,\rm f})v_{\rm esc} \tag{4.2}$$

where $\varepsilon_{*,\rm f}$ is the final SFE of the simulation and $v_{\rm esc} \equiv \sqrt{2GM_{\rm cl}/R_{\rm cl}}$ is our proxy for the escape speed from the cloud.

Figure 4.2 clearly shows that most of the radial momentum in the cold/warm gas is accumulated before $t_{\rm br}$. That is, the time $t_{\rm pr}$ when the radial momentum held in cold/warm gas exceeds the reference "escape" value of Equation 4.2 is prior to $t_{\rm br}$. For the **R5** model, the momentum in the hot gas continues to increase after $t_{\rm br}$, at a much higher rate than during the period when momentum was mostly stored in cold/warm gas. This likely does not occur in the **R20** model due to the decrease of $\dot{p}_w/M_*$ with the age of the stellar population.

In the analytic model of Lancaster et al. (2021b) we allowed for the momentum added to the shell to be enhanced above the input wind value $\dot{p}_w$ by a factor α_p. By comparing the total momentum input by winds (yellow lines) to the momentum that is actually accumulated in the gas, we can attempt to assess to what degree momentum is accumulated beyond the "Efficiently

Cooled" solution ($\alpha_p > 1$). It is important to note that in our current simulations there are additional effects that can change our interpretation of α_p when performing the comparison we just described. For example, since stars form in over-dense structures, gravity (and the negative momentum associated with collapse) can act to "crush" expanding bubbles. This could contribute to accumulated momentum lower than the total input value, appearing as $\alpha_p < 1$. At the same time, we are not measuring radial momentum with respect to a fixed source, which can be especially confounding at early times when a "super-bubble" enveloping the multiples sources has not yet formed. In addition, the contribution from background momentum at early times can be non-negligible. The combination of all of these effects could lead to either $\alpha_p < 1$ or $\alpha_p > 1$ at early times depending on the realization.

With these caveats in mind, we can see by comparison of the momenta in Figure 4.2, that in the **R20** model we quickly reach $\alpha_p \approx 1$. This is consistent with the "Efficiently Cooled" solution with some moderate build up of excess momentum when considering the caveats above.

In the dense **R5** model, however, it is apparent that $\alpha_p \lesssim 1$, which is also true for the **R2.5** model. This behaviour can be due both to the effects of gravity described above (which are especially strong in the dense models) and another effect. In the dense clouds, when wind bubbles/shells from individual sources collide with one another at small scales, momentum built up in shells can cancel and the corresponding kinetic energy thermalizes. The swept-up shells in these dense models are dense enough to cool efficiently; with reduced pressure, there is no re-acceleration. This results in a bubble evolution that is technically *less than momentum-conserving*.

Bubble Radius Evolution

In the right column of Figure 4.2 we show the temporal evolution of the effective radius of the wind-driven bubble, $\mathcal{R}_b$, defined as

$$\mathcal{R}_b = \left(\frac{3V_b}{4\pi}\right)^{1/3} . \tag{4.3}$$

Here V_b is the volume of the wind driven bubble, defined as the total volume of cells with temperature $T > 2 \times 10^6\,\mathrm{K}$ *or* with radial velocity $v_r > \mathcal{V}_w/2$ as measured with respect to the origin of the

simulation domain. Note that in the simulations the bubble is not always a single entity but rather an amalgamation of bubbles from each source which start to expand individually before percolating to become a larger "super-bubble." We use a single effective bubble radius here to give the simplest phenomenological comparison to our previous models, which assume a single, central source. We also sum over all wind inputs in making a prediction for the bubble radius.

For reference, in the right column of Figure 4.2 we show the expected bubble radial evolution for the "Efficiently Cooled" (momentum-driven) solution for two different assumed SFHs: 1) An instantaneous, delta-function SFH, which assumes that the final SFE is reached as soon as the first star forms (solid lines) and 2) a linear SFH given by

$$\varepsilon_*(t) = \frac{M_*(t)}{M_{\rm cl}} = \varepsilon_{\rm ff} \frac{t}{t_{\rm ff,0}} \tag{4.4}$$

where $t_{\rm ff,0}$ is the initial free-fall time of the cloud and the SFE per free-fall time, $\varepsilon_{\rm ff} = 0.25$, is set based on a fit to the early-time SFHs of the simulations (dashed lines). The first method will tend to over-predict the radial size since at early times it overestimates the stellar power driving the wind bubble. In principle, the latter model should work better, since it more closely follows the actual SFH, and indeed Figure 4.2 shows somewhat better agreement of this model with the numerical results at the time of breakout. Neither model accounts for the effects of gravity (which are most important in the denser clouds), however, or for the varying strength of the stellar winds with age (which are most important in the longer lived, larger clouds).

4.3.2 Star Formation Efficiency

Like other forms of feedback, winds can help to suppress star formation, but their effectiveness can be reduced by energy losses. Having established that wind energy is efficiently lost through both cooling and leakage, it is interesting to investigate the role winds play in suppressing star formation. To do this, we make use of theories that have been proposed in the literature to predict SFEs subject to feedback mechanisms in the form of momentum injection rate $\dot{p}$. In previous work that accounts for cloud inhomogeneity, this momentum has been conceived of as associated with

radiation, but the physical picture of competition between radially outward forces from feedback and inward forces from gravity is quite general, and can be equally well applied to momentum injection from a wind.

Since we evolve our simulations until most of the gas is either driven off the grid or locked in star particles, a straightforward way to assess star formation regulation is to measure the lifetime SFE

$$\varepsilon_{*,\mathrm{f}} \equiv \frac{M_{*,\mathrm{final}}}{M_{\mathrm{cl}}}. \tag{4.5}$$

As a reference value, in Table 4.1 we also give the SFE reached in simulations run for the same time period but without any feedback from stellar winds, which we denote $\varepsilon_{*,\mathrm{nfb}}$. Comparison between the simulations with and without feedback shows that at the highest surface density, only a few percent of the mass in the cloud is driven out by feedback. In contrast, half of the cloud's mass loss can be attributed to feedback in the low-density cloud.

We shall compare the measured SFE in the simulation as a function of cloud parameters to several different theoretical predictions. All of the theoretical models explored here will assume that the wind bubble is in the "Efficiently Cooled" limit in which there is no enhancement of momentum relative to the initial wind injection. That is, we assume $\alpha_p = 1$, even though, as we have seen, it can be either slightly greater or less than one depending on the environment.

In our predictions, we will use the mechanical luminosity of the winds per unit stellar mass

$$\Psi_w \equiv \frac{\mathcal{L}_w}{M_*} = \frac{\dot{M}_w V_w^2}{2M_*} \tag{4.6}$$

and the total radial momentum input rate for an equivalent single central source,

$$\dot{p}_w = \frac{2\Psi_w}{V_w} M_*; \tag{4.7}$$

here $\mathcal{L}_w$ is the total mechanical luminosity of all winds collectively, and $\mathcal{V}_w$ is the wind injection velocity. For our analytic predictions below, we simplify by using the initial value of Ψ_w determined by the SB99 code for a fully-sampled Kroupa IMF, which is approximately $10^{34}\,\mathrm{erg/s}/M_\odot$. We note

that in detail, the IMF-averaged Ψ_w stays relatively constant until an increase due to Wolf-Rayet Stars around $t \approx 3\,\mathrm{Myr}$ and subsequent decline beginning at $t \approx 4\,\mathrm{Myr}$ (see Figure 3 of Lancaster et al. (2021b)). While our numerical models employ a time-dependent IMF-averaged value of Ψ_w for each source, our analytic models adopt this simpler approach of constant Ψ_w.

Suppression of star formation in clouds occurs by driving mass out of the system. We consider a fluid element of mass M and cross-sectional area A at a distance r from a central cluster. If it absorbs all incident momentum $\dot{p} = \dot{p}_w A/(4\pi r^2)$ from a radially-flowing wind, the Eddington ratio between the wind force $\dot{p}$ and the gravitational force GM_*M/r^2 of the cluster on the fluid element is

$$\frac{\dot{p}}{GM_*M/r^2} = \frac{\Psi_w}{2\pi G \mathcal{V}_w \Sigma} \equiv \frac{\Sigma_{\rm Edd}}{\Sigma} \tag{4.8a}$$

$$= 0.57 \left(\frac{\Psi_w}{10^{34}\,\mathrm{erg/s/\,M_\odot}}\right) \left(\frac{\Sigma}{10^3\ \mathrm{M_\odot\,pc^{-2}}}\right)^{-1} \times \left(\frac{\mathcal{V}_w}{10^3\,\mathrm{km/s}}\right)^{-1}. \tag{4.8b}$$

Here, the gas surface density of the fluid element is $\Sigma = M/A$, and we have defined the Eddington surface density $\Sigma_{\rm Edd} \equiv \Psi_w/(2\pi G V_w)$ as the maximum value for which the feedback wind momentum exceeds gravity; for our adopted parameters this is $\Sigma_{\rm Edd} = 570 M_\odot\ \mathrm{pc^{-2}}$.

Lancaster et al. (2021a) Prediction

We begin by reviewing the simple prediction of Lancaster et al. (2021b) for the SFE, obtained under the assumption that all star formation occurs instantaneously at the center of a cloud, creating a cluster of mass $M_* = \varepsilon_* M_{\rm cl}$, and that the rest of the mass $(1-\varepsilon_*)M_{\rm cl}$ is swept into a spherical shell at the cloud radius $R_{\rm cl}$. For the force from the wind to exceed the gravity of the cluster plus the self-gravity of the shell, the condition

$$\dot{p}_w > \frac{GM_{\rm cl}^2}{R_{\rm cl}^2}\left(\varepsilon_*(1-\varepsilon_*) + \frac{(1-\varepsilon_*)^2}{2}\right) \tag{4.9}$$

must be satisfied. The above can be written as

$$8\frac{\Sigma_{\rm Edd}}{\Sigma_{\rm cl}} > \frac{1-\varepsilon_*^2}{\varepsilon_*}\,, \tag{4.10}$$

where $\Sigma_{\rm cl} \equiv M_{\rm cl}/\pi R_{\rm cl}^2$. This inequality may be solved to obtain the minimum ε_* given $\Sigma_{\rm Edd}/\Sigma_{\rm cl}$. For low $\Sigma_{\rm cl}$, i.e. $\Sigma_{\rm cl} \ll \Sigma_{\rm Edd}$, this yields $\varepsilon_* \approx \Sigma_{\rm cl}/(8\Sigma_{\rm Edd}) \propto \Sigma_{\rm cl}$, while for high $\Sigma_{\rm cl}$, $\varepsilon_* \approx 1 - 4\Sigma_{\rm Edd}/\Sigma_{\rm cl}$ (Lancaster et al., 2021b).

The above parallels simple scaling arguments for SFE as limited by radiation pressure, where instead of $\dot{p}_w$ the radiation momentum injection L/c (for L the bolometric luminosity) is used (e.g. Fall et al., 2010; Murray, 2011; Raskutti et al., 2016; Li et al., 2019b). The assumption of instantaneous star formation is, however, clearly inconsistent with the more realistic simulations carried out here.

Steady Star Formation

An alternative approach allows for the SFH to be extended in time, rather that instantaneous, while still occurring at the center of the cloud. Following the same derivation for bubble expansion as in Lancaster et al. (2021b) (ignoring the effects of gravity and assuming a constant momentum input rate per unit stellar mass $\dot{p}_w/M_*$), while setting $M_*/M_{\rm cl} = \varepsilon_* = \varepsilon_{\rm ff} t/t_{\rm ff,0}$, the bubble expands as

$$\frac{\mathcal{R}_b}{R_{\rm cl}} = \left[\frac{16\Sigma_{\rm Edd}}{3\Sigma_{\rm cl}\pi^2}\varepsilon_{\rm ff}\left(\frac{t}{t_{\rm ff,0}}\right)^3\right]^{1/4}\,, \tag{4.11}$$

where we have defined the initial free-fall time of the cloud as

$$t_{\rm ff,0} \equiv \sqrt{\frac{3\pi}{32G\bar{\rho}}} = \sqrt{\frac{\pi^2 R_{\rm cl}^3}{8GM_{\rm cl}}}\,. \tag{4.12}$$

If we then assume that star formation is immediately halted once the bubble reaches the edge of the cloud, we can obtain an estimate for ε_* by setting $\mathcal{R}_b = R_{\rm cl}$ in the above and solving for t. This gives us the final SFE $\varepsilon_{*,\rm f} = [3\pi^2\varepsilon_{\rm ff}^2\Sigma_{\rm cl}/(16\Sigma_{\rm Edd})]^{1/3}$ for an assumed $\varepsilon_{\rm ff}$.

This model may be accurate in large, low-density clouds where the effects of gravity on the wind

bubble expansion are actually quite small. However, there is no consideration for the ability of the swept-up shell to escape the gravity of the system, and if the bubble expands slowly enough this model will predict $\varepsilon_* > 1$, which is clearly unphysical.

Thompson & Krumholz (2016) Prediction

The models of Section 4.3.2 and Section 4.3.2 assume the driving source "sees" only a single gas surface density over all solid angles, given by the mean value for the cloud as a whole. In reality, since the clouds in which stars are born are supersonically turbulent, the surface densities viewed either externally or looking outward from the center will have a log-normal distribution (e.g. Raskutti et al., 2017; Kim et al., 2019a). Considering momentum injection associated with radiation pressure, Thompson & Krumholz (2016) pointed out that directions where the total line-of-sight surface density is sufficiently low can be "super-Eddington" even if the cloud as a whole is sub-Eddington. Along these lines of sight, gas may be driven out of the cloud.

Thompson & Krumholz (2016) denote the mass-weighted distribution of (logarithmic) surface density $x \equiv \ln\left(\Sigma/\bar{\Sigma}\right)$ by $p_-(x)$, where $\bar{\Sigma} \equiv \int \Sigma d\Omega/4\pi$ is the sky-averaged surface density and the mean of $p_-(x)$ is $\sigma^2_{\ln\Sigma}/2$. Integrating over the distribution,

$$\zeta_-(x) \equiv \int_{-\infty}^{x} p_-(x')dx' \tag{4.13a}$$

$$= \frac{1}{2}\left[1 - \mathrm{erf}\left(\frac{-2x + \sigma^2_{\ln\Sigma}}{2\sqrt{2}\sigma_{\ln\Sigma}}\right)\right] . \tag{4.13b}$$

Given a distribution of mass, Thompson & Krumholz (2016) posit an instantaneous loss rate of mass ejected from the cloud as

$$\dot{M}_{\mathrm{cloud,ej}} = \zeta_-(x_{\mathrm{crit}}(t))\frac{M_g(t)}{t_{\mathrm{ff}}(t)} , \tag{4.14}$$

where $M_g(t)$ and $t_{\mathrm{ff}}(t)$ are the instantaneous gas mass and free-fall time of the system[3], and x_{crit} is determined by the condition for a structure to be super-Eddington. At the same time, star

[3] $t_{\mathrm{ff}}(t)$ is defined here as in Equation 4.12 except with M_{cl} replaced by the sum of the instantaneous gas, $M_g(t)$, and stellar, $M_*(t)$, mass.

formation is assumed to follow

$$\dot{M}_* = \varepsilon_{\rm ff} \frac{M_g(t)}{t_{\rm ff}(t)} \,, \tag{4.15}$$

where $\varepsilon_{\rm ff}$ is a constant SFE per free-fall time, so that allowing for mass loss to both outflow and star formation (i.e. $M_g(t) = M_g(0) - M_*(t) - M_{{\rm cloud},w}(t)$), the average surface density evolves in time as $\bar{\Sigma} = 4R_{\rm cl}(t)\bar{\rho}(t)/3$. Thompson & Krumholz (2016) allow the cloud radius to evolve as well, but we keep this fixed.

Adapting from the case of radiation feedback to wind feedback, the limit in the integral over the distribution becomes $x_{\rm crit} = \ln(\Sigma_{\rm TK}/\bar{\Sigma})$ where $\Sigma_{\rm TK} = \Sigma_{\rm Edd}/(1 + M_g/M_*)$ is the Eddington surface density as defined in Thompson & Krumholz (2016), allowing for gravity of both stars and gas.

The above equations can be integrated jointly forward in time until all mass that was originally in gas is either in wind or stars. The final stellar mass then determines the final predicted SFE. This is a function of the initial cloud properties, the adopted Ψ_w, and the values assumed for the parameters $\varepsilon_{\rm ff}$ and $\sigma_{\ln\Sigma}$.

Raskutti et al. (2016) Prediction

Raskutti et al. (2016) also developed a prediction for the SFE of a cloud regulated by radiation pressure feedback that takes in to account the log-normal distribution in surface densities seen by a source particle. The theoretical model is very similar to that of Thompson & Krumholz (2016) except that, instead of integrating ODEs they consider the instantaneous state of a cloud. If some fraction, ε_*, of the original cloud mass has been gathered into a central star cluster and the remaining gas is distributed around this source with a log-normal distribution in surface densities, they calculate the fraction of the original cloud that would be super-Eddington as

$$\varepsilon_{\rm of}(\varepsilon_*) = (1 - \varepsilon_*)\zeta_-(x_{\rm crit}(\varepsilon_*)) \,, \tag{4.16}$$

where the only differences between this $x_{\rm crit}$ and that of Thompson & Krumholz (2016) are (1) a factor of 1/2 in the gas gravity term, and (2) the inclusion of a parameter to account for the possible contraction of the cloud as it evolves (which exists to a different degree in the Thompson

& Krumholz (2016) model).

Raskutti et al. (2016) argue that star formation proceeds until a SFE of

$$\varepsilon_{\rm min} = \underset{0<\varepsilon_*<1}{\arg\max}\, \varepsilon_{\rm of}(\varepsilon_*) \tag{4.17}$$

is reached. At this point, the maximum fraction of the original gas satisfies the Eddington condition and will (in their model) be immediately ejected. This corresponds to a minimum prediction for the SFE, since there is still some gas left in the shell at this point that is sub-Eddington. If all of this remaining gas collapses to form more stars then the final SFE will instead be

$$\varepsilon_{\rm max} = 1 - \varepsilon_{\rm of}(\varepsilon_{\rm min})\,. \tag{4.18}$$

To obtain SFE predictions (upper and lower bounds) a value for the parameter $\sigma_{\ln\Sigma}$ must be adopted, but no assumption for $\varepsilon_{\rm ff}$ is needed.

Comparison to Simulations

In Figure 4.3 we show the final SFEs for all of our simulations, displaying results based on the five different runs for each parameter set. For comparison we show the predictions of each of the analytic models described in the previous sections.

The assumptions and parameters used for each of these theories are as follows

- *Lancaster+21a*: The only free parameter is the momentum input rate per unit mass $\dot{p}_w/M_* = 2\Psi_w/\mathcal{V}_w$. We adopt a value 8.6 km/s/Myr, determined using the average over the first 1 Myr using SB99 (Leitherer et al., 1999). We use this value of $\dot{p}_w/M_*$ in all models.

- *Steady SFR*: We adopt $\varepsilon_{\rm ff} = 0.25$, broadly consistent with the SFH in our simulations.

- *Thompson & Krumholz*: As above we adopt $\varepsilon_{\rm ff} = 0.25$, and for the width of log-normal in surface density we adopt $\sigma_{\ln\Sigma} = 1.5$ as a value consistent with many of the simulations over much of the evolution.

- *Raskutti+16*: We display the minimum prediction given by Equation 4.17, also assuming no expansion or contraction of the cloud ($x = 1$ in their notation). We adopt $\sigma_{\ln\Sigma} = 1.5$ as above.

We first note that the agreement between the Lancaster et al. (2021b) prediction and our simulations is best for the highest surface density clouds. This is because the SFH most closely resembles an instantaneous starburst in the high-Σ regime, for which the star formation timescale is much less than the cloud disruption timescale (as we will see in Section 4.3.3). However, the Lancaster et al. (2021b) prediction significantly underestimates the measured SFE at low surface densities.

The steady star formation prediction does reasonably well at low surface densities, but quite poorly elsewhere. This is because the condition chosen to turn off star formation is arbitrary (when the bubble reaches the edge of the cloud) and does not take into account the effect of gravity in any way. There is also no built-in limit of star formation to prevent ε_* from exceeding unity, as it does for $\Sigma_{\rm cl} \gtrsim 10^4$ $\mathrm{M_\odot pc^{-2}}$.

The Thompson & Krumholz (2016) model does a much better job at capturing the overall trend in the simulation results, while still slightly overestimating the measured SFE. In principle the model could be made to fit better by adjusting its parameters, but our specific choices for the parameters are motivated by the simulations themselves.

The Raskutti et al. (2016) model, which has no explicit time dependence and assumes a constant PDF in Σ, does reasonably well at high $\Sigma_{\rm cl}$ and slightly over-predicts ε_* at low $\Sigma_{\rm cl}$. The latter could be due to a break-down of the single, centralized source or constant $\dot{p}_w/M_*$ assumptions (see below).

Since in practice $\sigma_{\ln\Sigma}$ is not constant in time, we additionally show the predictions of both the Thompson & Krumholz (2016) and Raskutti et al. (2016) models for $\sigma_{\ln\Sigma} = 0.75$ in Figure 4.3 as thin dashed lines. This value is chosen as comparable to the measured PDF variance at the onset of star formation. Adoption of this value leads to a slightly higher (lower) predicted SFE at higher (lower) Σ for both models. However, we caution that there is not a strong physical motivation for preferring this choice. Rather, the comparison provides a feeling for the parameter sensitivity of

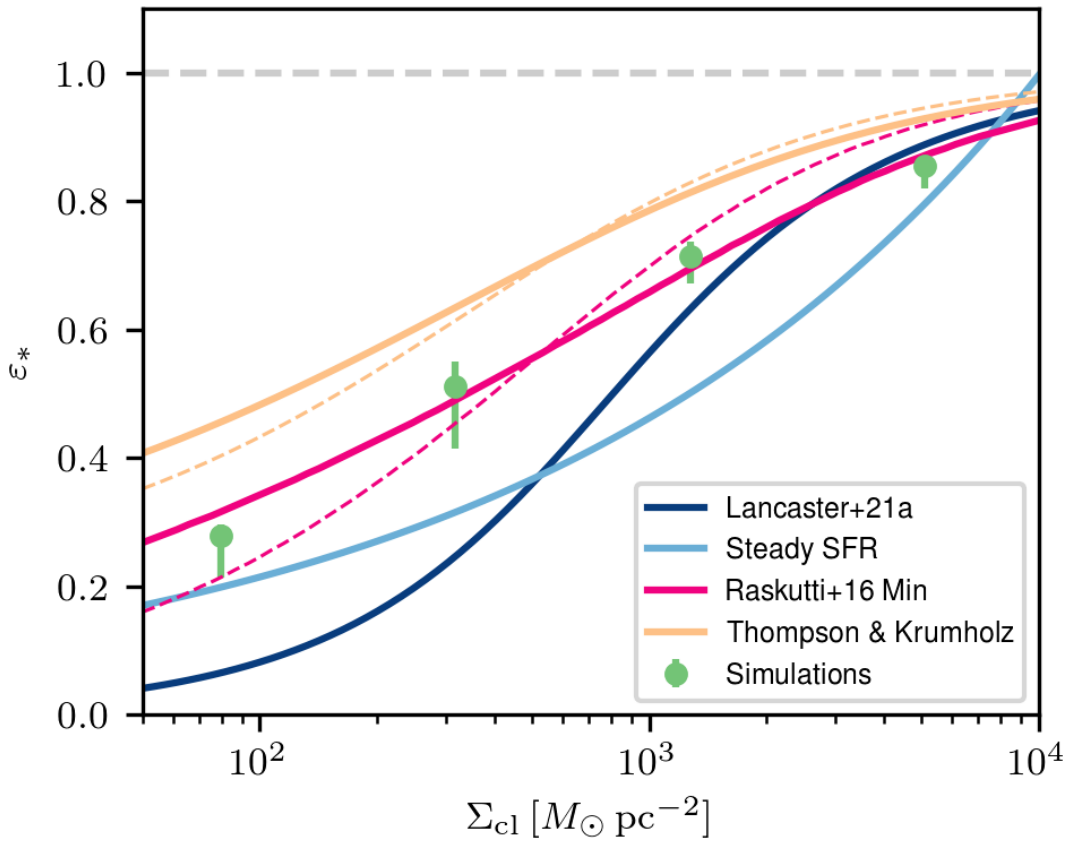

Figure 4.3 The final SFE realized in our simulations in comparison to analytic models. For each simulation parameter set (see Table 4.1) we show the median SFE as a point, with the range of the SFEs from all runs shown by the vertical error bars. Predictions for the SFE based on several different models are shown, as labeled. For lognormal-based models, solid lines denote $\sigma_{\ln \Sigma} = 1.5$ and dashed lines denote $\sigma_{\ln \Sigma} = 0.75$ (see text).

the two models.

As mentioned above, we have also investigated the effects of top-heavy IMFs in our denser models (**R5** and **R2.5**), motivated by observations of star clusters in dense environments (McCrady et al., 2005; Lu et al., 2013; Hosek et al., 2019). We find that the greater strength of the winds (larger $\dot{p}_w/M_*$) with a top-heavy IMF is noticeable, reducing the final SFEs from 71 to 53% and 85 to 75% in the **R5** and **R2.5** models respectively.

Finally, as we alluded to above, we note that the approximation of $\dot{p}_w \approx$ const. breaks down once the Wolf-Rayet stage of stellar evolution occurs around $\sim 3\,$Myr (see Lancaster et al. (2021b) Figure 3), with $\dot{p}_w$ increasing by a factor ~ 3 and then declining again over the next few Myr. As we shall show in the next section, the two lower-density models have lifetimes that extend into the Wolf-Rayet phase, so one might expect slightly lower ε_* than predicted under the model assumption of constant $\dot{p}_w/M_*$, as is indeed the case. Because their lifetimes are shorter, the higher $\Sigma_{\rm cl}$ simulations would not be significantly affected by the increase of $\dot{p}_w$ in the Wolf-Rayet stage.

4.3.3 Timescales

In Figure 4.4 we show various time-scales measured from the simulations, and how they depend on the surface density of the cloud. All timescales represent the time elapsed between the onset of star formation and the physical event described below, and in Figure 4.4 are plotted in units of the initial free-fall time in the cloud.

$t_{\rm br}$: The "breakout time" is when energy losses from the wind become dominated by bulk advection (leakage) of hot gas out of the cloud, rather than turbulent mixing and subsequent cooling (see Section 4.3.1).

$t_{\rm SF}$: The "star formation time" is when 95% of the final stellar mass has been formed in the simulation.

$t_{\rm dest}$: The "destruction time" is when the gas mass remaining on the grid drops to 5% of the initial cloud mass.

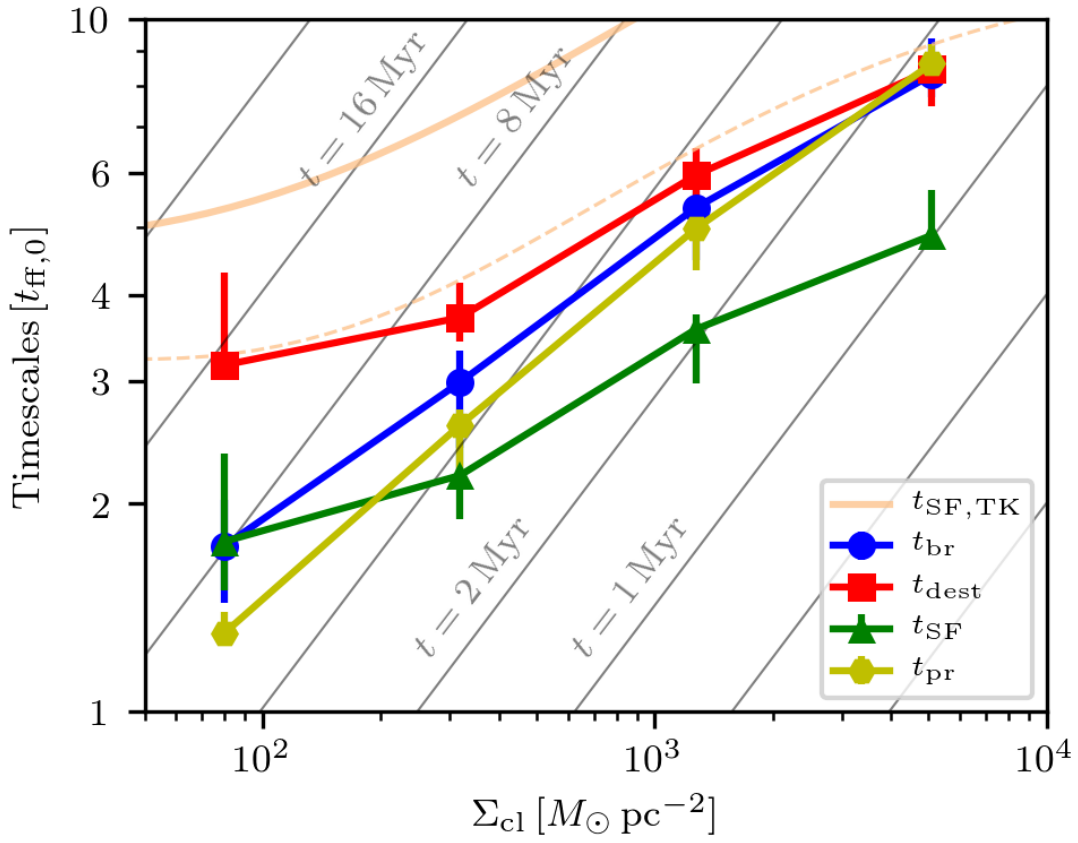

Figure 4.4 Timescales of key events, as measured in the simulations (see Section 4.3.3 for definitions); values are shown in units of the free-fall time. Lines of constant physical time are also shown as thin grey lines. The prediction of Thompson & Krumholz (2016) for $t_{\rm SF}$ is shown as beige lines for $\sigma_{\ln\Sigma} = 1.5$ (0.75) in solid (dashed) line styles.

$t_{\rm pr}$: The "radial momentum time" is when the total radial momentum carried in the cold/warm ($T < 2 \times 10^4\,{\rm K}$) gas exceeds the "escape momentum" defined in Equation 4.2.

Considering the various timescales together, Figure 4.4 reveals a common sequence in which winds halt star-formation while cooling is still dominating the wind's energy losses and acceleration is still occurring, but the winds eventually break out from the dense cloud gas, and the remaining gas is gradually driven out of the simulation domain. The momentum needed to disrupt the cloud

is always accumulated in the gas *before* advection begins to dominate over cooling losses ($t_{\rm pr} < t_{\rm br}$). Interestingly, it is also broadly true that $t_{\rm dest} \approx 2t_{\rm SF}$.

The details of evolution nevertheless vary over the range in surface densities probed by our simulations. At the lowest surface densities probed here, the momentum needed to eventually disrupt the cloud is acquired *before* star formation halts. In this case, star formation is a continuous process that proceeds in parts of molecular clouds while it is simultaneously being halted in other parts. However, at higher surface density, star formation essentially is halted and then winds engage in an extended battle to turn around and expel lower-density gas while also trying to break out of the cloud. In these denser clouds, $t_{\rm br}$, $t_{\rm pr}$, and $t_{\rm dest}$ all occur roughly simultaneously. For the highest surface density cloud, as we have shown, very little material is in practice driven away by feedback.

Since the model of Thompson & Krumholz (2016) provides for a full SFH, it gives a prediction for $t_{\rm SF}$. We include this prediction in Figure 4.4. The prediction overestimates the star-formation timescale by a factor of ≈ 2 for the $\sigma_{\ln \Sigma} = 0.75$ case (dashed line) and by a larger factor for the $\sigma_{\ln \Sigma} = 1.5$ value (solid line). The fact that star formation halts much more rapidly than the model predicts indicates that the model assumption of a wind acceleration timescale $t_{\rm ff}(t)$ is not borne out in our simulations. Potentially, other assumptions for the acceleration timescale (e.g. accounting for the distribution of Eddington ratios) could be explored, but a reformulation of this theory is beyond the scope of the present work.

4.3.4 Wind Pollution

One of the central goals of this work is to provide a first investigation of the incorporation of wind material in new stars, and its dependence on cloud environment. As a caveat, we note that the winds investigated here, from massive OB stars, are not very chemically distinct from their parent gas, especially before the onset of the Wolf-Rayet phase (Leitherer et al., 1992), and thus the "pollution" by these winds would not produce compositional signatures. The winds that are thought to self-enrich forming globular clusters presumably would have somewhat different physical properties (e.g. mass-loss rates, wind velocities), and this difference should be kept in mind when

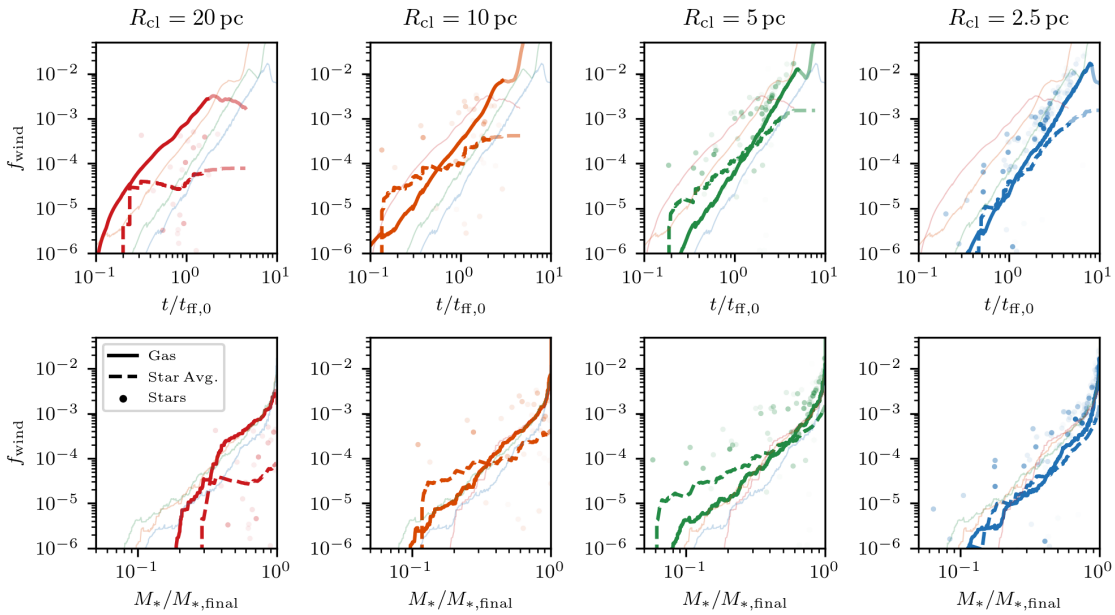

Figure 4.5 Evolution of the global fraction of wind mass $f_{\rm wind}$ in the gas (solid lines), in the stars overall (dashed lines), and in individual star particles (points, where more opaque points indicate more massive star particles). We show results as a function of time in units of the initial free-fall time (top row), and as a function of the fraction of the final stellar mass that has formed (bottom row). For the individual star particles, we show the fraction of their *initial* mass in wind material as a function of the time when they first formed (or fraction of stellar mass formed when they first formed, in the bottom row). Each panel also includes $f_{\rm wind}$ in gas from other models as thin, transparent lines. We show $f_{\rm wind}$ for the gas (stars) as opaque curves up until $t_{\rm br}$ ($t_{\rm SF}$), after which more transparent lines are shown. We note that the dashed lines include *all* star particles, even those with negligible enrichment that do not appear on this plot.

interpreting the results we present.

As discussed in Section 4.2, we use a passive scalar, injected with the wind material, to track how wind material is mixed into the surrounding gas and subsequently-forming stars. In Figure 4.5, we present the evolution of the *global* fraction of mass, in stars ($f_{\rm wind}, *$) and in gas ($f_{\rm wind}$), that originated from stellar winds. All simulations depicted in Figure 4.5 have identical random-phase initialization of their turbulence.

From Figure 4.5, the evolution of $f_{\rm wind}$ in the gas (solid lines) is remarkably similar across the simulations when the evolution is shown in units of the free-fall time. This is consistent with each of the simulations having nearly the same (linear) SFH at early times with $\varepsilon_{\rm ff} \approx 0.25$, which then implies $\dot{M}_w \propto t^2$ (in practice, the slope in the simulations is closer to $\dot{M}_w \propto t^{5/2}$). These lines significantly deviate when the wind bubbles break out, first causing $f_{\rm wind}$ to decrease as much wind material is advected off of the grid and then increase as all remaining, non-wind material is dispersed.

For the denser clouds, the fraction of wind material in star particles (dashed lines) very roughly tracks the evolution of $f_{\rm wind}$ in the gas, until star formation slows (dashed lines becoming transparent indicate 95% of star formation is complete). As we have seen in Figure 4.4, in denser clouds, star formation takes place over more free-fall times, resulting here in a more self-polluted stellar population.

In the denser clouds, polluted stars tend to form in gas that is preferentially more polluted than the average gas (points fall above the solid lines), indicating that mixing is less efficient in these clouds. This is somewhat counter-intuitive since one might expect that mixing would be more efficient in the denser clouds where the turbulent Mach numbers are higher, promoting a larger degree of turbulence compared to radial expansion of wind bubbles (see Figure 10 of Lancaster et al. (2021a)). However, as we have seen, when gravity is considered wind bubbles are much more easily contained in the dense clouds. Indeed when we look at the mass-weighted distribution of $f_{\rm wind}$ in the simulations, the denser clouds are much less well-mixed, explaining the trend we see here.

To the best of our knowledge, this sort of self-consistent analysis of pollution by the winds

from newly-formed stars is the first of its kind that has been shown in the star cluster formation literature. We anticipate that future analyses of this kind, including chemical enrichment from other wind sources, can be used to better understand proposed formation mechanisms for multiple populations in Globular Clusters (Bastian & Lardo, 2018; Gratton et al., 2019; Bailin, 2018), as well as chemical evolution within normal, redshift-zero star-forming clouds. However, it is important to keep in mind that there are many potentially important physical phenomena which we have not included that may or may not be important in different scenarios (radiative feedback, magnetic fields, dust, varying metallicity).

4.4 Summary and Discussion

The simulations and analyses presented here explore the applicability of the "Efficiently Cooled" stellar wind bubble model (Lancaster et al., 2021b,a) in the more realistic scenario where stars form self-consistently through gravitational collapse, which competes with cloud dispersal by stellar winds. We show the core principle of the "Efficiently Cooled" model holds: enough energy is removed through radiative cooling to make the wind bubbles momentum-driven rather than energy-driven (see Figure 4.2).

In the absence of losses, stellar winds would dominate other "early feedback" in star-forming clouds. The weak observational signatures of winds has led to suggestions that energy is efficiently removed by either (i) bulk advection of hot gas out of the cloud, or (ii) radiative cooling mediated by turbulent mixing. We show that over the time-scales relevant to star formation (see Figure 4.4), it is the latter process that is most important for removing energy injected by stellar winds. This conceivably depends upon the exact geometry of the cloud, and it is plausible that for highly porous clouds, bulk advection could dominate energy losses.

We apply theoretical models to make predictions for SFEs in clouds on the basis of "Eddington ratio-like" considerations of competition between gravity and wind forces, taking into account turbulence-driven substructure. We compare predictions of these theoretical models for SFEs to the numerical results from our simulations (see Figure 4.3). While our simulations include realistically

time-varying specific wind momentum input rate, the theoretical models assume $\dot{p}_w/M_*$ is constant, for simplicity. Despite this, we find that the models derived from Raskutti et al. (2016) follow the numerical results fairly well, while the Thompson & Krumholz (2016) models slightly over-estimate the final SFEs. Model assumptions regarding (i) constant momentum input rates, (ii) a constant SFE per free-fall time, $\varepsilon_{\rm ff}$, and (iii) a log-normal distribution of surface densities with constant variance are not fully satisfied, however, which may account for some of the deviations between numerical results and models. We also compare the Thompson & Krumholz (2016) prediction of the star formation duration $t_{\rm SF}$ to our numerical results, and find that the former overestimates our measurements of $t_{\rm SF}$, which we link to their assumption for the timescale for gas expulsion.

We do not attempt to make a direct comparison between our simulated SFE and observed values for different cloud regimes, given that important feedback effects are left out in our numerical models. Nevertheless, it is conceivable that stellar wind feedback is the dominant star formation regulation mechanism in very dense clouds (Levy et al., 2020; Lancaster et al., 2021b), and it is interesting to compare our models to observations in this regime. The SFEs we measure at high surface density are broadly consistent with the range inferred from observations of SSC-forming clouds at the centers of galaxies, which are generally $\varepsilon_* \gtrsim 70\%$ (Leroy et al., 2018; Emig et al., 2020). Due to the range of uncertainties associated with the observations, empirical SFEs are also broadly consistent with the SFEs in our simulations that assume stellar populations with top-heavy IMFs, as might be expected in these clouds (Hosek et al., 2019).

In typical Milky Way (or LMC/SMC) GMCs, similar to our lower density models, momentum-driven stellar wind feedback is not expected to be the dominant star formation regulation mechanism (Lancaster et al., 2021b). However, it is still interesting to quantitatively assess the effects of winds in this regime. Based on the work of Lopez et al. (2011); Rosen et al. (2014) and others, there are large discrepancies between observations of the hot gas pressure produced by winds and the classical Weaver et al. (1977) model, and in Lancaster et al. (2021b,a) we proposed that energy losses due to turbulently-mediated radiative cooling could explain these discrepancies. Inspection of the hot gas pressure in the more-realistic simulations presented here bear out this proposal, where our **R20** simulations show hot gas pressures ranging from $10^5 - 10^7\,{\rm K\,cm^{-3}}$ at $t \lesssim 3\,{\rm Myr}$, broadly consistent

with X-ray observations of nearby massive star-forming regions (Lopez et al., 2011, 2014).

Finally, using a passive scalar that is injected with the wind material, we investigate the process of wind pollution. The fraction of the gas originating in winds scales roughly as $f_{\rm wind} \propto t^{5/2} \propto M_*^{5/2}$, and for the densest cloud (model **R2.5**) the mean wind-mass fraction of the stellar population generally follows this up to the time of wind breakout. For the less-dense clouds the mean pollution of the stellar population increases less steeply in time, and individual star particles can have significantly higher or lower $f_{\rm wind}$ than the mean value at the time they form.

The increase of $f_{\rm wind}$ in time, combined with the fact that star-formation takes place over more dynamical times in denser clouds, implies stellar populations with larger fractions of wind material in denser clouds. This investigation opens the door for future direct numerical simulations to explore wind pollution and chemical self-enrichment in cluster-forming clouds in more depth (incorporating additional physical processes and winds that are more chemically enriched), with implications for the study of galactic archaeology and multiple populations in globular clusters (Freeman & Bland-Hawthorn, 2002; Bastian & Lardo, 2018).

4.5 Appendix: Effects of Mass Limit on Feedback

In this appendix we explore the effects of varying the prescription for the assignment of stellar wind power, $\mathcal{L}_w$, to a star particle. All simulations presented in this section have identical conditions to those simulations outlined in columns 2-5 of Table 4.1 but are run at half the resolution ($2\Delta x$ as given in column 6 of Table 4.1).

It has been shown in the literature (e.g. Grudić & Hopkins, 2019; Smith, 2021) that prescriptions for IMF sampling in imposing feedback can have significant consequences for the key results of a given simulation, despite being a rather arbitrary prescription for physics that is sub-grid to the simulation. To provide some sense of the systematic uncertainty in our results that arises from "model variance" in our simulations, we present here a few numerical experiments covering a small range of different prescriptions for the assignment of feedback to star particles.

The first prescription we use is the same outlined in the text, with $M_{\rm cut} = 10^3\,{\rm M}_\odot$. We also

run simulations here with the same prescription except with $M_{\rm cut} = 10^2\,{\rm M}_\odot$. Finally, we include a third prescription based on the Poisson sampling method outlined in Su et al. (2018) and also used in Grudić & Hopkins (2019). This method works by sampling a number of "O-stars" from a Poisson distribution whose mean depends on the mass of the sink particle to which we are assigning feedback. Specifically, for each star particle of mass $M_{*,\rm sink}$ we sample from a Poisson distribution of mean

$$\mu = \frac{M_{*,\rm sink}}{\Delta m}\,, \tag{4.19}$$

where $\Delta m = 100\ {\rm M}_\odot$ in our method and is meant to represent the mass at which one might expect to have at least one O-star. We will refer to the number of O-stars sampled from this distribution as $N_{\rm O,sink}$. Wind luminosity is then assigned to each O-star sampled in this way as

$$\mathcal{L}_{w,{\rm O-star}} = \Delta m \Psi_w\,. \tag{4.20}$$

The total wind luminosity of a given sink particle is then $N_{\rm O,sink}\mathcal{L}_{w,{\rm O-star}}$.

This method was originally implemented in Su et al. (2018) for galaxy scale simulations where, in general, $M_{*,\rm sink} \gg \Delta m$. Because of this, it was reasonable to assign $N_{\rm O,sink}$ in an unbiased way after one sampling from a Poisson distribution as outlined above. However, in our simulations, it is quite possible that when a star particle initially forms it has $M_{*,\rm sink} \ll \Delta m$. In our scenario, when one initially samples from the Poisson distribution it is likely that zero O-stars will be assigned. Since our sinks can grow in mass, we want to allow them *eventually* to sample from the Poisson distribution again. However, if we allowed this re-sampling every time step, we would essentially be biasing the sampling process, "flipping the coin" over and over again until we got $N_{\rm O,sink} > 0$ and then halting our sampling. To mitigate this process we sample for $N_{\rm O,sink}$ once when the star particle is formed and then afterwards only every time it has doubled in mass. Another approach to make the sampling unbiased would be to sample from a Poisson distribution at every accretion of mass dm with mean $dm/\Delta m$. However, this would still preferentially produce many sink particles with $N_{\rm O,sink} = 1$ when sinks are born with mass $M_{*,\rm sink} \ll \Delta m$, as accretion should immediately stop once $N_{\rm O,sink} \geq 1$. We have avoided this method in order to minimize the number of distinct

sources.

In Figure 4.6 we show a comparison of the results using the different prescriptions described above. For each model we show the history of how some gas forms stars while other gas is expelled from the cloud. In general, the models with $M_{\rm cut} = 10^2$ M$_\odot$ have lower final ε_* than when $M_{\rm cut} = 10^3$ M$_\odot$, and result in more massive outflows earlier in the simulations. This is to be expected, since reducing $M_{\rm cut}$ to 10^2 M$_\odot$ from 10^3 M$_\odot$ effectively increases the available mass that has active winds, increasing the wind luminosity and helping to drive material out of the cloud.

Interestingly, the Poisson sampling prescription results in very similar behavior to the $M_{\rm cut} = 10^2$ M$_\odot$ simulations, with the outflow and star formation histories only differing significantly for the densest simulations/smallest clouds. From inspecting the wind luminosities and distributions in $M_{*,\rm sink}$ and $N_{\rm O,sink}$ in these simulations we have determined that this stronger outflow is due to a larger effective wind luminosity caused by more sink particles with $M_{*,\rm sink} < \Delta m$ having $N_{\rm O,sink} \geq 1$ than expected from direct sampling. This is due to the above-mentioned sampling problem that was evidently only partially mitigated in our denser simulations by the fix we applied. This could potentially be ameliorated by a stricter sampling prescription, but exploring that possibility is beyond the scope of these tests.

As a comparison for the amount of variation between models, we also show the range of SFHs of the simulations presented in the main text which differ only in the initial turbulent velocity field (but are run at higher resolution than the simulations discussed above). These ranges are shown as shaded regions in Figure 4.6. For the lowest density clouds Figure 4.6 shows that the spread in results for varying luminosity assignment choices is similar to the variation seen between models with different turbulence seeds, but this is not true in the higher density simulations. For this reason, the prescription for assigning feedback to sink particles remains an important factor to consider when investigating star-forming cloud simulations.

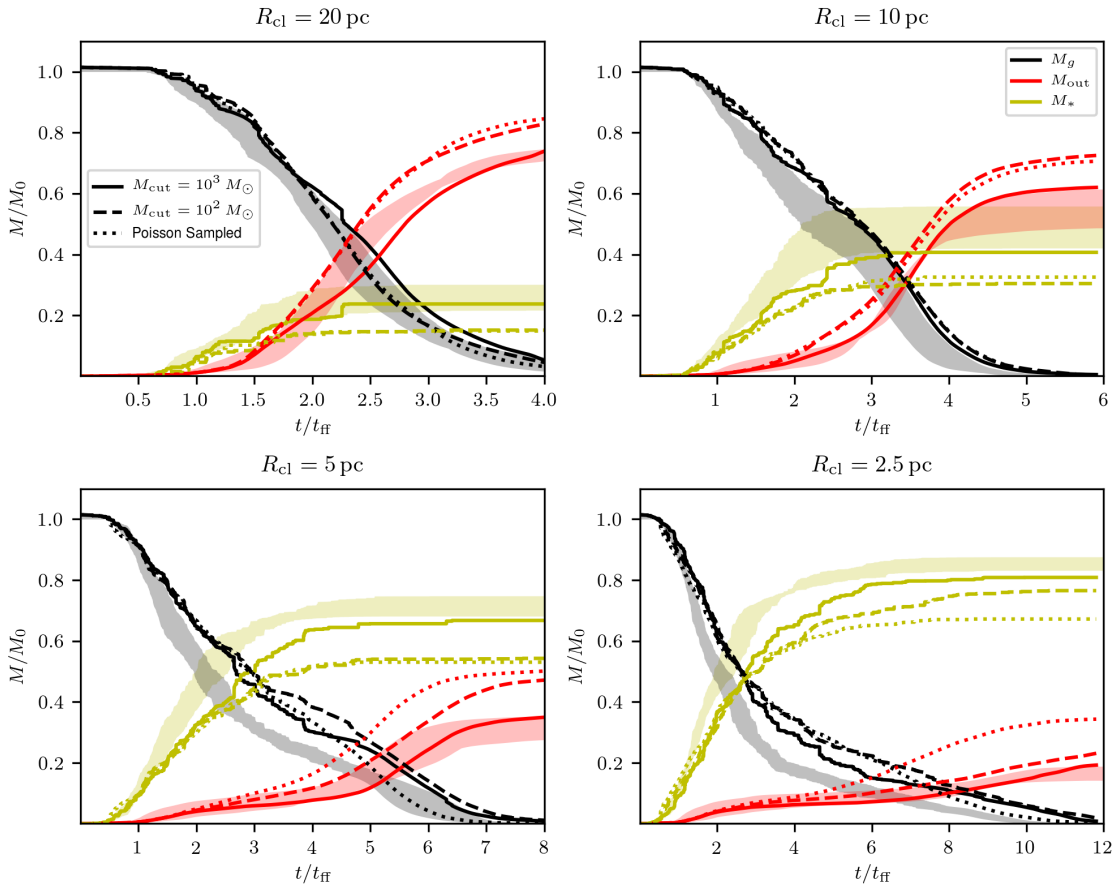

Figure 4.6 A comparison of results from different methods of assigning wind luminosity to star particles. Line style denotes the assignment method (see text). For each model, we show mass of gas on the grid (black), mass of stars (yellow), and mass that has flowed out of the simulation domain (red). The shaded regions show the range of histories given by the higher resolution simulations described in the main body of the text, which differ from one another only in the random phases used to generate the initial turbulent velocity field.

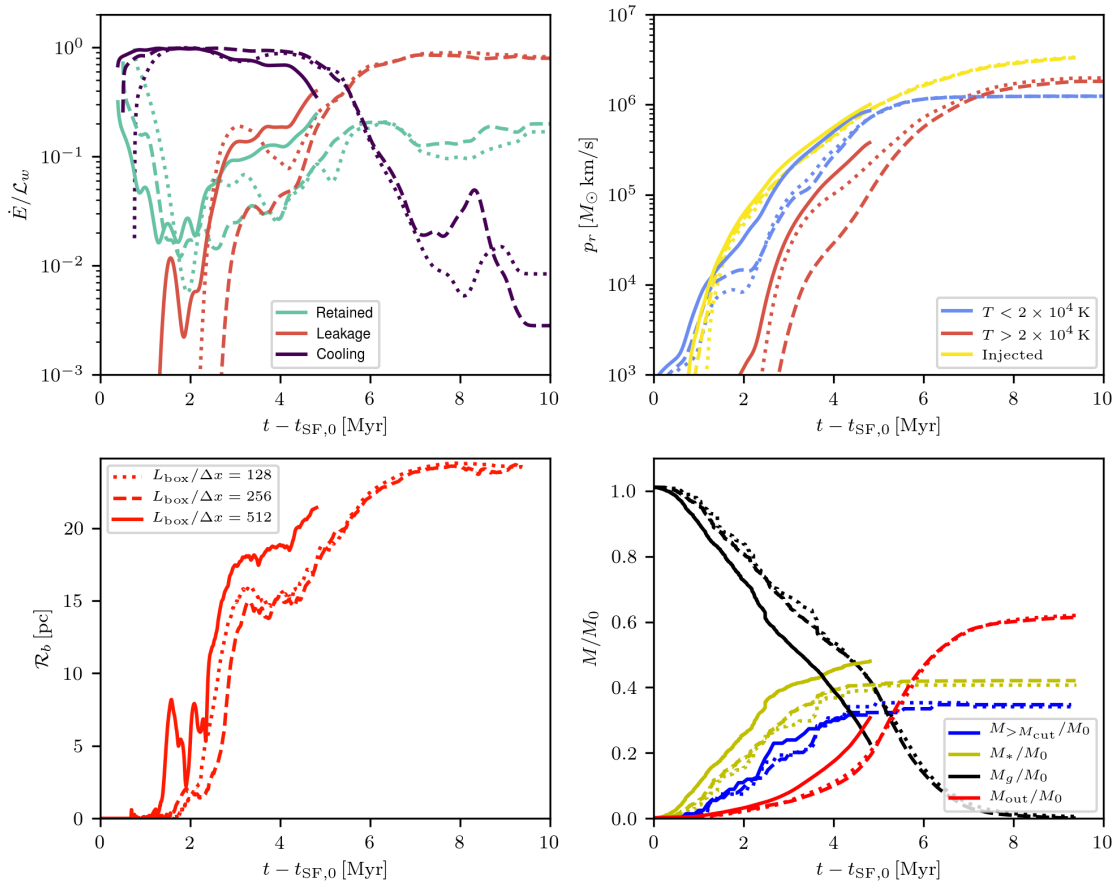

Figure 4.7 A resolution study of key history parameters for model **R10**. The line style denotes results from simulations with low resolution (dotted), fiducial resolution (dashed), and high resolution (solid). *Upper left*: wind energy losses and retained fraction (see labels), as in left column of Figure 4.2. *Upper right*: radial momentum carried in cool/warm gas and hot gas, along with the net momentum injected by the wind, as in middle column of Figure 4.2. *Lower left*: effective radius of the wind driven bubble, as in the right column of Figure 4.2. *Lower right*: mass history, showing total gas mass on the grid, gas advected out of the domain, and stellar mass, as in Figure 4.6. Also shown is the mass of stars above $M_{\rm cut} = 10^3$ $M_\odot$, which produces winds.

Table 4.2. $M_{\rm cut}$ parameter exploration.

Cloud Radius [pc]	$L_{\rm box}/\Delta x$	$M_{\rm cut}$ [$\rm M_\odot$]	$f_{>M_{\rm cut},{\rm final}}$ [a]
20	128	10^2	1.0
20	128	10^3	0.76
20	256	10^3	0.78
10	128	10^2	0.99
10	128	10^3	0.86
10	256	10^3	0.82
5	128	10^2	0.98
5	128	10^3	0.99
5	256	10^3	0.94
2.5	128	10^2	0.99
2.5	128	10^3	0.99
2.5	256	10^3	0.98

[a]Fraction of stellar mass above $M_{\rm cut}$ at the end of the simulation.

4.6 Appendix: Resolution Study

Here, we provide a resolution study of our simulations for the **R10** cloud model. The simulations presented here use a single set of random phases to initialize the turbulent velocity spectrum and all of the same numerical techniques as described in Section 4.2. Here we use the same prescription for assigning wind feedback to sink particles as described in the text, with $M_{\rm cut} = 10^3$ $\rm M_\odot$. All simulations have the same parameters as outlined in row 2 and columns 2-5 of Table 4.1. The only parameter varied is the spatial resolution, Δx, given in column 6 of Table 4.1. Specifically, we perform a simulation at half the nominal resolution given in Table 4.1 and a simulation at twice the nominal resolution, but for about half of the full simulation time due to computational cost.

Figure 4.7 presents evolution of several key quantities across the different resolutions. One quantity which we have not shown elsewhere is $M_{>M_{\rm cut}}$ which we define as the total mass of star particles that are more massive than $M_{\rm cut}$, the threshold used to determine whether or not a star particle has a wind. The total stellar mass and Ψ_w determine the total wind luminosity (modulo

the effects of independently aging star particles, which causes Ψ_w to vary mildly from source to source).

The simulations run at low and fiducial resolution (dotted and dashed lines) are quite similar: they have comparable energy loss histories and corresponding radial momentum ($t_{\rm pr}$) and breakout ($t_{\rm br}$) times, the evolution of their bubble sizes track one another, and their star formation histories are nearly identical. However, there is a very slight increase in the total stellar mass formed going from the low to the fiducial resolution. For the high resolution model, this trend continues and is greater in magnitude, with both a higher star formation rate and higher lifetime SFE than in the fiducial and low-resolution models. In contrast, the histories of the mass in particles that produce winds, $M_{>M_{\rm cut}}$ (blue lines in bottom right panel), is very similar across all resolutions. This is also mirrored by the similarity in the equivalent injected total wind momentum (yellow lines in upper right panel of Figure 4.7).

The differences/similarities in M_* vs. $M_{>M_{\rm cut}}$ histories reflect both the reduction in the mean initial sink particle mass at higher resolution, based on the particle creation criteria (see also Grudić et al. (2021) or Haugbølle et al. (2018) for a similar effect), and the prescription for assigning winds to sink particles. This comparison also provides additional evidence of the importance of feedback to limiting star formation. In the highest resolution simulations, many low-mass sink particles form that never grow sufficiently to have winds associated with them, and therefore do not help to disperse high-density collapsing structures or lower-density surrounding material. Rather, star formation continues until the mass in particles that *do* have winds is sufficient to remove the remaining cloud material. For the fiducial and low-resolution models, at late stages only $\sim 15-20\%$ of the stellar mass is in sink particles that do not provide feedback, but this increases to $\sim 30\%$ in the high-resolution model. This high-resolution model is therefore significantly "underpowered" relative to what it should be for a fully sampled IMF, accounting for its enhanced SFE.

We note that the highest resolution simulation transitions more quickly to the "breakout" phase than the fiducial and low-resolution models, based on the earlier dominance of leakage losses over cooling losses in the upper left panel of Figure 4.7. This could be due to some combination of the higher-resolution model having less ambient gas due to more total star formation (lower-right

of Figure 4.7) or higher contrasts in the density at high resolution, which increases porosity. The more rapid transition to breakout is also reflected in the more rapid growth of $\mathcal{R}_b$ for the highest resolution model (lower-left panel of Figure 4.7).

The differences in results as a function of resolution appear to arise from imposition of a mass cut that is far above the minimum sink mass at high resolution, so that many low mass sinks are "left behind" and never accrete enough ambient gas to reach $M_{\rm cut}$ and generate winds. In contrast, for the fiducial and low resolution models, inspection of late-time mass functions show that almost all particles have grown enough to host winds, consistent with the original design of our wind assignment prescription employing $M_{\rm cut}$. In future work, it will clearly be important to design a wind-assignment prescription that is more robust to changes in the sink mass function with resolution, while still having an astronomically realistic and numerically practical number of feedback sources. One way to do this is by directly sampling from a mass function to assign individual massive stars (with associated feedback) to the sink particles (e.g. Sormani et al., 2017).

Chapter 5

The Effects of Magnetic Fields and H II Regions on the Dynamics of Wind-Driven Bubbles

5.1 Introduction

In this chapter we discuss and present the final, as yet unpublished, work of this dissertation. In particular, we investigate how the theory of stellar wind-driven bubbles developed in Chapter 2 and verified in Chapter 3 can be modified when we consider the wind bubble expanding in to a magnetized medium and/or a medium that has been photo-ionized and heated. Both of these phenomena have the potential to change the physical picture and are both bound to be present in realistic star forming regions (Krumholz et al., 2019). In this Chapter we first briefly review, in Section 5.3, the theories for wind-driven bubbles presented in Chapter 2, meanwhile clarifying the conditions necessary for a Efficiently Cooled 'EC' wind-driven bubble solution to apply. We then develop a simplified model for the joint evolution of a wind-driven bubble and a surrounding H II region in Section 5.3.3 with many more details on the assumptions behind this model, and their

validity, provided in the appendices of this Chapter. Next, in Section 5.4, we describe the simulations we have run in order to test the changes to the EC bubble solution in the presence of H II regions and background magnetic fields. In Section 5.5 we present the results of these simulations and analyze several physical aspects of their solutions, comparing them to our developed theory where appropriate. As the reader will see, the developed theory is somewhat less satisfactory in providing a detailed description of our simulations with added physics than in the purely hydrodynamical work of Chapter 2 and Chapter 3. In Section 5.6 we discuss why this may be the case and what new theoretical developments will be needed to ameliorate this situation.

5.2 Definitions

In this section we briefly review some definitions of various quantities that we use throughout the remainder of the paper. In this work we are imagining the action of a central source of mechanical energy and ionizing radiation on the medium that surrounds the source. We refer to the high-pressure bubble that results from this injection of energy as a 'feedback bubble,' which, in this treatment, consists of the wind-driven bubble and the H II region. While our typical application considers this source to be a single O/B star or a star cluster consisting of several such stars, much of this formalism could be moderately modified to apply to the expansion of bubbles due to the winds of Active Galactic Nuclei (AGN) (Faucher-Giguère & Quataert, 2012) or of several sequential supernovae (SNe) (Mac Low & McCray, 1988; Kim et al., 2017a; El-Badry et al., 2019).

We characterize the background medium into which the source emits energy principally by its mean background mass density, $\bar{\rho}$. The mean number density of hydrogen ions is then given by $\overline{n}_{\rm H} \equiv \bar{\rho}/\mu_{\rm H} m_{\rm H}$ where $\mu_{\rm H}$ is the mean atomic weight per hydrogen nucleus and $m_{\rm H}$ is the mass of a proton. The central source emits a wind with constant (in time) velocity $\mathcal{V}_w$ and mass loss rate $\dot{M}_w$ into this background. Such a wind would have a mechanical luminosity $\mathcal{L}_w = \dot{M}_w \mathcal{V}_w^2/2$ and a momentum input rate $\dot{p}_w = \dot{M}_w \mathcal{V}_w$. This source can also emit ionizing radiation with an ionizing photon emission rate, Q_0, and average energy per ionizing photon of $h\nu_i$.

We will be interested in several summary physical quantities of the wind-driven bubble's evolu-

tion, such as its size, the momentum that it carries, and the energy (in various forms) or pressure of different phases of the gas. We wish to distinguish between the various idealized solutions discussed below and the 'true' evolution of these physical quantities (as measured in simulations or discussed in relation to the idealized theory). To this end we note that all variables representing the evolution of a physical quantity according to some idealized theory will be accompanied by appropriate capitalized, Roman-script subscripts. For example, the total momentum carried by the feedback bubble in the Weaver et al. (1977) solution shall be denoted, p_{W}. Unless otherwise noted, this always refers to *radial* momentum measured with respect to the source.

We would generally like to characterize a bubble's size by it's radius, however, for non-spherically symmetric solutions this is a poorly defined quantity. To circumvent this we define the 'effective' or 'volume-equivalent' radius, $\mathcal{R}$ associated with some volume V as

$$\mathcal{R} = \left(\frac{3V}{4\pi}\right)^{1/3}, \tag{5.1}$$

equivalent to the definitions given in Chapter 2 and Chapter 3. This will be applied throughout the text to refer to the radius of different regions.

5.3 Theory

5.3.1 Stellar Wind Bubbles

In this section we review the theory of the expansion of stellar wind bubbles. First, we present the classical 'energy-driven' solution for the expansion. Next we review the theory of Chapter 2 while clarifying the conditions necessary for such a wind-driven bubble solution to apply.

Classical Stellar Wind Bubble

We first consider the expansion of the wind bubble from such a source in to a perfectly uniform density medium, so that the mass density of the surrounding gas ρ is equal to $\bar{\rho}$ everywhere. The evolution of such a bubble has four distinct stages in time (as first investigated by, e.g. Avedisova,

1972; Falle, 1975; Steigman et al., 1975; Castor et al., 1975; Weaver et al., 1977). These stages are (1) free expansion, (2) adiabatic pressure-driving, (3) post-shell-formation pressure-driving, and (4) critically-cooling. For parameters ($\dot{M}_w$, $\mathcal{V}_w$, and $\bar{\rho}$) relevant for massive stars in a typical giant molecular cloud (GMC) stages (1) and (2) are generally short-lived ($\sim 5\,\mathrm{yr}$ and $\sim 10^3\,\mathrm{yr}$ respectively) and stage (4) usually only occurs after the death of the source star ($\sim 10^7\,\mathrm{yr}$ see Weaver et al., 1977), making stage (3) the most relevant for the overall evolution (see Section 5.7 for further discussion).

In stage (3) the wind bubble's radius, assumed to be the same as the radius of the thin shell of dense gas that is swept-up by the bubble, is given by

$$R_{\mathrm{W}}(t) = \left(\frac{125}{154\pi}\frac{\mathcal{L}_w t^3}{\bar{\rho}}\right)^{1/5} , \tag{5.2}$$

the pressure of the hot, shocked wind gas that drives the expansion is given by

$$P_{\mathrm{W}}(t) = \frac{5}{22\pi}\left(\frac{125}{154\pi}\right)^{-3/5}\left(\frac{\mathcal{L}_w^2\bar{\rho}^3}{t^4}\right)^{1/5} , \tag{5.3}$$

and the total radial momentum (almost entirely carried in the shell) is given by

$$p_{\mathrm{W}}(t) = \frac{4\pi}{5}\left(\frac{125}{154\pi}\right)^{4/5}\left(\mathcal{L}_w^4\bar{\rho}t^7\right)^{1/5} . \tag{5.4}$$

Including additional physics in the solution outlined above can change the structure and evolution of the bubble in several different ways. For example, Weaver et al. (1977) themselves argue that thermal conduction at the wind bubble interface leads to an evaporative mass flow from the 'contact discontinuity' at the boundary between the wind bubble and the shell. In the treatment of Weaver et al. (1977), this mass quickly becomes dominant over the mass injected by the wind, changing the temperature and density structure of the bubble. In certain regimes, this change in the bubble temperature and density can lead to the interior becoming radiative, causing a momentum-driven ($p_r \propto t$) evolution (Weaver et al., 1977; Silich & Tenorio-Tagle, 2013; Mac Low & McCray, 1988).

At the same time, the truly three-dimensional (3D) nature of any real wind-driven bubble means

that the interface between the wind and the shell is subject to an array of 3D instabilities (Vishniac, 1983, 1994; Vishniac & Ryu, 1989; Garcia-Segura et al., 1996a; Folini & Walder, 2006; Ntormousi et al., 2011; Pittard, 2013; Badjin et al., 2016). These instabilities not only change the spatial structure of the wind bubble interface but can also lead to mixing of the wind material with the ambient gas, which can be followed by subsequent cooling (McKee et al., 1984; Nakamura et al., 2006; Rosen et al., 2014). In the next section, we present our theory for how this sort of mixing can lead to drastic differences in the evolution of the wind-driven bubble.

The Efficiently Cooled Stellar Wind

In Chapter 2 we described a theory for how the energy-driven picture of Weaver et al. (1977) is altered when considering a wind bubble's expansion in to a medium with density inhomogeneities. In our picture, this background density structure leads to mixing at the interface between the wind-driven bubble and the surrounding medium, creating intermediate temperature ($T \sim 10^4\,\mathrm{K}$) gas that can cool efficiently. In particular, we noted that the amount of such cooling can be drastically enhanced by the 3D fractal structure of the interface, created through the mixing as well as the background density fluctuations themselves. The basic proposition of this work was that this interface cooling is severe enough to cause the bubble evolution to follow a momentum-driven solution rather than an energy-driven solution, as in the previous section.

In Chapter 2 we posited that the momentum carried by the bubble, p_r followed

$$p_r(t) = \alpha_p \dot{p}_w t \equiv \alpha_p p_{\mathrm{EC}}(t)\,, \tag{5.5}$$

where $p_{\mathrm{EC}}(t)$ is the idealized 'efficiently cooled' solution and α_p is the momentum enhancement factor, quantifying the amount by which the wind bubble carries momentum beyond the momentum input directly by the wind. If we allow α_p to vary arbitrarily, we can think of Equation 5.5 as a generic relationship between the 'true' evolution of the momentum and the efficiently cooled solution. For example, α_p would then have some time-dependent value if $p_r = p_{\mathrm{W}}(t)$. While it can be useful to think of α_p this way for the purposes of understanding the behaviour of the solution,

for the remainder of this section we will assume that α_p is approximately constant in time. As we will see in Section 5.5 (and previously shown in Chapter 3), this is a good assumption.

Under the additional assumptions of the statistical homogeneity and isotropy of the background medium, one can show that the evolution of the wind bubble's effective radius follows

$$\mathcal{R}_w(t) = \left(\frac{3\alpha_R \alpha_p}{2\pi} \frac{\dot{p}_w t^2}{\bar{\rho}} \right)^{1/4} \equiv (\alpha_R \alpha_p)^{1/4} \, R_{\rm EC}(t) \tag{5.6}$$

where α_R is assumed to be a constant which quantifies the deviations from statistical isotropy/homogeneity, and $R_{\rm EC}(t)$ is the idealized radial evolution of the wind bubble when $\alpha_p = \alpha_R = 1$.

In both the Weaver et al. (1977) and the momentum-driven solutions the thermal pressure in the hot, shocked wind (assumed to be isobaric) is given by the post-shock value, $P_w = 3\dot{p}_w/(16\pi\mathcal{R}_f^2)$, where $\mathcal{R}_f$ is the effective radius of the free-wind region. As discussed in the Appendix of Chapter 2, one can show that the relative volume of the free and post-shock wind is related to the momentum enhancement factor, α_p, as

$$\alpha_p = \frac{1}{4} \left[3 \left(\frac{\mathcal{R}_w}{\mathcal{R}_f} \right)^2 + \left(\frac{\mathcal{R}_w}{\mathcal{R}_f} \right)^{-2} \right] . \tag{5.7}$$

The above is again generally true for both solutions which each have very different behaviors for $\mathcal{R}_w/\mathcal{R}_f$. We can see from Equation 5.7 that in the limit that $\alpha_p \to 1$ we have $\mathcal{R}_f \to \mathcal{R}_w$ and thus that, in the idealized 'efficiently cooled' solution the entire bubble is made up of the free wind region. With this relation in mind we can then write down the hot, shocked wind pressure as

$$P_w = \frac{\beta_P}{\sqrt{\alpha_p \alpha_R}} P_{\rm EC} \, , \tag{5.8}$$

where

$$\beta_P \equiv \frac{2}{3}\alpha_p + \sqrt{\left(\frac{2}{3}\alpha_p \right)^2 - \frac{1}{3}} \tag{5.9}$$

is a function of α_p and

$$P_{\rm EC}(t) \equiv \frac{3\dot{p}_w}{16\pi R_{\rm EC}^2} \tag{5.10}$$

is the formal pressure of the hot, shocked wind in the idealized 'efficiently cooled' solution. Equation 5.10 is essentially a definition of a convenient variable since the hot shocked wind doesn't formally exist in the idealized EC solution. It is also convenient to note that $\beta_P \approx (3\alpha_p - 1)/2$ for $1 \leq \alpha_p \leq 4$.

Conditions for Momentum-Driven Solution

In Chapter 2 we presented various conditions under which a momentum-driven solution might apply. We would like to revisit and clarify those conditions here. Taking Equation 5.5 on its face, a momentum-driven solution applies whenever α_p is approximately constant. With the further context of Equation 5.7, we can say that a momentum-driven solution applies whenever the ratio $\mathcal{R}_w/\mathcal{R}_f$ is constant in time. Which leads us to ask, how might this occur?

In the spherical solution of Weaver et al. (1977) the ratio $\mathcal{R}_w/\mathcal{R}_f$ is essentially set by requiring that the radial velocity of the shocked wind matches the expansion velocity of the bubble at the bubble's edge. However, in the context of the inhomogeneous medium that the theory of Section 5.3.1 is meant to describe, the velocity in the shocked medium need not directly match the expansion velocity of the outer edge of the bubble. Indeed, in this theory the velocity in the shocked medium is not purely radial but has turbulent components. This leads us to seek a different boundary condition.

In Chapter 2 we compared the flux of energy arriving at the wind bubble's edge, Φ_w, to the effective flux of energy that is able to be cooled away by turbulent mixing, $\Phi_{\rm cool}$. We wrote $\Phi_w = 5P_w v_{\rm ps}(\mathcal{R}_w)/2$, where $v_{\rm ps}(\mathcal{R}_w)$ is the effective radial velocity of the shocked wind gas at the bubble radius, and evaluated $\Phi_{\rm cool}$ in the context of the turbulent radiative mixing layer (TRML) theory of Fielding et al. (2020) as

$$\Phi_{\rm cool} \approx \frac{5}{2} P_w v_t(L) \left[\frac{v_t(L) t_{\rm cool}}{L}\right]^{\frac{p-d}{1-p}} \left(\frac{\mathcal{R}_w}{L}\right)^d . \tag{5.11}$$

In the above, $v_t(L)$ denotes the scale of the turbulent velocity at some large, energy-containing scale L, below which the turbulent velocity field follows a structure function $v_t(\ell) \propto \ell^p$, $t_{\rm cool}$ is the

cooling time of the gas that cools most rapidly in the TRML, and d is the excess fractal dimension of the mixing surface. As noted in Fielding et al. (2020), Equation 5.11 is uncertain up to an order unity geometric factor. Let us call this geometric factor, α_C and define

$$\Phi_{\rm cool} \equiv \frac{5}{2} P_w v_{\rm eff} \tag{5.12}$$

with

$$v_{\rm eff} = \alpha_C v_t(L) \left[\frac{v_t(L) t_{\rm cool}}{L} \right]^{\frac{p-d}{1-p}} \left(\frac{\mathcal{R}_w}{L} \right)^d , \tag{5.13}$$

as the effective mixing velocity.

In Chapter 2 we termed a wind bubble's evolution to be 'efficiently cooled' if $\Phi_w \lesssim \Phi_{\rm cool}$. In comparing our definitions from above another way to write this condition would be

$$v_{\rm ps}(\mathcal{R}_w) \lesssim v_{\rm eff} \, . \tag{5.14}$$

In other words, the velocity at which gas is being provided to the TRML is less than its effective velocity to be mixed and cooled away.

In Chapter 3 we found that for $p = 1/3$, $d = 1/2$, and $\alpha_C = 1/4$ we had $v_{\rm ps}(\mathcal{R}_w) \approx v_{\rm eff}$ in our simulations. This suggests that this condition is not an inequality but an equality: the velocity at which gas is being provided to the TRML is equal to the effective velocity at which it can be mixed and cooled away. This gives us a new boundary condition on the velocity in the shocked wind gas. Following the assumptions of the Appendix of Chapter 2 we can write the radial velocity of the shocked wind gas as a function of radius as

$$v_{\rm ps}(r) = \frac{\mathcal{V}_w}{4} \left(\frac{r}{\mathcal{R}_f} \right)^{-2} . \tag{5.15}$$

with our new boundary condition, $v_{\rm ps}(\mathcal{R}_w) = v_{\rm eff}$ this gives us

$$\left(\frac{\mathcal{R}_w}{\mathcal{R}_f} \right)^2 = \frac{\mathcal{V}_w}{4 v_{\rm eff}} \, . \tag{5.16}$$

Applying this condition to Equation 5.7 we have the momentum enhancement factor as

$$\alpha_p = \frac{1}{4}\left[\frac{3\mathcal{V}_w}{4v_{\rm eff}} + \frac{4v_{\rm eff}}{\mathcal{V}_w}\right] . \tag{5.17}$$

So we see that, in this scenario, α_p is directly tied to the degree of mixing in the TRML. In particular, we have a momentum-driven solution ($\alpha_p \approx$ const.) exactly when $v_{\rm eff}$ is constant in time. In this way, $v_{\rm eff}$ becomes the one free parameter of this theory.

5.3.2 Spitzer Solution for an H II Region's Expansion

Here we briefly review the theory of expansion of H II regions. We imagine a uniform medium of density $\bar{\rho}$ at the center of which a source of isotropically radiated ionizing photons begins emitting at $t = 0$ with a rate Q_0. The mean energy of the ionizing photons is $h\nu_i$. At first, there is an R-type, supersonic expansion of the ionized region (Draine, 2011a), until the Strömgren radius, $R_{\rm St}$, is reached. The Strömgren radius is defined as (Strömgren, 1939)

$$R_{\rm St} = \left(\frac{3Q_0}{4\pi\alpha_B \overline{n}_{\rm H}^2}\right)^{1/3} , \tag{5.18}$$

with $\overline{n}_{\rm H}$ the mean number density of Hydrogen nuclei in the background medium and α_B the case B recombination rate coefficient (Draine, 2011a). The region confined by this radius is ionized on the ionization/recombination timescale $\tau_i = (\alpha_B \overline{n}_{\rm H})^{-1}$, typically on the order of $\sim 10^3$ yr for conditions typical of a GMC. Since this timescale is short compared with the time-scale for the evolution of the feedback bubble overall, it is generally assumed that the H II region's evolution begins at this point at $t = 0$.

The subsequent evolution is determined by assuming that all gas within the H II region is maintained in ionization/recombination equilibrium. That is, for an H II region with radius $\mathcal{R}_i$ and density of hydrogen nuclei $n_{{\rm H},i}$ we have

$$\frac{4\pi}{3}\mathcal{R}_i^3 \alpha_B n_{{\rm H},i}^2 = Q_0 . \tag{5.19}$$

We then write down a momentum equation for the evolution of the bubble as

$$\frac{d}{dt}\left(M_{\rm sh}\frac{d\mathcal{R}_i}{dt}\right) = 4\pi\mathcal{R}_i^2 P_{\rm II}\,, \tag{5.20}$$

where $M_{\rm sh}$ is the mass of the shell of shocked ambient material carried by the H II region and $P_{\rm II} = \rho_i c_i^2$ is the thermal pressure of the H II region (where ρ_i is the density and c_i is the isothermal sound speed, assumed to be constant). It is then typically assumed that $M_{\rm sh} = 4\pi\mathcal{R}_i^3\bar{\rho}/3$, that is, that all gas that used to be contained within the bubble's radius is now in the shell. This is completely wrong at the time that the Strömgren sphere is first developed since at this point there is no shell. This will be a bad assumption at early times but more correct once the H II region has begun to expand, we will return to this below. With $M_{\rm sh} = 4\pi\mathcal{R}_i^3\bar{\rho}/3$, we then use Equation 5.19 to replace the pressure in the H II region, resulting in the overall momentum equation

$$\frac{d}{dt}\left(\frac{\mathcal{R}_i^3}{3}\frac{d\mathcal{R}_i}{dt}\right) = c_i^2\mathcal{R}_i^2\left(\frac{R_{\rm St}}{\mathcal{R}_i}\right)^{3/2}\,. \tag{5.21}$$

Solving this ODE using the ansatz $\mathcal{R}_i(t) = R_{\rm St}\left(1+at\right)^b$ for some, constants a and b gives us the Spitzer (1978) solution

$$R_{\rm Sp}(t) = R_{\rm St}\left(1+\frac{7}{2\sqrt{3}}\frac{c_i t}{R_{\rm St}}\right)^{4/7}\,. \tag{5.22}$$

The numerical coefficient on t above differs by a constant factor from the original Spitzer (1978) solution. The above version, due to Hosokawa & Inutsuka (2006), was found to better match the evolution of $\mathcal{R}_i$ in one-dimensional simulations.

In using the above solution to infer the momentum imparted to the ambient medium it is natural to take $p_r = M_{\rm sh}dR_{\rm Sp}/dt$, as we assumed in writing Equation 5.20. As we mentioned above, taking $M_{\rm sh} = 4\pi\mathcal{R}_i^3\bar{\rho}/3$ is very wrong at early times ($t < t_{{\rm d},i}$, the sound-crossing time) since the H II region has not begun to expand yet. Using this assumption anyway we would get

$$p_{r,{\rm Sp}}(t) = \frac{8\pi}{3\sqrt{3}}\bar{\rho}c_i R_{\rm St}^3\left(1+\frac{7}{2\sqrt{3}}\frac{c_i t}{R_{\rm St}}\right)^{9/7}\,. \tag{5.23}$$

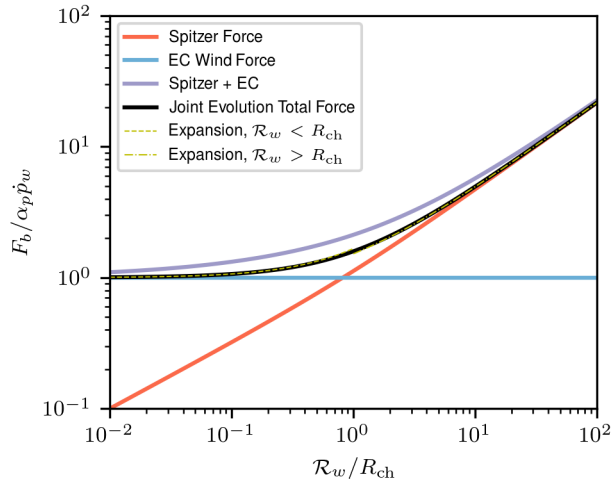

Figure 5.1 Similar to Figure 3 of Kim et al. (2016), we present the force exerted by the bubble in our joint evolution model as a function of $\mathcal{R}_w/R_{\rm ch}$. In black we show the actual force exerted in the joint evolution model of Section 5.3.3, given by the right hand side (RHS) of Equation 5.25. We show approximations to this equation for $\mathcal{R}_w > R_{\rm ch}$ (Equation 5.32) and $\mathcal{R}_w < R_{\rm ch}$ (Equation 5.31). In blue we show the force exerted by an efficiently cooled wind, $\alpha_p \dot{p}_w$, in red we show the force in the Spitzer solution (RHS of Equation 5.20), we show the sum of these in purple.

Setting $t = 0$ in the above we see that the momentum is finite at the beginning of the evolution of the bubble, which is clearly not physical. This assumption will be particularly bad for large H II regions, (essentially large Q_0), where the time during which the Spitzer solution would apply accurately before the bubble broke out of its nascent cloud would be small. A simple adjustment to this momentum inference is to use the shell mass $M_{\rm sh} = 4\pi\mathcal{R}_i^3(\bar{\rho} - \rho_i)/3$, that is subtract out the mass that is in the H II region's interior. Though this deduction is not consistent with the derivation of Equation 5.20, we will see that it can be more accurate. This assumption gives us the adjusted inferred momentum

$$p_{r,\rm Sp,adj}(t) = p_{r,\rm Sp}(t)\left(1 - \left(\frac{R_{\rm St}}{R_{\rm Sp}}\right)^{3/2}\right), \tag{5.24}$$

which indeed is zero at $t = 0$. A similar criteria for the momentum, which does not account for the evolution of the density within the H II region, is suggested in Pittard et al. (2022).

5.3.3 Joint Evolution of Stellar Wind Bubbles and H II Regions

In this section we seek a theory to describe the joint evolution of a stellar wind bubble and the photo-ionized H II region that always surrounds it in the case of massive O and B type stars that we consider here. As above, this discussion ignores the dynamical importance of magnetic fields. We also ignore the importance of direct radiation pressure in changing the physical structure of the H II region (Krumholz & Matzner, 2009; Draine, 2011b; Kim et al., 2016), and any external pressures or the effects of gravity on slowing the shell (Rahner et al., 2019; Geen et al., 2020).

Effective Momentum Equation

We now seek to describe the joint evolution of a wind-driven bubble and an H II region. We imagine that the wind-driven bubble has come into equilibrium with the H II region with no net momentum flux being carried across the outer edges of the wind bubble. We will assume that the wind-driven bubble's evolution is given by a momentum-driven solution, with some arbitrary, constant momentum enhancement factor, α_p, as described in Section 5.3.1. During this evolution we also assume that the H II region maintains ionization-recombination equilibrium. This joint evolution model is similar to the model presented in Section 5 of Geen et al. (2020). The time-scales over which such a state is obtained and the range of appropriate initial conditions for this state are discussed in Section 5.8.

Requiring that there is no net momentum flux across the wind boundary means that forces balance on the surface of the wind bubble. In the momentum-driven evolution the force on the wind bubble's surface is $\alpha_p \dot{p}_w$ whereas the force on the wind bubble from the H II region is $4\pi\mathcal{R}_w^2 P_{\rm II}$. Here we are including both thermal pressure and Reynolds Stress terms from the wind, but ignoring the contribution of Reynolds Stress in the H II region to this force balance. Force balance then gives $P_{\rm II} = \alpha_p \dot{p}_w / 4\pi\mathcal{R}_w^2$.

We can obtain a new momentum equation for this evolution by working from Equation 5.20 and

replacing $P_{\rm II}$ with the above. This gives us

$$\frac{d}{dt}\left(\frac{4\pi}{3}\bar{\rho}\mathcal{R}_i^3\frac{d\mathcal{R}_i}{dt}\right) = \alpha\dot{p}_w\left(\frac{\mathcal{R}_i}{\mathcal{R}_w}\right)^2 , \tag{5.25}$$

where we have again assumed $M_{\rm sh} = 4\pi\mathcal{R}_i^3\bar{\rho}/3$. In order to solve the above differential equation we must then have a relationship between $\mathcal{R}_i$ and $\mathcal{R}_w$. This relationship will come from (i) the force balance we've derived above and (ii) ionization-recombination equilibrium.

The force balance condition derived above, along with $P_{\rm II} = \rho_i c_i^2$, gives us ρ_i in terms of $\mathcal{R}_w$ as

$$\rho_i = \frac{\alpha_p\dot{p}_w}{4\pi c_i^2\mathcal{R}_w^2} . \tag{5.26}$$

In the context of the joint evolution, where all gas in the wind bubble is hot enough to be collisionally ionized, the ionization-recombination equilibrium condition is modified from Equation 5.19 to

$$\frac{4\pi}{3}\left(\mathcal{R}_i^3 - \mathcal{R}_w^3\right)\alpha_B n_{{\rm H},i}^2 = Q_0 . \tag{5.27}$$

which we can re-write as

$$\rho_i = \mu_{\rm H} m_{\rm H}\left(\frac{3Q_0}{4\pi\alpha_B(\mathcal{R}_i^3 - \mathcal{R}_w^3)}\right)^{1/2} , \tag{5.28}$$

where $m_{\rm H}$ is the mass of the Hydrogen nucleus and $\mu_{\rm H}$ is the mean atomic weight per hydrogen nucleus.

Equating Equation 5.26 and Equation 5.28 we have a relationship for $\mathcal{R}_i$ in terms of $\mathcal{R}_w$ as

$$\mathcal{R}_i = \mathcal{R}_w\left(1 + \frac{\mathcal{R}_w}{R_{\rm ch}}\right)^{1/3} , \tag{5.29}$$

where

$$R_{\rm ch} \equiv \frac{\alpha_B}{12\pi(\mu_{\rm H} m_{\rm H} c_i^2)^2}\frac{\dot{p}_w^2\alpha_p^2}{Q_0} \tag{5.30}$$

is the characteristic radius at which the force exerted by an efficiently-cooled wind bubble is equal to the thermal pressure force exerted by an H II region (Lancaster et al., 2021b; Krumholz & Matzner,

2009; Kim et al., 2016).

Together, Equation 5.25 and Equation 5.29 constitute an ordinary differential equation (ODE) in one variable, either $\mathcal{R}_i$ or $\mathcal{R}_w$. Using these above relations, in the limit that $(\mathcal{R}_w/\mathcal{R}_i)^3 \ll 1$ (the wind bubble doesn't disturb the evolution too much) we can write the force exerted by the bubble, F_b, also given by the right hand side of Equation 5.25 as

$$F_b \approx F_{b,\mathrm{Sp}} + \frac{\alpha_p \dot{p}_w}{2} \frac{\mathcal{R}_w}{\mathcal{R}_i} \tag{5.31}$$

where $F_{b,\mathrm{Sp}}$ is the force exerted in the Spitzer (1978) solution. Similarly, in the opposite limit, which we could characterize as $\mathcal{R}_w \ll R_{\mathrm{ch}}$, we have

$$F_b \approx \alpha_p \dot{p}_w \left(1 + \frac{2}{3} \frac{\mathcal{R}_w}{R_{\mathrm{ch}}}\right) \tag{5.32}$$

so that the momentum input is just slightly above the momentum-driven solution. In Figure 5.1 we graphically compare these different approximations to the total force along with the force exerted in the Spitzer and EC wind solutions. We see that the simple approximation $F_b = \alpha_p \dot{p}_w + F_{b,\mathrm{Sp}}$ tends to slightly over-estimate the actual force exerted.

We could use Equation 5.29 to explicitly substitute out $\mathcal{R}_w$ for $\mathcal{R}_i$ or vice versa but the chances of finding an analytic solution do not seem particularly good. So we will proceed by numerical integration. In either case, we will need initial conditions. In Section 5.9 we discuss various assumptions for the initial conditions and eventually choose two different ICs based on their success in recovering separate characteristics of our simulations, described below.

5.4 Simulations

In order to confront the various theoretical interpretations and predictions laid out in Section 5.3, we run a suite of numerical simulations of wind-driven bubbles both wind and without background magnetic fields and additional radiative feedback. We run our simulations with the magneto-hydrodynamics (MHD) code *Athena* (Stone et al., 2008) supplemented with several additional

Table 5.1. Parameters of simulation suite.

Name	Dynamics	Wind On	Radiation On
`Hydro`	HD	✓	X
`Hydro Rad`	HD	✓	✓
`Hydro Rad Only`	HD	X	✓
`MHD`	MHD	✓	X
`MHD Rad`	MHD	✓	✓
`MHD Rad Only`	MHD	X	✓

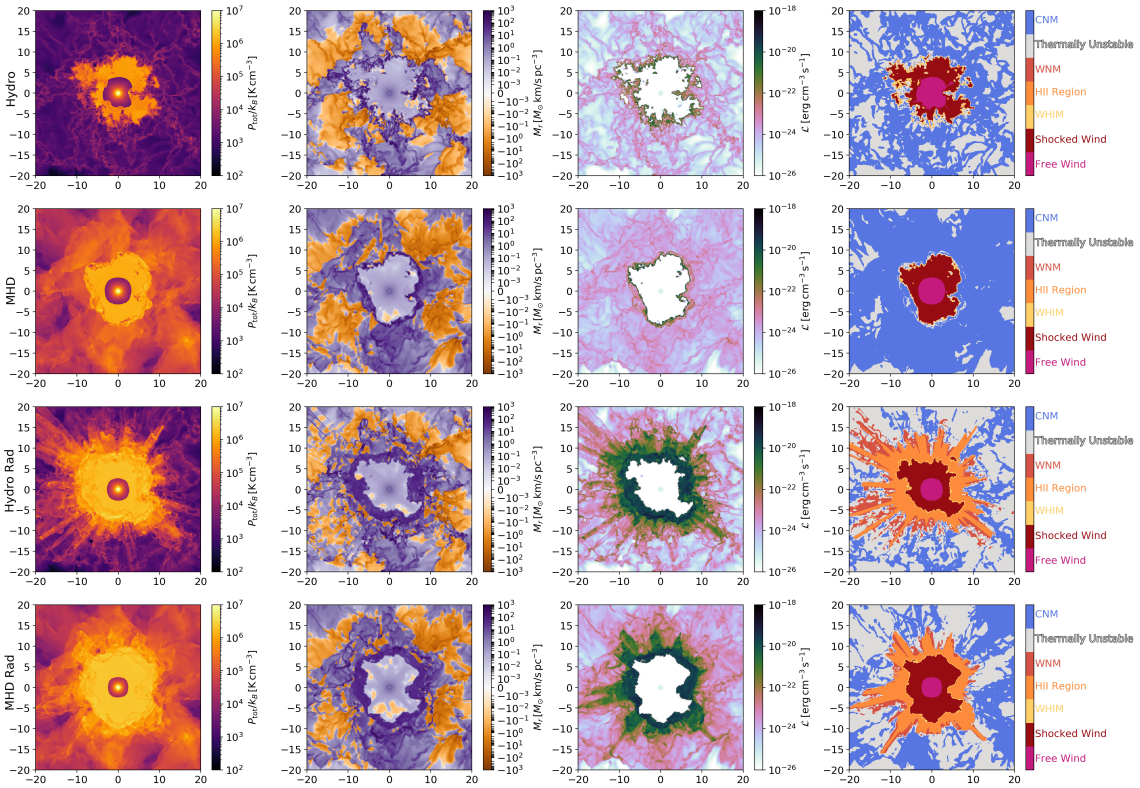

Figure 5.2 We show slices through the $z = 0$ plane of our high resolution simulations, with $L_{\rm box}/\Delta x = 512$ at approximately the time when $\mathcal{R}_w = L_{\rm box}/6$. The rows give snapshots from each of four simulations, from top to bottom these are: `Hydro`, `MHD`, `Hydro Rad`, and `MHD Rad`. The columns show slices of different physical quantities, from left to right these are: (i) total pressure, including thermal and magnetic terms as appropriate, (ii) radial momentum of the gas, (iii) the total volumetric radiative cooling, and (iv) a schematic that separates the slice into different phases, indicated by color.

Table 5.2. Definitions of gas phases.

Phase	Temperature Condition	Velocity Condition	x_e Condition
Free Stellar Wind	$T > 10^6\,\mathrm{K}$	$v_r > \mathcal{V}_w/2$	
Shocked Stellar Wind	$T > 10^6\,\mathrm{K}$	$v_r < \mathcal{V}_w/2$	
WHIM	$10^4\,\mathrm{K} < T < 10^6\,\mathrm{K}$		
H II Region	$6085\,\mathrm{K} < T < 10^4\,\mathrm{K}$		$x_e > 0.9$
Warm Neutral Gas	$6085\,\mathrm{K} < T < 10^4\,\mathrm{K}$		$x_e < 0.9$
Thermally Unstable Gas	$181\,\mathrm{K} < T < 6085\,\mathrm{K}$		
Cold Neutral & Molecular Gas	$T < 181\,\mathrm{K}$		

Note. — Names assigned to gas phases based on temperature, velocity, and x_e conditions

physics that are part of the *Athena*-TIGRESS code base (Kim & Ostriker, 2017; Kim et al., 2020b). Our simulations are running using the linearized Roe Riemann solver (Roe, 1981) with second order, piecewise linear spatial reconstruction, and the unsplit van Leer-type integrator of Stone & Gardiner (2009). We run our simulations with outflow boundary conditions.

We include (photo-)chemistry and heating/cooling as implemented in (CITE JGK+2022). We follow the non-equilibrium abundance of hydrogen species (H, H^+, and H_2) and equilibrium abundance of carbon- and oxygen-bearing species (C, C^+, O, O^+, CO). The heating and cooling rates for cold and warm gas ($T < 2 \times 10^4\,\mathrm{K}$) are calculated using local density, temperature, species abundances, radiation energy density, and cosmic ray ionization rate. For cooling (by helium and metals) in hot gas ($T > 3.5 \times 10^4\,\mathrm{K}$), we adopt Gnat & Ferland (2012)'s ion-by-ion CIE cooling rates tabulated as a function of temperature. For cooling at intermediate temperature ($2.0 \times 10^4\,\mathrm{K} < T < 3.5 \times 10^4\,\mathrm{K}$), we make a smooth transition between non-equilibrium cooling and the CIE cooling using a sigmoid function. For physical conditions considered in our simulations, the main coolants are C^+, O, grain-assisted recombination, and Lyα in cold and warm neutral gas, forbidden line emission from metal ions in warm photoionized gas, Lyα in (non-photoionized) warm-hot gas in turbulent mixing layers, and thermal bremsstrahlung emission and line emission from metal ions in shocked hot winds.

For the background heating, we include FUV heating via the grain photoelectric effect. We assume the uniform mean intensity at FUV wavelengths with the density-dependent attenuation applied as $J_k = J_k^{\rm Draine} e^{-\tau_k}$. Here $J_k^{\rm Draine}$ is the Draine (1978)'s interstellar radiation field $J_{\rm LW} = 0.3 \times 10^{-3}\,{\rm erg\,s^{-1}\,cm^{-2}\,sr^{-1}}$ and $J_{\rm PE}^{\rm Draine} = 1.8 \times 10^{-3}\,{\rm erg\,s^{-1}\,cm^{-2}\,sr^{-1}}$ for LW and PE bands, respectively (described further below); $\tau_k = n_{\rm H} L_{\rm shld} \sigma_{{\rm d},k}$ with shielding length $L_{\rm shld} = 5\,{\rm pc}(n_{\rm H}/10^2\,{\rm cm^{-3}})^{-0.7}$ (CITE JGK+2021). We also adopt a constant primary CR ionization rate of $2.0 \times 10^{-16}\,{\rm s^{-1}}$, which is the dominant source of ionization in the neutral gas.

We use the 'hybrid' wind injection method as described in Lancaster et al. (2021a). In this method, mass and energy are injected within an 'injection region.' The relative amount of thermal/kinetic energy that is injected is smoothly interpolated between purely thermal injection at the center of the injection region and purely kinetic energy at the edge of the injection region. We also apply the first-order flux correction in the wind injection region, but we do this before the second-order corner-valued electric fields are calculated in the van-Leer integrator (Stone & Gardiner, 2009; Gardiner & Stone, 2005). For our runs with radiative feedback, we use the adaptive-ray tracing (ART) implementation of Kim et al. (2017b). We perform radiative transfer in three separate bands: (i) the photo-electric (PE; $110.8\,{\rm nm} < \lambda \leq 206.6\,{\rm nm}$) band, (ii) the Lyman-Werner (LW; $91.2\,{\rm nm} < \lambda \leq 110.8\,{\rm nm}$) band and, (iii) the Lyman Continuum (LyC; $\lambda \leq 91.2\,{\rm nm}$) or Hydrogen-ionizing band. The PE and LW bands are primarily responsible for heating of the background through the photo-electric effect on dust grains and the photo-dissociation of H_2 and CO, respectively. The Lyman-Continuum band is the main band of dynamical interest for this work. We assume an average photon energy of 9.25, 12.2, 20 eV in the PE, LW, and LyC bands respectively.

In all of the simulations presented here we choose background conditions of the ambient gas that are typical for a Milky Way-like giant molecular cloud (GMC). Specifically, we imagine a cloud of total mass $M_{\rm cl} = 10^5\ {\rm M_\odot}$ and radius $R_{\rm cl} = 20$ pc. This implies a mean background density of $\bar{\rho} = 2.02 \times 10^{-22}\,{\rm g\,cm^{-3}}$ or a mean number density of hydrogen nuclei $\overline{n}_{\rm H} = \bar{\rho}/\mu_{\rm H} m_{\rm H} = 86.25\,{\rm cm^{-3}}$, where we have assumed the mean molecular weight per hydrogen nucleus, $\mu_{\rm H} = 1.4$. The simulations are run in a box with side-length $L_{\rm box} = 2R_{\rm cl}$ at varying resolution. Initially, the density is uniform throughout the simulation domain. In our simulations with magnetic fields we additionally include

a uniform field $\mathbf{B} = B_0\hat{\mathbf{z}}$ throughout the domain with $B_0 = 13.5\,\mu$G. This choice of field strength is motivated by a dimension-less mass-to-flux ratio, μ_Φ, of 2 as in the 'α-series' models of Kim et al. (2021a).

In order to create a realistic background density field, we initially 'stir' our background density fields as in Lancaster et al. (2021a). Specifically, we initialize a Gaussian random field with a power spectrum $|v_k| \propto k^{-2}$ with wave-number k for $2 \leq kL_{\rm box}/2\pi \leq 64$. We normalize the magnitude of the velocity field so that the kinetic energy per unit mass in the domain, $\tilde{E}_K$ is twice what the gravitational potential energy per unit mass, $\tilde{W}$, would be in a GMC of $M_{\rm cl} = 10^5$ M$_\odot$ and $R_{\rm cl} = 20\,$pc. We then allow the turbulence to decay until $\tilde{E}_K = \tilde{W}$.

After creating the density inhomogeneity in the background through mixing we place a source of constant luminosity wind and/or radiative feedback at the center of the domain. Throughout the paper, the onset of feedback will be referred to as $t = 0$. We choose the parameters of the feedback by averaging these properties over the first 2 Myr of evolution as dictated by the `Starburst99` (SB99) (Leitherer et al., 1999, 2014) for the 'standard' output at solar-metallicity using a Kroupa IMF (Kroupa, 2001) along with the Geneva, non-rotating stellar tracks (Ekström et al., 2012). This gives us a wind mechanical luminosity per unit stellar mass of $\mathcal{L}_w/M_* = 9.75 \times 10^{33}\,{\rm erg\,s^{-1}}$ M$_\odot^{-1}$, a mass loss rate per unit stellar mass of $\dot{M}_w/M_* = 2.965 \times 10^{-3}$ Myr^{-1}, a luminosity per unit solar mass of $\mathcal{L}_{\rm PE}/M_* = 318.42\,L_\odot\,{\rm M}_\odot^{-1}$, and $\mathcal{L}_{\rm LW}/M_* = 148.57\,L_\odot\,{\rm M}_\odot^{-1}$ in the PE and LW bands respectively, and an ionizing photon emission rate per unit stellar mass of $\Xi \equiv Q_0/M_* = 4.106 \times 10^{44}\,{\rm s^{-1}}$ M$_\odot^{-1}$. We do not include the effects of direct radiation pressure feedback (radiation provides no source term to the momentum equation), in order to create a better comparison against the theory developed in Section 5.3, which does not include the effects of radiation pressure.

We run 6 different types of simulation corresponding to different choices along three axes:

(1) The inclusion or exclusion of magnetic fields.

(2) The choice of feedback: stellar wind feedback alone, radiative feedback alone, or both.

Table 5.1 provides a listing of these choices.

Each of these simulations are run at three different spatial resolutions $L_{\rm box}/\Delta x = 128$, 256, and

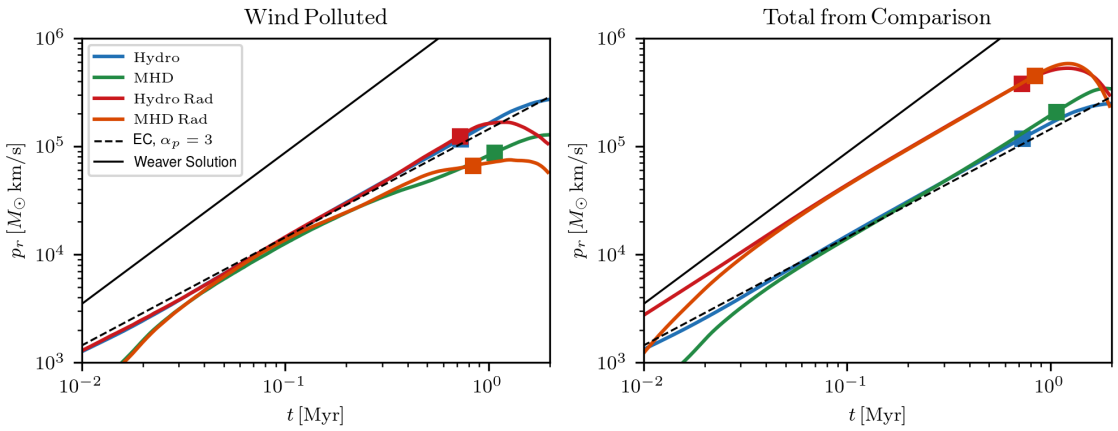

Figure 5.3 We show the radial momentum measured in each of our $L_{\rm box}/\Delta x = 256$ simulations. In each panel we show the evolution of the `Hydro` (blue), `Hydro Rad` (red), `MHD` (green), and `MHD Rad` (orange) runs. Squares on each simulation curve indicate the time when wind material first begins to leave the simulation domain, we should not expect our idealized simulations to apply after this point. We also show the expected theoretical radial momentum evolution in the Weaver model given by Equation 5.4 (black line) and the Efficiently Cooled model, given by Equation 5.5, with $\alpha_p = 3$ (black dashed line). *Left panel*: Total radial momentum evolution carried in wind-polluted material with $f_{\rm wind} > 10^{-4}$. *Right panel*: Total excess radial momentum in simulation, measurement described in text.

512. The highest resolution simulations are run for approximately 1 Myr while all other simulations are run for 2 Myr. A slice through the $z = 0$ plane for our highest resolution simulations with stellar wind feedback is shown in Figure 5.2 for the time at which $\mathcal{R}_w \approx R_{\rm cl}/3 = L_{\rm box}/6$. In particular we display slices in the (i) total pressure, including thermal and magnetic pressure terms as appropriate, (ii) the radial momentum of the gas, measured with respect to the feedback source, (iii) the total volumetric rate of radiative cooling, and (iv) a breakdown of the domain into distinct phases, which are listed in Table 5.2. Here, we intend WHIM to mean 'warm-hot ionized medium' analogous to the 'Ionized' phase of Lancaster et al. (2021a). Other differences in phase definitions between Lancaster et al. (2021a) and this work are mostly due to the change in the module we using for cooling and heating physics. We additionally separate between the warm neutral medium and the H II region using the abundance of free electrons, $x_e \equiv n_e/n_{\rm H}$, where n_e is the number density of free electrons.

Throughout the majority of the paper we will solely be concerned with those simulations that include stellar wind feedback, though we will reference the radiative feedback-only simulations occasionally where appropriate. For each choice of resolution and choice of hydrodynamics solver (pure hydrodynamics or MHD) we also run separate simulations which include no feedback but just evolve the background turbulence. We refer to these as the 'no feedback' simulations and we use them for comparison purposes in the next section.

5.5 Analysis and Results

In this section we present various results of our numerical simulations and compare them to the various theoretical predictions described in Section 5.3. In presenting predictions of the Spitzer evolution for an H II region as discussed in Section 5.3.2, we assume an ionized gas sound speed of $c_i = 10\,{\rm km/s}$.

5.5.1 Momentum Evolution

The most fundamental, and dynamically important, proposition of the EC theory for the expansion of stellar wind-driven bubbles is that the net radial momentum carried by the bubble increases linearly in time, with some enhancement factor, α_p, above the input wind momentum: $p_r = \alpha_p \dot{p}_w t$. Having demonstrated in Lancaster et al. (2021a) that this proposition holds across a wide range of parameter space for purely hydrodynamical simulations without radiation feedback, it is natural to start by asking if this still holds when we include additional physics.

Tracking Total Momentum

Measuring the total momentum in the simulation domain is more complicated here than in our previous simulations, due to the new physics included here. In (Lancaster et al., 2021a) we measured the total momentum carried by the wind bubble by taking the total momentum carried in 'wind-polluted gas,' defined as any grid-cell with a fraction of its mass coming from wind material, $f_{\rm wind} > 10^{-4}$. Both magnetic fields and radiative feedback can complicate this method's attempt at giving a full accounting of momentum that is *due to the wind-driven bubble*. Principally, this is because both the presence of magnetic fields and an H II region should present significant external stresses, pushing back on the expansion of the bubble, such that $\alpha_p \dot{p}_w$ is no longer an accurate description of the *net* force acting at the bubble's surface, we shall return to this below.

However, the background magnetic fields also be able to transfer momentum forward, out of wind-polluted gas, if the local magneto-sonic or Alfvén speed exceeds the propagation speed of the wind front (see e.g. Offner & Liu, 2018). This means that momentum that truly has been injected in to the background medium by the wind is no longer tracked by 'wind-polluted' gas. To some extent this would already break the assumption of our theory that external stresses are negligible. Regardless, this is an important effect to keep in mind.

When considering the addition of radiative feedback, there is then momentum imparted to the background medium through work done by the H II region. This momentum would not necessarily be captured by wind-polluted gas, but at the same time, we would not necessarily like to include it in our accounting if we are only interested in the momentum injected due to the wind. As we

mentioned above, the pressure of the H II region may also push back on the wind-driven bubble, decreasing the *net* momentum injected by the wind.

Keeping both of these effects in mind we measure the total momentum carried in the wind-driven bubble in two different ways. The first is identical to the measurement method of Lancaster et al. (2021a), using wind-polluted gas with $f_{\rm wind} > 10^{-4}$ and summing all radial momentum in such gas as one measurement of the total radial momentum. The results using this method are shown in the left hand panel of Figure 5.3. As we can see, all simulations initially follow the EC solution with $\alpha_p = 3$ (chosen by-eye to qualitatively match the simulation evolution). In fact, it is quite interesting, given the external stress that the H II region provides both on the wind-driven bubble and the surrounding material, that this accounting momentum in the `Hydro Rad` simulation closely follows the EC solution. For the MHD simulations the momentum carried by the bubbles eventually drops below the EC solution. This could be either due to (i) momentum-carried out of wind polluted gas by MHD waves, as discussed above, or (ii) the EC solution does not apply.

We investigate which of these scenarios is true with our second measurement method. Here we measure the total radial momentum in the simulation domain as compared with our 'no-feedback' simulations. This allows us to see all momentum that has been injected by feedback, but not necessarily solely from the wind. The results of this measurement method are shown in the right panel of Figure 5.3. Comparing the `Hydro` and `MHD` runs we can see that, now that we have included all radial momentum in the simulation domain, the two simulations agree. This indicates that the EC solution still applies and that the disagreement in the last measurement was simply due to MHD waves moving momentum out of wind-polluted gas. Considering the simulations with radiative feedback, the total momentum is much greater than the EC solution due to the momentum incurred from the expansion of the H II region. This is what we investigate next, after briefly reviewing the correct momentum for the Spitzer solution.

Momentum Carried by an H II Region

As discussed in Section 5.3.2, the Spitzer solution, strictly interpreted, implies that the there is a non-zero amount of momentum carried by the H II region at $t = 0$, as we can observe from

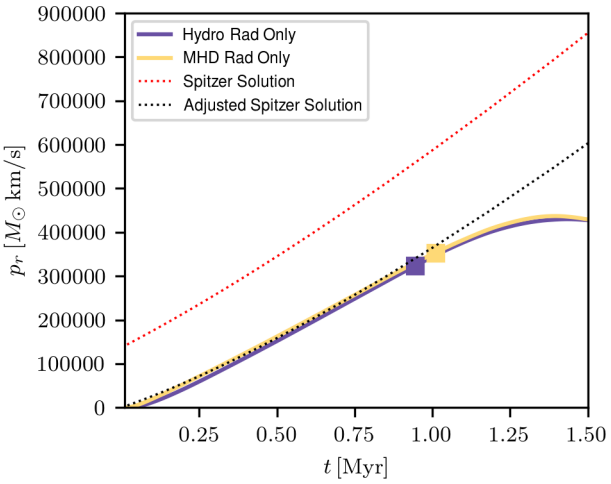

Figure 5.4 We show the evolution of the total radial momentum carried by the H II region for the `Hydro Rad Only` (purple) and `MHD Rad Only` (yellow) simulations. The simulations shown here have a resolution of $L_{\rm box}/\Delta x = 512$. Squares on each line indicate the time at which significant momentum begins to leave the simulation domain. We compare this evolution with the predicted radial momentum evolution for the Spitzer solution, as given by Equation 5.23 (red dotted line) and the adjusted Spitzer solution as given by Equation 5.24 (black dotted line). The adjusted solution is clearly a better match to the momentum evolution of the simulated H II regions. It is important to note that, unlike Figure 5.3, we use a linear scale here, which de-emphasizes the earliest time evolution.

Equation 5.23. In that section we suggested an adjustment to this formal solution that recovers zero radial momentum at $t = 0$ by subtracting the mass interior to the H II region from the mass assumed to be carrying all of the momentum in the bubble's shell. This resulted in Equation 5.24.

In Figure 5.4 we compare Equation 5.23 and Equation 5.24 to the total radial momentum in our simulations with radiation feedback only. It is clear that the adjusted solution, indicated by the black dotted line, is a much better match to the simulated solution than the strictly interpreted Spitzer momentum, shown as a red dotted line. Throughout the remainder of the paper we will use the adjusted momentum evolution, given by Equation 5.24, as the 'correct' momentum evolution of an ionized gas pressure-driven H II region. It should be noted that this difference will be most extreme when the size of the Strömgren sphere is not small compared to the size of the cloud that is being considered (or the radial range of expansion being considered) as is the case in our simulations.

Joint Evolution Models for Momentum

We now compare the theoretical models for the joint evolution of an H II region and a stellar wind-driven bubble described in Section 5.3.3 to our simulations which include both of these effects. In Figure 5.5 we compare the total radial momentum evolution in the `Hydro Rad` and `MHD Rad` simulations (the same quantity shown in the right panel of Figure 5.3) to several different theoretical predictions.

In particular, we show the adjusted Spitzer solution, given by Equation 5.24 and discussed in the previous section. This would only be expected to be an accurate description of the momentum evolution in the simulations if the effects of the wind-driven bubble were completely negligible, which indeed is not the case. We also show the sum of the momentum given by this adjusted Spitzer solution and the EC solution, given by Equation 5.5, with $\alpha_p = 3$ as a black dot-dashed line. This prediction constitutes perhaps the simplest theoretical prediction that we might expect to work and indeed similar models have been employed elsewhere in the literature to combine the effects of two different feedback mechanisms (e.g. Murray et al., 2010). Indeed, this simple prediction does quite well in predicting the momentum evolution, but under-estimates the simulated results

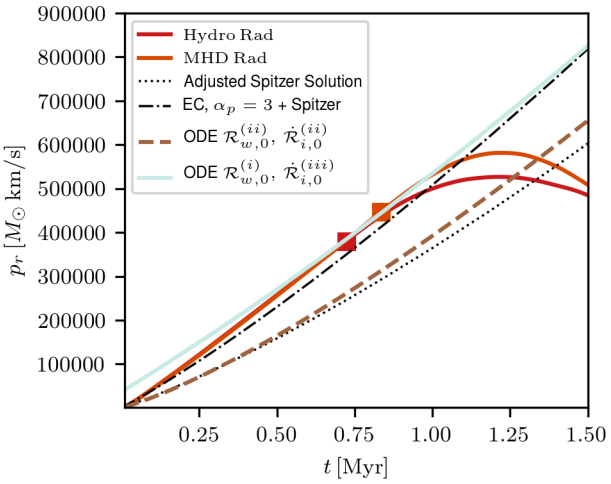

Figure 5.5 We show a comparison of the momentum evolution of the `Hydro Rad` and `MHD Rad` simulation at $L_{\rm box}/\Delta x = 256$ resolution to various theoretical models. The evolution shown here is the same as that shown in the right panel of Figure 5.3 for these simulations. Squares on these curves indicate the time at which the wind bubble breaks out from the simulation domain. For theoretical comparisons we show (i) the adjusted Spitzer solution given in Figure 5.4 (black dotted line), (ii) the sum of this adjusted Spitzer solution and the momentum from a $\alpha_p = 3$ EC solution (black dot dashed line), and (iii) two different solutions to the ODE given by Equation 5.25 with different assumed initial conditions, discussed in Section 5.9 (blue and brown lines). The colors shown here for these ODE solutions correspond to the same colors and line-styles shown in Figure 5.15.

by about 10%.

We also compare our simulations to solutions of the ODE we derived in Section 5.3.3, Equation 5.25. In particular we choose two different sets of initial conditions out of the six possible choices discussed in Section 5.9. One model uses the 'second choice' for the initial condition of the wind bubble's radius $\mathcal{R}_{w,0}^{(ii)}$, accounting for changes in the H II region incurred by the wind in the equilibrium radius, and the second choice for the initial velocity condition, $\dot{\mathcal{R}}_{i,0}^{(ii)}$, which assumes the initial expansion of the feedback bubble is identical to the Spitzer solution. This is chosen for its success in comparing to the radial evolution of the bubble, as we describe further below. For this model we compute the total momentum evolution using Equation 5.55, analogous to the adjusted Spitzer solution in its correction for the mass carried by the shell. We justify this choice in Section 5.10. This first solution tends to significantly underestimate the momentum carried by the wind bubble. If we were to not include the adjustment, it would significantly over-estimate the evolution.

The second model uses the 'first choice' for the initial condition of the wind bubble's radius $\mathcal{R}_{w,0}^{(ii)}$ which assumes the wind bubble 'begins' at the equilibrium radius, R_E, and the third choice for the initial velocity, $\dot{\mathcal{R}}_{i,0}^{(iii)}$, which ties the initial velocity, and hence initial momentum, to the momentum that we would expect to have been injected by the wind up until the time that the wind-driven bubble comes in to equilibrium with the H II region. This choice gives a physically meaningful starting point to the momentum derived directly from the solution and we would therefore expect for this choice to give an accurate description of the simulated momentum evolution. However, this choice also assigns non-zero momentum to the solution at $t = 0$, which is not physical. So, we would expect the momentum to be over-estimated at early times but approach the correct answer at late times, $t > t_E$. Indeed, this is the case, as we can see in Figure 5.5, the ODE solution matches the simulations within a few percent at late times before the wind-driven bubble has broken out of the simulation domain.

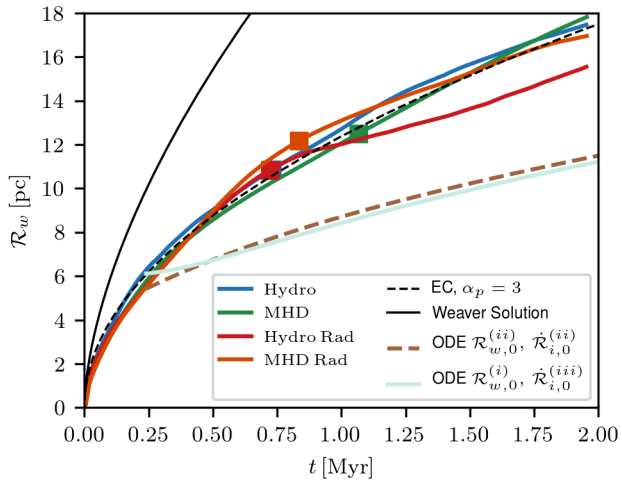

Figure 5.6 We show the evolution of the effective radii of the wind-driven bubbles in each of our simulations with stellar wind feedback. Color coding is identical to Figure 5.3 with squares indicating the time at which wind material begins to leave the simulation domain. For comparison we show the radial evolution of a wind-driven bubble according to the Weaver et al. (1977) solution, given by Equation 5.2 (black line) and the EC solution with $\alpha_p = 3$ (black dashed line). We also show the prediction for the wind bubble's evolution from the ODE solutions described in Section 5.10. Color coding here is identical to Figure 5.5. These curves are shifted forward in time so that they begin at t_E, the time at which the wind bubble is in equilibrium with the H II region, as described in Section 5.8.

5.5.2 Bubble Radial Expansion

Having confirmed that the evolution of radial momentum matches our expectations from the EC theory for wind-driven bubble evolution, along with the joint evolution theory, we now examine the overall volumetric expansion of the bubble. We first investigate the expansion of the stellar wind-driven bubble and then the expansion of the feedback bubble overall, including the H II region.

Wind-Driven Bubble Expansion

In Figure 5.6 we show the evolution of the wind-driven bubble's effective radii in each of our simulations including stellar wind feedback at a spatial resolution of $L_{\rm box}/\Delta x = 256$. In these simulations we measure the effective radii of the wind-driven bubble's using Equation 5.1, where the volume is defined by all gas that is in the Hot shocked wind phase or the free stellar wind phase.

This consists of all gas with temperature $T > 10^6\,\mathrm{K}$ or radial velocity $v_r > \mathcal{V}_w/2$, similar to the definition given in Lancaster et al. (2021a).

It is clear from Figure 5.6 that the simulations very closely follow the predictions of the EC theory with $\alpha_p = 3$, consistent with the momentum evolution described in the previous section. In particular, in our simulations with the added physics of background magnetic fields and photo-ionization feedback, the wind-driven bubble still follow this predicted evolution very well and fall far below the evolution expected by a Weaver et al. (1977) type solution.

We also show in Figure 5.6 the radial evolution of the wind bubble predicted by the two ODE solutions we compared our simulations against in Figure 5.5. For comparison, we shift the predictions given by these ODE solutions forward in time by t_E, roughly the time it takes for the stellar wind-driven bubble to come in to equilibrium with the surrounding H II region. We do this since t_E is meant to represent the starting point for the numerical solutions to Equation 5.25 that we give here (discussed further in Section 5.8). We see that the radial evolution of the wind-driven bubbles in the `Hydro Rad` and `MHD Rad` simulations are quite a bit faster than the predictions of the ODE solutions.

This disagreement likely results from two separate effects having to do with invalidity of certain assumptions of our model. First, our model assumes that all of the wind-driven bubble's momentum is transferred to the edge of the H II region before the bubble continues to evolve further. In reality, the wind bubble will need some time to transfer the momentum forward through the photo-ionized gas. During this time the wind-driven bubble may continue to expand 'normally' depending on the density, velocity, and pressure structure of the H II region. This effect essentially is due to the breakdown of our assumption that, t_E, is short compared to the dynamical time of the wind-driven bubble, $t_{\mathrm{d},i}$.

Second, and more complex, the fact that the wind-driven bubble has come in to equilibrium with the H II region would, in our model, mean that the wind-driven bubble is no longer compressing the photo-ionized gas into a shell around it. In the Weaver et al. (1977) model as well as the EC model, the cooling that occurs in the compressed shell removes approximately 35% of the injected wind energy. In transitioning to a regime where the H II region is no longer being compressed and

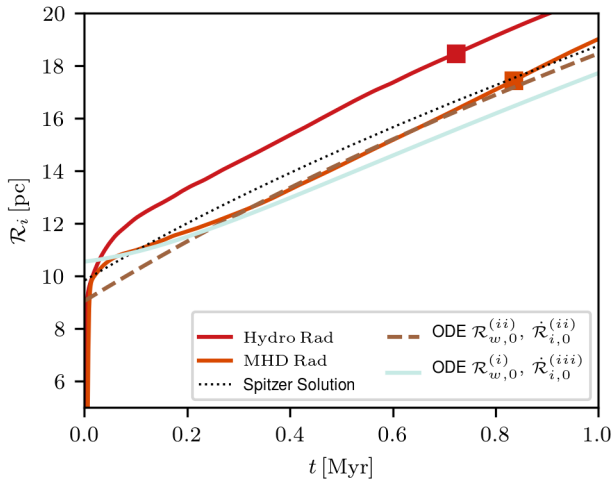

Figure 5.7 We show the evolution of the effective radii of the full feedback bubbles (wind-driven bubble and H II region) in each of our simulations with both stellar winds and photo-ionizing radiation feedback. Color coding is identical to Figure 5.3 with squares indicating the time at which wind material begins to leave the simulation domain. For comparison we show the radial evolution of a D-type H II region given by the Spitzer solution, Equation 5.22. We also show the prediction for the feedback bubble's evolution from the ODE solutions described in Section 5.10. The model solution shown here are identical to those shown in Figure 5.6.

cooled, the wind bubble may revert temporarily (as it comes into equilibrium with the H II region) to a 'thick-shell' evolution as in the early stages of the Weaver et al. (1977) model. This would mean a corresponding increase in the pressure of the shocked wind as the thick shell pushes backward on it. This increased pressure may allow the wind bubble to continue to expand above the rate one would expect once it is in equilibrium with the H II region (i.e. the evolution predicted by the ODE models). How this plays out quantitatively, and why it seems to work in such a way as to perfectly continue the radial expansion we would expect from the EC solution as it had been evolving are as yet unclear. However, we will verify below that some of the physical phenomena described above do indeed occur.

Expansion of Entire Feedback Bubble

We now turn to the radial expansion of the joint feedback bubble and how this compared with the evolution we would expect from the model developed in Section 5.3.3. In Figure 5.7 we compare the evolution of the effective radius of the wind-driven bubble combined with the H II region to the evolution predicted but the same ODE solutions we described above. In particular, for the volume that describes $\mathcal{R}_i$, we use all gas within the H II Region, the WHIM, and the two stellar wind phases, as defined in Table 5.2.

We note that this definition of effective radius may not be as successful a description of the *dynamically important* volume of the H II Region, as it was for the wind-driven bubble. This is because, in the case of the photo-ionized gas, low-column density sight-lines from the source are subject to supersonic, R-type ionization front expansion. Such expansion increases the volume of the H II region but doesn't necessarily increase the *dynamically important* volume since this gas is preferentially lower density and thus under-pressured compared to the dynamically important part of the H II region. We can see examples of these regions as 'fingers' of the H II region in the `Hydro Rad` and `MHD Rad` snapshots shown in Figure 5.2. These regions also need not come in to equilibrium with the rest of the H II region as variations in the column density over the sky and over time cause these R-type ionized regions to spontaneously recombine as a dense bit of gas passes between them and the ionizing source. With this effect in mind, we would imagine that our definition of $\mathcal{R}_i$ used here would *overestimate* the correct, dynamically relevant value. In observing Figure 5.2 we can see that the prominence of these 'fingers' is somewhat reduced in the `MHD Rad` simulation. This may lead us to believe that our definition is more applicable to this simulation. We see this same effect when comparing $\mathcal{R}_i$ in the `Hydro Rad Only` and `MHD Rad Only` simulations to the Spitzer solution, with the `MHD Rad Only` simulation providing a closer match to the expected Spitzer solution.

In comparing the models and simulations in Figure 5.7 we see that, indeed, the `MHD Rad` simulation is a better match to our models than the `Hydro Rad` simulation. In particular, the $\mathcal{R}_{w,0}^{(ii)}$, $\dot{\mathcal{R}}_{i,0}^{(ii)}$ model (brown dashed line) gives quite a good description of the evolution of the `MHD Rad` simulation, especially after $t_E \approx 0.24\,\mathrm{Myr}$ when the model should apply best. That said, the models

fall short at early times, where indeed they should not apply. In fact we can observe some interesting behaviour at early times that is discussed in the development of the model. In particular, we can see that $\mathcal{R}_i$ in the `MHD Rad` simulation falls below the Spitzer evolution (black dotted line) at $t < t_E$. As discussed further in Section 5.9, this is presumably due to the development of the shell of photo-ionized gas around the wind-driven bubble. Since this shell is at higher density, it will re-combine more efficiently, decreasing the volume able to be ionized by the central source and hence decreasing the size of the H II region.

Overall, we can see that the radial evolution of the wind bubble is very consistent with the expectations of the EC theory, as shown in Figure 5.6. Additionally, the evolution of the joint feedback bubble is relatively within the range of expectations of our joint solution model, though there are caveats to this comparison, mostly having to do with the simplifying assumptions of the model.

5.5.3 Cooling

Radiative cooling is also an important part of the EC wind-driven bubble's evolution and, given the broad consistency with the EC solution in the past sections, it is interesting to examine how the cooling overall and its phase structure changes with out added physics. In this section we will present measurement of *net* cooling, that is any radiative cooling that occurs with the heating provided to a gas cell either by radiative heating from the source at the center of the domain or background heating subtracted out. When measuring the net cooling in the 'background' phases (the CNM/Molecular gas, the thermally unstable phase, and the WNM) we only include contributions from wind polluted gas with $f_{\rm wind} > 10^{-4}$.

In Figure 5.8 we show the breakdown of the total net cooling by phase as a fraction of the integrated energy injected by the stellar wind. We see that, in all simulations, the cooling is dominated by cooling in the WHIM phase that exists between the wind-driven bubble and its surroundings, consistent with the EC theory. We can also observe that the cooling in the WHIM is approximately the same in all simulations at approximately $\sim 70\%$ of the injected wind energy.

What is more, we can see that the next principal contribution comes from material cooling in

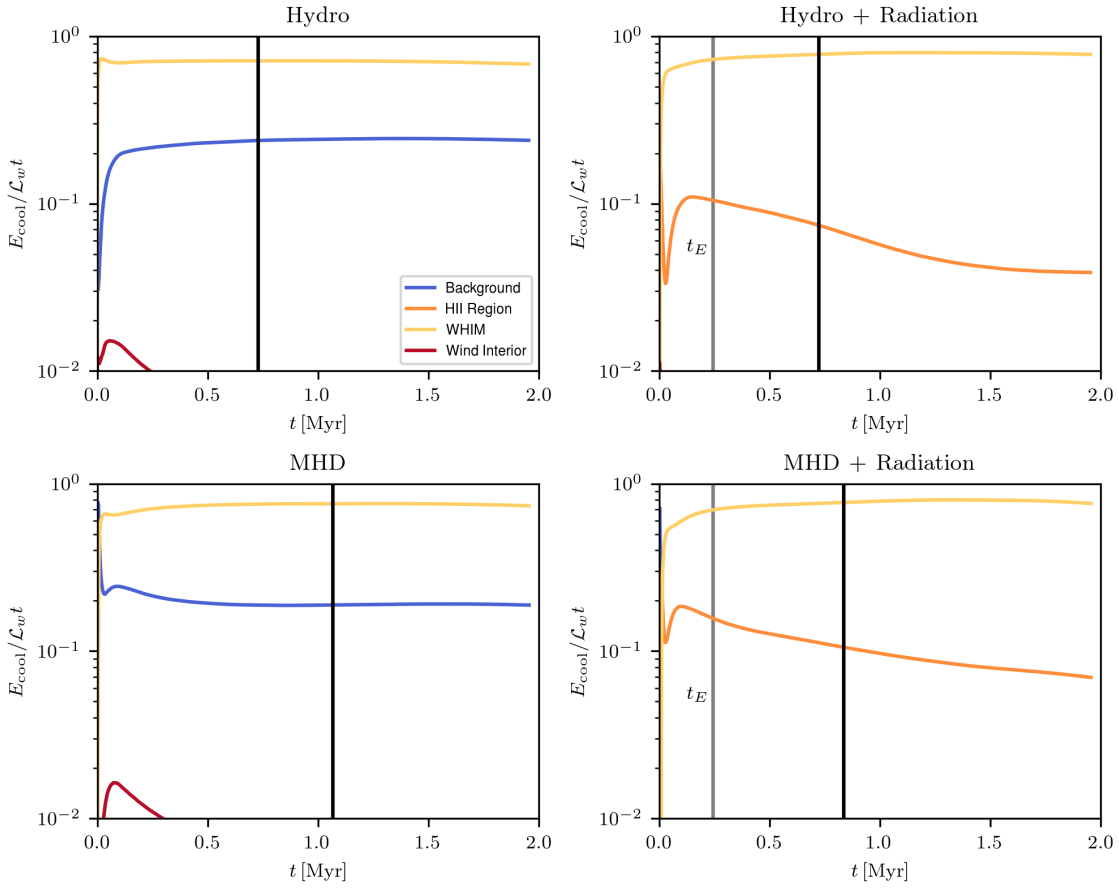

Figure 5.8 The evolution of the net integrated cooling displayed as a fraction of the net injected wind energy and split up by phase. The phases include (i) the 'Background' (dark blue) which is a sum of net cooling across the CNM/Molecular phase, the thermally unstable phase, and the WNM phase, (ii) the H II region (orange), (iii) the WHIM (yellow), and (iv) the wind-driven bubble's interior (dark red). Color coding for the WHIM and H II region phases correspond to the same coloring in the schematic phase plots of Figure 5.2. Panels represent the (clockwise from top left) `Hydro`, `Hydro Rad`, `MHD Rad`, and `MHD` simulations. Results show here are for the simulations run at $L_{\rm box}/\Delta x = 256$ resolution. In the panels on the right, we indicate t_E with a vertical grey line. Finally, we indicate the times at which wind material first begins to break out of the cloud as a vertical black line in each panel.

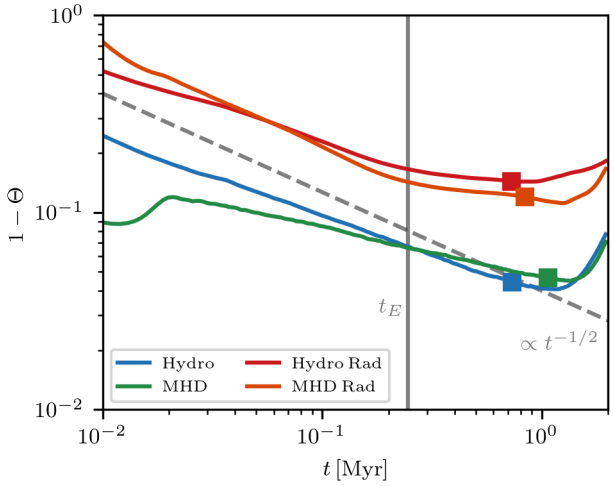

Figure 5.9 The fraction of the total injected wind energy that is retained within the simulation domain as a function of time for the same simulations displayed in Figure 5.8. As in other figures, the squares indicate the times at which the wind-driven bubble first breaks out to the simulation domain. As guides we also indicate the equilibrium time, t_E, and an evolution proportional to $t^{-1/2}$.

the shell of material swept up by the wind-driven bubble. As we noted in Section 5.5.2, even in the Weaver et al. (1977) model, this gas is responsible for for cooling away 35% of the injected wind energy. In the simulations without photo-ionizing radiation this cooling occurs in the 'background' gas and removes only $\sim 20\%$ of the wind energy. In the simulations with photo-ionizing radiation, this cooling occurs within the H II region. We see that, again, cooling in this shell accounts for approximately $\sim 10 - 20\%$ of the total injected wind energy at early times. However, once the wind-driven bubble comes in to equilibrium with the H II region at $t \approx t_E$, cooling in this swept-up phase decreases as the wind-driven bubble is no longer compressing the H II region. This is the exact effect we alluded to above. This reached equilibrium does not mean that net cooling in the H II region is reduced to nothing, as details of the equilibrium may depend the wind driven bubble's ability to push on the H II region and force it to a new density and pressure in order to remain in equilibrium.

Having investigated the phase structure of the cooling it is also informative to see how the total

cooling compares. As in Lancaster et al. (2021b,a) we define

$$\Theta \equiv \frac{\int \dot{E}_{\rm cool} dt}{\mathcal{L}_w t} \tag{5.33}$$

as the fraction of the winds energy that is lost to cooling. It is important to note that, unlike Lancaster et al. (2021b), we define Θ here in an integrated sense rather than in terms of the instantaneous cooling compared to the instantaneous wind luminosity (e.g. $\dot{E}_{\rm cool}/\mathcal{L}_w$). In Figure 5.9 we show $1 - \Theta$, the fraction of the wind's energy that is retained within the domain as a function of time. We immediately see that the simulations with radiative feedback appear to retain more energy than the simulations without radiative feedback. This is most likely mis-leading since the *net* cooling that we are comparing against here includes heating terms photoelectric heating from dust grains due to absorption of FUV photons in the H II Region. This means that what really appears as "more retained wind energy" is simply the contribution of the FUV heating. Unfortunately, we did not track the necessary quantities in our simulations to quantitatively check this assertion.

We can also see in Figure 5.9 that the net cooling in the simulations with radiation begins to level off at $t \approx t_E$, this is the same effect that we saw from Figure 5.8 in that the H II region begins to cool less efficiently at this time, as it is no longer being compressed. Overall, we see that roughly each simulation seems to follow the $1 - \Theta \propto t^{-1/2}$ behavior that is expected from the EC solution, as laid out in Lancaster et al. (2021b). There are expected to be variations in this scaling based on the relative amounts of turbulent energy, so the fact that the simulations do not exactly follow this scaling is not particularly surprising. It is also important to note how this apparent scaling can be viewed as consistent with Figure 5.8, where it appears that the cooling in the dominantly-cooling phases is approximately constant in time. This is mostly due to the fact that Figure 5.9 is displayed with a logarithmic scale in time, emphasizing the early time evolution where indeed there is much more evolution in the cooling in each term. Additionally, while the cooling in each phase doesn't appear to evolve very much, even considering only the time before the wind breaks out, only small changes are required to change the scaling in Figure 5.9, since so much of the energy is cooled away.

Another caveat to keep in mind is that the accounting of cooling in the `MHD` simulation may

not be entirely accurate since we measure cooling in the wind-driven bubbles shell by measuring the net cooling in the wind-polluted gas in the background phases. As discussed in Section 5.5.1, this may not be an accurate accounting of all gas affected by the wind-driven bubble in the MHD simulations since MHD waves may be able to propagate the disturbance caused by the wind-driven bubble ahead of the bubble's surface.

Overall, we find here that the phase structure and total amount of cooling that occurs in each of our simulations is broadly consistent with the expectations from the EC bubble theory.

5.5.4 Pressure

Finally, we examine the pressure in the hot, shocked stellar wind. It is the pressure in this gas that is solely responsible for the expansion of the wind-driven bubble in the Weaver et al. (1977) model and still primarily responsible in the EC model with $\alpha_p > 1$ (Lancaster et al., 2021b). In Figure 5.10 we show the shocked wind gas pressure as a function of time and as a function of the wind-driven bubble's effective radius, $\mathcal{R}_w$. We show the bubble evolution as a function of radius since, in the EC theory, it is really the bubble's effective radius that sets the internal pressure (see Equation 5.8).

Broadly, we can see that each simulation generally follows the expectations for the EC theory with $\alpha_p = 3$, which is shown as a black dashed line. However, we do see that the pressure in our simulations with magnetic field or radiation feedback exhibit marginally higher pressures than the purely hydro-dynamical simulation. In the context of the nearly identical evolution of these simulations in $\mathcal{R}_w(t)$ and momentum carried by the wind-driven bubble as a function of time, this makes sense, In particular, both the simulations with magnetic fields and those in which the wind-driven bubble expands in to a surrounding H II region, there are added external stresses (higher thermal pressure or magnetic tension in the background) that the wind-driven bubble must work against. In order to have an identical radial momentum and volumetric evolution, then these bubble's would need higher internal pressure, or other stresses, in order to push back against the added external stresses.

A telltale sign that this is indeed what is occurring in the simulations with radiative feedback is

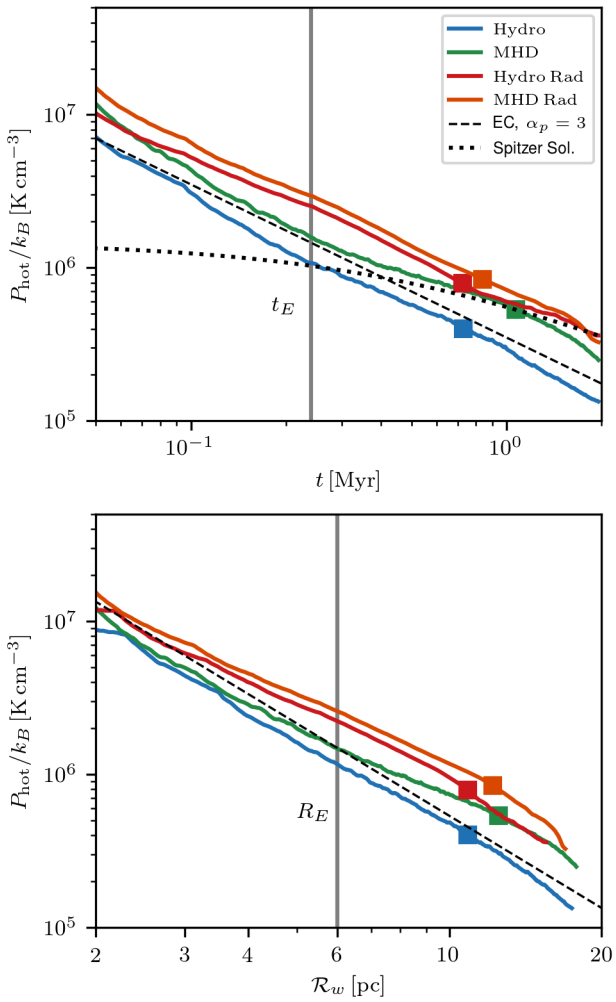

Figure 5.10 The pressure in the hot, shocked stellar wind in each simulation as a function of time (top panel) and the wind-driven bubble's effective radius (bottom panel). Squares indicate when the win-driven bubbles first breakout of the simulation domain. For comparison we show the pressure evolution of a EC wind-driven bubble, as given by Equation 5.8 (black dashed line) and the pressure evolution expected for an H II region according to the Spitzer Solution (black dotted line). We also indicate t_E (top panel) and $R_E = R_{\rm EC}(t_E)$ (bottom panel) with vertical grey lines.

the marked increase in the shocked wind's pressure above the EC solution when the bubble comes in to equilibrium with the H II region. This is especially clear in the bottom panel of Figure 5.10. This added pressure was alluded to in Section 5.5.2 as being additionally caused by the re-adjustment of the bubble structure that occurs when cooling becomes much weaker in the swept up shell of ionized gas at $t \approx t_E$.

This increase in pressure accompanied by no major change in the scaling of the hot gas pressure with respect to time or $\mathcal{R}_w$ at $t > t_E$ are counter to our intuition developed in Section 5.3.3 for the combined evolution of the H II region. In that picture, the wind-driven bubble's pressure should be the same as the H II region and the scaling should change based on the balance of these pressures and how they evolve jointly. Instead, it seems, the wind-driven bubble's pressure adjusts to whatever it needs to be in order to maintain the $p_r \approx \alpha_p \dot{p}_w t$ behavior it had been maintaining. How can this be? In the next section, we investigate this question in the context of the theory for effective mixing velocity, which is directly related to the momentum enhancement factor, α_p as described in Section 5.3.1.

5.5.5 Effective Mixing Velocity

The main success of the EC theory was its tying of the amount of cooling that occurs in the mixing layer to the fractal structure of the bubble's surface and the behavior of turbulence in the hot shocked wind (Lancaster et al., 2021b,a). Here we make the same comparison of the effective mixing velocity, $v_{\rm eff}$, given by Equation 5.13, to the mean radial velocity of shocked wind gas as it reaches the mixing layer, given by Equation 5.15. In the findings of Lancaster et al. (2021a), these velocities followed one another, if one chooses the correct scaling factor α_C for the effective cooling. We build our comparison by evaluating each quantity that contributes to the calculation of $v_{\rm eff}$ and $v_{\rm ps}(\mathcal{R}_w)$. For all quantities in this section we use our highest resolution simulations at $L_{\rm box}/\Delta x = 512$ resolution.

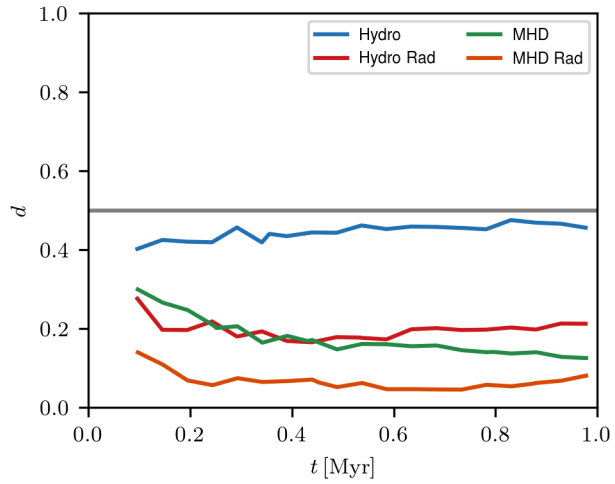

Figure 5.11 The excess fractal dimension of the wind-driven bubbles in each of our simulations with stellar wind feedback at a spatial resolution of $L_{\rm box}/\Delta x = 512$. We measure d using the 'Area Method' of Fielding et al. (2020) and Lancaster et al. (2021a) with an iso-temperature surfaces at $T = 10^5\,\mathrm{K}$ and on scales $\ell = 8\Delta x \approx 0.6\,\mathrm{pc}$.

Fractal Dimension of Wind-Driven Bubble's Surface

We begin with the excess fractal dimension of the bubble's surface, d, which quantifies the degree to which the wind-driven bubble's surface is folded and distorted by both structure in the background and turbulent instabilities at the interface. We measure this quantity in our simulations using the 'Area Method' of Fielding et al. (2020) and Lancaster et al. (2021a). This method measures the fractal dimension of the bubble surface by measuring the area of iso-temperature surfaces in our simulations on different physical scales, $A_w(\ell)$. The excess fractal dimension is then defined as the logarithmic derivative of the measurement:

$$d \equiv \frac{d \log A_w(\ell)}{d \log \ell}\,. \tag{5.34}$$

This quantity, being the derivative of a function of ℓ, is then itself a function of the scale ℓ. For the excess fractal dimensions shown here, in Figure 5.11, we measure $A_w(\ell)$ using iso-temperature surfaces at $T = 10^5\,\mathrm{K}$ though we verified that the results are insensitive to any temperature choice

that tracks the mixing layer: $T = 10^{4.5} - 10^{6}\,\mathrm{K}$.

In Figure 5.11 we display the measured excess fractal dimension, measure on scales $\ell = 8\Delta x \approx 0.6\,\mathrm{pc}$. The measurement of d is marginally dependent upon the scale on which it is measured for reasons at both large and small scale. At small scales we approach the resolution limit and no surface defined on a grid can appear fractal on scales approaching the grid-scale, since the surface is unable to form smaller scale structure. At large enough scales, we are measuring the fractal dimension on scales that are comparable to the size of the surface at early times in the evolution, and thus do not accurately capture the structure. The chosen scale of $8\Delta x$ provides an appropriate balance between these two factors of the range of time that we explore. We also only calculate d for $t > 0.1\,\mathrm{Myr}$ so that the wind-driven bubble is large enough when we begin to measure d on these scales.

Examining Figure 5.11 it is clear that d is a relatively constant function of time in our simulations, though it does seem to decrease at early times in the simulations with added physics. This is especially pronounced in the `MHD` simulation. This could be due to the increased strength of the magnetic field at the bubble's surface, due to magnetic draping, acting to suppress instabilities on small scales. In principal, if this were the case, we would see this effect first on the smallest scales and later on larger scales. Unfortunately, we do not have the dynamic range in scales to observe this effect.

The more striking result apparent from Figure 5.11, and visually apparent from Figure 5.2, is that the `MHD` and `Hydro Rad` simulations both have significantly lower fractal dimensions than the `Hydro` simulation, and the `MHD Rad` simulation has an even lower d. This is not particularly unexpected since the main seeds for the fractal nature of the bubble are (i) interactions with over-dense structures in the background gas and (ii) growth of instabilities at the surface, especially around these dense structures. In our MHD simulations, more over-dense structures are prevented from forming in the background gas due to the added magnetic pressure and the growth of most instabilities is suppressed, usually in a scale-dependent way, by the presence of magnetic fields. For example, the Kelvin-Helmholz (KH) instability is suppressed when the shear velocity between the layers is less than the local Alfvén speed. At the same time, the presence of an H II region acts

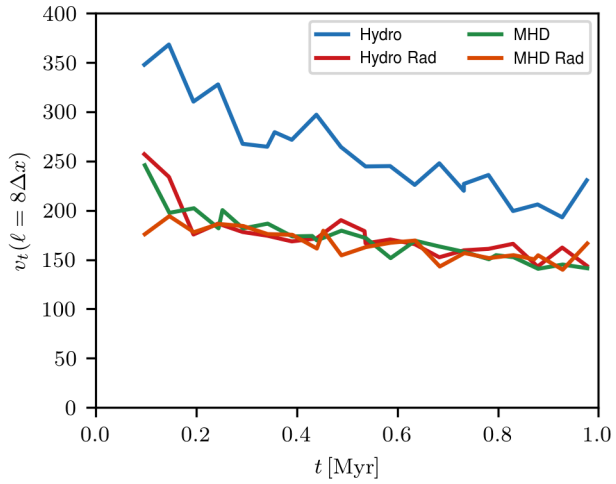

Figure 5.12 The scale of turbulent motions in the hot, shocked wind gas in each of our simulations with stellar wind feedback at a spatial resolution of $L_{\rm box}/\Delta x = 512$. Turbulent motions are measured on a spatial scale $\ell = 8\Delta x \approx 0.6\,{\rm pc}$, details given in text.

to either destroy the over-densities in the background through photo-evaporation (after which the dense gas spreads through the H II region on the sound-crossing time) or to remove them through the rocket effect (Elmergreen, 1976; McKee et al., 1984).

Turbulent Velocity Field

Next we evaluate the evolution of turbulent motions in the hot, shocked wind material. To do this we measure the structure function of non-radial velocities in the hot shocked wind, defined in Table 5.2, with the same method as that given in Section 4.5 of Lancaster et al. (2021a). Briefly, this involves, at each simulation snapshot, taking 200 sample grid positions, $\mathbf{x}_i$ in the shocked wind and measuring

$$|\delta \mathbf{u}_t|^2(r) = \frac{\sum_{|\mathbf{x}_i - \mathbf{x}_j| = r} |\mathbf{u}_t(\mathbf{x}_i) - \mathbf{u}_t(\mathbf{x}_j)|^2}{\sum_{|\mathbf{x}_i - \mathbf{x}_j| = r}} \,, \tag{5.35}$$

where $\mathbf{u}_t \equiv \mathbf{v} - (\mathbf{v} \cdot \hat{\mathbf{r}})\hat{\mathbf{r}}$ is the non-radial component of the velocity field. We define the turbulent velocity at scale ℓ, $v_t(\ell)$, as the median of $\sqrt{3|\delta \mathbf{u}_t|^2(\ell)/2}$ over these 200 sample measurements. The factor of $\sqrt{3/2}$ is included in order to attempt to re-account for the lost radial component of the

turbulent motions.

In Figure 5.12 we show results of these measurements on a scale $\ell = 8\Delta x$, identical to the scale on which d was measured in the previous section. We see that, despite the noisy fluctuations in our measurements, the `Hydro` simulation has much larger magnitude turbulent motions than the other simulations whose evolution seems to be statistically identical. While we have no theory from which to predict this turbulent velocity scale from first principles, we do have an idea of where they come from. In particular, as we discussed in Lancaster et al. (2021b,a), these turbulent motions are created through growth of non-linear instabilities at the mixing layer, but can also be seeded and greatly enhanced by the free stellar wind directly interacting with dense gas. This direct interaction creates bow-shocks which seed turbulent motions on the scale of the wind speed in the shocked wind. As we can heuristically tell from Figure 5.2, such direct interaction does occur in the `Hydro` simulation though it does not appear to occur in the other simulations. This effect seems consistent with the lower fractal dimension in the new simulations, which would imply less 'foldedness' and hence a lower likelihood of dense gas penetrating deep into the wind bubble interior. While this may explain the lower value of the turbulent velocity in these simulations, it does not explain the excellent agreement between these simulations. Since we do not have a direct theory for the development of this turbulence, this remains somewhat of a mystery.

The Effective Mixing Velocity

Putting together our measurement from the past two sections we are prepared to measure the effective velocity for mixing in the TRML between the wind-driven bubble and the surrounding gas. In terms of our simulations, we define this effective mixing velocity as

$$v_{\rm eff}(\ell) = v_t(\ell) \left(\frac{\mathcal{R}_w}{\ell} \right)^{d(\ell)} . \tag{5.36}$$

This equation would be identical to Equation 5.13 if we took $\ell \to \ell_{\rm cool}$ and $\alpha_C = 1$. However, we do not resolve the cooling scale in our simulations, so instead we use Equation 5.36 with measurements on the smallest scale, ℓ, that we believe we can trust. For reasons outlined in the previous two

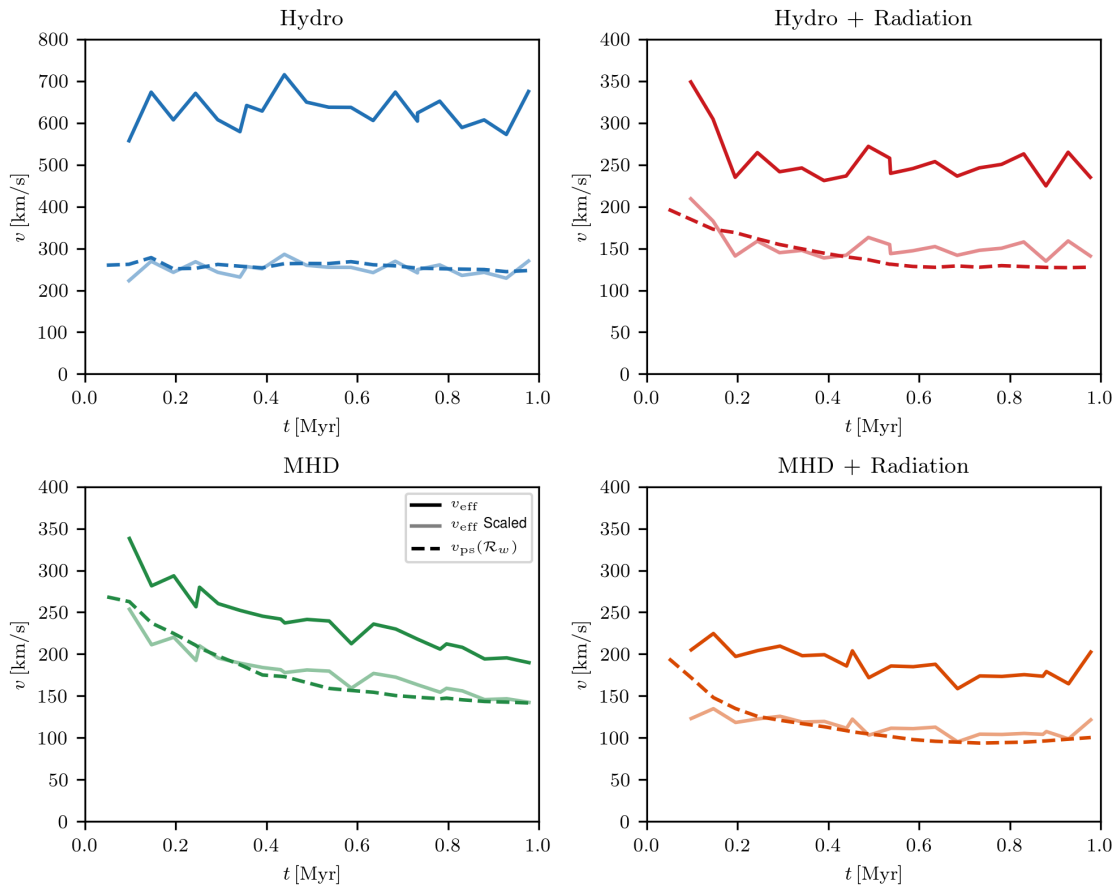

Figure 5.13 The effective mixing velocity, $v_{\rm eff}$, calculated using Equation 5.36 along with the measurements presented in Figure 5.11 and Figure 5.12 (solid lines) in each of our simulations with wind feedback. We compare this with the mean radial velocity of gas in the shocked wind gas as it reaches the mixing layer, calculated using Equation 5.37. We also include a scaled version of the $v_{\rm eff}$ measurements, equivalent to a choice of α_C in Equation 5.13, and chosen so that the scaled $v_{\rm eff}$ measurements best match the $v_{\rm ps}(\mathcal{R}_w)$ measurements (translucent solid lines). The values of α_C chosen are 0.4, 0.6, 0.75, and 0.6 for the `Hydro`, `Hydro Rad`, `MHD`, and `MHD Rad` simulations respectively. It is important to note that the results for the `Hydro` simulation are shown on a much larger scale than the other simulations.

sections, we choose $\ell = 8\Delta x \approx 0.6\,\mathrm{pc}$ in our highest resolution simulations.

As in Lancaster et al. (2021a), we want to compare this effective mixing velocity with the mean radial velocity of shocked wind gas as it reached the mixing layer. As described in Appendix A of Lancaster et al. (2021b) and reviewed in Section 5.3.1, this is given by

$$v_{\rm ps}(\mathcal{R}_w) = \frac{\mathcal{V}_w}{4}\left(\frac{\mathcal{R}_w}{\mathcal{R}_f}\right)^{-2}. \tag{5.37}$$

In Figure 5.13 we compare the evolution of these two velocity scales in time. We provide both a un-scaled and scaled version of the $v_{\rm eff}$ measurements, essentially amounting to choices of $\alpha_C = 1$ and an α_C that will bring the $v_{\rm eff}$ measurements in to closest agreement with the $v_{\rm ps}(\mathcal{R}_w)$ measurements. The chosen α_C values to get this agreement are 0.4, 0.6, 0.75, and 0.6 for the `Hydro`, `Hydro Rad`, `MHD`, and `MHD Rad` simulations respectively. It should be noted that, while these are of the same order of magnitude, these correction factors are not the same across these simulations and are not the same as the $\alpha_C = 0.25$ value used for comparison in Lancaster et al. (2021a). With that said, we have no concrete theory for what the value of α_C *should* be and it may indeed depend upon factors such as the excess fractal dimension of the TRML. With this caveat in mind, it is quite reassuring to see that, accounting for the statistical fluctuations in $v_{\rm eff}$, the general evolution of these quantities do track one another.

As we discussed in Section 5.3.1, the momentum enhancement factor, α_p, should be directly tied to the ratio $\mathcal{R}_w/\mathcal{R}_f$ as laid out in Equation 5.7. Given the fact that all of the wind-driven bubbles seem to closely follow the EC solution with $\alpha_p = 3$, as laid out in Section 5.5.1 and Section 5.5.2, it is interesting to compare the inferred α_p in each simulation from $v_{\rm ps}(\mathcal{R}_w)$. This is especially interesting given that $v_{\rm ps}(\mathcal{R}_w)$ does *not* seem consistent across the simulations in Figure 5.13.

We should note that, if we know that $v_{\rm eff} \approx v_{\rm ps}(\mathcal{R}_w)$ then α_p is also equivalently determined by $v_{\rm eff}$ through Equation 5.37. Given the results displayed in Figure 5.13, it is clear that the $v_{\rm eff} \approx v_{\rm ps}(\mathcal{R}_w)$ can be more complicated than our theory previously appreciated. For this reason we will measure the inferred momentum enhancement factor using our direct measurements of $\mathcal{R}_w/\mathcal{R}_f$, which is straightforward to measure from the simulations. We show the results of this

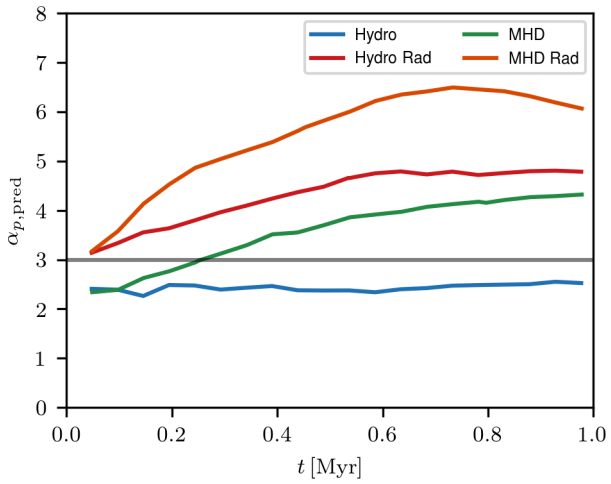

Figure 5.14 The momentum enhancement factor of the wind-driven bubble as predicted using Equation 5.7. For reference we indicate $\alpha_p = 3$ with a horizontal grey line.

calculation in Figure 5.14.

It is apparent that our simulations with background H II regions and magnetic fields exhibit significantly higher momentum enhancement at the surface of their wind-driven bubbles as compared with the `Hydro` simulation and that these differences grow in time. This is likely because, in each of these simulations, there are significant external stresses that can act at the wind-driven bubbles surface. In the case of the `MHD` simulation, there are the external stresses provided by the strong magnetic field (both pressure and tension) that is 'swept-up' at the wind-driven bubble's, this effect grows in time as the bubble drapes more and more field lines over it's surface as it grows. This stress can be some-what ameliorated if, as we discussed in Section 5.5.1, the magneto-sonic of Alfvén speed become greater than the velocity of the bubbles surface, allowing the magnetic field to rarify ahead of the bubble, transferring momentum forward. In the case of the `Hydro Rad` simulation, the cold, dense shell of the `Hydro` simulation is forced to be at $T \sim 10^4$K from the photo-ionizing radiation and hence at much higher pressure than it would otherwise be. This shell is then, presumably, over-pressured with respect to the rest of the H II region and begins to expand in to it, creating a thick shell. The inner part of this shell would presumably be in stress equilibrium

with the wind-driven bubble, meaning that the actual forces that determine the net momentum evolution are being applied somewhere within this thick shell or at it's interface with the rest of the H II region. In the `MHD Rad` simulation, both of these effects likely play a role.

In both of these scenarios, external stresses at the wind-driven bubble's surface push back on the bubble, likely coming in to a force balance at the bubble's surface, and transferring where the net forces are being applied forward radially: either in to a magnetically dominated region or a photo-ionized thick shell. If the net stress (thermal or Reynolds) drops between the wind-driven bubble's surface and the region where net forces are being exerted, it would make sense that an effective $\alpha_p > 3$ could be exerted at the bubble's surface while the net momentum injection of the solution overall still behaved as though $\alpha_p = 3$. Now, given this more complicated picture, with the external stresses, it is not clear why an overall $\alpha_p = 3$ like evolution should be maintained in the bubble evolution overall. Unraveling this mystery would depend upon a more complete theory of how the net force moves forward from the wind-driven bubble in to a thick shell or magnetically dominant region. We discuss the prospects for such a model below.

5.6 Discussion

In Section 5.5 we have demonstrated that, while all of our simulated wind-driven bubbles seem to follow some of the hallmarks of an EC solution with $\alpha_p = 3$, some aspects of the physical picture we have drawn do not hold together. In particular, when comparing the `Hydro Rad` and `MHD Rad` simulations with the joint evolution theory developed in Section 5.3.3 we see key predictions, including the predicted wind-driven bubble's effective radius (e.g. Figure 5.6), do not bare out. As suggested by the time-scale analysis carried out in Section 5.8, this is likely due to the incorrectness of our assumptions around the time-scale and nature of an equilibrium being established between the wind-driven bubble and the surrounding H II region.

In particular, our theory assumes that all of the mass swept-up by the wind-driven bubble either exists in a cold, thin shell at the bubble's surface, or is immediately evenly distributed throughout the H II region (see Section 5.8). Such a treatment ignores the fact that the shell must maintain

a temperature $T \sim 10^4\,\mathrm{K}$ and that this shell will likely come in to force equilibrium with the wind-driven bubble, forming a thick shell where actual net momentum deposition is being applied somewhere within or at the edge of the shell. The details of this process would depend upon the detailed structure the the shell takes in terms of its thermal pressure and velocity structure as a function of radius.

In fact, upon inspection of Figure 5.2, we can see that a similar phenomenon occurs in the `MHD` simulation: a 'thick shell' that carries the momentum of the wind-driven bubble and is in pressure-equilibrium with it, precedes the expansion of the wind-driven bubble. In this case, the external stress is being provided by the strength of the magnetic field that is swept-up and draped around the expanding bubble. Presumably, due to the strong presence of the magnetic fields, the structure of this thick shell will be quite different than the one present in the `Hydro Rad` simulation, yet it has a similar effect.

Before returning to some of the oddities of the behavior presented at the end of Section 5.5, let's consider what a better version of the theory for the joint evolution of the wind-driven bubble developed in Section 5.3.3 might look like. In such a theory, we would want to account for how exactly the wind-driven bubble comes in to equilibrium with the H II region. This would be most easily accomplished if we had two, coupled ODE momentum equations: one accounting for the expansion of the wind-driven bubble in to the H II region and another accounting for the back reaction of the H II region in terms of ionization status and/or its thermal expansion in to the surrounding gas. Such a model would need some assumed physical structure to the shell swept-up by the wind-driven bubble which would then determine its density and thus its effect on the ionization-recombination equilibrium of the H II region and thus the H II regions size. In the context of the inhomogeneous backgrounds that we consider here, we may also want to find a way to account for the fact that some fraction of ionizing photons are 'wasted' on low-density, under-pressurized gas that is photo-ionized far from the source as ionizing radiation moves through low-density channels. This could perhaps be quantified with an effective escape fraction that reduces Q_0. We leave the full development of this more advanced model for a joint evolution to future work.

We've established above that our theories do not account for the formation of a thick-shell

around a wind-driven bubble where the net forces may actually be applied somewhere within the shell. However, we have seen in Section 5.5.1 and Section 5.5.2 that, despite the external stresses presumably becoming significant in these thick shells, all of our simulations seem to follow an EC solution with $\alpha_p = 3$. How can this be consistent? As we have seen in Section 5.5.5, it seems as though, when facing these external stresses, the turbulence at the radiative mixing layer, and the hence the interior structure of the wind-driven bubble, adjust so that the stress being exerted at the bubble's surface increases, as we see in Figure 5.14. The fact that this adjustment occurs is interesting in and of itself, but that it occurs in such a way as to seemingly perfectly maintain an EC-like solution with $\alpha_p = 3$ solution for the wind-driven bubble is odd, to say the least. This clearly points to some governing principal of the wind-driven bubble's evolution that we are missing in our current theoretical models. Unfortunately, like the more advanced joint evolution model, we must leave this for future work.

5.7 Appendix: Stages of Spherical Wind Expansion

At the earliest stages of the expansion of a stellar wind bubble the wind expands ballistically so that the wind radius increases linearly in time: $\mathcal{R}_w = \mathcal{V}_w t$. This regime ends when the mass of the shell becomes an impediment to the ballistic expansion, causing the bubble expansion to slow and a shock to propagate backward (in the frame of the shock) in to the freely expanding wind. We can determine the radius at which this occurs by setting the mass displaced by the wind bubble, $M_{\rm sh} = 4\pi\bar{\rho}\mathcal{R}_w^3/3$, equal to the mass injected by the wind up until that time, $M_w = \dot{M}_w t = \dot{M}_w \mathcal{R}_w/\mathcal{V}_w$, which we can put together to solve for the shock radius

$$R_{\rm shock} = \sqrt{\frac{3}{4\pi}\frac{\dot{M}_w}{\mathcal{V}_w\bar{\rho}}}\,. \tag{5.38}$$

For parameters typical of an O star in a Milky Way like giant molecular cloud (GMC) ($\dot{M}_w = 3\times10^{-6}\,M_\odot\,{\rm yr}^{-1}$, $\mathcal{V}_w = 2000\,{\rm km/s}$, and $\bar{\rho} = 2\times10^{-22}\,{\rm g/cm}^3$) we have $R_{\rm shock} \approx 10^{-2}\,{\rm pc}$ which occurs at $t_{\rm shock} = \sqrt{3\dot{M}_w/4\pi\mathcal{V}_w^3\bar{\rho}} \approx 5\,{\rm yr}$. As the time-scale for early feedback is typically on

the order of millions of years (Chevance et al., 2022), this is clearly a very short lived evolutionary stage and is probably even shorter lived when one considers the realistic density distributions around newly born massive stars.

Once the wind interior has been shock heated, the next stage of the wind bubble expansion (described in Section II of Weaver et al. (1977)) consists of a pressure-driven phase before the shocked ISM has had the time to cool and condense into a thin shell. The time for this transition, the 'shell formation time,' is given by the cooling time of the swept up gas, $t_{\rm sf} \equiv e/|de/dt|$ where e is the energy density of the shocked ISM. Following similar calculations presented in the literature (e.g. Castor et al., 1975; Mac Low & McCray, 1988; Koo & McKee, 1992b; Kim et al., 2017a) we can calculate $t_{\rm sf}$ given the temperature of the shocked shell of ISM gas, $T_{\rm sh}$ and the cooling function $\Lambda(T_{\rm sh})$ of this gas. Following Mac Low & McCray (1988) we can derive

$$t_{\rm sf} = 6.5 \times 10^2 \,{\rm yr} \left(\frac{\mathcal{L}_w}{10^{37}\,{\rm erg/s}} \right)^{0.29} \left(\frac{n_{\rm H}}{100\,{\rm cm^{-3}}} \right)^{-0.71} , \tag{5.39}$$

where $n_{\rm H}$ here is the number density of hydrogen nuclei in the shocked ISM gas. Clearly, for conditions typical of star forming regions in the Milky Way, this is also a very short lived phase.

5.8 Appendix: Assumptions for Joint Evolution

In this Appendix we justify some of the assumptions that go in to our model for the joint evolution of a wind bubble and an H II region that is laid out in Section 5.3.3. This naturally leads us to discuss how the joint evolution of a wind and H II region is established and thereby the initial conditions for such an evolution in Section 5.9.

Since the initial thermal pressure in the H II region is finite, $P_{\rm II}(t=0) = \bar{\rho} c_i^2$, and the pressure in the shocked-wind in either Equation 5.3 or Equation 5.8 formally becomes infinite as $t \to 0$[1], there will be a time period during which the wind bubble expands, unimpeded, into the surrounding H II region. We can get a rough estimate of when this evolution ends by calculating when the force exerted by the shocked wind, $\alpha_p \dot{p}_w$ matches the force that would be exerted on the wind-driven

[1] Of course, these solutions only apply after some finite time, even if it is quite early in the evolution.

bubble by an H II region at the background density, $4\pi\mathcal{R}_w^2\bar{\rho}c_i^2$. This gives us force equality at a radius[2] of

$$R_E \equiv \sqrt{\frac{\alpha_p \dot{p}_w}{4\pi\bar{\rho}c_i^2}} = 1.5\,\mathrm{pc}\left(\frac{\alpha_p\dot{p}_w}{10^4\,M_\odot\,\mathrm{km/s/Myr}}\right)^{1/2}\left(\frac{\overline{n}_\mathrm{H}}{100\,\mathrm{cm}^{-3}}\right)^{-1/2}\left(\frac{c_i}{10\,\mathrm{km/s}}\right)^{-1}, \tag{5.40}$$

and a time

$$t_E \equiv \frac{1}{4\pi c_i^2}\sqrt{\frac{2\pi}{3}\frac{\alpha_p\dot{p}_w}{\bar{\rho}}} = 5.99\times10^4\,\mathrm{yr}\left(\frac{\alpha_p\dot{p}_w}{10^4\,M_\odot\,\mathrm{km/s/Myr}}\right)^{1/2}\left(\frac{\overline{n}_\mathrm{H}}{100\,\mathrm{cm}^{-3}}\right)^{-1/2}\left(\frac{c_i}{10\,\mathrm{km/s}}\right)^{-2}, \tag{5.41}$$

where we have assumed $\alpha_R = 1$. In order to see if this evolution makes up a significant fraction of the overall feedback bubble's evolution we can compare t_E to the free-fall time of a cloud, t_ff, since clouds are generally thought to be fully disrupted on the order of a few free-fall times (Chevance et al., 2020b, 2022; Lancaster et al., 2021c; Kim et al., 2021a). The free-fall time is given as

$$t_\mathrm{ff} \equiv \sqrt{\frac{3\pi}{32G\bar{\rho}}} = 4.35\times10^6\,\mathrm{yr}\left(\frac{\overline{n}_\mathrm{H}}{100\,\mathrm{cm}^{-3}}\right)^{-1/2}. \tag{5.42}$$

So we see that $t_E/t_\mathrm{ff} \sim 0.01$ is independent of the mean density of the cloud, $\bar{\rho}$, and only depends on the properties of the wind and the temperature of the H II region[3]. From this we can conclude that there is a significant fraction of the bubble's evolution that occurs while both the wind and the H II region are in pressure equilibrium.

The time-scale for this evolution to be reached is also long compared with the ionization-recombination time-scale for the gas ($\tau_i/t_E \sim 0.02$). It is then reasonable to assume that the H II region maintains ionization-recombination equilibrium during this evolution.

In setting up the initial conditions for the joint evolution we would additionally like to assume that the H II region has no dynamical effect on the background gas before the wind-bubble comes in to pressure equilibrium with it. To see if this is a valid approach we can compare t_E to the initial dynamical expansion time-scale for the Hosokawa & Inutsuka (2006) version of the Spitzer (1978)

[2]It is convenient to remember that one can also define the characteristic radius as $R_\mathrm{ch} \equiv R_E^4/R_\mathrm{St}^3$.

[3]These dependencies are also true for the equivalent expression derived from the Weaver et al. (1977) solution for the pressure, though $t_E/t_\mathrm{ff} \sim 0.16$ in this case.

solution,

$$t_{\mathrm{d},i} = \frac{R_{\mathrm{Sp}}(t=0)}{\dot{R}_{\mathrm{Sp}}(t=0)} = \frac{\sqrt{3}}{2}\frac{R_{\mathrm{St}}}{c_i} = 5.78\times10^5\,\mathrm{yr}\left(\frac{Q_0}{10^{50}\,\mathrm{s}^{-1}}\right)^{1/3}\left(\frac{\overline{n}_{\mathrm{H}}}{100\,\mathrm{cm}^{-3}}\right)^{-2/3}\left(\frac{c_i}{10\,\mathrm{km/s}}\right)^{-1}. \tag{5.43}$$

If we want to assume that the H II region doesn't evolve dynamically as it comes in to pressure equilibrium with the wind-driven bubble we want $t_E/t_{\mathrm{d},i} \ll 1$. From our calculations above we have this ratio as

$$\frac{t_E}{t_{\mathrm{d},i}} = 0.10\left(\frac{\alpha_p\dot{p}_w}{10^4\,M_\odot\,\mathrm{km/s/Myr}}\right)^{1/2}\left(\frac{Q_0}{10^{50}\,\mathrm{s}^{-1}}\right)^{-1/3}\left(\frac{\overline{n}_{\mathrm{H}}}{100\,\mathrm{cm}^{-3}}\right)^{1/6}\left(\frac{c_i}{10\,\mathrm{km/s}}\right)^{-1}. \tag{5.44}$$

So we see that $t_E/t_{\mathrm{d},i}$ is small, but not negligible. The assumption that the H II region has no dynamical effect on the background before coming in to pressure equilibrium with the wind therefore does not strictly hold. This assumption will be even worse if the wind-driven bubble evolves according to an energy-driven solution.

The comparison of t_E to $t_{\mathrm{d},i}$ is also important for the validity of an equilibrium being quickly established between the wind bubble and the H II region. As the wind bubble rapidly expands to reach equilibrium with the H II region, it sweeps up mass that is photo-ionized and heated to the H II region's temperature, T_{II}. This shell of photo-ionized gas will be in equilibrium with the wind bubble on its interior edge and overly-dense (and therefore overly pressurized) with respect to the rest of the H II region on it's outer edge. The mass in this shell will be redistributed throughout the region roughly over the sound-crossing time, $t_{\mathrm{d},i}$, but as we saw above, this is only a few times larger than the equilibrium time, t_E. So a true equilibrium, with the H II region at a constant density, the shell having re-distributed its mass, will only properly occur after a few sound crossing times (depending on the ratio of R_E to R_{St}). All of this to say, our model assumes that the equilibrium is set up relatively quickly, and this may not be the case, as we will see in our simulations.

5.9 Appendix: Initial Conditions for Joint Evolution

In order to solve Equation 5.25, which is a second order, non-linear ODE we will need a two initial conditions (i) interchangeably $\mathcal{R}_{i,0} = \mathcal{R}_i(t = 0)$ or $\mathcal{R}_{w,0}$ and (ii) the derivative in time of either of these. Below we will discuss multiple different choices that could be made for both initial conditions. We will choose which to use based on which provides the best comparison against our simulations.

Assuming that the wind bubble is in pressure equilibrium with the H II region throughout the evolution gives us Equation 5.26. Applying this condition at $t = 0$ would give us our initial condition for $\mathcal{R}_w$ if we knew the initial density in the H II region, $\rho_{i,0}$. There are a few different assumptions we could make here, basically related to different assumptions on how mass that is swept up by the wind is redistributed in the H II region.

We could assume, as in the Spitzer solution, that $\rho_{i,0} = \bar{\rho}$. This would be equivalent to assuming that the wind bubble has swept up a shell of material without disturbing the rest of the H II region and that that mass is considered part of the wind bubble, even though it would be at $T \sim 10^4\,\mathrm{K}$. However, if this shell is at $T \sim 10^4\,\mathrm{K}$ and at much higher densities than the H II region, this would break our assumption of force balance within the bubble. That aside, taking $\rho_{i,0} = \bar{\rho}$ would give us $\mathcal{R}_{w,0} = R_E$. We will call this first choice for the initial condition $\mathcal{R}^{(i)}_{w,0}$.

We could also assume that the mass that has been displaced by the wind-driven bubble is distributed evenly throughout the H II region at the beginning of the evolution so that

$$\frac{4\pi}{3}\bar{\rho}\mathcal{R}^3_{i,0} = \frac{4\pi}{3}\rho_{i,0}\left(\mathcal{R}^3_{i,0} - \mathcal{R}^3_{w,0}\right) .$$

It is important to keep in mind that this is at odds with our assumption that the H II region has no dynamical effect before it comes into pressure equilibrium with the wind-driven bubble, since we are assuming here that the H II region is able to dynamically redistribute its mass on a short timescale. That aside, Using this equation along with Equation 5.26 and Equation 5.29 gives us a

quadratic equation for $\mathcal{R}_{w,0}$ with solution

$$\mathcal{R}_{w,0} = R_E \left(\sqrt{1 + \frac{R_E^6}{4R_{\rm St}^6}} - \frac{R_E^3}{2R_{\rm St}^3} \right) . \tag{5.45}$$

This represents essentially the opposite extreme of the assumption on the initial density. We will call this first choice for the initial condition $\mathcal{R}_{w,0}^{(ii)}$.

Next we need a condition for what the time derivative of $\mathcal{R}_i$ or $\mathcal{R}_w$ is. The simplest assumption would be $\dot{\mathcal{R}}_i = \dot{\mathcal{R}}_w = 0$, which would make sense with our assumption that the H II region has had no dynamical effect on the background when the joint evolution begins. We will refer to this choice as $\dot{\mathcal{R}}_{i,0}^{(i)}$. However, this would also mean that we would start with zero momentum, ignoring the momentum that the wind has already injected at this point.

We could also take motivation from the Spitzer solution to assume

$$\frac{d\mathcal{R}_i}{dt}(t=0) = \frac{2c_i}{\sqrt{3}} , \tag{5.46}$$

though this would mostly work for simplicity and easy of comparison to the Spitzer (1978) solution. We will refer to this choice as $\dot{\mathcal{R}}_{i,0}^{(ii)}$.

Finally, we could also require that the initial momentum match the momentum that has been injected by the wind while the equilibrium has been set up. This would give us

$$\frac{d\mathcal{R}_i}{dt}(t=0) = \frac{3\alpha_p \dot{p}_w t_E}{4\pi\bar{\rho}\mathcal{R}_{i,0}^3} . \tag{5.47}$$

We will refer to this choice as $\dot{\mathcal{R}}_{i,0}^{(iii)}$.

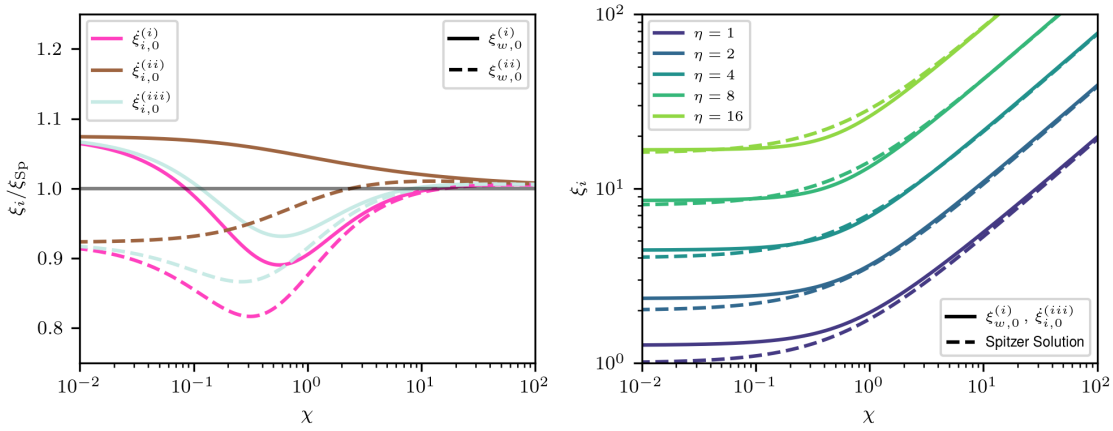

Figure 5.15 We examine solutions to our equation for an effective joint evolution of a wind-driven bubble and an H II region, Equation 5.49. *Left Panel*: For an assumed value of $\eta = 6.63$ (appropriate for the simulations presented in Section 5.5) we examine the effects of the various initial conditions proposed in Section 5.9, relative to the Spitzer solution, Equation 5.53. *Right Panel*: We compare our numerical solution for Equation 5.49 with the initial conditions corresponding to the solid, light blue line in the left panel, to the Spitzer solution for several values of η.

5.10 Appendix: Dimensionless Equation for Joint Evolution

In order to quickly explore the parameter space it is helpful to describe the joint evolution equation, Equation 5.25, in dimensionless form. To that end we can define

$$\xi \equiv \frac{\mathcal{R}}{R_{\rm ch}} \ , \ \chi \equiv \frac{t}{t_{{\rm d},i}} \tag{5.48}$$

where $t_{{\rm d},i}$ is the initial dynamical expansion time of the Strömgren Sphere, defined in Section 5.8. In this way we have $\xi_i \equiv \mathcal{R}_i / R_{\rm ch}$ and $\xi_w \equiv \mathcal{R}_w / R_{\rm ch}$. With these definitions our equation becomes

$$\frac{d}{d\chi}\left(\xi_i^3 \frac{d\xi_i}{d\chi}\right) = \frac{9}{4}\eta^{7/2}\left(1+\xi_w\right)^{2/3} \tag{5.49}$$

with η the one free parameter of the model defined as,

$$\eta \equiv \frac{R_{\rm St}}{R_{\rm ch}} \tag{5.50}$$

essentially quantifying the relative strength of the wind and photo-ionized gas. For $\eta < 1$ the Strömgren sphere will be contained within $R_{\rm ch}$ and the feedback bubble will most-likely be dominated by the wind expansion for a significant fraction of its lifetime. Our model assumes that the wind-driven bubble and the H II region have come in to equilibrium with one another, which generally is only a valid assumption when η is significantly larger than 1. Of course, for $\eta \gg 1$, the H II region is mostly undisturbed by the wind-driven bubble and then our model is not useful for the opposite reason. In our simulations we have $\eta = 6.63$ for $\alpha_p = 3$.

For the definitions given in Equation 5.48 we can re-write our initial conditions on $\mathcal{R}_{w,0}$ given above as:

$$(i)\ \xi_{w,0} = \eta^{3/4} \quad , \quad (ii)\ \xi_{w,0} = \sqrt{\eta^{3/2} + \frac{1}{4}} - \frac{1}{2} \tag{5.51}$$

either of which then gives us $\xi_{i,0} = \xi_{w,0}(1 + \xi_{w,0})^{1/3}$. Our initial conditions on $d\mathcal{R}_i/dt$ are

$$(i)\ \dot{\xi}_{i,0} = 0 \quad , \quad (ii)\ \dot{\xi}_{i,0} = \eta \quad , \quad (iii)\ \dot{\xi}_{i,0} = \frac{3\eta^{13/4}}{2\sqrt{2}\xi_{i,0}^3} \ , \tag{5.52}$$

where $\dot{\xi} \equiv d\xi/d\chi$. We will refer to the two initial conditions on $\xi_{w,0}$ as $\xi_{w,0}^{(i)}$ and $\xi_{w,0}^{(ii)}$, and the three initial conditions on $\dot{\xi}_{i,0}$ as $\dot{\xi}_{i,0}^{(i)}$, $\dot{\xi}_{i,0}^{(ii)}$, and $\dot{\xi}_{i,0}^{(iii)}$.

We can also write the Spitzer solution, Equation 5.22, in dimensionless form as

$$\xi_{\rm Sp} = \eta \left(1 + \frac{7}{4}\chi\right)^{4/7} . \tag{5.53}$$

In Figure 5.15 we compare the various initial conditions we have laid out here to the Spitzer solution as given in Equation 5.53. It is clear from the left hand panel of Figure 5.15 that while all of the different initial conditions approach a limit that is quite similar (if not slightly advanced from) the Spitzer solution, the early time evolution is considerably different.

We will ultimately choose between these different initial condition options by comparing against our simulations. However, it is enlightening to perform this comparison in as many different physically meaningful variables as possible, to ensure that the solution indeed matches our expectations. The most meaningful physical variable to compare against, in addition to the bubble's effective

radius, is the momentum carried by the bubble. However, as we noted in Section 5.3.2, with a numerical model like this it is important to carefully discriminate your interpretation of the momentum output by the model. As in the Spitzer solution, this essentially reduces to different choices for the mass carried in the bubble's shell, $M_{\rm sh}$. The simplest interpretation is to take $M_{\rm sh} = 4\pi\bar{\rho}\mathcal{R}_i^3/3$, as we assumed in writing down Equation 5.25 (or equivalently, Equation 5.49). This assumption would lead us to the solution for the total momentum carried by the bubble

$$p_{r,1} = M_{\rm sh}\frac{d\mathcal{R}_i}{dt} = \frac{4\pi}{3}\bar{\rho}R_{\rm ch}^3\frac{t_{{\rm d},i}}{R_{\rm ch}}\xi_i^3\dot{\xi}_i \tag{5.54}$$

where we have assumed a solution for $\xi(\chi)$ is given.

This chosen interpretation of the momentum may be appropriate if, for example, we chose the $\dot{\xi}_{i,0}^{(iii)}$ initial condition, which gives a physically meaningful initial starting point for the momentum equation, thereby assigning more physical meaning to the momentum used in the evolution equation. If, however, we used $\dot{\xi}_{i,0}^{(ii)}$, which is simply based on the Spitzer solution, we would likely want to subtract the mass included in the bubble interior from $M_{\rm sh}$. If we take $M_{\rm sh} = 4\pi\bar{\rho}\mathcal{R}_i^3 - 4\pi\rho_i(\mathcal{R}_i^3 - \mathcal{R}_w^3)/3$, this would give us the momentum as

$$p_{r,2} = p_{r,1}\left(1 - \frac{\eta^{3/2}}{\xi_w(1+\xi_w)}\right). \tag{5.55}$$

This would be especially appropriate for the $\xi_{w,0}^{(ii)}$ initial condition, where we have assumed the mass swept-up by the wind shell has been redistributed within the H II region, so that this would be an accurate accounting of the mass contained within the bubble. Of course, all of these predictions assume that all of the momentum is carried in the shell, which can itself be an inaccurate description of the evolution, as we discussed at the end of Section 5.8.

Chapter 6

Prospects for Future Work

While the dynamics of feedback bubbles around massive stars are such a fundamental aspect of star formation in our universe, as we outlined in Chapter 1, there is a reason that, after ostensibly 80 years of study, there is still ongoing work to be done. Principally, this because there is *so much physics* that is relevant to the dynamics of these objects and often simply including one additional physical reality or effect can re-orient one's entire understanding of the dynamics. I am grateful to have, with this dissertation, been so fortunate as to been able to investigate and explain (to some extent) some small piece of this puzzle. With that in mind, there are of course several possible avenues for work to extend the work of this thesis.

The most obvious first avenue for follow-up work is to provide a solid theoretical understanding for the results presented in Chapter 5. At the end of that chapter we described how the formation of thick-shells of dense gas around the wind-driven bubbles in our simulations with photo-ionizing radiation and background magnetic fields imply that there are significant forces being applied at the wind-driven bubble's surface, these forces tend to increase in time as the bubble sweeps up more gas, both creating an even more over-pressurized section of the H II region and/or creating a stronger magnetic field at the interface. Correspondingly, we see a decrease in the effective mixing at the bubble's turbulent, radiative mixing layer in these simulations, and an increase in the effective stress being applied at the wind-driven bubble's surface. That is, the wind-driven bubble feels the

exterior forces, and adjusts so that it exerts a larger force. The balance of these effects seems to play out in a way that maintains the same wind-driven bubble evolution that we see in the purely hydrodynamical case. How exactly this occurs requires the development of a more sophisticated theory that explains the development of these thick shells around the wind-driven bubbles. The development of such a theory is necessary for the work in Chapter 5 to be considered finished.

Moving beyond this, we would more generally like to include more aspects of feedback processes from massive stars in to our theoretical picture of the evolution of feedback bubbles. Principal among these is the effect of direct radiation pressure. Inclusion of this effect should change the density structure of the H II region (Draine, 2011b; Kim et al., 2016), thus likely affecting how the shell around the wind-driven bubble develops as it expands in to the H II region. Additionally, the effects of re-processed infrared radiation from dust grains may be an important factor to consider in some parts of the parameter space of star formation in the universe. However, recent theoretical investigations have suggested that this is not the case (Skinner & Ostriker, 2015; Menon et al., 2022).

Underlying the theory of our efficiently cooled wind-driven bubble solution, as outlined in Chapter 2, is the theory of turbulent, radiative mixing layers (TRMLs) of Fielding et al. (2020). In fact there are many other works that have explored this topic (Gronke & Oh, 2018, 2020a,b; Tan et al., 2021; Yang & Ji, 2022). Despite this extensive work, there are many outlying questions about the dynamics of these mixing layers. Of particular importance to our application of TRMLs is the effect that thermal conduction across the interface has in both creating the intermediate temperature gas that cools efficiently and thermally evaporating gas from the mixing layer, thus mass-loading the wind-driven bubble. In our simulations, and indeed in the simulations of Fielding et al. (2020), all intermediate temperature gas is created through numerical mixing of the hot and cold gas. In reality, this gas should be created through thermal conduction. Though the effect of conduction are explored in Tan et al. (2021), in reality there will be anisotropic thermal conduction across this interface due to the presence of background magnetic fields. Investigating how this plays out in detail is extremely important to understanding how TRMLs work in the context of stellar wind-driven bubbles.

Finally, throughout this dissertation we have presented several theoretical models which we have compared to detailed, three-dimensional simulations of the relevant processes. However, we have only provided, in Chapter 2, minimal comparisons of the predictions of these models to real world observations of star-forming regions. This work was, after all, in part motivated by the apparent missing wind energy in star-forming regions in the Milky Way and Large Magellanic Cloud (Lopez et al., 2011; Rosen et al., 2014). This lack of comparison was partly by design: since the works of Chapter 2 and Chapter 3 did not include the important dynamical effects of photo-ionizing radiation, background magnetic fields, and direct radiation pressure, we did not feel that they were really compatible with comparison to real star-forming regions. However, we have now run several simulations with all (except direct radiation pressure) of these important physical effects. We now believe that we can provide meaningful comparisons to observed star-forming regions in the Milky Way. This is especially timely given the ongoing work of the SOFIA Legacy program FEEDBACK (Schneider et al., 2020), which aims to provide a spectroscopic survey of [C II] 158μm and [O III] 63μm emission in several star-forming regions in the Milky Way, allowing for detailed dynamical constraints on the photo-dissociation regions (PDRs). Combining this data with archival X-ray observations from *Chandra* to track the wind-driven bubbles along with upcoming radio recombination line surveys (Anderson et al., 2021), which provide insight in to the structure of the H II region, will likely allow for some strong physical constraints on the dynamics of these regions. Further, the full-information of our three-dimensional simulations will likely allow us to test some of the assumptions that observers use to interpret their data, for example: the clumping factor of ionized gas: $\left\langle n_{\mathrm{H},i}^2 \right\rangle / \left\langle n_{\mathrm{H},i} \right\rangle^2$.

With these future works we may be able to finally come to understand one key part of the vast and interesting problem of how star formation works in our universe. Though, given past experience, it seems likely that there will be complicating surprises along the way.

Bibliography

Abbott, D. C. 1982, ApJ, 259, 282, doi: 10.1086/160166

Agertz, O., Kravtsov, A. V., Leitner, S. N., & Gnedin, N. Y. 2013, ApJ, 770, 25, doi: 10.1088/0004-637X/770/1/25

Anderson, L. D., Luisi, M., Liu, B., et al. 2021, ApJS, 254, 28, doi: 10.3847/1538-4365/abef65

Avedisova, V. S. 1972, Soviet Ast., 15, 708

Badjin, D. A., Glazyrin, S. I., Manukovskiy, K. V., & Blinnikov, S. I. 2016, MNRAS, 459, 2188, doi: 10.1093/mnras/stw790

Bailin, J. 2018, ApJ, 863, 99, doi: 10.3847/1538-4357/aad178

Bally, J. 2016, AR&AA, 54, 491, doi: 10.1146/annurev-astro-081915-023341

Barnes, A. T., Longmore, S. N., Battersby, C., et al. 2017, MNRAS, 469, 2263, doi: 10.1093/mnras/stx941

Barnes, A. T., Longmore, S. N., Dale, J. E., et al. 2020, MNRAS, 498, 4906, doi: 10.1093/mnras/staa2719

Bastian, N., & Lardo, C. 2018, AR&AA, 56, 83, doi: 10.1146/annurev-astro-081817-051839

Blondin, J. M., Wright, E. B., Borkowski, K. J., & Reynolds, S. P. 1998, ApJ, 500, 342, doi: 10.1086/305708

Bucciantini, N., Amato, E., Bandiera, R., Blondin, J. M., & Del Zanna, L. 2004, A&A, 423, 253, doi: 10.1051/0004-6361:20040360

Cantó, J., Raga, A. C., & Rodríguez, L. F. 2000, ApJ, 536, 896, doi: 10.1086/308983

Capriotti, E. R., & Kozminski, J. F. 2001, PASP, 113, 677, doi: 10.1086/320809

Castor, J., McCray, R., & Weaver, R. 1975, ApJL, 200, L107, doi: 10.1086/181908

Cheng, Y., Wang, Q. D., & Lim, S. 2021, MNRAS, 504, 1627, doi: 10.1093/mnras/stab1040

Chevalier, R. A., & Clegg, A. W. 1985, Nature, 317, 44, doi: 10.1038/317044a0

Chevance, M., Kruijssen, J. M. D., Vazquez-Semadeni, E., et al. 2020a, SSRv, 216, 50, doi: 10.1007/s11214-020-00674-x

Chevance, M., Kruijssen, J. M. D., Hygate, A. P. S., et al. 2020b, MNRAS, 493, 2872, doi: 10.1093/mnras/stz3525

Chevance, M., Kruijssen, J. M. D., Krumholz, M. R., et al. 2022, MNRAS, 509, 272, doi: 10.1093/mnras/stab2938

Choi, J., Dotter, A., Conroy, C., et al. 2016, ApJ, 823, 102, doi: 10.3847/0004-637X/823/2/102

Cowie, L. L., & McKee, C. F. 1977, ApJ, 211, 135, doi: 10.1086/154911

Dale, J. E. 2017, MNRAS, 467, 1067, doi: 10.1093/mnras/stx028

Dale, J. E., & Bonnell, I. A. 2008, MNRAS, 391, 2, doi: 10.1111/j.1365-2966.2008.13802.x

Dale, J. E., Ercolano, B., & Bonnell, I. A. 2012, MNRAS, 424, 377, doi: 10.1111/j.1365-2966.2012.21205.x

Dale, J. E., Ngoumou, J., Ercolano, B., & Bonnell, I. A. 2013, MNRAS, 436, 3430, doi: 10.1093/mnras/stt1822

—. 2014, MNRAS, 442, 694, doi: 10.1093/mnras/stu816

Draine, B. T. 2011a, Physics of the Interstellar and Intergalactic Medium

—. 2011b, ApJ, 732, 100, doi: 10.1088/0004-637X/732/2/100

Dunne, B. C., Chu, Y.-H., Chen, C. H. R., et al. 2003, ApJ, 590, 306, doi: 10.1086/375010

Dwarkadas, V. V. 2022, Galaxies, 10, 37, doi: 10.3390/galaxies10010037

Dwarkadas, V. V., & Rosenberg, D. L. 2013, High Energy Density Physics, 9, 226, doi: 10.1016/j.hedp.2012.12.003

Ekström, S., Georgy, C., Eggenberger, P., et al. 2012, A&A, 537, A146, doi: 10.1051/0004-6361/201117751

El-Badry, K., Ostriker, E. C., Kim, C.-G., Quataert, E., & Weisz, D. R. 2019, MNRAS, 490, 1961, doi: 10.1093/mnras/stz2773

Elmergreen, B. G. 1976, ApJ, 205, 405, doi: 10.1086/154291

Emig, K. L., Bolatto, A. D., Leroy, A. K., et al. 2020, ApJ, 903, 50, doi: 10.3847/1538-4357/abb67d

Evans, Neal J., I., Heyer. Marc-Antoine Miville-Deschênes, M., & Merello, Q. N.-L. M. 2021, arXiv e-prints, arXiv:2107.05750. https://arxiv.org/abs/2107.05750

Evans, Neal J., I., Dunham, M. M., Jørgensen, J. K., et al. 2009, ApJS, 181, 321, doi: 10.1088/0067-0049/181/2/321

Fall, S. M., Krumholz, M. R., & Matzner, C. D. 2010, ApJL, 710, L142, doi: 10.1088/2041-8205/710/2/L142

Falle, S. A. E. G. 1975, A&A, 43, 323

Faucher-Giguère, C.-A., & Quataert, E. 2012, MNRAS, 425, 605, doi: 10.1111/j.1365-2966.2012.21512.x

Fielding, D. B., Ostriker, E. C., Bryan, G. L., & Jermyn, A. S. 2020, ApJL, 894, L24, doi: 10.3847/2041-8213/ab8d2c

Fierlinger, K. M., Burkert, A., Ntormousi, E., et al. 2016, MNRAS, 456, 710, doi: 10.1093/mnras/stv2699

Folini, D., & Walder, R. 2006, A&A, 459, 1, doi: 10.1051/0004-6361:20053898

Franco, J., Shore, S. N., & Tenorio-Tagle, G. 1994, ApJ, 436, 795, doi: 10.1086/174955

Freeman, K., & Bland-Hawthorn, J. 2002, AR&AA, 40, 487, doi: 10.1146/annurev.astro.40.060401.093840

Fujita, S., Tsutsumi, D., Ohama, A., et al. 2021, PASJ, 73, S273, doi: 10.1093/pasj/psaa005

Fukushima, H., Yajima, H., Sugimura, K., et al. 2020, MNRAS, 497, 3830, doi: 10.1093/mnras/staa2062

Gagné, M., Oksala, M. E., Cohen, D. H., et al. 2005, ApJ, 628, 986, doi: 10.1086/430873

Garcia-Segura, G., Langer, N., & Mac Low, M. M. 1996a, A&A, 316, 133

Garcia-Segura, G., Mac Low, M. M., & Langer, N. 1996b, A&A, 305, 229

Gardiner, T. A., & Stone, J. M. 2005, Journal of Computational Physics, 205, 509, doi: 10.1016/j.jcp.2004.11.016

Gatto, A., Walch, S., Naab, T., et al. 2017, MNRAS, 466, 1903, doi: 10.1093/mnras/stw3209

Geen, S., Bieri, R., Rosdahl, J., & de Koter, A. 2021, MNRAS, 501, 1352, doi: 10.1093/mnras/staa3705

Geen, S., Hennebelle, P., Tremblin, P., & Rosdahl, J. 2015a, MNRAS, 454, 4484, doi: 10.1093/mnras/stv2272

—. 2016, MNRAS, 463, 3129, doi: 10.1093/mnras/stw2235

Geen, S., Pellegrini, E., Bieri, R., & Klessen, R. 2020, MNRAS, 492, 915, doi: 10.1093/mnras/stz3491

Geen, S., Rosdahl, J., Blaizot, J., Devriendt, J., & Slyz, A. 2015b, MNRAS, 448, 3248, doi: 10.1093/mnras/stv251

Geen, S., Soler, J. D., & Hennebelle, P. 2017, MNRAS, 471, 4844, doi: 10.1093/mnras/stx1765

Girichidis, P., Offner, S. S. R., Kritsuk, A. G., et al. 2020, SSRv, 216, 68, doi: 10.1007/s11214-020-00693-8

Gong, H., & Ostriker, E. C. 2013, ApJS, 204, 8, doi: 10.1088/0067-0049/204/1/8

Gratton, R., Bragaglia, A., Carretta, E., et al. 2019, A&A Rv, 27, 8, doi: 10.1007/s00159-019-0119-3

Gronke, M., & Oh, S. P. 2018, MNRAS, 480, L111, doi: 10.1093/mnrasl/sly131

—. 2020a, MNRAS, 492, 1970, doi: 10.1093/mnras/stz3332

—. 2020b, MNRAS, 494, L27, doi: 10.1093/mnrasl/slaa033

Grudić, M. Y., Guszejnov, D., Hopkins, P. F., Offner, S. S. R., & Faucher-Giguére, C.-A. 2021, MNRAS, doi: 10.1093/mnras/stab1347

Grudić, M. Y., & Hopkins, P. F. 2019, MNRAS, 488, 2970, doi: 10.1093/mnras/stz1820

Grudić, M. Y., Hopkins, P. F., Faucher-Giguère, C.-A., et al. 2018, MNRAS, 475, 3511, doi: 10.1093/mnras/sty035

Grudić, M. Y., Kruijssen, J. M. D., Faucher-Giguère, C.-A., et al. 2020, arXiv e-prints, arXiv:2008.04453. https://arxiv.org/abs/2008.04453

Güdel, M., Briggs, K. R., Montmerle, T., et al. 2008, Science, 319, 309, doi: 10.1126/science.1149926

Haid, S., Walch, S., Seifried, D., et al. 2018, MNRAS, 478, 4799, doi: 10.1093/mnras/sty1315

Harper-Clark, E., & Murray, N. 2009, ApJ, 693, 1696, doi: 10.1088/0004-637X/693/2/1696

Haugbølle, T., Padoan, P., & Nordlund, Å. 2018, ApJ, 854, 35, doi: 10.3847/1538-4357/aaa432

He, C.-C., Ricotti, M., & Geen, S. 2019, MNRAS, 489, 1880, doi: 10.1093/mnras/stz2239

Hennebelle, P., & Iffrig, O. 2014, A&A, 570, A81, doi: 10.1051/0004-6361/201423392

Heyer, M., & Dame, T. M. 2015, AR&AA, 53, 583, doi: 10.1146/annurev-astro-082214-122324

Hosek, Matthew W., J., Lu, J. R., Anderson, J., et al. 2019, ApJ, 870, 44, doi: 10.3847/1538-4357/aaef90

Hosokawa, T., & Inutsuka, S.-i. 2006, ApJ, 646, 240, doi: 10.1086/504789

Howard, C. S., Pudritz, R. E., & Harris, W. E. 2017, MNRAS, 470, 3346, doi: 10.1093/mnras/stx1363

Iffrig, O., & Hennebelle, P. 2015, A&A, 576, A95, doi: 10.1051/0004-6361/201424556

Johnson, K. E., Leroy, A. K., Indebetouw, R., et al. 2015, ApJ, 806, 35, doi: 10.1088/0004-637X/806/1/35

Jones, B. D., & Williams, J. R. 2017, Engineering Computations, 34, 1204, doi: 10.1108/EC-02-2016-0052

Kennicutt, Robert C., J. 1998, AR&AA, 36, 189, doi: 10.1146/annurev.astro.36.1.189

Kim, C.-G., Kim, W.-T., & Ostriker, E. C. 2008, ApJ, 681, 1148, doi: 10.1086/588752

Kim, C.-G., & Ostriker, E. C. 2017, ApJ, 846, 133, doi: 10.3847/1538-4357/aa8599

—. 2018, ApJ, 853, 173, doi: 10.3847/1538-4357/aaa5ff

Kim, C.-G., Ostriker, E. C., & Kim, W.-T. 2013, ApJ, 776, 1, doi: 10.1088/0004-637X/776/1/1

Kim, C.-G., Ostriker, E. C., & Raileanu, R. 2017a, ApJ, 834, 25, doi: 10.3847/1538-4357/834/1/25

Kim, C.-G., Ostriker, E. C., Somerville, R. S., et al. 2020a, ApJ, 900, 61, doi: 10.3847/1538-4357/aba962

Kim, C.-G., Ostriker, E. C., Fielding, D. B., et al. 2020b, ApJL, 903, L34, doi: 10.3847/2041-8213/abc252

Kim, J.-G., Kim, W.-T., & Ostriker, E. C. 2016, ApJ, 819, 137, doi: 10.3847/0004-637X/819/2/137

—. 2018, ApJ, 859, 68, doi: 10.3847/1538-4357/aabe27

—. 2019a, ApJ, 883, 102, doi: 10.3847/1538-4357/ab3d3d

—. 2019b, ApJ, 883, 102, doi: 10.3847/1538-4357/ab3d3d

Kim, J.-G., Kim, W.-T., Ostriker, E. C., & Skinner, M. A. 2017b, ApJ, 851, 93, doi: 10.3847/1538-4357/aa9b80

Kim, J.-G., Ostriker, E. C., & Filippova, N. 2021a, ApJ, 911, 128, doi: 10.3847/1538-4357/abe934

—. 2021b, ApJ, 911, 128, doi: 10.3847/1538-4357/abe934

Klein, R. I., McKee, C. F., & Colella, P. 1994, ApJ, 420, 213, doi: 10.1086/173554

Koo, B.-C., & McKee, C. F. 1992a, ApJ, 388, 93, doi: 10.1086/171132

—. 1992b, ApJ, 388, 103, doi: 10.1086/171133

Koyama, H., & Inutsuka, S.-i. 2002, ApJL, 564, L97, doi: 10.1086/338978

Krause, M., Fierlinger, K., Diehl, R., et al. 2013, A&A, 550, A49, doi: 10.1051/0004-6361/201220060

Krause, M. G. H., Charbonnel, C., Bastian, N., & Diehl, R. 2016, A&A, 587, A53, doi: 10.1051/0004-6361/201526685

Krause, M. G. H., & Diehl, R. 2014, ApJL, 794, L21, doi: 10.1088/2041-8205/794/2/L21

Kroupa, P. 2001, MNRAS, 322, 231, doi: 10.1046/j.1365-8711.2001.04022.x

Kruijssen, J. M. D., Schruba, A., Chevance, M., et al. 2019, Nature, 569, 519, doi: 10.1038/s41586-019-1194-3

Krumholz, M. R., & Matzner, C. D. 2009, ApJ, 703, 1352, doi: 10.1088/0004-637X/703/2/1352

Krumholz, M. R., McKee, C. F., & Bland -Hawthorn, J. 2019, AR&AA, 57, 227, doi: 10.1146/annurev-astro-091918-104430

Krumholz, M. R., & Tan, J. C. 2007, ApJ, 654, 304, doi: 10.1086/509101

Lada, C. J., Lombardi, M., & Alves, J. F. 2010, ApJ, 724, 687, doi: 10.1088/0004-637X/724/1/687

Lancaster, L., Ostriker, E. C., Kim, J.-G., & Kim, C.-G. 2021a, ApJ, 914, 90, doi: 10.3847/1538-4357/abf8ac

—. 2021b, ApJ, 914, 89, doi: 10.3847/1538-4357/abf8ab

—. 2021c, ApJL, 922, L3, doi: 10.3847/2041-8213/ac3333

Larson, R. B. 1969, MNRAS, 145, 405, doi: 10.1093/mnras/145.4.405

Lee, E. J., Miville-Deschênes, M.-A., & Murray, N. W. 2016, ApJ, 833, 229, doi: 10.3847/1538-4357/833/2/229

Leitherer, C., Ekström, S., Meynet, G., et al. 2014, ApJS, 212, 14, doi: 10.1088/0067-0049/212/1/14

Leitherer, C., Robert, C., & Drissen, L. 1992, ApJ, 401, 596, doi: 10.1086/172089

Leitherer, C., Schaerer, D., Goldader, J. D., et al. 1999, ApJS, 123, 3, doi: 10.1086/313233

Leroy, A. K., Schinnerer, E., Hughes, A., et al. 2017, ApJ, 846, 71, doi: 10.3847/1538-4357/aa7fef

Leroy, A. K., Bolatto, A. D., Ostriker, E. C., et al. 2018, ApJ, 869, 126, doi: 10.3847/1538-4357/aaecd1

Levy, R. C., Bolatto, A. D., Leroy, A. K., et al. 2020, arXiv e-prints, arXiv:2011.05334. https://arxiv.org/abs/2011.05334

Li, H., Vogelsberger, M., Marinacci, F., & Gnedin, O. Y. 2019a, MNRAS, 487, 364, doi: 10.1093/mnras/stz1271

—. 2019b, MNRAS, 487, 364, doi: 10.1093/mnras/stz1271

Lochhaas, C., & Thompson, T. A. 2017, MNRAS, 470, 977, doi: 10.1093/mnras/stx1289

Lopez, L. A., Krumholz, M. R., Bolatto, A. D., Prochaska, J. X., & Ramirez-Ruiz, E. 2011, ApJ, 731, 91, doi: 10.1088/0004-637X/731/2/91

Lopez, L. A., Krumholz, M. R., Bolatto, A. D., et al. 2014, ApJ, 795, 121, doi: 10.1088/0004-637X/795/2/121

Lu, J. R., Do, T., Ghez, A. M., et al. 2013, ApJ, 764, 155, doi: 10.1088/0004-637X/764/2/155

Lucy, L. B., & Solomon, P. M. 1970, ApJ, 159, 879, doi: 10.1086/150365

Mac Low, M.-M., & McCray, R. 1988, ApJ, 324, 776, doi: 10.1086/165936

Mackey, J., Gvaramadze, V. V., Mohamed, S., & Langer, N. 2015, A&A, 573, A10, doi: 10.1051/0004-6361/201424716

Matzner, C. D. 2002, ApJ, 566, 302, doi: 10.1086/338030

Matzner, C. D., & McKee, C. F. 2000, ApJ, 545, 364, doi: 10.1086/317785

McCrady, N., Graham, J. R., & Vacca, W. D. 2005, ApJ, 621, 278, doi: 10.1086/427487

McCray, R., & Kafatos, M. 1987, ApJ, 317, 190, doi: 10.1086/165267

McKee, C. F., van Buren, D., & Lazareff, B. 1984, ApJL, 278, L115, doi: 10.1086/184237

McLeod, A. F., Dale, J. E., Evans, C. J., et al. 2019, MNRAS, 486, 5263, doi: 10.1093/mnras/sty2696

McLeod, A. F., Kruijssen, J. M. D., Weisz, D. R., et al. 2020, ApJ, 891, 25, doi: 10.3847/1538-4357/ab6d63

Menon, S. H., Federrath, C., & Krumholz, M. R. 2022, arXiv e-prints, arXiv:2206.14190. https://arxiv.org/abs/2206.14190

Michaut, C., Cavet, C., Bouquet, S. E., Roy, F., & Nguyen, H. C. 2012, ApJ, 759, 78, doi: 10.1088/0004-637X/759/2/78

Murray, N. 2011, ApJ, 729, 133, doi: 10.1088/0004-637X/729/2/133

Murray, N., Quataert, E., & Thompson, T. A. 2010, ApJ, 709, 191, doi: 10.1088/0004-637X/709/1/191

Nakamura, F., McKee, C. F., Klein, R. I., & Fisher, R. T. 2006, ApJS, 164, 477, doi: 10.1086/501530

Ntormousi, E., Burkert, A., Fierlinger, K., & Heitsch, F. 2011, ApJ, 731, 13, doi: 10.1088/0004-637X/731/1/13

Oey, M. S., Herrera, C. N., Silich, S., et al. 2017, ApJL, 849, L1, doi: 10.3847/2041-8213/aa9215

Offner, S. S. R., & Chaban, J. 2017, ApJ, 847, 104, doi: 10.3847/1538-4357/aa8996

Offner, S. S. R., & Liu, Y. 2018, Nature Astronomy, 2, 896, doi: 10.1038/s41550-018-0566-1

Olivier, G. M., Lopez, L. A., Rosen, A. L., et al. 2020, arXiv e-prints, arXiv:2009.10079. https://arxiv.org/abs/2009.10079

Ostriker, J. P., & McKee, C. F. 1988, Reviews of Modern Physics, 60, 1, doi: 10.1103/RevModPhys.60.1

Pellegrini, E. W., Baldwin, J. A., & Ferland, G. J. 2011, ApJ, 738, 34, doi: 10.1088/0004-637X/738/1/34

Penston, M. V. 1969, MNRAS, 144, 425, doi: 10.1093/mnras/144.4.425

Pittard, J. M. 2013, MNRAS, 435, 3600, doi: 10.1093/mnras/stt1552

Pittard, J. M., Kupilas, M. M., & Wareing, C. J. 2022, MNRAS, 510, 2797, doi: 10.1093/mnras/stab3707

Portegies Zwart, S. F., McMillan, S. L. W., & Gieles, M. 2010, AR&AA, 48, 431, doi: 10.1146/annurev-astro-081309-130834

Rahner, D., Pellegrini, E. W., Glover, S. C. O., & Klessen, R. S. 2017, MNRAS, 470, 4453, doi: 10.1093/mnras/stx1532

—. 2019, MNRAS, 483, 2547, doi: 10.1093/mnras/sty3295

Raskutti, S., Ostriker, E. C., & Skinner, M. A. 2016, ApJ, 829, 130, doi: 10.3847/0004-637X/829/2/130

—. 2017, ApJ, 850, 112, doi: 10.3847/1538-4357/aa965e

Ressler, S. M., Quataert, E., & Stone, J. M. 2020, MNRAS, 492, 3272, doi: 10.1093/mnras/stz3605

Roe, P. L. 1981, Journal of Computational Physics, 43, 357, doi: 10.1016/0021-9991(81)90128-5

Rogers, H., & Pittard, J. M. 2013, MNRAS, 431, 1337, doi: 10.1093/mnras/stt255

Rosen, A. L., Lopez, L. A., Krumholz, M. R., & Ramirez-Ruiz, E. 2014, MNRAS, 442, 2701, doi: 10.1093/mnras/stu1037

Sano, T., Nishihara, K., Matsuoka, C., & Inoue, T. 2012, ApJ, 758, 126, doi: 10.1088/0004-637X/758/2/126

Scannapieco, E., & Brüggen, M. 2015, ApJ, 805, 158, doi: 10.1088/0004-637X/805/2/158

Schneider, E. E., & Robertson, B. E. 2017, ApJ, 834, 144, doi: 10.3847/1538-4357/834/2/144

Schneider, N., Simon, R., Guevara, C., et al. 2020, PASP, 132, 104301, doi: 10.1088/1538-3873/aba840

Schroeder, M. 1991, Fractals, chaos, power laws. Minutes from an infinte paradise (Dover Publications, INC.)

Silich, S., & Tenorio-Tagle, G. 2013, ApJ, 765, 43, doi: 10.1088/0004-637X/765/1/43

Skinner, M. A., & Ostriker, E. C. 2015, ApJ, 809, 187, doi: 10.1088/0004-637X/809/2/187

Smith, M. C. 2021, MNRAS, 502, 5417, doi: 10.1093/mnras/stab291

Smith, N. 2014, AR&AA, 52, 487, doi: 10.1146/annurev-astro-081913-040025

Sormani, M. C., Treß, R. G., Klessen, R. S., & Glover, S. C. O. 2017, MNRAS, 466, 407, doi: 10.1093/mnras/stw3205

Spitzer, L. 1978, Physical processes in the interstellar medium, doi: 10.1002/9783527617722

Steigman, G., Strittmatter, P. A., & Williams, R. E. 1975, ApJ, 198, 575, doi: 10.1086/153636

Stone, J. M., & Gardiner, T. 2009, NewA, 14, 139, doi: 10.1016/j.newast.2008.06.003

Stone, J. M., Gardiner, T. A., Teuben, P., Hawley, J. F., & Simon, J. B. 2008, ApJS, 178, 137, doi: 10.1086/588755

Strömgren, B. 1939, ApJ, 89, 526, doi: 10.1086/144074

Su, K.-Y., Hopkins, P. F., Hayward, C. C., et al. 2018, MNRAS, 480, 1666, doi: 10.1093/mnras/sty1928

Sundqvist, J. O., Puls, J., & Owocki, S. P. 2014, A&A, 568, A59, doi: 10.1051/0004-6361/201423570

Sutherland, R. S., & Dopita, M. A. 1993, ApJS, 88, 253, doi: 10.1086/191823

Tan, B., Oh, S. P., & Gronke, M. 2021, MNRAS, 502, 3179, doi: 10.1093/mnras/stab053

Tenorio-Tagle, G., Silich, S., Palouš, J., Muñoz-Tuñón, C., & Wünsch, R. 2019, ApJ, 879, 58, doi: 10.3847/1538-4357/ab2455

Thompson, T. A., & Krumholz, M. R. 2016, MNRAS, 455, 334, doi: 10.1093/mnras/stv2331

Thompson, T. A., Quataert, E., & Murray, N. 2005, ApJ, 630, 167, doi: 10.1086/431923

Toalá, J. A., & Arthur, S. J. 2018, MNRAS, 478, 1218, doi: 10.1093/mnras/sty1127

Townsley, L. K., Broos, P. S., Chu, Y.-H., et al. 2011, ApJS, 194, 16, doi: 10.1088/0067-0049/194/1/16

Townsley, L. K., Broos, P. S., Feigelson, E. D., et al. 2006, AJ, 131, 2140, doi: 10.1086/500532

Townsley, L. K., Feigelson, E. D., Montmerle, T., et al. 2003, ApJ, 593, 874, doi: 10.1086/376692

Tsang, B. T. H., & Milosavljević, M. 2018, MNRAS, 478, 4142, doi: 10.1093/mnras/sty1217

Turner, J. L., Consiglio, S. M., Beck, S. C., et al. 2017, ApJ, 846, 73, doi: 10.3847/1538-4357/aa8669

Utomo, D., Sun, J., Leroy, A. K., et al. 2018, ApJL, 861, L18, doi: 10.3847/2041-8213/aacf8f

Vink, J. S., de Koter, A., & Lamers, H. J. G. L. M. 2001, A&A, 369, 574, doi: 10.1051/0004-6361:20010127

Vink, J. S., & Sander, A. A. C. 2021, MNRAS, doi: 10.1093/mnras/stab902

Vishniac, E. T. 1983, ApJ, 274, 152, doi: 10.1086/161433

—. 1994, ApJ, 428, 186, doi: 10.1086/174231

Vishniac, E. T., & Ryu, D. 1989, ApJ, 337, 917, doi: 10.1086/167161

Vutisalchavakul, N., Evans, Neal J., I., & Heyer, M. 2016, ApJ, 831, 73, doi: 10.3847/0004-637X/831/1/73

Walch, S., & Naab, T. 2015, MNRAS, 451, 2757, doi: 10.1093/mnras/stv1155

Walch, S. K., Whitworth, A. P., Bisbas, T., Wünsch, R., & Hubber, D. 2012, MNRAS, 427, 625, doi: 10.1111/j.1365-2966.2012.21767.x

Wall, J. E., Mac Low, M.-M., McMillan, S. L. W., et al. 2020, arXiv e-prints, arXiv:2003.09011. https://arxiv.org/abs/2003.09011

Wareing, C. J., Pittard, J. M., & Falle, S. A. E. G. 2017, MNRAS, 470, 2283, doi: 10.1093/mnras/stx1417

Weaver, R., McCray, R., Castor, J., Shapiro, P., & Moore, R. 1977, ApJ, 218, 377, doi: 10.1086/155692

Whitmore, B. C. 2003, in A Decade of Hubble Space Telescope Science, ed. M. Livio, K. Noll, & M. Stiavelli, Vol. 14, 153–178

Whitworth, A. 1979, MNRAS, 186, 59, doi: 10.1093/mnras/186.1.59

Wolfire, M. G., & Cassinelli, J. P. 1987, ApJ, 319, 850, doi: 10.1086/165503

Wünsch, R., Palouš, J., Tenorio-Tagle, G., & Ehlerová, S. 2017, ApJ, 835, 60, doi: 10.3847/1538-4357/835/1/60

Wünsch, R., Tenorio-Tagle, G., Palouš, J., & Silich, S. 2008, ApJ, 683, 683, doi: 10.1086/589967

Yang, Y., & Ji, S. 2022, arXiv e-prints, arXiv:2205.15336. https://arxiv.org/abs/2205.15336